Viscoplastic damage analysis of plate-shell structures subjected to impact loading

Lukasz Pyrzowski

ÉCOLE DOCTORALE SCIENCES ET TECHNOLOGIE

Institut PRISME / Faculty of Civil and Environmental Engineering

THÈSE EN COTUTELLE INTERNATIONALE présentée par:

Łukasz PYRZOWSKI

soutenue le: 26 novembre 2010

pour obtenir le grade de:

Docteur de l'Université d'Orléans
et de l'Ecole Polytechnique de Gdansk

Discipline: Génie mécanique

ANALYSE VISCO-PLASTIQUE DE L'ENDOMMAGEMENT DES PLAQUES ET COQUES SOUMISES AUX IMPACTS

VISCOPLASTIC DAMAGE ANALYSIS OF PLATE-SHELL STRUCTURES SUBJECTED TO IMPACT LOADING

THÈSE dirigée par:

M. Krzysztof WOZNICA	Professeur, ENSI de Bourges
M. Paweł KŁOSOWSKI	Professeur, Ecole Polytechnique de Gdansk

RAPPORTEURS:

M. Ryszard PĘCHERSKI	Professeur, Institute of Fundamental Technological Research, Polish Academy of Sciences
M. Géry DE SAXCÉ	Professeur, Université Sciences et Technologies de Lille

---

JURY:

M. Bogdan ZADROGA	Professeur, Ecole Polytechnique de Gdansk Président du jury
M. Ryszard PĘCHERSKI	Professeur, Institute of Fundamental Technological Research, Polish Academy of Sciences
M. Géry DE SAXCÉ	Professeur, Université Sciences et Technologies de Lille
M. Krzysztof WOZNICA	Professeur, ENSI de Bourges
M. Paweł KŁOSOWSKI	Professeur, Ecole Polytechnique de Gdansk

Acknowledgements

The author is extremely grateful to supervisors prof. Paweł Kłosowski and prof. Krzysztof Woznica for care and introducing to the world of scientific research. He appreciates all long discussions and remarks, which have made creating of this work possible.

Special thanks are addressed to prof. Krzysztof Woznica for the warmly welcoming in Bourges and to Olivier Pennetier for all his help during realization of the laboratory test program.

The author would like to thank prof. Jacek Chróścielewski for all accurate remarks and comments.

All presented numerical simulations were performed by computers of the Academic Computer Centre in Gdansk (CI TASK).

Finally, the author thanks his dear family and friends for their faith and support.

Contents

1. Introduction

1.1. Foreword

The main problem, which is considered in this work, is the investigation of plate-shell structures response due to impact loadings caused by gas mixture explosions. This rather complex phenomenon is studied in the context of its mechanical aspects. The main field of interest is the ductile fracture prediction, which occurs in impact subjected plate-shell structures during their inelastic dynamic response. This phenomenon can be assigned to the field of failure mechanics. A primary problem of this domain is associated with formulation of sufficiently simple and accurate criterion of crack initiation and propagation for both regular and singular stress concentrations in structural elements involving multiaxial stress states. The design against failure is a fundamental importance in everyday engineering practice. The area of potential applications is very wide. Starting from the assessment of safety against the damage threat posed by internal explosion on-board commercial aircrafts in the aeronautical industry, through assuring the reliability against the metallic pressurised vessels accidents caused by explosions or ductile tearing of pipelines in the industrial transport or storage of fluids, the metal-forming processes such as stamping and extrusion in aluminium and steel industries (also automotive engineering), army applications, such as a ballistic penetration – projectile impact of steel plates, finishing with the general problems of life prediction and many others. The presented work focuses on the experimental investigations, modelling and numerical simulations of the considered problem. The different model analyses, verifications and comparison studies give the field to discuss and to draw conclusions.

1.2. Aim and range

The following aim and range have been stated for this work:

- The literature review concerning the area of different approaches to failure designing, especially the numerical fracture modelling in ductile materials;
- Elaborating the effective subroutines (in FORTRAN for MSC.MARC system) for geometrically and physically non-linear analysis including damage and fracture criterions;
- Creating and executing the laboratory tests program incorporating the experiments on the plates subjected to explosions and uniaxial experiments necessary for material parameters identification;

- Performing the identification of material constants for the assumed constitutive model, their verification, calibrating the fracture criterion parameters;
- Creating the plate's model;
- Performing the example numerical simulations with different fracture criterions, the verifications by comparing obtained results to experiments;
- The discussion of results and conclusions.

1.3. Literature review

The first studies, which have begun the scientists' interest in the failure designing, are the works of Wieghardt [188], Inglis [82] and Griffith [71], [72] from the early 1920s. In that time Griffith has developed the original concept of fracture energy, which is assumed as the beginning of the fracture mechanics. His first hypothesis was that brittle materials contain elliptical microcracks, which introduce high stress concentrations near their tips. The Griffith's work was ignored by the engineering community for almost thirty years. In the 1950s, the extension of his theory was provided by Irwin [83]. He extended the model to an arbitrary crack and proposed the criterion for its growth. Irwin also showed that the stress field in the area of crack tip is completely determined by the parameter K (stress intensity factor) related to the three different crack opening modes. After Irwin the further development of the Griffith's model was continued. In 1957 McClintock and Walsh [122] introduced the friction between crack faces, in 1959 Barenblatt [16] and in 1960 Dugdale [60] made the first attempts at including the cohesive forces in the crack tip region, in 1961 Kaplan [91] focused on the possibility of applying the fracture model to concrete. In the late 1960s the first extensions to ductile fracture processes was initiated. Rice [147] showed that the energy release rate can be expressed as a path-independent line integral called the J-integral. Wells [185] proposed a parameter called crack tip opening displacement. One of the first fracture mechanics finite element applications was performed in 1976 by Hillerborg et al. [80]. They proposed the model where the constitutive relation is described by a material softening law between tensile stress and local opening, instead of a stress versus strain relation. Recent trends in fracture mechanics include dynamic investigations on nonlinear materials, fracture mechanics of microstructures and modelling related to local, global and geometry-dependent fractures.

Nowadays, fracture mechanics concerned in the lifetime analyses of structures creates a huge part in the solid mechanics domain. Unfortunately, it has still one crucial limitation. In

general, a structural fracture may be decomposed into two steps: the crack initiation, and the crack propagation. The classic fracture mechanics has been developed to study the evolution of a pre-existing crack. This causes that the stage of crack initiation in this approach is quite problematic.

While the fracture mechanics theories were being developed, in 1958 the new approach to the failure designing was formed. The pioneer of the new idea was Kachanov [88]. He introduced a damage variable to describe the microdefect density locally in a creeping material. The notation was that that damage could be measured by the volume fraction of voids. This became the fundament to continuum damage mechanics. One year later Rabatnov [146] furthered this idea with the evolution of void density equations based on the concept of effective stress in damaged materials. The first paper in English, which described the new theory, was published by Odqvist and Hult [135] in 1961. The later more known publications are Chaboche [41] in 1981 presenting the general theory and several applications to a turbine blade refractory alloy, Murakami [129] in 1983 discussing the notion and the practical procedures, Lemaitre and Chaboche [112] in 1990 the monograph of solid mechanics, containing one chapter with the description of damage theory and Lemaitre [109] in 1996 presenting a course on damage mechanics.

The key concept for this theory is the damage evolution law obtained from the thermodynamic potential and the potential of dissipation. The shape of second potential has not been well established in literature, during the theory development different damage evolution laws were proposed. The first after the pioneers was Lemaitre [111] who in 1984 introduced the most popular till now damage evolution equations for the ductile damage. After him many other models occurred: in 1986 Tai and Yang [165], in 1992 Wang [184], in 1993 Chandrakanth and Pandey [44], in 1997 Bonora [28], in 2000 Armero and Oller [9], Dhar et al. [57], in 2004 Lin et al. [114].

The continuum damage is not limited to ductility only. It was also applied in the analyses of brittle materials like rock by Shao and Khazraei [154], concrete by Flórez-López [65], Peng and Meyer [139], Faming and Zongjin [63], Kuna-Ciskał and Skrzypek [103], graphite by Kaji et al. [89], laminates and composites by Maire and Chaboche [119], Allen [3], Edlund and Volgers [61] and even of a human bone by Taylor et al. [167].

The original concept of damage mechanics was created for an isotropic material, in such case the damage variable is represented by a scalar value. At the beginning of 1980s the first efforts have been done to find realistic models to describe anisotropic damage phenomena. As the first attempt, the vectorial damage variables were introduced by Kracinovic and Fonseka

[98], [99]. In further attempts, two approaches were proposed. The general anisotropy model, where the damage variable is represented by the fourth order tensor, analyzed by Lecke and Onat [105], Chaboche [40] and Kracinovic [97] and the simplified orthotropic model, where the damage variable is represented by the second order tensor, analyzed by Murakami and Ohno [130], Chow and Wang [46], Voyiadjis and Kattan [182] and Lemaitre [110]. In the anisotropic damage modelling the effective stress tensor is usually non-symmetric. The solution avoiding a complicated theory is the symmetrisation of this tensor. Such procedure was analyzed by Lu and Chow [116] or Voyiadjis and Park [183].

The further extension of continuum damage mechanics was done by deriving a large strain theory in elastic-plastic damage analysis. In 1990 Combescure and Yin [52] proposed a generalization of the discrete Kirchhoff theory to the analysis for large displacement and large strain with some applications to damage mechanics. At the beginning of 2000s a theory for large strain in elastic-plastic damage was analyzed by Brünig [37]. He used a multiplicative decomposition of the metric transformation tensor into elastic and damage-plastic parts. In the same time Menzel and Steinmann [124] proposed a theoretical and computational model for the treatment of anisotropic damage at large strains, Kaliske et al. [90] introduced the constitutive relations for elastometric materials large strain modelling.

In the damage modelling the essential problem is the experimental identification of the damage variable evolution. The reliable measurement is still nowadays a challenging task. In 1987 Lemaitre and Dufailly [113] described possible approaches. The experimental procedures to estimate the damage evolution can be classified in two main groups direct and non-direct measurements, where this last group can be divided to destructive and non-destructive methods. The practical examples of identifications using the results of load-unload tensile tests were presented by Amar and Dufailly [5], Alves et al. [4], Mashayekhi et al. [120] and Ambroziak [6]. Recently this problem was also analyzed by Celentano and Chaboche [39], they proposed a new procedure of damage measurement including the correction factor eliminating the triaxial effects occurring during experimental tension tests.

The continuum damage mechanics has began the continuous, micromechanical approach in the failure designing. It made this kind of modelling more attractive then global, discontinuous approaches such as fracture mechanics because the model parameters depend on the material only, not on the geometry. The theory based on such assumptions is also better adapted to the analysis of the crack initiation in a crack-free body.

But damage mechanics is not the only approach, which has been developed on the basis of micromechanical models. Soon after the continuum damage theory pioneers in the late 1960s

McClintock [121] and Rice and Tracy [148] studied the role played by growth of microvoids in ductile fracture. This new idea has began the new group models, sometimes called the porosity models, based on the observation that ductile damage develops at microstructural level in form of voids and cavities, which may grow differently according to the plastic strain and the stress triaxiality level. From a general point of view, in these models, porosity has the major effect to shrink the material yield surface with the progression on the deterioration process. The failure was postulated to occur when the cavity radius would reach a critical value specific for the material.

On the basis of this new theory in the middle of 1970s Gurson [74], [75] developed the widely known pours ductile material model and fracture model. At the beginning of 1980s the modifications introduced by Tvergaard [172], [173] and Tvergaard and Needleman [174] made this model more complete. The initial formulation was extended to include the acceleration in the failure process induced by void coalescence. In 1985 Thomason [170] proposed the plastic limit load model for void coalescence. In 2001 Zhang [200] integrated the models of Gurson and Thomason and proposed a so-called complete Gurson model. The similar model to Gurson's but with a slightly different dependency in the hydrostatic term was proposed by Rousselier [151] in 1987. In 1992 Besson and Abouaf [24] extended the modified Gurson model to viscoplasticity. In 1993 Gologanu et al. [70] proposed the modification by introducing a void shape parameter, which allowed considering the anisotropic damage effects in cavity based modelling. This idea was further used also by Benzerga et al. [23], Siruguet and Leblond [158].

Recently the micromechanical studies have been performed in order to correlate voids evolution and interaction with the resulting macroscale material yield function. The role of smaller size voids in a ductile damage was investigated by Tvergaard and Niordson [175] and incorporated into the Gurson model by Wen et al. [186]. The 3D voided unit cell based approach investigating the role and effects associated with the crystallographic orientation of the matrix material was analyzed by Schacht et al. [153]. Bonfoh et al. [27] used the modified Gurson theory to model damage evolution initiated by secondary included particles debonding in a policrystaline material.

The Gurson model for a single material involves over ten parameters, which need to be calibrated. The material parameters are not physically based and cannot be directly measured. Typically, an iterative calibration procedure, involving numerical simulations and experimental data is necessary. In 1998 an attempt of the parameters calibrating was made by Faleskog et al. [62], [68]. Later Rivalin et al. [149] determined the parameters by comparing

tests on experimental samples with the finite element simulation, Prahl et al. [144] used a period homogenization approach, Springmann and Kuna [160], [161] developed a non-linear optimization identification procedure.

The results of experiments performed by Shockey et al. [156] have shown that coalescence mechanism can be treated as a nucleation and growth process on a smaller scale. This simplifies the description (also identification) of the intrinsic micro-damage process by taking into account only the nucleation and growth mechanism. Such approach was used by Łodygowski and Perzyna [117] in investigation of the fracture in the polycrystalline solids under dynamic loading process.

The porosity damage models are related to a specific micromechanism of failure, this is the main deference between this theory and the continuum damage models presented earlier, where damage is one of the thermodynamics variables that affect the material stiffness. One of the similarities is that both approaches are called the fully coupled, which means that the damage effect is introduced directly into the overall constitutive equations and affects all the thermomechanical fields according to the appropriate coupling theory.

The third and up till now last group in ductile failure modelling, which has been developed on the basis of micromechanical models is the approach called abrupt failure criteria. These criteria predict the occurrence of failure in the material when a chosen parameter in a model reaches its critical value or a criterion is satisfied. In this approach no coupling exists between the variable that accounts for progressive damage and other variables as strain, stress, etc. The concepts of McClintock [121] and Rice and Tracy [148], the initial studies in the porosity models, can be also joined to this group. In their work the parameter, which is characteristic and the fracture occurs when it reaches critical value is the cavity volume fraction.

During the development of abrupt failure methods many criteria have been formulated. In the 1950 Freudenthal [67] proposed the criterion of total plastic work, which postulates that the initiation and propagation of a crack is dominated by a critical value of the absorbed plastic energy. The simple criterion predicting the occurrence of failure in the moment when the equivalent plastic strain reaches a critical value was used by Datsko in 1966 [54]. In 1968 Cockcroft and Latham [51] postulated that fracture is controlled by maximum principal tensile stress integrated over the plastic strain path. This last criterion was modified in 1972 by Brozzo et al. [36], who introduced an explicit dependence on hydrostatic stress, in 1979 by Oh et al. [136], who introduced the normalization of the maximum principal tensile stress by the equivalent stress and in 1990 by Clift et al. [49], who replaced the maximum principal

tensile stress by the equivalent stress. In 1978 Norris et al. [131] proposed en empirical criterion based only on the hydrostatic stress and one material constant. In 1981 Atkins [10] modified the last criterion by introducing an explicit dependence on the deformation path. In 1985 Johnson and Cook [85] is postulated that the critical equivalent fracture strain is a monotonic function of the stress triaxiality. This model has become very popular in commercial codes, since in 1989 Johnson and Holmquist [86] published a table of material fracture data for a number of structural materials. In 2004 Bao and Wierzbicki [14], [15] studied the model based on assumption that fracture initiates at the critical point of a structure when the accumulated equivalent plastic strain with a suitable triaxiality weighing functions reaches a critical value. In this works they determined these functions in the wide range of stress triaxiality from eleven different tests. In 2005 Wierzbicki et al. [191] presented calibration and evaluation of seven most popular fracture models. In 2010 Bai and Wierzbicki [12] proposed the ductile fracture criterion, where the Mohr-Coulomb model [128], [53] is used. A large majority of the criterions presented in this group belongs to empirical methods, based on extensive test programs. Their calibration for new materials sometimes requires comprehensive series of experiments involving tensile tests on unnotched and notched bars, upsetting tests and sheer tests.

Recently, in the failure analysis new models, which links the different approaches classified in groups presented above, occurred. In 2001 Chaboche et al. [43] introduced interface damage mechanics developed as a part of continuum damage mechanics, with capabilities intermediate between the damage and fracture mechanics. The main reason of developing this model is simulating various scales of composite debonding effects, such as decohesion between matrix and fibres and delamination in laminates. In 2006 Chaboche et al. [42] proposed a continuum damage mechanics approach with plastic compressibility. This model modified the classical formalism of damage mechanics in order to describe plastic compressibility in the context of ductile damage. A new damage state variable was introduced. This variable plays role of porosity in micromechanics based approaches like Gurson's model. In 2007 Xue [199] proposed a new damage plasticity model. Fracture is postulated to occur when the accumulated equivalent plastic strain, modified by the function of the stress triaxiality and the deviatoric state parameter reaches a limiting value equal to one. This model has a construction similar to the abrupt failure methods, however introducing additionally the material weakening mechanism into the constitutive model by coupling the yield function and associated flow rule with the damage, moves it into the coupled methods.

Since the beginning of numerical methods development researchers have tried to simulate the damage and fracture process. Many methods have been proposed to implement the presented above models.

The example of the fracture mechanics implementation is the nodal relaxation method used frequently in the finite element analysis. The crack is modelled by releasing nodes one by one in order to enable the crack tip to propagate through the mesh. This method very often is improved by the advanced remeshing techniques. The simulations of this kind were performed in 1998 by Trädegård et al. [171] using characterization of the crack tip fields strength by the value of J-integral, in 2000 and 2003 by Bouchard et al. [35], [34] applying different crack propagation criteria, in 2001 by Andersson et al. [8] using the calculation of first mode stress intensity factor, in 2008 by Souiyah et al. [159] using the displacement extrapolation method [73] to calculate the stress intensity factors.

The other technique to simulate the propagation is the cohesive element approach. The cohesive elements originate from the concept of cohesive zone [60], [17]. In these type elements the numerical separation process is described by the cohesive law, which defines the relation between crack surface traction and the surface opening displacement. This technique was used in 1994 by Xu and Needleman [197] and in 1999 by Miller et al. [126] to simulate crack growth in brittle solids, in 2005 by Cirak et al. [50] to analysis the fracture and fragmentation in thin-shells, in the same year by Zhou et al. [201] to simulate the dynamic crack propagation in brittle materials using the cohesive rate-dependent model.

In contrast to above methods, where cracks are limited to element boundaries, the extended finite element method (X-FEM) has been developed. Here the concept of the discontinuous displacement has been incorporated within a finite element formulation based on the partition of unity concept [11]. The displacement discontinuities are represented by means of additional degrees of freedom. Cracks can be located arbitrarily in the finite element mesh. The first applications of this approach were done in 1999 by Belytschko and Black [19] and Moës et al. [127]. The comprehensive survey of the extended finite element method was done by Abdelaziz and Hamouine [1]. Recently this method was used by Meschke and Dumstorff [125], Belytschko and Gracie [20], Benvenuti [22], Xu and Yuan [198].

The failure modelling approaches are based also on other methods then the finite element analysis. The two examples can be given. The first is the meshless method. Its application to the fracture prediction was proposed in 1995 by Belytschko and Lu [21]. Up till now there have been quite a few works using this method. The examples are: Hao et al. [79], Rabczuk and Belytschko [145], Bordas et al. [30], Duflot and Nguyen-Dang [59]. The second example

is the boundary element method used in the fracture mechanics: Carpinteri et al. [38], Frangi [66].

The most popular approach in the ductile fracture numerical modelling is performing analysis using the classic finite element method. The crack initiation and propagation is modelled by deactivation/deleting elements which fulfil the assumed fracture criterion. One of the firsts authors, who applied this method are Taupin et al. [166] in 1996. They simulated the blanking in the metal forming process using the McClintock criterion and compared the results with experiments, reaching a relatively good correlation. Further many others followed the same method. In 2001 Besson et al. [25] simulated the cup-cone fracture in round bars and plane strain specimens using the Gurson and Rousselier models. In 2008 Teng [169] analyzed the same phenomenon using the continuum damage mechanics. He compared his results with experiment. In 2003 Børovik et al. [32] analyzed the influence of stress triaxiality and strain rates on the basis of the tension tests performed on the smooth and notched specimens using in simulations the Johnson-Cook criterion. In 2005 Bonora et al. [29] performed similar analysis of the stress triaxial state influence. They used their own non-linear continuum damage model and compared the results of simulations with experiments. In 2007 Xue [199] simulated the tension tests of the smooth specimens with emphasis on crack path prediction using his own model.

The alternative approach to element deactivation in the finite element method is changing the material parameters in elements, which are considered as broken/damaged. Rivalin et al. [149], who analyzed ductile tearing of the pipeline-steel wide plates using the extended Gurson-Tvergaard-Needleman model, proposed replacing the behaviour of broken elements by an elastic behaviour with very low stiffness (the value of Young modulus of 1 MPa). Hambli and Badie-Levet [77] and Hambli [76], who simulated fracture prediction during extrusion and sheet-metal blanking process using the continuous damage mechanics, proposed increasing abruptly in the damaged elements the value of damage parameter from critical to the value near 1, decreasing considerably their stiffness.

The extension of presented approach is applying the adaptive remeshing to the finite element method. This additional procedure is due to the large geometrical distortion of finite elements and the adaptation to the physical behaviour of the solution. Recently this kind of analysis became very popular. In 2002 Børovik et al. [33] presented the simulation of the thick steel plates perforation with the different shape noses using the continuum damage model with own modifications. The simulations were performed with fixed and adaptive mesh, the results were compared with experiments reaching close correlation. In the same

year, Borouchaki et al. [31] used adaptation of the element size with respect to the damage in metal forming fracture prediction. In 2005 Lee and Wierzbicki [107] simulated fracture prediction of thin plates under localized impulsive loading. They compared analytical and numerical solutions for discing and petalling phenomena. In numerical analysis they used Bao and Wierzbicki fracture criterion and both fixed and adaptive mesh methods. In 2008 Labergere et al. [104] and Saanouni [152] used this method in simulation of metal forming using the continuum damage mechanics.

The finite element method is nowadays the most popular and powerful tool in mechanics, including the damage and fracture analysis. A large majority of researchers use this method in the local approach, unfortunately sometimes it causes problems. One of them is the pathological localization and mesh dependence associated with materials softening. This problem is essential in quasi-brittle materials but also important in the ductile failure. The solution, which attempts to overcome this problem, is applying the non-local models including the regularization techniques. The examples of such approach are the works of Łodygowski and Perzyna [118], who used the relaxation time as a regularization parameter in thermoviscoplasticity theory, Addessi et al. [2], who analyzed a plastic non-local damage model for cementious materials, Rodriguez-Ferran et al. [150], who proposed a new damage model based on non-local displacements and presented two versions of application: integral-type and gradient, Mediavilla et al. [123], who introduced the discrete crack modelling of ductile fracture driven by non-local softening plasticity.

The present work focuses attention on the experimental and numerical investigation on the behaviour of circular metallic plates subjected to impulse loadings. The problem of plates responses to dynamic loads have been already analyzed by many authors. The first studies were concerned on experimental and analytical analysis of permanent deformations in plates subjected to uniformly distributed impulses. Florence [64] in 1966 performed an analytical solution for simply supported circular plates based on the bending theory of rigid-plastic plates and compared results to experiments. Jones [87] in 1968 considered taking into account membrane stresses in a study of simply supported circular plates. Wierzbicki [190] in 1954, Perrone [141] in 1967, Kelley and Wilshaw [92] in 1968, Wierzbicki and Florence [192] in 1970 considered in analysis a viscoplastic theory taking into account the large deflections and strain rate sensitivity comparing results with experiments. The displacement of the plate's centre as a function of time during dynamic response on explosive loadings was examined by Duffey [58] in 1967. Bodner and Symonds [26], Symonds and Chon [164] both in 1979 applied the mode approximation technique to simulate large deflections of viscoplastic

structures and compared results with experiments on circular plates loaded impulsively. Nurick [132] in 1985 proposed a new experimental technique involving the use of light interference, which improved the deflection time history measurement of plates subjected impulsively. Nurick and Martin [133] in 1989 discussed their experimental results and presented an empirical relationship between the deflection-thickness ratio and a function of impulse, plate geometry, plate dimensions and material properties. The dynamic response of shock wave subjected plates was also analyzed by Pennetier and Renard [140] in 1998, Kłosowski et al. [96] in 2000, Woznica and Kłosowski [195] in 2000, Woznica et al. [196], Jacinto et al. [84], Stoffel et al. [163] all in 2001, Veldman [180] in 2006, Wiśniewski et al. [194] in 2007 and many others.

Recently more often, beside the dynamic response, also the fracture prediction in plates is investigated. Teeling-Smith and Nurick [168] in 1991 performed experiments conducted on fully clamped circular mild steel plates subjected to a uniformly distributed impulse and analyzed numerically the deformation and tearing. Olson et al. [137] in 1993 analyzed the experimental and numerical results of the fracture initiation in clamped square mild steel plates subjected to uniformly distributed blast pressure loading. Wierzbicki [189] in 1999 presented analytical solutions for plate's petalling under explosive and impact loading. Kreja et al. [102] in 2001, Kreja and Schmidt [101] in 2004 modelled the plastic ductile damage evolution and collapse of plates and shells in the quasi-static conditions. Shen [155] in 2002 studied experimentally and theoretically the failure of circular plates struck by masses. Lee et al. [108] in 2004 analyzed numerically the fracture in thin plates under hemi-spherical punch. Day et al. [56] in 2006 performed the fracture experiments on projectile impact of steel plates. Daudonnet [55] in 2006 considered in numerical analysis the fracture of plates subjected to explosions. Stoffel [162] in 2007 analyzed the anisotropic ductile damage and failure of shock wave-loaded plates. Veldman [179] in 2008 investigated experimentally the effects of pre-pressurization on fracture in blast-loaded reinforced rectangular aluminium plates. Pęcherski et al. [143] in 2009 studied the effect of strain rate on ductile fracture in the dynamic double shear tests with thermographic observations.

The author is aware of the fact that the presented literature review does not exhaust the full state of art in the analyzed field. Despite the relatively young age of this solid mechanics sub-discipline in the last decades high interests among researchers caused very fast development. The intention of the author of this review is to present the approaches which had significant influence on the discipline evolution and which are widely used in the fracture

modelling. For each mentioned method only a limited number of publications is presented, of course those are only examples among many others.

2. Theoretical foundations

2.1. Abstract

This chapter contains the description of models, which are in common use in damage and fracture mechanics analysis. Firstly, the assumed constitutive model is presented. Further, the examples of different approaches to the failure modelling are discussed. Four main groups are here distinguished and described: fracture mechanics, continuum damage mechanics, the porous solids plasticity models and the abrupt failure criteria. The selection of models, which are considered in further analysis, is finally done.

2.2. Introduction

One of the main parts of this work is the numerical simulation of the plates subjected to impact loadings. The plates are submitted to large plastic deformations and fracture. Such analysis requires applying non-linear material models. Initially, an appropriate constitutive law should be chosen. The author used the earlier experiences of the researchers who were interested in the shock wave-loaded plates behaviour analysis: Kłosowski et al. [96], Woznica and Klosowski [195], Woznica et al. [196], Stoffel [162], Stoffel et al. [163], and decided to use, descended from the model of Perzyna [142], the viscoplastic model proposed by Chaboche [112]. This model was successfully employed by the mentioned authors. Its main advantage is universality. Of course before application to the current problem an appropriate identification of material parameters and its results verification should be performed. Secondly, the choice of a suitable fracture model and criterion describing correctly the initiation and propagation of cracks should be done. Here different approaches are considered, some of them are chosen to the numerical analysis applications.

2.3. Constitutive model

The chosen constitutive model in the considered study is based on two main assumptions: the material is isotropic and the strains are small. The second condition allows employing the additive decomposition of the strain rate into its elastic and inelastic parts

$$\dot{\boldsymbol{\varepsilon}}=\dot{\boldsymbol{\varepsilon}}^{E}+\dot{\boldsymbol{\varepsilon}}^{I}, \tag{2.1}$$

where $\dot{\boldsymbol{\varepsilon}}$ is the total strain rate, $\dot{\boldsymbol{\varepsilon}}^{E}$ and $\dot{\boldsymbol{\varepsilon}}^{I}$ are the elastic and inelastic strain rates.

	State variables		Associated variables
	Observable variables	Internal variables	
Elasticity	Temperature, T Total strain, $\boldsymbol{\varepsilon}$		Specific entropy, S Stress, $\boldsymbol{\sigma}$
Viscoplasticity		Inelastic strain, $\boldsymbol{\varepsilon}^I$ Isotropic hardening, r Kinematic hardening, $\boldsymbol{\alpha}$	Stress, $\boldsymbol{\sigma}$ Isotropic hardening stress, R Kinematic hardening stress, $\mathbf{X}$

Tab. 2-1. Summary of the state and associate variables

The derivation of the constitutive equation for a given material can be done in the framework of the thermodynamics of irreversible phenomena through a certain number of so-called state variables. These variables distinguished into observable and internal and their associated variables are presented in Tab. 2-1. For the material characterization introducing the thermodynamic potential, from which the state laws can be derived, is necessary. Usually the Helmholtz free energy ψ, which is a scalar function of all state variables, is used. The expression of the state potential can be determined taking into account the state coupling between variables. It is possible to uncouple the state potential into the elastic behaviour and inelastic (hardening), with the specific free energy being decomposed as

$$\psi = \psi^E(\boldsymbol{\varepsilon}^E, T) + \psi^I(\mathrm{a}, r, T). \tag{2.2}$$

The elastic part of the free energy function can be expressed as follows

$$\psi^E = (1/2\rho)\left(\mathbf{a}:\boldsymbol{\varepsilon}^E:\boldsymbol{\varepsilon}^E\right), \tag{2.3}$$

where ρ is the material density, $\mathbf{a}$ is an elasticity tensor. By the definition of the associated variable, the stress can be derived from the potential ψ^E to give the law of state

$$\boldsymbol{\sigma} = \rho\frac{\partial\psi^E}{\partial\boldsymbol{\varepsilon}^E} = \mathbf{a}:\boldsymbol{\varepsilon}^E. \tag{2.4}$$

The elastic strain can be evaluated by reversing the equation (2.4)

$$\boldsymbol{\varepsilon}^E = \frac{1+\nu}{E}\boldsymbol{\sigma} - \frac{\nu}{E}Tr(\boldsymbol{\sigma})\mathbf{I}, \tag{2.5}$$

where E is the elastic modulus, v is the Poisson's ratio and $\mathbf{I}$ is the metric tensor.

The thermodynamic state potential allows writing relations between observable state variables and associated variables. For the internal variables it allows only to definite their associated variables. To describe the evolution of the internal variables (the dissipation

process) the dissipation potential function (a positive convex function of associated thermodynamic variables) φ^* is needed

$$\varphi^* = \Omega(\boldsymbol{\sigma}, R, \mathbf{X}). \tag{2.6}$$

The complementary law of evolution is expressed by the normality property

$$\dot{\boldsymbol{\varepsilon}}^I = \frac{\partial \Omega}{\partial \boldsymbol{\sigma}}. \tag{2.7}$$

To describe the evolution of the inelastic strain the viscoplastic constitutive Chaboche model was chosen. In this model the dissipation function Ω is defined as

$$\Omega = \frac{K}{n+1}\left\langle \frac{J\left(\boldsymbol{\sigma}' - \mathbf{X}'\right) - R - k}{K} \right\rangle^{n+1}, \qquad J(a_{ij}) = \sqrt{\tfrac{3}{2} a^{ij} a_{ij}}, \tag{2.8}$$

where $\boldsymbol{\sigma}'$ and $\mathbf{X}'$ are the deviatoric parts of the stress and kinematic hardening tensors, respectively, k is the initial yield stress, K and n are the viscous material parameters. The angle brackets $\langle x \rangle$ are referred to the McCauley brackets: $\langle x \rangle = \frac{1}{2}(x + |x|)$.

The inelastic strain rate is derived from the equation (2.7) earlier substituted by (2.8)

$$\dot{\boldsymbol{\varepsilon}}^I = \frac{3}{2}\dot{p}\frac{\boldsymbol{\sigma}' - \mathbf{X}'}{J\left(\boldsymbol{\sigma}' - \mathbf{X}'\right)}, \tag{2.9}$$

where accumulated plastic strain rate $\dot{p}$ is given by

$$\dot{p} = \left\langle \frac{J\left(\boldsymbol{\sigma}' - \mathbf{X}'\right) - R - k}{K} \right\rangle^{n}. \tag{2.10}$$

The kinematic hardening tensor $\mathbf{X}$ and the isotropic hardening scalar R are expressed as

$$\dot{\mathbf{X}} = \frac{2}{3} a \dot{\boldsymbol{\varepsilon}}^I - c\mathbf{X}\dot{p}, \quad \dot{R} = b(R_1 - R)\dot{p}, \tag{2.11}$$

where a, c, b and R_1 are hardening material parameters.

2.4. Damage and fracture models

2.4.1. Fracture mechanics

In the fracture mechanics field of interest are all kind of defects understood as the stress concentrators in the form of cracks, flaws or notches. The problem is to study an influence of applied loads, defects geometry, environmental conditions and a material behaviour on the fracture process in solids. The fracture mechanics is the powerful tool in the crack

propagation analysis but it avoids the problem of the crack initiation, which is very important for this work. That is why only the brief review of these mechanics field foundations are presented here.

The first approach in the fracture mechanics is the energy criterion, which states that the crack extension occurs when the energy available for the crack growth is sufficient to overcome the resistance of a material. This approach was proposed by Griffith [71], [72] and later developed by Irwin [83]. For example, in an infinite plate presented in Fig. 2-1, subjected to remote tensile stress for the crack of length $2a$ the energy realise rate G is given by [7]

$$G_e = \frac{\pi\sigma^2 a}{E}. \tag{2.12}$$

At the moment of fracture $G_e = G_{ec} = 2\gamma$, where G_{ec} is the critical energy realise rate – the material's resistance to fracture and γ is the energy necessary to create the unit of a free surface.

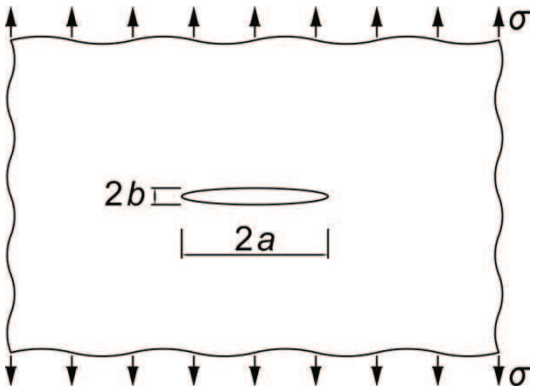

Fig. 2-1. Infinite plate with the elliptic crack under tension stress

The alternative to energy criterion is the stress intensity approach based on the stress function used to determination of the stress and displacement field near the crack tip proposed by Westergaard [187]. In this approach three ways of applying a force to enable a crack to propagate are distinguished (Fig. 2-2):

mode I – opening, a tensile stress normal to the plane of the crack,

mode II – sliding, a shear stress acting parallel to the plane of the crack and perpendicular to the crack front,

mode III – tearing, a shear stress acting parallel to the plane of the crack and parallel to the crack front.

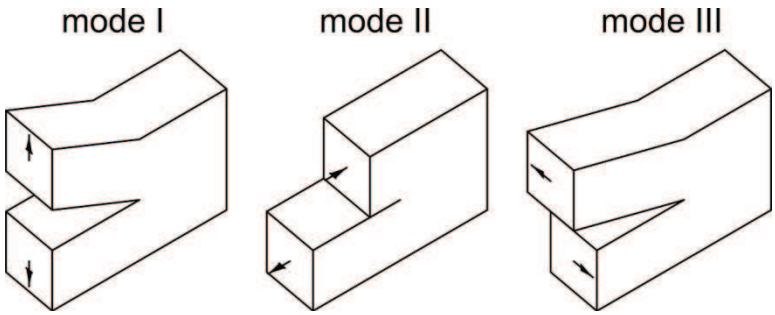

Fig. 2-2. Types of cracks loadings

For each type of the crack loading the following stress field responds [7]

$$\sigma_{ij}^{T} = \frac{K_T}{\sqrt{2\pi r}} f_{ij}^{T}(\theta),\ T = I, II, III, \tag{2.13}$$

where r and θ are the polar coordinates with the beginning point in the crack tip, K_T is the stress intensity factor for each type of the crack.

As the example the stress and displacement fields near the tip of mode I crack in the infinite plate under plane-stress conditions, shown in Fig. 2-3, are presented.

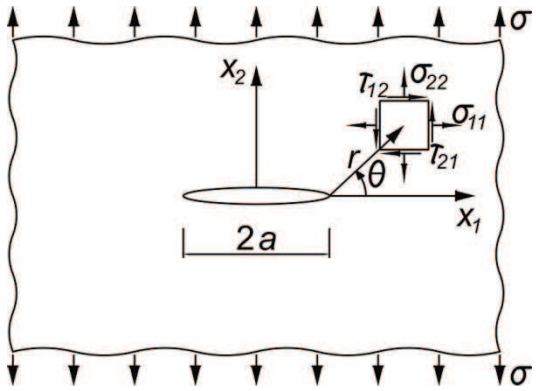

Fig. 2-3. Stress field near the crack tip in infinite plate

The stress components are expressed by the following formulas

$$\begin{aligned}
\sigma_{11} &= \frac{K_I}{\sqrt{2\pi r}} \cos\frac{\theta}{2}\left(1 - \sin\frac{\theta}{2}\sin\frac{3\theta}{2}\right),\\
\sigma_{22} &= \frac{K_I}{\sqrt{2\pi r}} \cos\frac{\theta}{2}\left(1 + \sin\frac{\theta}{2}\sin\frac{3\theta}{2}\right),\\
\tau_{12} &= \frac{K_I}{\sqrt{2\pi r}} \cos\frac{\theta}{2}\sin\frac{\theta}{2}\cos\frac{3\theta}{2}.
\end{aligned} \tag{2.14}$$

The displacements are defined as

$$u_1 = \frac{K_I}{E}\sqrt{\frac{r}{2\pi}}\cos\frac{\theta}{2}\left(3-\nu-\left(1+\nu\right)\cos\theta\right),$$
$$u_2 = \frac{K_I}{E}\sqrt{\frac{r}{2\pi}}\sin\frac{\theta}{2}\left(3-\nu-\left(1+\nu\right)\cos\theta\right). \tag{2.15}$$

The stress intensity factor in this case is given by

$$K_I = \sigma\sqrt{\pi a}. \tag{2.16}$$

The displacement of crack edges in its area (Fig. 2-4) is defined by

$$[\![u_2]\!] = \frac{2}{E}\sigma\sqrt{a^2 - x_1^2}. \tag{2.17}$$

The maximum displacement called the crack opening displacement *COD* occurs in the half length of the crack

$$COD = \frac{4}{E}\sigma a. \tag{2.18}$$

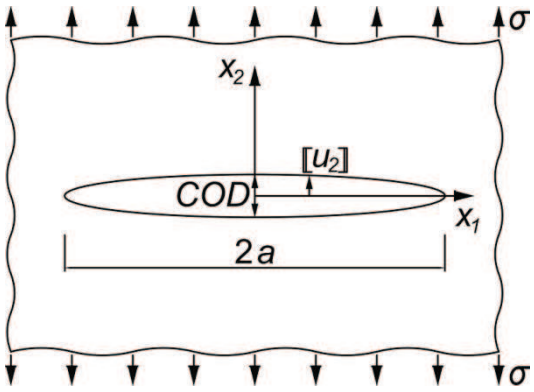

Fig. 2-4. Crack edges displacement

Of course, for the other crack types, body dimensions and stress conditions different formulas not discussed here describing the stress and displacement fields are necessary.

In the stress intensity approach the failure occurs when $K_I = K_{Ic}$, where K_{Ic} is a fracture toughness (a measure of material resistance) determined by experiments.

The energy and stress intensity approaches represents the methods of linear elastic fracture mechanics, the extension to the plasticity was proposed by Rice [147], who applied the path-independent *J*-integral to the analysis of conditions for a crack propagation. The integral is defined as follows (Fig. 2-5)

$$J = \int_\Gamma \left(W dx_2 - \mathbf{p}\frac{\partial \mathbf{u}}{\partial x_1} ds \right), \tag{2.19}$$

where Γ denotes a curve surrounding the crack tip, **p** is the surface force vector, **u** is the displacement vector and *W* is the strain energy density

$$W = \int_0^{\boldsymbol{\varepsilon}} \boldsymbol{\sigma} : d\boldsymbol{\varepsilon}. \tag{2.20}$$

The physical interpretation of the *J*-integral is the rate of change of potential energy with respect to the incremental change of the crack length.

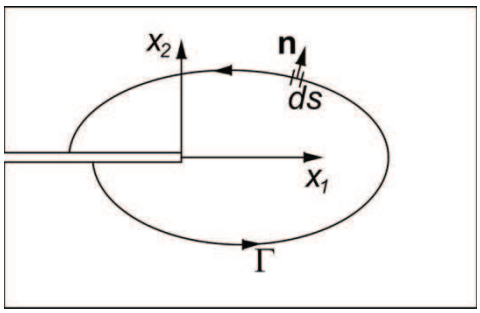

Fig. 2-5. Two-dimensional cracked body

The *J*-integral in the non-linear fracture mechanics has a similar task as the stress intensity factor in the linear mechanics. It determinates the field of stress near the crack tip. As the *J*-integral is path-independent, usually the easiest possible contour Γ, which is the circle with radius *r*, is being chosen. In such case the stress field is given by the following formula [69]

$$\sigma_{ij} = \sigma_o \left(\frac{J}{\alpha \sigma_o \varepsilon_o l_{\mathrm{n}} r} \right)^{\frac{1}{n+1}} \tilde{\sigma}_{ij}(\theta, n), \tag{2.21}$$

where σ_o, α, n are the material constants, $\varepsilon_o = \sigma_o / E$, l_n is the constant depending on n and $\tilde{\sigma}_{ij}$ is the nondimensional function of θ depending on n, the crack type, and the stress state.

2.4.2. Continuum damage mechanics

The continuum damage mechanics has began the continuous, micromechanical approach in the failure analysis. This theory gives a possibility of simulating the crack initiation and propagation. It is fully coupled with the constitutive law that affects the weakening of the material stiffness. This approach is chosen for further analysis in this work, that is why the detailed description including coupling with the Chaboche constitutive model is presented.

The continuum damage mechanics is based on the statement that the damage is mainly the process of initiation and growth of microcracks and cavities in a material's structure. This process is mechanically represented by the damage variable *D* proposed by Kachanov [88].

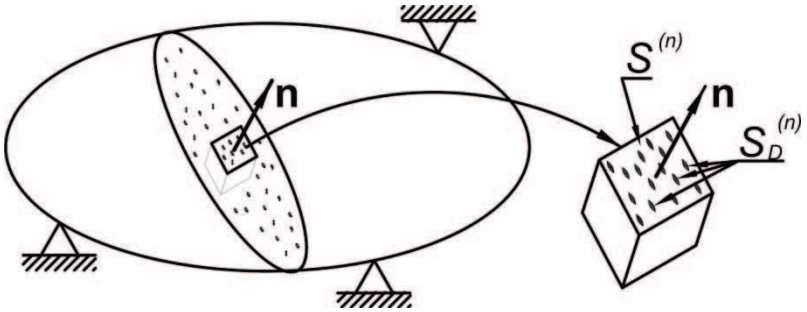

Fig. 2-6. Damaged body

Considering a volume element in a damaged body presented in Fig. 2-6 at macro-scale, that is of a size large enough to contain many defects and small enough to be considered as a material point of mechanics of continua, and a plane cross-section defined by its normal vector **n**, the damage variable $D_{(n)}$ can be expressed as

$$D_{(n)} = \frac{S_D^{(n)}}{S^{(n)}}, \tag{2.22}$$

where $S^{(n)}$ is the area of the intersection of the plane with the volume element and $S_D^{(n)}$ is the effective area of the intersection of all microcracks or cavities which lie on $S^{(n)}$.

According to this definition, the damage variable depends on the choice of the normal **n**, therefore a tensor formulation for this parameter should be used. Assuming the isotropy of damage, which means uniform distribution of cracks and cavities in all directions, $D_{(n)}$ does not depend upon **n** and becomes a scalar value D, which is bounded by the values of 0 (undamaged material) and 1 (fully broken).

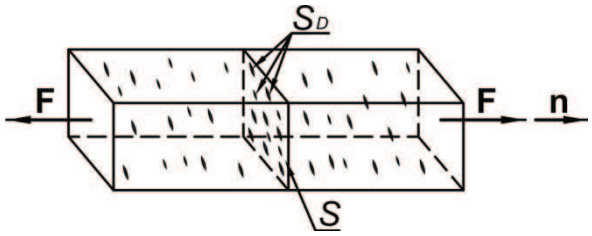

Fig. 2-7. Damaged body at uniaxial loading state

The important step in development of the continuum damage theory was introducing the concept of effective stress by Rabotonov [146]. Considering a volume element in uniaxial loading conditions, presented in Fig. 2-7, usually the stress is calculated as

$$\sigma = \frac{F}{S}, \tag{2.23}$$

but if the material is damaged and the defects are open, no microforces acts on the surfaces of microcracks or cavities represented by S_D, then the stress should be related to the effective surface $\tilde{S} = S - S_D$, thus the effective stress are defined as

$$\tilde{\sigma} = \frac{F}{S - S_D}. \tag{2.24}$$

Introducing to this equation the damage variable definition (2.22) the effective stress $\tilde{\sigma}$ are expressed as

$$\tilde{\sigma} = \frac{\sigma}{1 - D}. \tag{2.25}$$

At this stage of theory development for each type of defect and mechanism of damage a micromechanical analysis should be done. To avoid this problem Lemaitre [109] proposed the strain equivalence principle. The statement postulated that every strain behaviour of a damaged material is represented by constitutive equations of an undamaged material in the potential of which the stress is simply replaced by the effective stresses.

The defined damage variable D is a new internal variable considered in the framework of the thermodynamics. Its associated variable is the damage energy release rate Y. Both complement variables presented in Tab. 2-1. The extended state potential in the form of decomposed free energy is expressed as

$$\psi = \psi^E(\boldsymbol{\varepsilon}^E, T, D) + \psi^I(\boldsymbol{\alpha}, r, T). \tag{2.26}$$

The elastic part of the free energy including damage has the following form

$$\psi^E = \frac{(1 - D)}{2\rho}\left(\boldsymbol{\varepsilon}^E : \mathbf{a} : \boldsymbol{\varepsilon}^E\right). \tag{2.27}$$

According to the strain equivalence principle the stress component can be calculated as

$$\boldsymbol{\sigma} = \rho\frac{\partial \psi^E}{\partial \boldsymbol{\varepsilon}^E} = (1 - D)\mathbf{a} : \boldsymbol{\varepsilon}^E. \tag{2.28}$$

After reversing the equation (2.28) the elastic strain are expressed as

$$\boldsymbol{\varepsilon}^E = \frac{1 + \nu}{E}\frac{\boldsymbol{\sigma}}{1 - D} - \frac{\nu}{E}\frac{\mathrm{Tr}(\boldsymbol{\sigma})}{1 - D}\mathbf{I}. \tag{2.29}$$

By the definition of the associated variable, the damage strain energy release rate can be derived from the potential ψ^E [109]

$$Y = \rho\frac{\partial \psi^E}{\partial D} = -\frac{1}{2}\boldsymbol{\varepsilon}^E : \mathbf{a} : \boldsymbol{\varepsilon}^E. \tag{2.30}$$

Considering W_E as the density of the elastic strain energy

$$W_E = \int \boldsymbol{\sigma} : d\boldsymbol{\varepsilon}^E = \frac{1}{2}(1-D)\boldsymbol{\varepsilon}^E : \mathbf{a} : \boldsymbol{\varepsilon}^E, \tag{2.31}$$

we can establish the relation between Y and W_E

$$-Y = \frac{W_E}{1-D}. \tag{2.32}$$

Splitting the density of the elastic strain energy W_E into two parts: the shear energy part and the hydrostatic energy part and using the law of linear isotropic elasticity coupled with damage [109] the final formula for the damage strain energy release rate can be obtained

$$-Y = \frac{\sigma_{eq}^{\ 2}}{2(1-D)^2 E} R_\nu, \tag{2.33}$$

where R_ν is the triaxiality function

$$R_\nu = \frac{2}{3}(1+\nu) + 3(1-2\nu)\left(\frac{\sigma_H}{\sigma_{eq}}\right)^2, \tag{2.34}$$

where σ_H / σ_{eq} is the stress traxiality ratio, which contains σ_{eq} the Huber-Misses equivalent stress and σ_H the hydrostatic stress, expressed as

$$\sigma_{eq} = \left[\frac{3}{2}\left(\boldsymbol{\sigma} - \frac{1}{3}\mathrm{Tr}(\boldsymbol{\sigma})\mathbf{I}\right) : \left(\boldsymbol{\sigma} - \frac{1}{3}\mathrm{Tr}(\boldsymbol{\sigma})\mathbf{I}\right)\right]^{1/2}, \qquad \sigma_H = \frac{1}{3}\mathrm{Tr}(\boldsymbol{\sigma}). \tag{2.35}$$

To describe the evolution of the damage variable the dissipation potential function including damage is needed. In case of viscoplastic and damage effects, it is possible to note from experimental observation that damage does not depend explicitly upon $\boldsymbol{\sigma}$, R, $\mathbf{X}$. Therefore, it is possible to separate the dissipation effect in damage and the viscoplastic flow contribution [28]

$$\varphi^* = \varphi^D(Y, \dot{p}, D) + \varphi^I(\boldsymbol{\sigma}, R, \mathbf{X}, D). \tag{2.36}$$

The damage evolution is expressed by the generalized normality law

$$\dot{D} = -\dot{\lambda}\frac{\partial \varphi^D}{\partial Y}, \tag{2.37}$$

where $\dot{\lambda}$ is the plasticity multiplier expressed as

$$\dot{\lambda} = \dot{p}(1-D). \tag{2.38}$$

To describe the evolution of the damage variable the isotropic damage model proposed by Lemaitre was chosen [109], [111]. The dissipation function φ^D is written as a power function of Y

$$\varphi^D = \frac{S}{s+1}\left(\frac{-Y}{S}\right)^{s+1}\left(1-D\right)^{-\beta}, \tag{2.39}$$

where S, s and β are damage material parameters. The evolution of the damage variable is derived from the equation (2.37) earlier substituted by (2.38) and (2.39)

$$\dot{D} = \left(-\frac{Y}{S}\right)^{s}\dot{p}\left(1-D\right)^{-\beta+1}. \tag{2.40}$$

The dissipation function φ^I for the Chaboche model coupled with damage is defined as

$$\varphi^I = \Omega(\boldsymbol{\sigma}, R, \mathbf{X}, D) = \frac{K}{n+1}\left\langle\frac{\left(J\left(\boldsymbol{\sigma}'-\mathbf{X}'\right)/\left(1-D\right)\right)-R-k}{K}\right\rangle^{n+1}. \tag{2.41}$$

The inelastic strain rate derived from equation (2.7) earlier substituted by (2.41) has the following form

$$\dot{\boldsymbol{\varepsilon}}^I = \frac{3}{2}\dot{p}\frac{\boldsymbol{\sigma}'-\mathbf{X}'}{J\left(\boldsymbol{\sigma}'-\mathbf{X}'\right)}, \tag{2.42}$$

where the accumulated plastic strain rate $\dot{p}$ is given by

$$\dot{p} = \left\langle\frac{\left(J\left(\boldsymbol{\sigma}'-\mathbf{X}'\right)/\left(1-D\right)\right)-R-k}{K}\right\rangle^{n}. \tag{2.43}$$

Both kinematic and isotropic hardening formulas have the same form as in the model without damage – equations (2.11).

The fracture in the continuum damage mechanics model occurs when the damage variable reaches a critical value D_{cr}, which depends on the material and the stress state. In the uniaxial stress state the critical value of damage is considered as a material parameter D_{1cr}, which can be identified from the pure tension test. In three dimensions the fracture criterion is given by the following formula

$$D_{cr} = D_{1cr}\frac{\sigma_u^{\,2}}{\tilde{\sigma}^{*2}} \le 1, \tag{2.44}$$

where σ_u is the ultimate stress – the maximum value of stress obtained in the tension test and $\tilde{\sigma}^*$ is the effective damage equivalent stress given by

$$\tilde{\sigma}^* = \frac{\sigma_{eq}}{(1-D)} R_v^{1/2}. \tag{2.45}$$

2.4.3. Porous solid plasticity models

The porous plasticity models are based on the assumption that the effect of ductile damage is taken into account in the yield condition by a porosity term that progressively shrinks the yield surface. The first in this group is the model proposed by Gurson [75], [74]. He derived this model from the Rice and Tracey [148] analysis of an isolated void. The damage variable in this approach corresponds with the void volume fraction or porosity denoted as *f*. In the model initial formulation the yield surface Φ is given by the following expression

$$\Phi = \left(\frac{\sigma_{eq}}{\sigma_0}\right)^2 + 2f\cosh\left(\frac{\mathrm{Tr}(\boldsymbol{\sigma})}{2\sigma_0}\right) - 1 - f^2 = 0, \tag{2.46}$$

where σ_0 is the flow stress of the matrix material.

The most popular version of the Gurson's model is the extended approach proposed by Tvergaard and Needleman [174]. The modified model includes not only the nucleation and growth of the voids as the origin version but also their coalescence, which induces the acceleration in the failure process. In this model the isotropic damage is represented by the effective porosity f^*. The Gurson's yield surface is generalized in the following form [200]

$$\Phi = \left(\frac{\sigma_{eq}}{\sigma_0}\right)^2 + 2q_1 f^* \cosh\left(\frac{q_2\,\mathrm{Tr}(\boldsymbol{\sigma})}{2\sigma_0}\right) - 1 - \left(q_1 f^*\right)^2 = 0, \tag{2.47}$$

where q_1 and q_2 are the material coefficients which are assumed to be constant. The effective porosity function f^* accounts for the effects of rapid void coalescence [200]

$$f^* = \begin{cases} f & \text{if } f < f_c, \\ f_c + \left(1/q_1 - f_c\right)\left(f - f_c\right)/\left(f_f - f_c\right) & \text{if } f \geq f_c, \end{cases} \tag{2.48}$$

where f_c is the volume fraction of voids at which the void coalescence starts and f_f is the void volume fraction at final fracture.

The evolution of f is the sum of the nucleation contribution f_n and the growth of existing voids f_g

$$\dot{f} = \dot{f}_n + \dot{f}_g. \tag{2.49}$$

The void nucleation law generally is taken as

$$\dot{f}_n = A\dot{\varepsilon}^I_{eq} + B\left(\dot{\sigma}_m + \dot{\sigma}_{eq}\right), \tag{2.50}$$

where A and B are the strain and stress controlled void nucleation intensity, respectively, $\dot{\varepsilon}^I_{eq}$ is the equivalent plastic strain rate, $\dot{\sigma}_m$ is the mean normal stress rate.

The growth of existing voids law generally is written as

$$\dot{f}_g = \left(1-f\right)\mathrm{Tr}\left(\dot{\boldsymbol{\varepsilon}}^I\right). \tag{2.51}$$

In this model the material loses all stress-carrying capacity – the fracture occurs, when $f \to f_f$ and $f^* \to 1/q_1$.

The Gurson model contains up to ten material constants which should be identified before application. Some of them are not physically based and cannot be directly measured for a material. For example, the parameters $q_1$and q_2 governing the voids growth and the parameter f_c should be determined from numerical micromechanics analysis, the initial void volume fraction and the nucleation parameters can be estimated only from micrographs analysis at different states of deformation. Such complicated identification causes problems in applications with a specific material for which parameters have not been estimated before by other researchers.

Similar to the Gurson's model, the damage is also represented by the porosity variable f, in the model proposed by Rousselier [151]. The difference is that Rousselier based his model on the thermodynamical considerations whereas the first one was derived from the micromechanical description of the porous material. This model's description is omitted, as well as the further development of this both representative approaches for the porous plasticity methods, as these models are not chosen for further applications in the present work.

2.4.4. Abrupt failure criteria

In the abrupt failure criteria approach the fracture is predicted to occur when one chosen variable, uncoupled from other internal variables, reaches its critical value. Those criteria are relatively simple and very often based on recourse of experimental data. One of the first examples is the criterion, which origin comes from the Huber's strength of materials theory [81] formulated at the beginning of 20th century, postulating that the fracture occurs when the

equivalent plastic strain $\bar{\varepsilon}^I$ reaches a critical value $\bar{\varepsilon}_f^I$ (the equivalent plastic strain at fracture)

$$\bar{\varepsilon}^I = \bar{\varepsilon}_f^I, \tag{2.52}$$

where for incompressible plastic material $\bar{\varepsilon}^I$ is defined as

$$\bar{\varepsilon}^I = \sqrt{2/3}\sqrt{\left(\varepsilon_1^I\right)^2 + \left(\varepsilon_2^I\right)^2 + \left(\varepsilon_3^I\right)^2}, \tag{2.53}$$

where ε_1^I, ε_2^I and ε_3^I are the principal plastic strains.

In the further development of this approach it has been accepted that generally the criteria should take into account the deformation path, because the current state of the material is not enough to characterise damage [51], [131], [10]. Therefore, fracture criteria should be expressed in general form as

$$C = \int_0^{\varepsilon_f^*} f\left(\text{process parameters}\right) d\varepsilon^*, \tag{2.54}$$

where ε^* is usually the equivalent, total or plastic strain and ε_f^* is the value of this strain at failure.

One of the first criterions formulated in this form is the Freudenthal's approach [67], based on micromechanics, which postulates that the fracture is dominated by a critical value of the plastic work W^I

$$C = W^I = \int_0^{\bar{\varepsilon}_f^I} \sigma_{eq}\, d\bar{\varepsilon}^I. \tag{2.55}$$

The alternative to previous one, is the criterion of maximum plastic shear work considered by Lee and Shaffer [106]

$$C = \int_0^{\gamma_f^I} \tau_{\max}^{xy}\, d\gamma_{\max}^{I\,xy}, \tag{2.56}$$

where $\tau_{\max}^{xy}$ is the maximum shear stress in plane *xy*, $\gamma_{\max}^{I\,xy}$ is the maximum plastic shear strain in plane *xy* and γ_f^I is the maximum plastic shear strain at failure.

Cockcroft and Latham assumed that the maximum principal stress σ_1 is the most relevant in the initiation of fracture

$$C = \int_0^{\bar{\varepsilon}_f^I} \sigma_1\, d\bar{\varepsilon}^I. \tag{2.57}$$

Recently, Daudonnet [55] used the criterion, which assumes that the total strain energy density W is constant

$$C = W_{cr} = \int_0^{\boldsymbol{\varepsilon}_f} \boldsymbol{\sigma} : d\boldsymbol{\varepsilon}. \tag{2.58}$$

The pioneer experimental work performed in 1911 by von Kármán [181], further continued by Hancock and Mackenzie [78], Tai and Yang [165] and many others showed that the fracture in the same material will occur at different strain levels depending on the state of stress. The first attempt to include this phenomenon in the abrupt fracture criteria was performed by introducing the hydrostatic stress σ_H into formulas. The experiments showed that the material ductility decrees rapidly as the hydrostatic stress σ_H grows.

Brozzo et al. [36] based his criterion on the experimental evidence and introduced σ_H into the process function

$$C = \int_0^{\bar{\varepsilon}_f^I} \frac{2\sigma_1}{3\left(\sigma_1 - \sigma_H\right)} d\bar{\varepsilon}^I. \tag{2.59}$$

Norris et al. [131] proposed the criterion based only on the hydrostatic stress σ_H

$$C = \int_0^{\bar{\varepsilon}_f^I} \frac{1}{\left(1 - c_N \sigma_H\right)} d\bar{\varepsilon}^I, \tag{2.60}$$

where c_N is the material parameter.

Wilkins et al. [193] introduced the fracture criterion based on the dependence of fracture strain on the hydrostatic and deviatoric states

$$C = \int_0^{\bar{\varepsilon}_f^I} \frac{1}{\left(1 - a\sigma_H\right)^{\lambda}} \left(2 - A\right)^{\mu} d\bar{\varepsilon}^I \text{ in } R_c, \tag{2.61}$$

where A, a, λ and μ are the material constants, R_c is the critical dimension of the fracture zone.

The second and more popular approach is introducing the stress triaxiality ratio σ_H / σ_{eq}, which is recognized as the most influential factor, that controls initiation of the ductile fracture in different states of stress. This factor is also used in the already mentioned models: the continuum damage and the porous plasticity. Recently Bao [13] performed fifteen different tests covering a wide range of stress triaxialities and constructed the fracture locus in the space of equivalent plastic strain at fracture versus the stress triaxiality ratio, Fig. 2-8.

Oyane et al. [138] developed the ductile fracture criterion for metal powders and porous materials that include the stress triaxiality

$$C = \int_0^{\bar{\varepsilon}_f^I} \left[1 + \left(\frac{1}{A_{Oy}} \right) \left(\frac{\sigma_H}{\sigma_{eq}} \right) \right] d\bar{\varepsilon}^I, \tag{2.62}$$

where A_{Oy} is the material parameter.

Johnson and Cook [85] postulated that the critical equivalent fracture plastic strain is a monotonic function of the stress triaxiality

$$\bar{\varepsilon}_f^I = C_1 + C_2 \exp\left(C_3 \frac{\sigma_H}{\sigma_{eq}} \right), \tag{2.63}$$

where C_1, C_2 and C_3 are the constants determined from tensile or shear tests with high triaxiality.

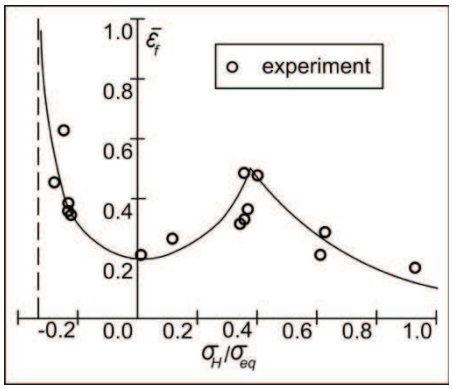

Fig. 2-8. Dependence of the equivalent plastic strain at fracture on the stress triaxiality [13]

Bao and Wierzbicki [15] studied the condition for fracture in the following form

$$C = T_{cr} = \int_0^{\bar{\varepsilon}_f^I} f\left(\frac{\sigma_H}{\sigma_{eq}} \right) d\bar{\varepsilon}^I, \tag{2.64}$$

where $f\left(\sigma_H/\sigma_{eq}\right)$ is the suitable triaxiality weighing function determined in the wide range of the stress triaxiality $\left(-1/3 \le \sigma_H/\sigma_{eq} \le 1\right)$ from eleven different tests. Lee et al. [108] used this criterion in the fracture prediction of thin plates under hemi-spherical punch. In the range of expected stress triaxiality for that problem $\left(1/3 \le \sigma_H/\sigma_{eq} \le 2/3\right)$ the weight function has been assumed as linear:

$$C = T_{cr} = \int_0^{\bar{\varepsilon}_f^I} \left(\frac{\sigma_H}{\sigma_{eq}} \right) d\bar{\varepsilon}^I. \tag{2.65}$$

The criteria, which are presented in this group, are only the examples chosen from a large group formed during development of this approach. For the further analysis three different fracture criterions are chosen. First is the simplest, based on the critical value of the equivalent plastic strain at fracture (Huber). Second is based on micromechanics, precisely the total strain energy density constancy assumption, used by Daudonnet. Third is the last presented, based on the triaxiality stress ratio dependency.

2.5. Summary

In this chapter, the assumed constitutive law is described. Also the survey of models, which are in often use in fracture and damage analysis, is presented. Four groups are here distinguished. The models for the further applications have been chosen: the continuum damage model as the example of fully coupled approach and three different criterions from abrupt methods as the examples of uncoupled approach.

3. Numerical tools

3.1. Abstract

The numerical study considered in this work has been performed using the commercial finite element system. This chapter contains the description of only the most important, from the analyzed phenomenon point of view, numerical tool choices which, have been made during the preparation of simulations. The description includes the short review of selected finite elements, chosen approach in the large displacement analysis, detailed algorithms of used user-subroutines, equation of motion integration method, contact effect and adaptive mesh features capability.

3.2. Introduction

The extensive part of the performed work is the numerical study of analyzed phenomenon. All numerical calculations have been carried out using the MSC.Marc software. It is a multipurpose finite element method program for advanced engineering simulations. The system gives, among many others, a possibility of performing linear or nonlinear analyses in the static and dynamic regimes. Its great advantage is the openness (a user may define and implement his own subroutines), which enable performing analysis of advanced problems.

3.3. Elements selected for numerical analyses

Marc includes an extensive finite elements library. It allows modelling various types of structures, such as: plane stress, plane strain, axisymmetric, full three-dimensional solids and shell-type ect. For the numerical analyses considered in this work three different element types have been chosen. Two of them are the 2-D analysis dimension shells and one is the axisymmetrical shell element.

The first one is the four-node bilinear thick-shell element – called in Msc.Marc type 75, see [177]. This Lagrange type low order element is based on the Mindlin theory. The bilinear interpolation is used for the coordinates, displacements and rotations. The membrane strains are obtained from the displacement field and the curvatures from the rotation field. Due to its simple formulation, it is less expensive than the standard higher order shell elements, therefore it is very attractive in nonlinear dynamic analyses. This element is not very sensitive to distortion. As all low order elements, is threaded by the locking effect [47]. Here, to avoid

this effect, the transverse shear strains are calculated at the middle of edges and interpolated to the integration points. In this way the element exhibits a correct behaviour also in the limiting case of thin shells.

The element is defined by the (x, y, z) coordinates of the four nodes, see Fig. 3-1. The integration over the middle surface is performed numerically by the full integration Gauss algorithm. The integration through the shell thickness is made by the Simpson's rule. The element has six degrees of freedom per node: u, v, w – displacements along global x, y, z-axis respectively and ϕ_x, ϕ_y, ϕ_z – rotations about global x, y, z-axis respectively. The generalized output strain components are: $\varepsilon_{11}, \varepsilon_{22}, \varepsilon_{12}$ – middle surface stretches, $\kappa_{11}, \kappa_{22}, \kappa_{12}$ – middle surface curvatures and γ_{23}, γ_{31} – transverse shear strains, all in local ($\underset{\sim}{V}_1$, $\underset{\sim}{V}_2$, $\underset{\sim}{V}_3$) orthogonal surface directions. The output stresses are $\sigma_{11}, \sigma_{22}, \sigma_{12}, \sigma_{23}, \sigma_{31}$ in local directions given at equally spaced layers through thickness.

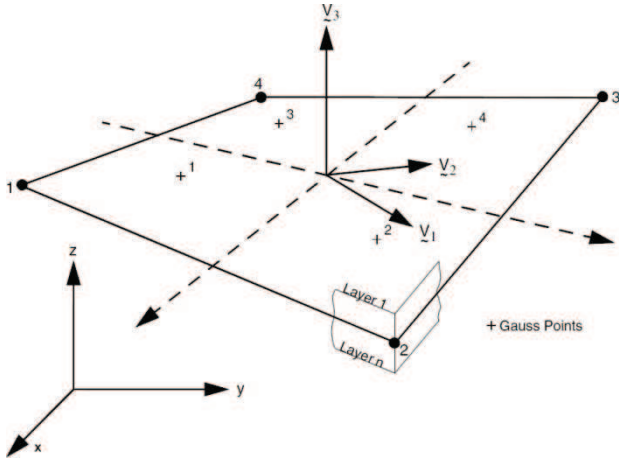

Fig. 3-1. Four-node bilinear thick-shell element [177]

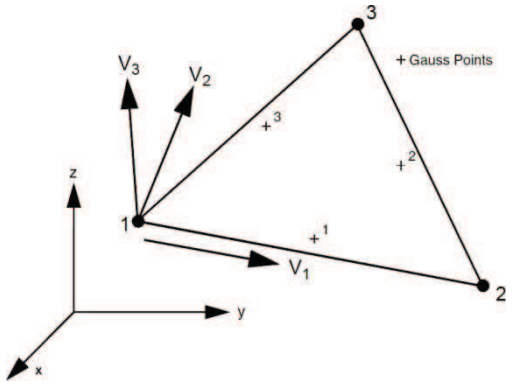

Fig. 3-2. Three-node bilinear thin-triangular shell element [177]

The second element type is three-node bilinear thin-triangular shell element – type 138, see [177]. This element is based on the discrete Kirchhoff theory. Similarly to the previous one, the simple formulation makes this element very attractive in nonlinear dynamic analyses. This element is also not very sensitive to distortion and uses the same integration algorithms as previous described, except of the number of Gauss points, which in this case is three, see Fig. 3-2. The degrees of freedom are the same, the generalized output strains do not include the transverse shear components and the output stresses are limited to $\sigma_{11}, \sigma_{22}, \sigma_{12}$.

The third element is three-node thick curved axisymmetrical shell element – type 89 (Fig. 3-3), see [177]. In this element, the quadratic displacement assumption based on the global displacement and rotation is introduced. The protection against the locking effect is ensured by application of the reduced integration. The two-point Gauss integration (the points are close to the outside nodes) is used along the element for the stiffness calculation, and three-point integration for the mass and pressure determination is applied. The integration through the shell thickness is made by the Simpson's rule. The element has three degrees of freedom per node: *u*, *v* – axial (parallel to symmetry axis), and radial (normal to symmetry axis) displacements, respectively and ϕ – right hand rotation. The generalized output strains are ε_s – meridional membrane, ε_Θ – circumferential membrane, γ_t – transverse shear, χ_s – meridional curvature and χ_Θ – circumferential curvature. The output stresses are σ_s – meridional, σ_Θ – circumferential and σ_t – transverse.

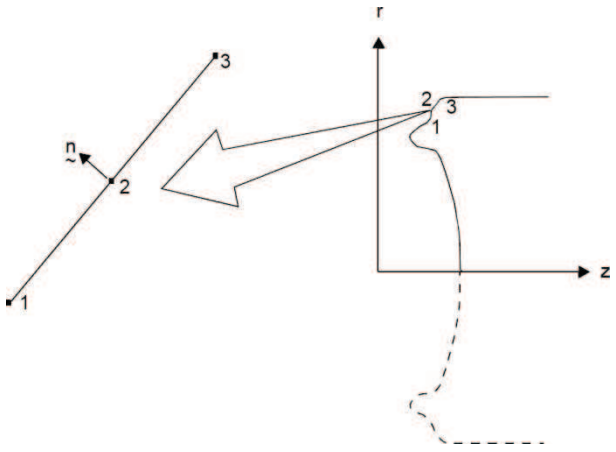

Fig. 3-3. Three-node thick curved axisymmetrical shell element [177]

The strain-displacement relationships used in all presented elements are suitable for large displacement – small strains analyses and are described below. Also all constitutive relations,

including user-defined subroutines, can be applied. The presented elements in the performed computations have been divided into five layers.

3.4. Large displacement analysis

In order to obtain the adequate results of the numerical simulations in the studied problem, the large displacements must be considered. There are two natural classes of large deformation problems: large displacement – small strain and large displacement – large strain. In the considered study, due to assumptions made in Chapter 2, the first class analysis has been chosen.

The kinematic of deformation for structural elements is naturally described in the Lagrangian formulation. In this method a finite element mesh (as well as local coordinate stystems) is attached to a material and moves through space along with a material. In such case, there is no difficulty in establishing stress or strain histories at a particular material point and the treatment of free surfaces is natural and straightforward.

The Lagrangian approach can be classified in two categories: the total Lagrangian and the updated Lagrangian variant [18]. In the total Lagrangian approach, all tensors are referred to initial configuration, at time $t = 0$. The equilibrium is expressed with the original undeformed state as the reference. In the updated Lagrangian approach all tensors are referred to the updated configuration of the body, at time t.

The equilibrium can be formulated as the principle of virtual work. In the total Lagrangian approach this principle, for an arbitrary body during its motion caused by external forces, has the following form [95]

$$\int_V \mathbf{S}^T \delta\mathbf{E} dV + \int_V \left[\left(\mathbf{f}_0{}^T - \rho \ddot{\mathbf{u}}^T \right) \delta\mathbf{u} \right] dV - \int_A \left(\boldsymbol{\mu}_0 \dot{\mathbf{u}} \right)^T \delta\mathbf{u}\, dA - \int_A \mathbf{p}_0{}^T \delta\mathbf{u}\, dA = 0, \tag{3.1}$$

where V and A are the volume and area, respectively, taken from initial configuration, $\mathbf{S}$ is the second Piola-Kirchhoff stress tensor, $\mathbf{E}$ is the Green-Lagrange strain tensor, $\mathbf{f}_0$ is the volumetric force vector referred to the initial configuration, ρ is the mass, $\boldsymbol{\mu}_0$ is the viscous damping tensor of the surface damping forces referred to the initial configuration, $\mathbf{p}_0$ is the vector of forces applied to the surface, $\mathbf{u}$ is the displacement vector in an arbitrary point (superposed dots indicate differentiation with respect to time) and $\delta\mathbf{u}$ is the virtual displacement.

Since the stresses and strains in the searched time step are unknown, for solution, the following incremental decomposition are used

$$\mathbf{S}_{t+\Delta t} = \mathbf{S}_t + \Delta\mathbf{S}, \tag{3.2}$$

$$\mathbf{E}_{t+\Delta t} = \mathbf{E}_t + \Delta\mathbf{E}. \tag{3.3}$$

The incremental strains are further decomposed into elastic $\Delta\mathbf{E}^E$ and inelastic $\Delta\mathbf{E}^I$ parts

$$\Delta\mathbf{E} = \Delta\mathbf{E}^E + \Delta\mathbf{E}^I. \tag{3.4}$$

After linearization and adaptation to the finite element method the principle of virtual work (3.1) can be written as the incremental equation of motion

$$\mathbf{M}\Delta\ddot{\mathbf{q}} + \mathbf{C}\Delta\dot{\mathbf{q}} + \left(\mathbf{K} + \mathbf{K}_G + \mathbf{K}_S\right)\Delta\mathbf{q} = \mathbf{R}_{t+\Delta t} - \mathbf{Q}_t, \tag{3.5}$$

where

$$\Delta\ddot{\mathbf{q}} = \ddot{\mathbf{q}}_{t+\Delta t} - \ddot{\mathbf{q}}_t, \quad \Delta\dot{\mathbf{q}} = \dot{\mathbf{q}}_{t+\Delta t} - \dot{\mathbf{q}}_t, \quad \Delta\mathbf{q} = \mathbf{q}_{t+\Delta t} - \mathbf{q}_t, \tag{3.6}$$

$\mathbf{q}, \dot{\mathbf{q}}$ and $\ddot{\mathbf{q}}$ are the vectors of finite elements nodal displacements, velocities and accelerations, respectively, related with $\mathbf{u}, \dot{\mathbf{u}}$ and $\ddot{\mathbf{u}}$ by the following dependences, where $\mathbf{N}$ is the shape function matrix

$$\mathbf{u} = \mathbf{N}\mathbf{q}, \quad \dot{\mathbf{u}} = \mathbf{N}\dot{\mathbf{q}}, \quad \dot{\mathbf{u}} = \mathbf{N}\dot{\mathbf{q}}, \tag{3.7}$$

$\mathbf{M}$ and $\mathbf{C}$ are the mass and viscous damping, respectively, $\mathbf{R}_{t+\Delta t}$ is the applied external forces vector, $\mathbf{Q}_t$ is the vector of nodal balanced forces, $\mathbf{K}, \mathbf{K}_G$ and $\mathbf{K}_S$ are the linear, geometrical and stress related stiffness matrixes, respectively.

In the updated Lagrangian approach all variables are referred to the updated (at time *t*) configuration. The principle of virtual work in this approach has the following form

$$\int_v \boldsymbol{\sigma}^T \delta\boldsymbol{\varepsilon}\, dv + \int_v \left[\left(\mathbf{f}^T - \rho\ddot{\mathbf{u}}^T\right)\delta\mathbf{u}\right] dv - \int_a \left(\boldsymbol{\mu}\dot{\mathbf{u}}\right)^T \delta\mathbf{u}\, da - \int_a \mathbf{p}^T\delta\mathbf{u}\, da = 0, \tag{3.8}$$

where v and a are the volume and area, respectively, taken from updated configuration, $\boldsymbol{\sigma}$ is the Cauchy stress tensor, $\boldsymbol{\varepsilon}$ is the Hencky strain tensor and $\mathbf{f}, \boldsymbol{\mu}, \mathbf{p}$ are the same vectors/tensors as in equation (3.1), but here referred to updated configuration. The incremental stress decomposition used in this case is given as

$$\boldsymbol{\sigma}_{t+\Delta t} = \boldsymbol{\sigma}_t + \Delta\boldsymbol{\sigma}. \tag{3.9}$$

Considering the strain increment the following relations holds

$$\boldsymbol{\varepsilon}_{t+\Delta t} = \Delta\boldsymbol{\varepsilon}, \tag{3.10}$$

where the increment is further decomposed as it is shown in equation (3.4).

After linearization and adaptation to the finite element method the principle of virtual work (3.8) can be transformed to the incremental equation of motion

$$\mathbf{M}\Delta\ddot{\mathbf{q}} + \mathbf{C}\Delta\dot{\mathbf{q}} + \left(\mathbf{K}_G + \mathbf{K}_S\right)\Delta\mathbf{q} = \mathbf{R}_{t+\Delta t} - \mathbf{Q}_t. \tag{3.11}$$

In the considered numerical study the updated Lagrangian formulation has been applied. This selection has been forced by using the large rotation during the analyses [176]. In such case the nonlinear terms in the curvature expressions may no longer be neglected. Applying the updated Lagrangian approach in Marc system follows that the program uses and prints the Cauchy stress tensor $\boldsymbol{\sigma}$ (also called as true stress) and energetically conjugated the Hencky strain tensor $\boldsymbol{\varepsilon}$ (also called as true or logarithmic strain).

3.5. User-defined subroutines

Among an extensive number of user-defined subroutines available in the Marc program, the following three have been applied in the considered numerical studies: UVSCPL – definition of the inelastic strain rate, UACTIVE – activate or deactivate elements and PLOTV – user-selected postprocessing of element variables, see [178].

The UVSCPL subroutine allows implementing an arbitrary elastic-viscoplastic material law to compute the inelastic strain increment. The user must define the inelastic strain increment $\Delta\boldsymbol{\varepsilon}_t^I$ and the stress increment $\Delta\boldsymbol{\sigma}_t$. This subroutine is used to implement the chosen material law, which is the viscoplastic Chaboche model, and to calculate all considered fracture criterion parameters: D_{cr_t} – current (at time t) critical value in damage criterion, $\overline{\varepsilon}_t^I$ – equivalent plastic strain criterion, T_t – stress triaxiality ratio based criterion and W_t – total strain energy density criterion (the selection of active criterion in the particular simulations is performed in UACTIVE). Two different versions of this subroutine have been created: the uncoupled constitutive law and the constitutive law coupled with the damage theory. The integration of constitutive law variables and the fracture parameters is performed by the trapezoidal rule. The algorithms used in the UVSCPL are presented in the form of a flow chart in Fig. 3-4 to Fig. 3-6. The tensor $\mathbf{C}$, which is used in this algorithms, is the constitutive tensor.

The UACTIVE subroutine allows deactivation of elements in a structure. This user subroutine is called at the beginning of analysis and at the end of each increment.

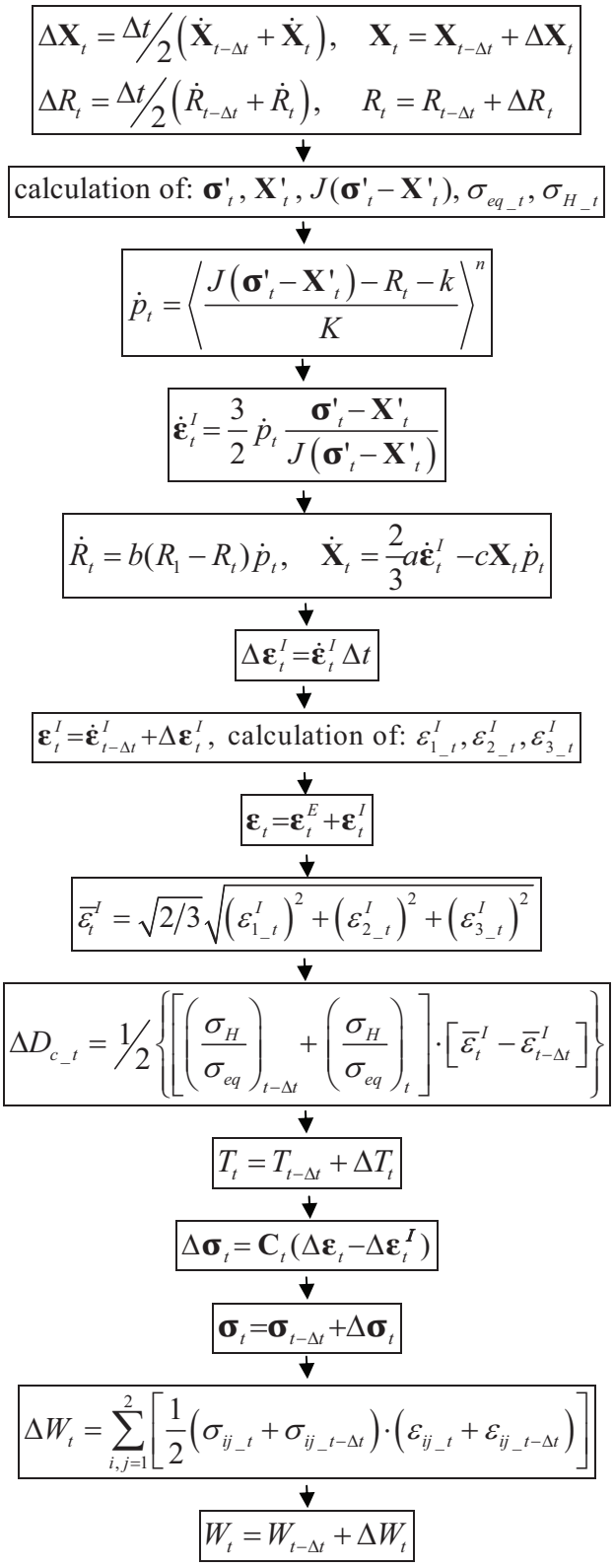

Fig. 3-4. Flow chart of the UVSCPL subroutine, uncoupled version

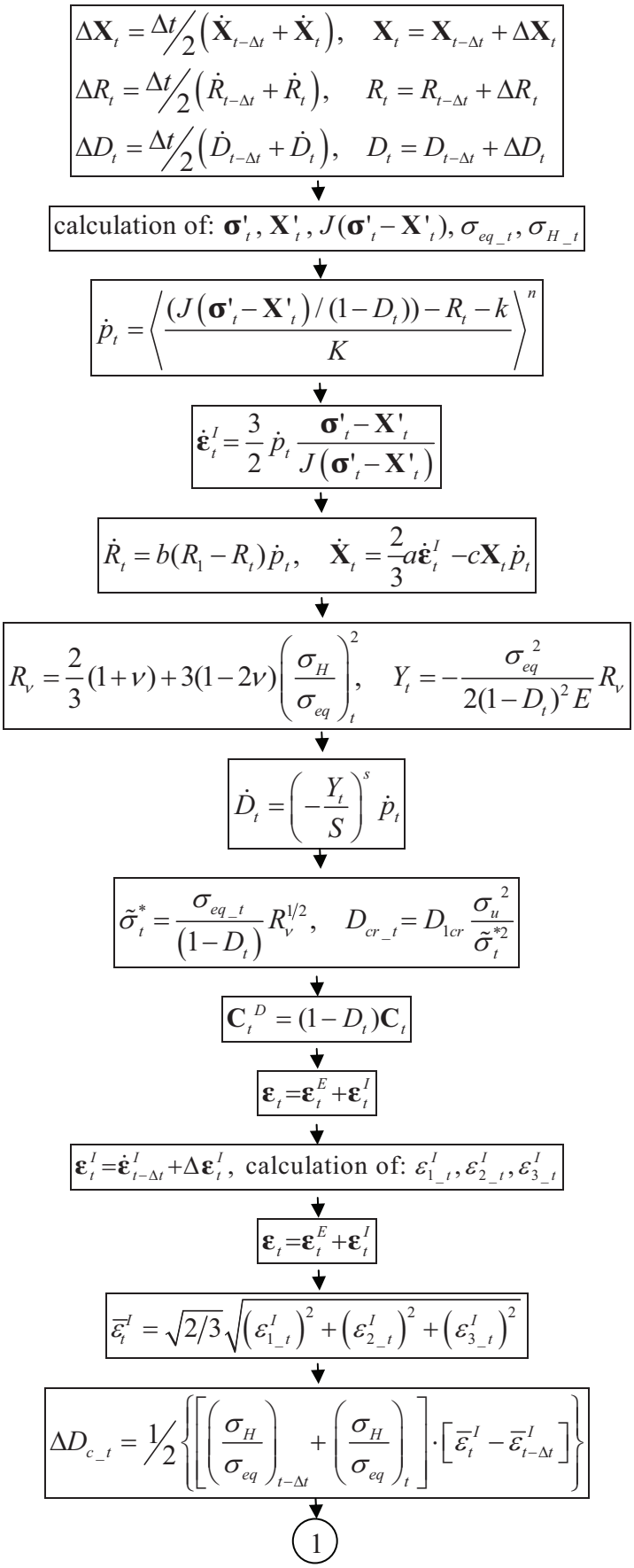

Fig. 3-5. Flow chart of the UVSCPL subroutine, coupled version, (1/2)

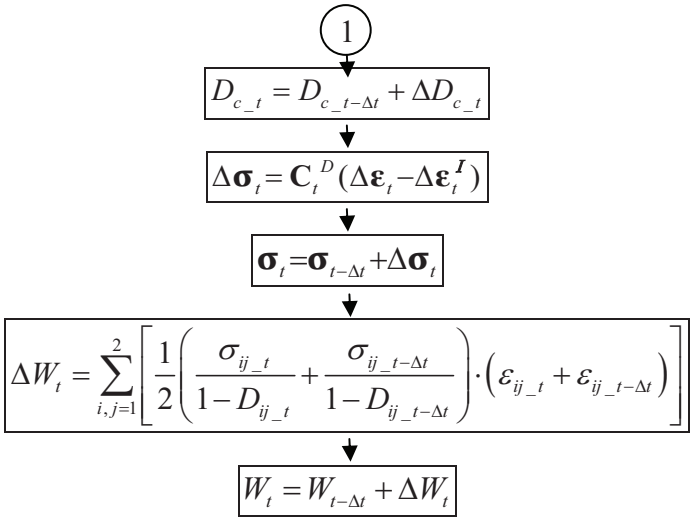

Fig. 3-6. Flow chart of the UVSCPL subroutine, coupled version, (2/2)

A deactivated element does not contribute to the load, mass, stiffness, or internal force calculation. This subroutine controls which criterion is used in the particular simulations.

In all considered studies the divided into five layers shell elements have been used. Elements should be deactivated when they fulfil the assumed fracture criterion. The question is, when the deactivation should start. If the criterion is fulfilled: in one layer only (appeared as first), in a few layers (some part of the cross-section) or in all layers (through all height of the cross-section). Finally, to study this problem the calculations have been performed using three different methods. In the first approach an element has been deleted when the assumed fracture criterion has been fulfilled in each integration point of its any single layer (1/5 layer, which is 20 % of the cross-section). In the second one an element has been removed when at least three layers have been fractured (3/5 layers, which is 60 % of the cross-section). In the third one the deactivation of an element has occurred when the criterion has been fulfilled in its all integration points (5/5 layers, which is 100 % of the cross-section).

The PLOTV subroutine allows a user to define an element variable to be written to the post file. It enables plotting the values of variables appearing in user subroutines. In the considered analyses this procedure has been used to get output of the damage parameter D, the equivalent plastic strain $\bar{\varepsilon}^I$, the total strain energy density W, the stress triaxiality ratio σ_H/σ_{eq} and the triaxiality stress ratio fracture condition parameter T.

3.6. Integration of the motion equation

The equation of motion numerical integration methods can be divided into approaches based on modal superposition (usually used in linear analysis) and into so-called direct

methods. The second group can be divided into explicit and implicit methods. The characteristic feature of the explicit methods is calculation of the motion parameters in the searched time step $t+\Delta t$ on the basis of the equation written for the time step t. In the implicit methods the motion parameters in the searched time step $t+\Delta t$ are calculated on the basis of the equation written in the same time step. This causes the necessity of iterations.

The Marc program offers the possibility of using methods, which are representative for all mentioned groups. In the considered numerical study the direct, the implicit single-step Houbolt method has been used. The basis of this approach can be found in [48].

The characteristic for the single-step methods is that, they rely only on the initial conditions provided at the beginning of a time step t and on evaluating the motion parameters at time points within the time interval $[t;t+\Delta t]$. This simplifies the procedure in relation to multistep methods (the original Houbolt method), because it does not employ any historical information from the earlier time steps than t.

In this work the incremental nonlinear form of motion equation presented in equation (3.11) has been considered. The expressions for displacement and velocity in the single-step Houbolt method are

$$\begin{aligned}\mathbf{q}_{t+\Delta t} &= \mathbf{q}_t + \Delta t\dot{\mathbf{q}}_t + \beta\Delta t^2\ddot{\mathbf{q}}_t + \beta_1\Delta t^2\ddot{\mathbf{q}}_{t+\Delta t},\\ \dot{\mathbf{q}}_{t+\Delta t} &= \dot{\mathbf{q}}_t + \gamma\Delta t\ddot{\mathbf{q}}_t + \gamma_1\Delta t\ddot{\mathbf{q}}_{t+\Delta t},\end{aligned} \tag{3.12}$$

where $\beta=\gamma$ and $\beta_1=\gamma+\gamma_1$. The parameters γ and γ_1 influence on the algorithm's overshot and the global error growth behaviour usually are assumed as $\gamma=-1/2$ and $\gamma_1=3/2.$ To start this algorithm the initial value of acceleration is necessary. It can be calculated as

$$\ddot{\mathbf{q}}_{t=0} = \mathbf{M}^{-1}\left(\mathbf{R}_{t=0} - \mathbf{C}\dot{\mathbf{q}}_{t=0} - \mathbf{Q}_{t=0}\right). \tag{3.13}$$

3.7. Contact phenomena

The considered numerical simulations required the ability to model the contact phenomena. Marc allows performing such analysis. In the program there are defined two types of bodies – deformable and rigid [176]. Deformable bodies are simply meshed as a collection of finite elements. Their deformation is prescribed using the conventional methods of applying displacements, forces or loads to elements. Rigid bodies are composed of curves or surfaces. It is not necessary to define the complete rigid structure, only the bounding surface or curve needs to be specified. The motion of rigid bodies is possible and can be prescribed by velocity, position or load. The detection of contact is realized during the

incremental procedure. Each potential contact node is first checked to see whether it is near a contact segment. To assure the efficiency in the large number of nodes case, a bounding box algorithm is used, see [115]. It allows determining quickly whether a node is near a segment. If the node falls within the box more sophisticated technique – the iterative penetration checking procedure is used. In the direct contact procedure, while contact does not occur, target nodes on the deformable bodies have no constraints. Once the contact is detected, the degrees of freedom are transformed to a local system and a constraint is imposed. The contact phenomena implemented in the Marc system allows introducing the modelling of friction. Two models are available in the program: the Coulomb model and the shear friction model, see [134]. In the performed simulations, the friction has not been considered.

3.8. Adaptive mesh

The generation of adaptive mesh improves the accuracy of obtained solutions. During calculation this capability increases the number of elements and nodes. In the Marc program the adaptive mesh can be applied for lower-order elements only [176]. Among the chosen elements this feature cannot be used with the axisymmetrical shell. The adaptive meshing procedure works by dividing an element and internally tying nodes to insure compatibility. For the quadrilaterals and triangles, the number of elements expands by four with each subdivision. When the adaptive meshing occurs, the discontinuities are created in the mesh, see Fig. 3-7. To ensure compatibility, node B is effectively tied to nodes A and C, node D is effectively tied to nodes C and E. This procedure occurs internally and does not conflict with user-defined contact. The adaptive meshing subdivision occurs when a particular adaptive criterion is satisfied. Among many possibilities, the equivalent values criterion has been chosen. An element is subdivided when the assumed absolute value of equivalent total strain is reached.

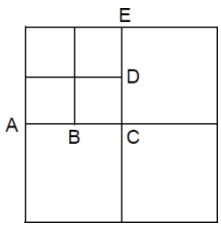

Fig. 3-7. Discontinuities in the adaptive mesh [176]

3.9. Summary

The described in this chapter numerical tools give the possibility of performing geometrically and materially nonlinear axisymmetrical or 2-D shell analyses. Additionally the subroutine, which deactivates elements, allows simulating the crack initiation and propagation. All these features have been used in the attempt of the fracture prediction analyses described in the further chapters.

4. Experimental tests

4.1. Abstract

The following chapter contains the detail overview of all experimental tests, which have been performed during realization of this work. The laboratory tests consisted of: experiments on plates subjected to explosions, quasi-static experiments on plates and uniaxial experiments on bar samples. For each group the detailed description of the research stands, experimental procedures and the results are presented.

4.2. Introduction

Experimental testing is the best verification for all new theories and models in the mechanics field. The comparison analyses, where results of numerical simulations are referred to experiments give the unequivocal answer if an assumed model or theory is correct or wrong. A laboratory test is appropriate when it is repeatable and gives an exact answer for a stated problem. Unfortunately, sometimes it is not easy to fulfil completely these circumstances. The best known problem is that of boundary conditions determination. This could be: the determination of loading conditions, specimen's fixing, etc.

The laboratory tests performed for the requirements of this work have been realized in Institute PRISME in Bourges, and in Gdańsk University of Technology in Faculty of Civil and Environmental Engineering, Department of Structural Mechanics and Bridges. All realized experiments have been executed with a very high carefulness.

4.3. Experiments on plates

The experiments on thin metallic plates subjected to various well controlled dynamic excitations – gas mixture explosions are the key laboratory tests for this study. The results of these experiments are the base for final verification of fracture prediction numerical simulations. The quasi-static experiment gives the information, which can be useful in determination of the boundary conditions. Its result can be employed in the verification of conditions applied in the assumed model.

4.3.1. Research stand and experimental devices

The main part of the research stand is a rigid steel tube inside which it is appropriate to perform detonations (designed to withstand very high overpressure up to 15 MPa) presented in Fig. 4-1. This tube is composed of two separate parts between which a specimen – a plate, could be mounted. Its main dimensions are 194 mm of inner diameter, 12.5 mm of wall's thickness and 1310 mm of full length, see Fig. 4-2. All experimental devices used during experiments are presented in the connection diagram in Fig. 4-3. Both parts of the tube have its own manometers protected by high pressure resistant valves. The longer part of the tube is connected to a vacuum pump and a gas cylinder with an explosive mixture. The device is equipped with an igniter connected to a high voltage generator and two sensors measuring pressure during explosions, which are installed just before and behind a specimen. These sensors are connected to amplifiers and in turn to an oscilloscope, which records pressure time histories.

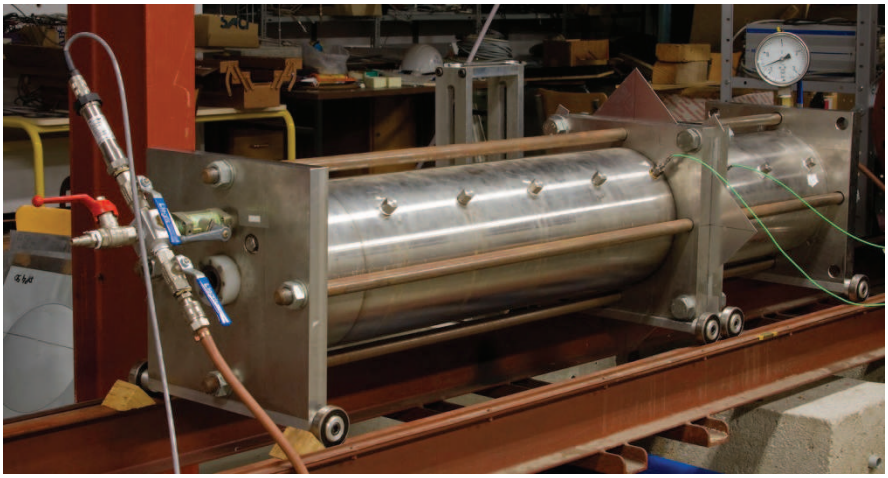

Fig. 4-1. Research stand – the tube used in experiments

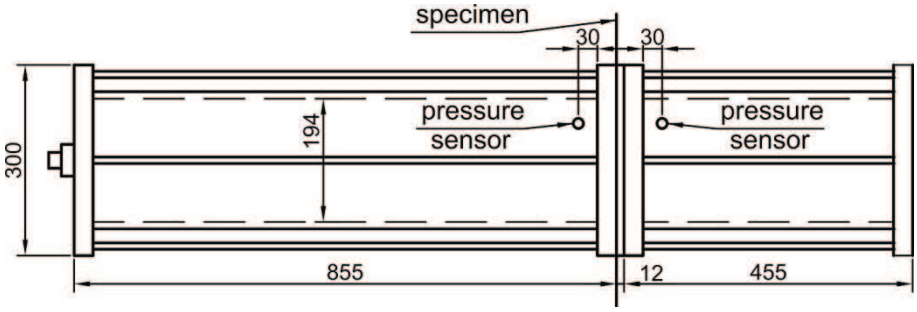

Fig. 4-2. Main dimensions of the tube

An important element for the experiments in the research stand is the additional plate presented in Fig. 4-4 fixed just behind a specimen. Thanks to the special 12 mm radius circle

rounding of its inside edge, it prevents cutting out circles along the specimen's fixing during the tests.

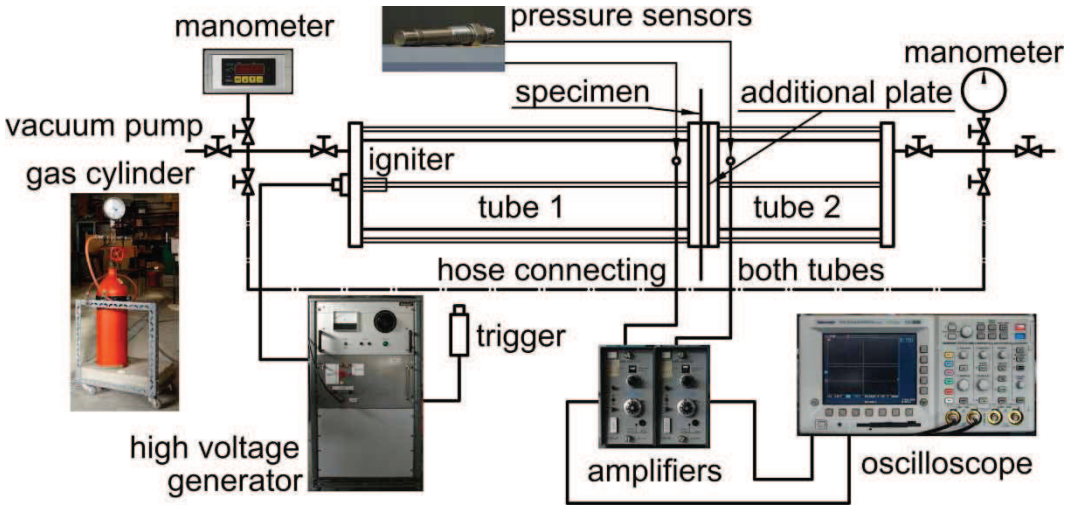

Fig. 4-3. Connection diagram of experimental devices

4.3.2. Experimental work in dynamic tests

The experiments have been performed on specimens made from Al2017 aluminium alloy 1 mm thickness sheets. These sheets have been cut into 330x330 mm square plates. The gas mixture, which has been used for the experiments, is the stoechiometric mixture of propane and oxygen, during the explosion the following reaction occurred: $C_3H_8 + 5O_2 \rightarrow$ $\rightarrow 4H_2O + 3CO_2$. There are two possibilities of igniting the explosion: by a spark and then the result is a deflagration or by an electric filament (the capacitors discharge through a thin copper wire which instantaneously melts creating plasma) resulting in a detonation. The detailed description of these methods can be found in Pennetier at al. [140]. The shock ignited by the second method is very stable, whereas by the first is partly stochastic. That is why in

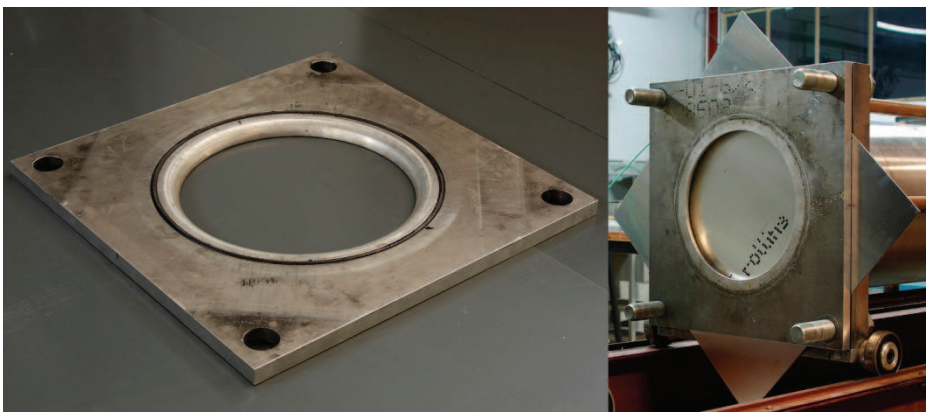

Fig. 4-4. Additional plate

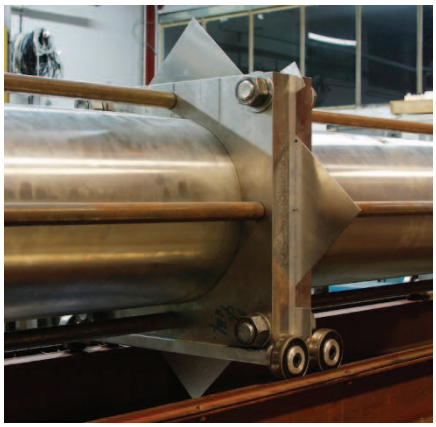

Fig. 4-5. Specimen's fixing

the experiments the detonation has been applied. The initial gas mixture pressures used for the explosions are: 0.25, 0.3, 0.4, 0.5, 0.6, 0.7 and 0.8 bars.

The procedure of a single test includes the following actions:

- fixing the plate between both parts of the tube by four screws and the system of two o-rings, Fig. 4-5;
- preparing the igniter by soldering a wire and installing in a special opening, Fig. 4-6;
- pumping out air from both parts of the tube simultaneously until reaching vacuum;
- separating both parts by closing the valves in the connecting hose;
- in the same time, filling the first part of the tube with gas mixture of an appropriate pressure and the second part with air of the same pressure (due to the balance of pressures in both tubes the specimen remains flat);
- closing all valves and igniting the explosion by an electric filament induced by the capacitors discharge;
- during the test registering pressure time histories on the oscilloscope, Fig. 4-7;
- unscrewing the plate and measuring its geometry after an experiment.

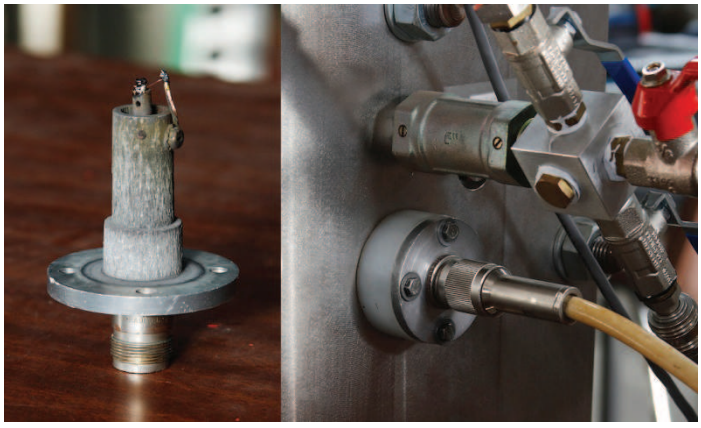

Fig. 4-6. Igniter and its installation

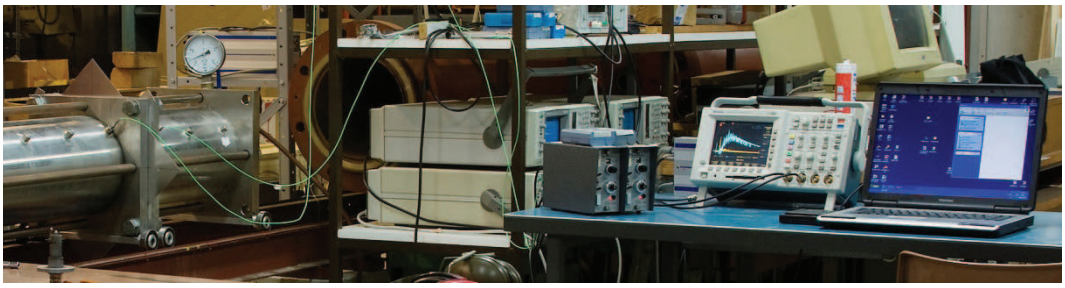

Fig. 4-7. Registering of the pressure time histories

During each test a special attention is necessary, working with explosive gas mixture require keeping restrict safety conditions and high concentration.

4.3.3. Results of dynamic experiments

During the experimental program eighteen succeeded tests on plates subjected to explosions have been performed. For better organization the following designations to particular experiments have been used: *x_y*, where *x* signifies the initial pressure, *y* signifies the following number of the succeeded test for this initial pressure. For example the designation "05_1" means that it is the first test with initial pressure 0.5 bar.

The first analyzed results of the experiments are the registered pressure time histories. During each test, the pressure histories have been registered with frequency of $2.5 \cdot 10^5$ 1/s. The pressure histories have been recorded by two sensors installed just before and behind the plate. The pressure, which is assumed as acting exactly on the specimen, is calculated as a difference, an example is presented in Fig. 4-8. All eighteen pressure time histories are presented in Annex 1, here for the initial pressures from 0.3 to 0.8 bar one chosen example is shown in Fig. 4-9.

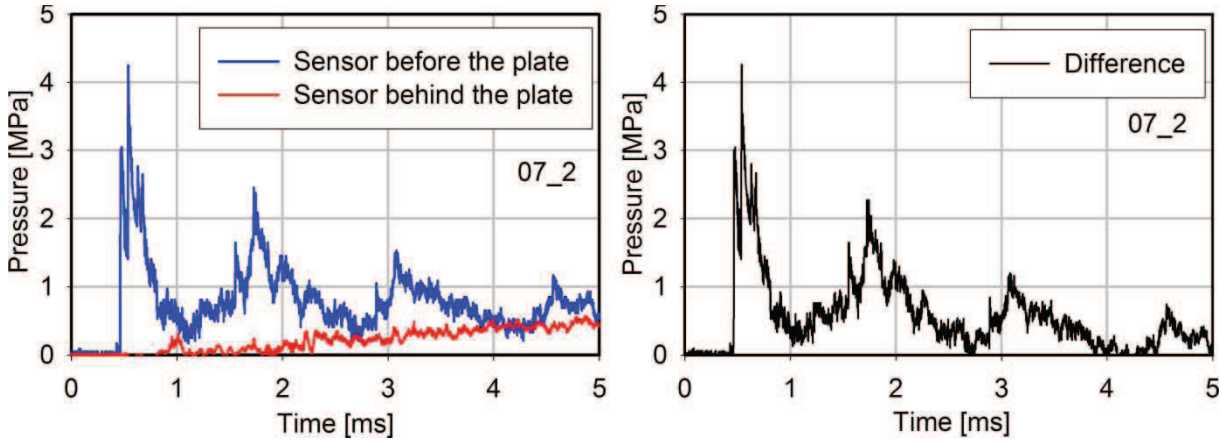

Fig. 4-8. Calculating of active pressure time histories, example for initial pressure 0.7 bar

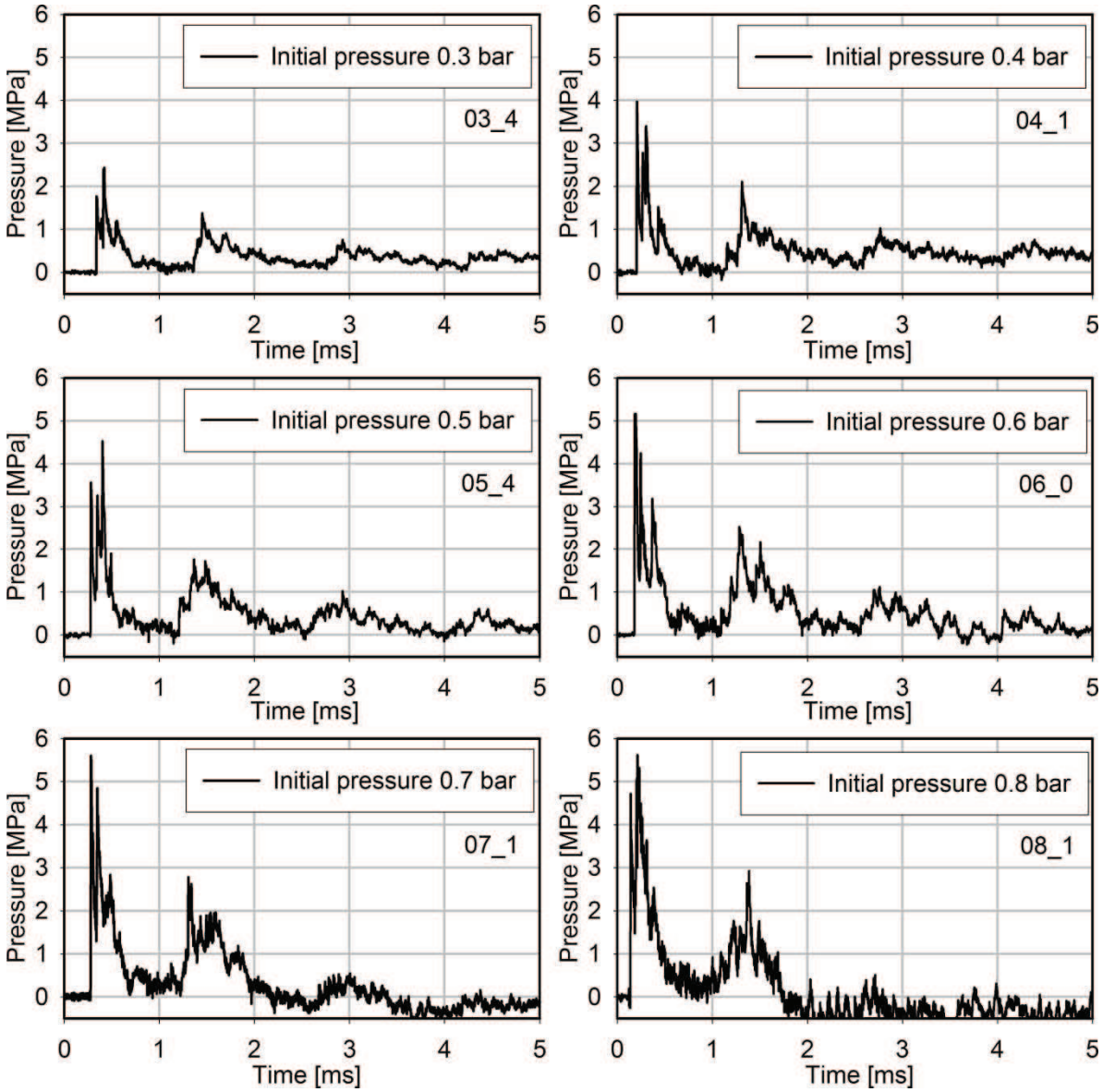

Fig. 4-9. Pressure time histories

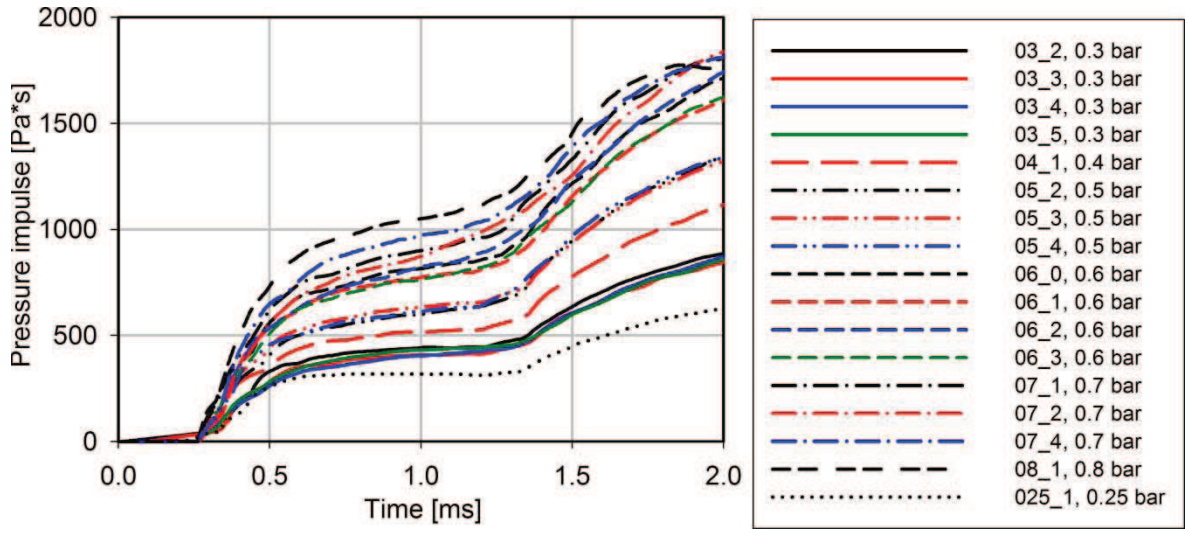

Fig. 4-10. Pressure impulses

In all presented pressure time histories it can be noticed that the first hit of the explosion is the strongest, the following pressure maxims seems to be rebounds of gases inside the tube. For better visualisation of the explosions power during first hit after detonation the pressure impulses has been calculated for each pressure time history by integrating its function with respect to time, the result is presented in Fig. 4-10. The average values of the impulses, for each initial pressure, are shown in Fig. 4-11. In the presented plots it is noticeable how the impulses are growing with increasing the gas mixture initial pressure.

The photos of all tested plates after an experiment are presented in Annex 2, here the examples for the initial pressures from 0.3 to 0.8 bar are shown in Fig. 4-12. For the lowest initial pressures the plates are only permanently deflected, for the higher pressures the characteristic fracture occurred. In these plates in their centre region circle-shaped pieces of material have been cut out. Increasing the pressure followed cutting out circles of higher diameters. The highest applied initial pressure has caused the petelling fracture of plate.

The geometry of all tested plates, except the plate damaged by the explosion with initial pressure 0.8 bar (petelling fracture), have been measured. These measurements have been made in two directions going through plates' middle points: the first one along the plate diagonal and the second one parallel to the plate side. The example results are presented in Fig. 4-13 and Fig. 4-14. The measurements show that the square shape of specimens does not influence the axisymmetrical deformation of tested plates, therefore in further numerical applications an axisymmetrical analysis can be performed and in the verifications the average value of two measurements can be used. The average geometries (cross-sections) of all tested plates with initial pressures from 0.3 to 0.7 bars are presented in Annex 3.

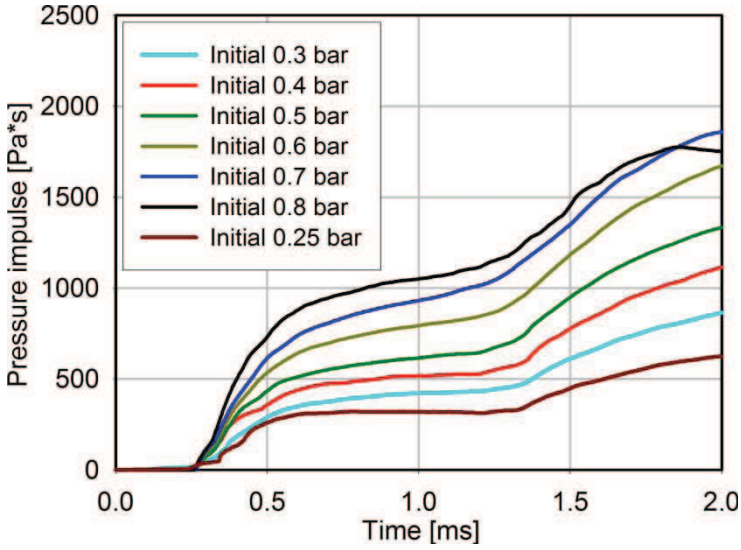

Fig. 4-11. Average values of pressure impulses for each pressure level

Fig. 4-12. Plates after experiments

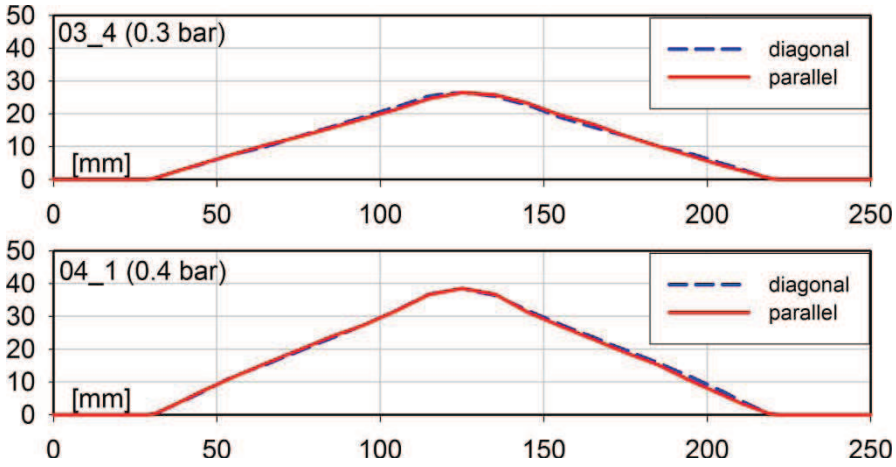

Fig. 4-13. Plates after experiments – intersections

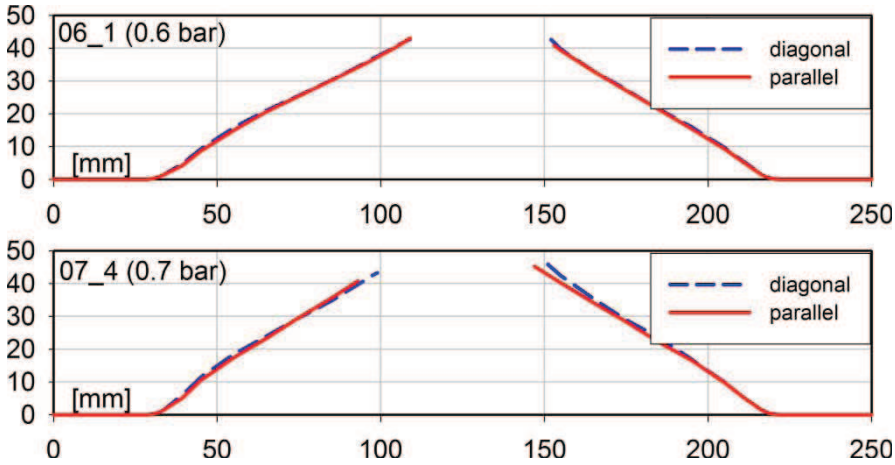

Fig. 4-14. Plates after experiments – intersections

In the test performed with the lowest initial pressure 0.25 bar, additionally, the deflection in the middle point of plate has been registered using an optic sensor. Performing this experiment has required disassembling of the second part of tube, see Fig. 4-15. Such a test, due to safety conditions, has been realized only for the lowest impact, where the fracture of plate has not been expected. The registered pressure and middle point deflection time histories are presented in Fig. 4-16. The initial 4 mm deflection of plate is caused by the negative pressure in the first tube (lack of the second tube precluded the pressure balance on both sides of the specimen).

In the plates, which have been damaged by cutting out almost circle shaped pieces of material, the equivalent diameters of holes are calculated. This measurement has been done by importing the pictures of plates in the appropriate scale to the program AutoCad. After import for every plate a hole's circumference has been marked and its area has been measured using program's tools. Then the circle's diameter of the same area has been calculated. The examples of this procedure are shown in Fig. 4-17, all results are presented in Annex 4.

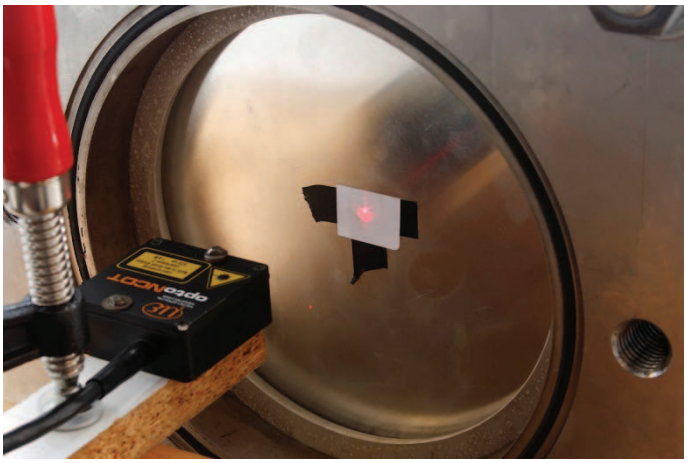

Fig. 4-15. Optic sensor measuring deflection of the plate

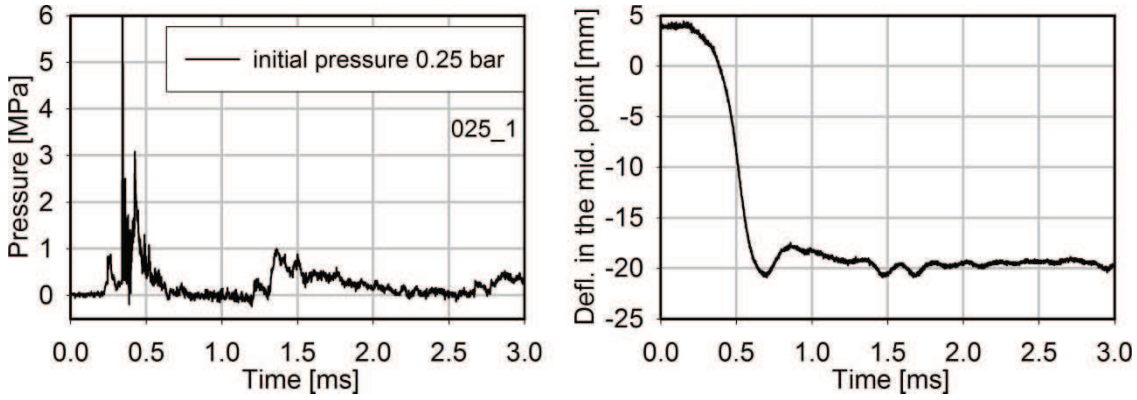

Fig. 4-16. Pressure and deflection time histories, test 0.25 bar

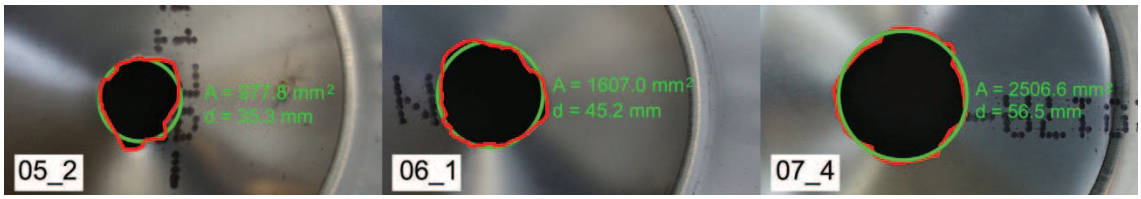

Fig. 4-17. Equivalent hole diameter measurement

Initial pressure	Test designation	Max. deflection [mm]	Hole diameter [mm]
0.25 bar	025_1	20.0	
0.3 bar	03_2	25.2	-
	03_3	28.2	-
	03_4	26.5	-
	03_5	26.3	-
0.4 bar	04_1	38.5	-
0.5 bar	05_2	-	35.3
	05_3	-	30.8
	05_4	-	34.2
0.6 bar	06_0	-	41.9
	06_1	-	45.2
	06_2	-	34.5
	06_3	-	38.7
0.7 bar	07_1	-	58.7
	07_2	-	39.3
	07_3	-	40.0
	07_4	-	56.5

Tab. 4-1. Characteristic results of the plates' measurement

All characteristic results, which are the maximum deflections in the middle points of plates or the equivalent hole diameters are listed in Tab. 4-1. The differences in these results for particular initial pressures are relatively high, especially for its higher values. That is why

the relationship between every presented characteristic result and its impulse obtained during the test are checked. The values of impulses are taken for the time step of 0.9 ms, which is the end time of main impact in all experiments. The setting-up is presented in Fig. 4-18. The results show that relationship between the plates' geometries after experiments and the values of pressure impulses is noticeable. Two results: tests 07_2 and 07_3 seem to unfit. This might be caused by the problems with the igniter during the last tests. The first has been conditionally accepted (its result is similar to the 0.6 bar tests). The second has been rejected for the further analyses.

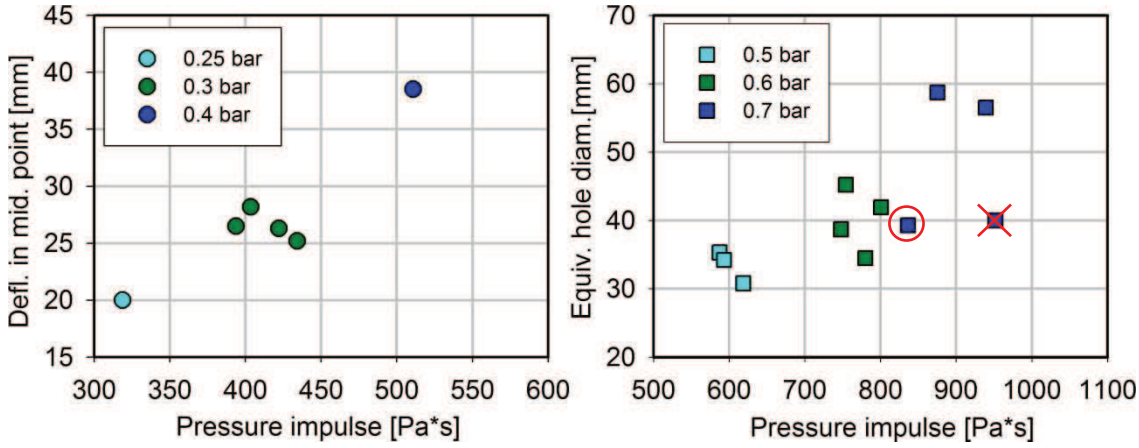

Fig. 4-18. Plates geometry referred to pressure impulses

4.3.4. Experimental work in quasi-static test

The dynamic experiments on plates have exhibited that the specimens fixing in the tube does not fulfil typical support conditions such as a full clamping. During the explosion, the plate have been slid and folded inside the fixing area in half height, see Fig. 4-19. That is why

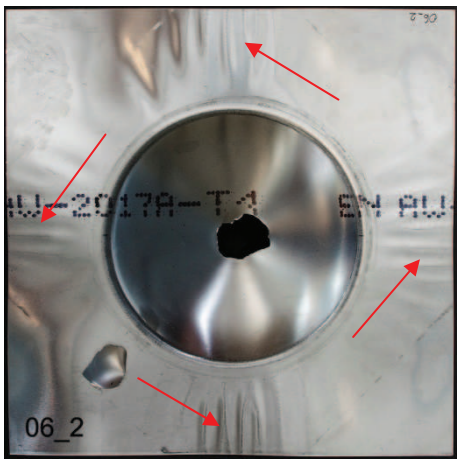

Fig. 4-19. Folding of the plate in the fixing area

the static experiment has been performed. The result of the static experiment will be used further for boundary condition modelling.

The research stand, for performing static experiments, has been prepared in the same way as in the dynamic test with the lowest initial pressure. Also in this test the second part of the tube has been disassembled and the middle point deflection has been measured. The static loading has been applied by slowly increasing air pressure in the first part of the tube up to the value of 2 bar.

4.3.5. Result of quasi-static experiment

The result of experiment is the middle point deflection vs. pressure value curve presented in Fig. 4-20. The maximum pressure level of 2 bar have assured elastic behaviour of the plate, after reducing the loading to the starting point the plate's deflection have came back to the zero value.

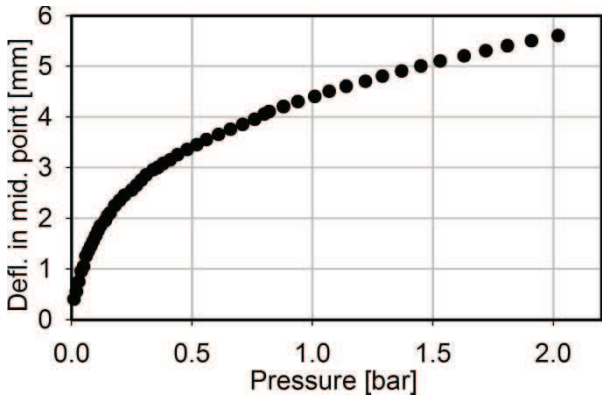

Fig. 4-20. Result of static experiment

4.4. Uniaxial experiments

The uniaxial experiments have been performed in purpose of the further material parameters identification. The specimens for these tests have been prepared from the material used in the main experiments. They have been cut from the virgin aluminium plates as flat rectangular of size of 150x12x1 mm along and across sheet's rolling directions. All uniaxial experiments have been performed using the Zwick/Roell Z020 test machine equipped with an extensometer presented in Fig. 4-21. The machine's clamps spacing has been set to 75 mm, the gauge length to 40 mm. All tests have been carried out at room temperature.

Fig. 4-21. Test machine with the extensometer

4.4.1. Tension tests with constant strain rates

The tension tests have been performed for five different constant strain rates: 0.0001 1/s, 0.0005 1/s, 0.001 1/s, 0.005 1/s and 0.01 1/s. Both kinds of the specimens, cut along and across sheet's rolling directions, have been tested to the rupture. For all chosen rates (except 0.0001 1/s) two the same tests have been realized. The results (true stress vs. true strain curves) of all experiments are presented in Annex 5, here some examples are shown in Fig. 4-22.

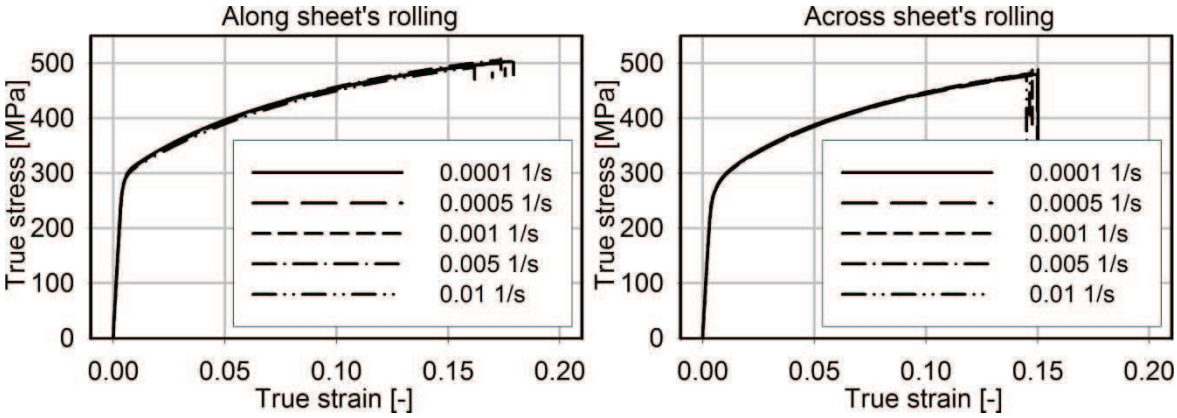

Fig. 4-22. Results of tension tests with constant strain rates

4.4.2. Load-unload tension cyclic tests

The load-unload tension tests have been performed with a constant strain rate 0.0005 1/s in the loading phases, the unloading phases have been controlled by force, decreasing down to zero value with the same velocity. The successive cycles have been proceeded with 0.015 of

the total strain increment. Also here both kinds of the specimens, cut along and across the sheet's rolling direction, have been tested. For each kind, two tests have been realized. The results of all experiments are presented in Annex 5, here the examples are shown in Fig. 4-23. The results are presented as the plots of uniaxial force value vs. displacement. It will be suitable in further identifications.

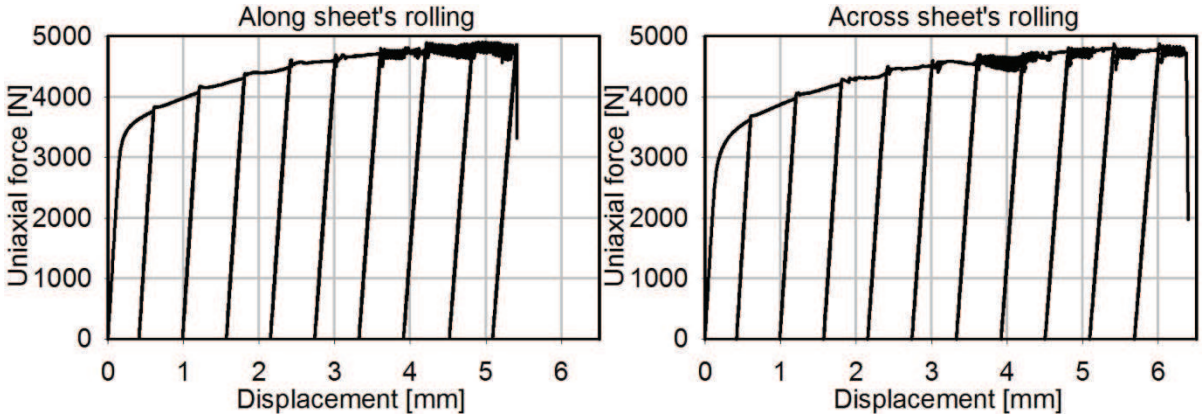

Fig. 4-23. Results of load-unload tension cyclic tests

4.5. Summary

All experimental work has been performed with the highest possible to achieve precision during the realization and during elaborating the results. The author has been actively engaged in all experiments, which have been performed. All elaboration of results has been done by him. The experimental results, which have been acquired, are the base of the further work: material parameters identification and finally modelling of the main problem and its verification.

5. Material parameters identification

5.1. Abstract

The description of the aluminium alloy Al2017 material parameters identification is the main subject of the present chapter. The calibration procedures of the elastic modulus, the offset yield stress and the other assumed constitutive model parameters including damage are presented. This identification has been made on the basis of the uniaxial laboratory tests results. Due to the assumption made in Chapter 2 concerning the isotropy of the material, all parameters have been identified separately from the results of tests on the specimens cut along and across sheet's rolling and later the mean values have been calculated. After identifications suitable verifications have been performed.

5.2. Introduction

Material parameters identification is a basic stage for further numerical modelling analysis. Usually the assumed model parameters can be calibrated using different methods. Proposed approaches very often depend on the experiments, which are chosen for identification. A selection of appropriate method, precise experiments and an accurate calibration are necessary conditions for a correct identification. After each calibration procedure a verification of obtained material parameters is indispensable.

During the procedures of identification, calculation of the different mathematical quantities is required. In the present work very often it is necessary to obtain the arithmetic mean value

$$\bar{y} = 1/n \sum_{i=1}^{n} y_i, \tag{5.1}$$

where y_i is an i-th value (from a collection size n) of a function obtained in experiment or identification. Also the standard deviation, as a measure of the variability or dispersion, is calculated

$$s_d = \sqrt{\frac{1}{n-1} \sum_{i=1}^{n} \left(y_i - \bar{y} \right)^2}. \tag{5.2}$$

In more complicated procedures of identification very often different approximations are needed. In all such occurrences in the present work, the curve fitter tool offered by the commercial program SigmaPlot has been used. Nevertheless, the author has prepared his own

procedure for each identification. The program uses the Marquardt-Levenberg algorithm to find the coefficients of the independent variables that give the best fit between the equation and the data. This algorithm seeks the values of parameters that minimize the sum of the squared differences between the values of the observed and predicted values of the dependent variable [157]

$$SS = \sum_{i=1}^{n} w_i \left(y_i - \hat{y}_i \right)^2, \tag{5.3}$$

where SS is the minimized sum, y_i, $\hat{y}_i$ are the observed and the predicted value of the dependent variable, respectively, and w_i is the weight parameter.

The verification of identification results requires a parameter, which indicates a fitting between numerical simulations and experiments. In all verifications in the present work coefficients of determination r^2 and correlation $r = \sqrt{r^2}$ have been calculated ([95], [45])

$$r^2 = \frac{S_t - S_r}{S_t}, \qquad S_r = \sum_{i=1}^{n} \left(y_i - f_i \right)^2, \qquad S_t = \sum_{i=1}^{n} \left(y_i - \bar{y} \right)^2, \tag{5.4}$$

where f_i is an i-th value of a function obtained in approximation. The values of correlation coefficient changes between $r \in \langle 0;1 \rangle$, $r = 1$ means full fitting, $r \approx 0$ means very low or lack of fitting.

5.3. Identification of elastic modulus and yield stress

The first performed identification is the estimation of the elastic modulus E and the yield stress $R_{p0.2}$. For the purpose of this identification the results of uniaxial tension tests with constant strain rate yield stress has been used.

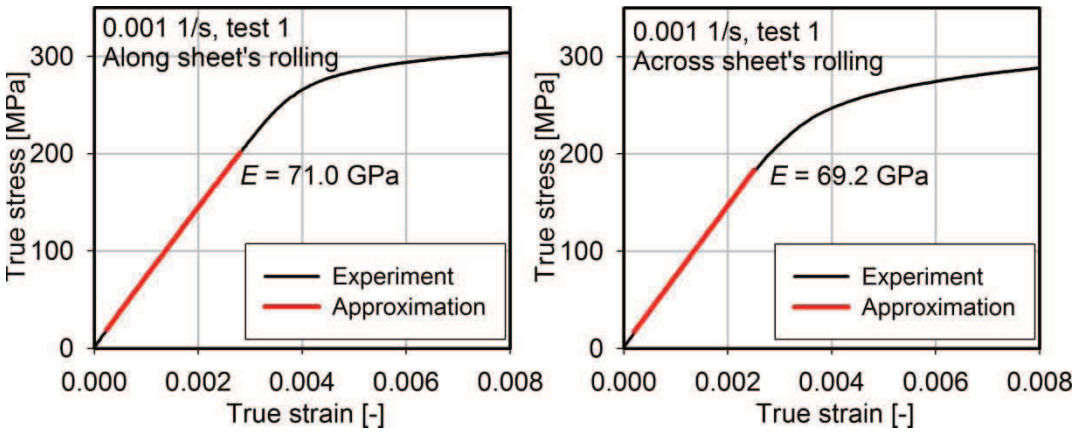

Fig. 5-1. Elastic modulus identification

The values of the elastic modulus have been estimated by approximating the elastic range of strain-stress tension test curve by a linear function $f(x) = ax + b$. The identification has been performed separately for all tension tests results and then the mean value has been calculated. All approximations are presented in Annex 6, here the examples of two tension tests for the specimens cut along and across sheet's rolling direction are shown in Fig. 5-1. The results of all particular identifications, the mean value of elastic modulus and the standard deviations are presented in Tab. 5-1.

Test	Specimens cut along sheet's rolling E [GPa]	Specimens cut across sheet's rolling E [GPa]
0.0001 1/s	69.8	67.6
0.0005 1/s, t1	70.9	68.7
0.0005 1/s, t2	70.7	68.3
0.001 1/s, t1	71.0	69.2
0.001 1/s, t2	71.5	70.4
0.005 1/s, t1	72.0	69.5
0.005 1/s, t2	70.6	70.0
0.01 1/s, t1	71.3	70.4
0.01 1/s, t2	70.5	69.2
Mean values	**70.9**	**69.2**
Standard deviations	0.64	0.95
Mean value	**70.1**	

Tab. 5-1. Results of elastic modulus identification

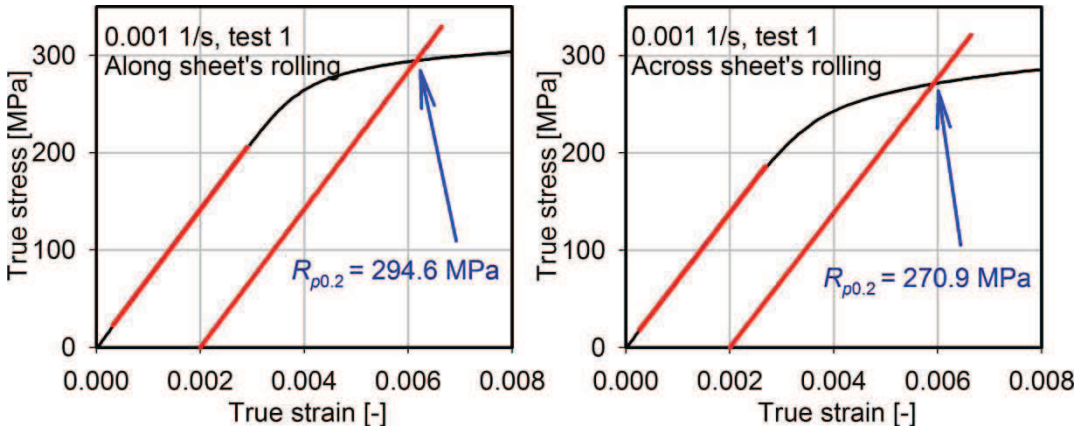

Fig. 5-2. Offset yield strength identification

The tested material has not shown the distinct yield stress, that is why the offset yield stress $R_{p0.2}$ had to be identified. These values are estimated as stress responding to the intersection point of the strain-stress curve with a line parallel to the elastic range of this

curve. The offset between the curve and the line expressed in strain values has been assumed as 0.2 %. The identifications for all tension tests are presented in Annex 6, here the examples are shown in Fig. 5-2. The results of all particular identifications and the mean values of the offset yield stress for each strain rate are presented in Tab. 5-2.

Test	Specimens cut along sheet's rolling $R_{p0.2}$ [MPa]		Specimens cut across sheet's rolling $R_{p0.2}$ [MPa]		Mean value
0.0001 1/s	294.3	294.3	270.4	270.4	282.3
0.0005 1/s, t1	292.9	293.8	269.4	269.2	281.5
0.0005 1/s, t2	294.7		269.0		
0.001 1/s, t1	294.6	295.3	270.9	271.5	283.4
0.001 1/s, t2	296.0		272.2		
0.005 1/s, t1	296.4	294.0	269.5	270.3	282.1
0.005 1/s, t2	291.6		271,2		
0.01 1/s, t1	295.2	293.5	271.0	270.9	282.2
0.01 1/s, t2	291.8		270.8		

Tab. 5-2. Results of offset yield strength identification

5.4. Identification of Chaboche model parameters

This identification is performed on the basis of the procedure given in [95]. Estimating the material parameters requires writing the Chaboche model equations in uniaxial loading conditions. The deviators of the stress tensor $\boldsymbol{\sigma}'$ and the kinematic hardening tensor $\mathbf{X}'$ in such conditions have the following form

$$\boldsymbol{\sigma}' = \begin{bmatrix} \frac{2}{3}\sigma & 0 & 0 \\ 0 & -\frac{1}{3}\sigma & 0 \\ 0 & 0 & -\frac{1}{3}\sigma \end{bmatrix}, \quad \mathbf{X}' = \begin{bmatrix} \frac{2}{3}X & 0 & 0 \\ 0 & -\frac{1}{3}X & 0 \\ 0 & 0 & -\frac{1}{3}X \end{bmatrix}, \tag{5.5}$$

where σ is the stress and X is the kinematic hardening, both in uniaxial loading conditions. The invariant J of the above tensors difference can be written as

$$\mathrm{J}\left(\boldsymbol{\sigma}' - \mathbf{X}'\right) = \left|\sigma - X\right|. \tag{5.6}$$

The basic Chaboche model formulas can be written in the following way

$$\dot{\varepsilon}^I = \gamma \left\langle \frac{|\sigma - X| - R - k}{K} \right\rangle^n \operatorname{sgn}(\sigma - X), \tag{5.7}$$

$$\dot{X} = \frac{2}{3} a \dot{\varepsilon}^I - cX \left| \dot{\varepsilon}^I \right|, \tag{5.8}$$

$$\dot{R} = b\left(R_1 - R\right) \left| \dot{\varepsilon}^I \right|, \tag{5.9}$$

where $\dot{\varepsilon}^I$ is the inelastic strain rate in uniaxial loading conditions. Both hardening functions can be integrated explicitly

$$X = \theta \frac{2}{3} \cdot \frac{a}{c} + \left(X_0 - \frac{2}{3} \cdot \frac{a}{c} \right) \exp\left(-c\left(\varepsilon^I - \varepsilon_0^I \right) \right), \tag{5.10}$$

$$R = R_1 \left(1 - \exp\left(-b \left| \varepsilon^I \right| \right) \right), \tag{5.11}$$

where $\theta = \operatorname{sgn}(\sigma - X) = \pm 1$, X_0 and ε_0^I are the initial values of the kinematic hardening and inelastic strain functions. The equation (5.7) can be transformed to the following stress function

$$\sigma = X\left(\varepsilon^I, X_0, \varepsilon_0^I \right) + \theta R\left(\left| \varepsilon^I \right| \right) + \theta k + \theta K \left| \dot{\varepsilon}^I \right|^{1/n}. \tag{5.12}$$

The Chaboche model material parameters can be identified from the uniaxial fully reversible cyclic loading tests or the tension tests with constant strain rate (for several different strain rates). Despite of better effectiveness of the first method, the second had to be chosen, as the specimens (cut from the one millimetre thickness aluminium alloy sheet) have been too sensitive to buckling, so the compression loading phase in cyclic test has been unrealizable.

For the identification of the Chaboche model parameters, the results of the tensile tests with at least three different strain rates are necessary. In this work the results of five different strain rates are used.

The procedure of identification requires the following functions calculated from the laboratory test: stress σ, total strain ε, inelastic strain ε^I and inelastic strain rate $\dot{\varepsilon}^I$. The first two functions have been prepared during elaborating the uniaxial tests results in Chapter 5.3. The functions of the inelastic strain are calculated directly from the equation

$$\varepsilon_{pl} = \varepsilon - \frac{\sigma}{E}. \tag{5.13}$$

The computation of the inelastic strain rate functions is more complicated. In calculations, the following rule of numerical differentiation has been applied [45]

$$\dot{\varepsilon}^I\left(t_i\right)=\frac{\varepsilon^I\left(t_i\right)-\varepsilon^I\left(t_{i-1}\right)}{dt}+O\left(dt\right)\ \ i=2,3,...,n\,. \tag{5.14}$$

Unfortunately, after using in calculations the results of laboratory tests directly with the above formula, it has been found that the inelastic strain rate functions are not smooth enough for the identification. This problem has been solved by approximating the strain by the polynomial time funcions of degree 1 and the stress by the polynomials of degree 10. In these actions only the values behind the proportionality limit are taken. Recalculating the inelastic strain rate using the results of approximation gives smooth enough functions (after approximation two methods of the inelastic strain rate calculation are possible: by analytical differentiation or by the numerical differentiation – using the rule (5.14), the same results have been obtained by both methods).

Two examples of this procedure for different kind of specimens and strain rates are presented. The first one for the specimen cut along sheet's rolling and tested with 0.001 1/s (test 1). The following strain and stress functions have been obtained after approximations (Fig. 5-3)

$$\varepsilon\left(t\right)=9.69\cdot10^{-4}t-6.22\cdot10^{-4}, \tag{5.15}$$

$$\begin{aligned}\sigma\left(t\right)=&-1.13\cdot10^{-12}t^{10}+3.91\cdot10^{-10}t^{9}-5.92\cdot10^{-8}t^{8}+5.11\cdot10^{-6}t^{7}-2.79\cdot10^{-4}t^{6}+\\&+0.01t^{5}-0.24t^{4}+3.69t^{3}-35.61t^{2}+195.76t-164.49.\end{aligned} \tag{5.16}$$

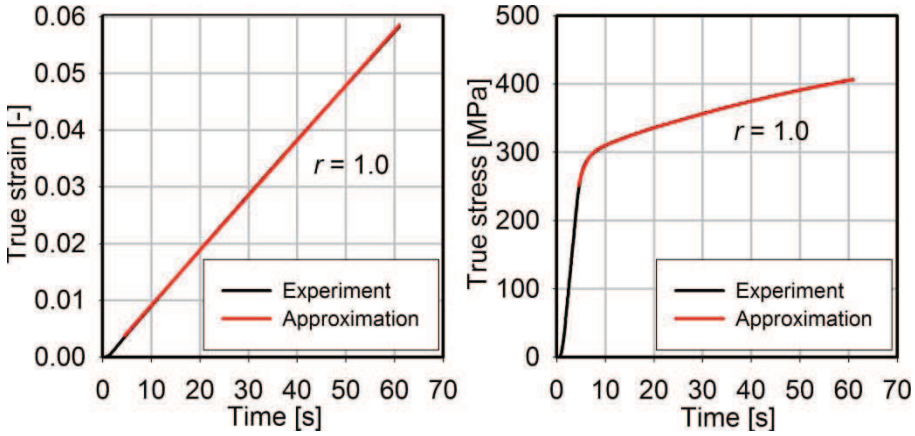

Fig. 5-3. Approximation of the strain and stress functions, example 1

The strain-stress graph after this procedure is presented in Fig. 5-4. The final results obtained for inelastic strain and inelastic strain rate using the results of approximation are presented in

Fig. 5-5. It has been found that the difference between the inelastic strain function before and after approximation is very small, but as it has been mentioned before, for the inelastic strain rate function, such procedure is necessary.

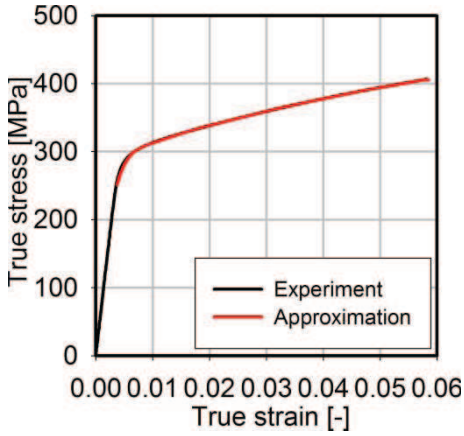

Fig. 5-4. Stress versus strain after approximations, example 1

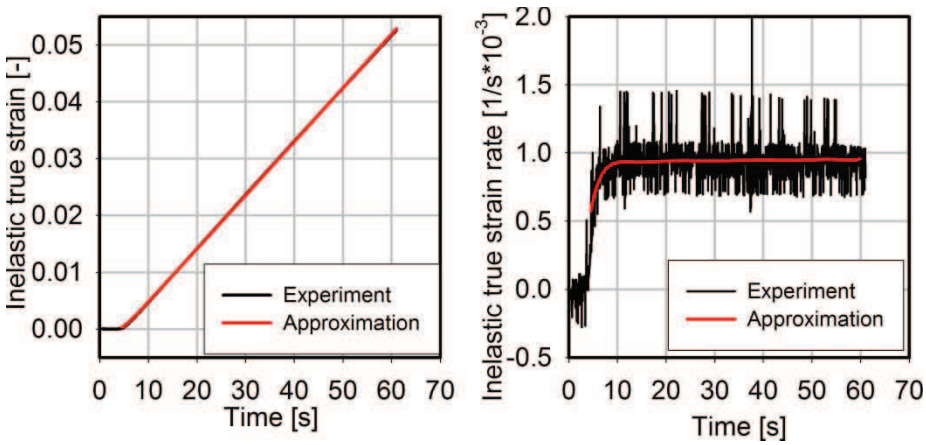

Fig. 5-5. Functions of inelastic strain and its rate before and after approximations, example 1

The second example is presented for the specimen cut across sheet's rolling direction and tested with 0.01 1/s (test 1). The following strain and stress functions have been obtained (Fig. 5-6)

$$\varepsilon(t) = 9.68 \cdot 10^{-3} t - 9.72 \cdot 10^{-3}, \tag{5.17}$$

$$\begin{aligned} \sigma(t) = {} & -0.012t^{10} + 0.55t^{9} - 10.66t^{8} + 120.66t^{7} - 8.77 \cdot 10^{2} t^{6} + 4.27 \cdot 10^{3} t^{5} + \\ & - 1.41 \cdot 10^{4} t^{4} + 3.1 \cdot 10^{4} t^{3} - 4.38 \cdot 10^{4} t^{2} + 3.57 \cdot 10^{4} t - 1.25 \cdot 10^{4}. \end{aligned} \tag{5.18}$$

The strain-stress graph after above approximations is presented in Fig. 5-7 and the final results in Fig. 5-8. The conclusions are the same as in the first example. The preparation of all other tension tests plots proceeded in a similar way and the effects are as good as in presented examples.

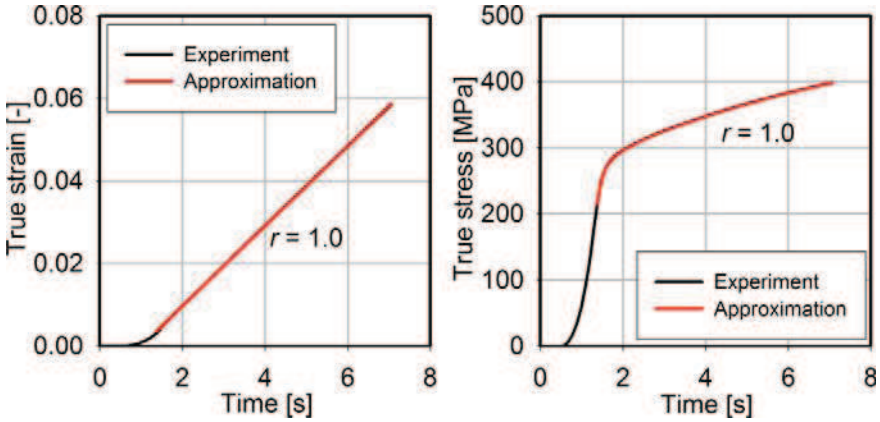

Fig. 5-6. Approximation of the strain and stress functions, example 2

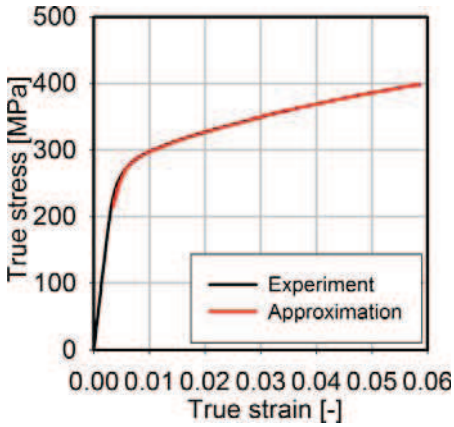

Fig. 5-7. Stress versus strain after approximations, example 2

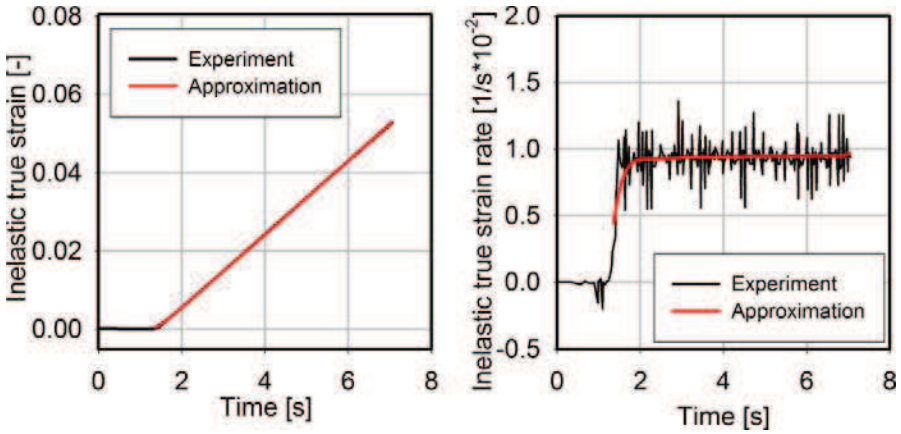

Fig. 5-8. Functions of inelastic strain and its rate before and after approximations, example 2

The identification should be started with estimating the value of the parameter k, which is the yield stress for theoretical zero strain rate. The graph presenting the dependence of the estimated offset yield stress to the test's strain rates is shown in Fig. 5-9. It has been found that the material in room temperature shows very weak viscous properties, the values of yield stress are almost constant for different strain rates. The parameter k has been assumed as equal to the average value. The result is presented in Tab. 5-3.

The very weak viscous properties in room temperature in analyzed material has caused necessity of making assumptions for parameters controlling viscosity in the model: n and K. The values have been established as: n = 10, K = 5 MPa. This assumption has been done on the basis of the identification presented in [93], where it has been shown that such parameters work well in the aluminium alloy material with similar characteristics.

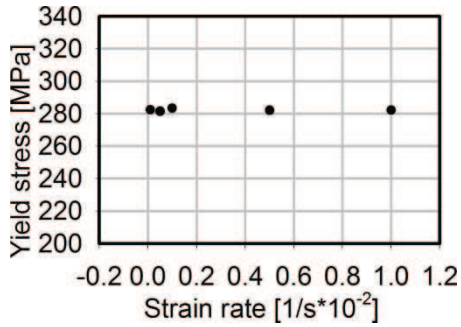

Fig. 5-9. Offset yield stress versus strain rates

Strain rates [1/s]	0.0001	0.0005	0.001	0.005	0.01	Mean values	Mean value
Along, $R_{p0.2}$ [MPa]	294.3	293.8	295.3	294.0	293.5	**294.2**	**282.3**
Across, $R_{p0.2}$ [MPa]	270.4	269.2	271.5	270.3	270.9	**270.5**	

Tab. 5-3. Mean value of offset yield stress

The last step of identification, estimating the values of hardening parameters: a, c, b and R_1, is realized by approximation of the laboratory tests results: function of stress σ, inelastic strain ε^I and inelastic strain rate $\dot{\varepsilon}^I$. The main formula, which is used for this approximation, is the stress function given by equation (5.12) and its components, hardening functions, defined in equations (5.10) and (5.11). The identification is made on the basis of uniaxial tension tests, where the initial values of the kinematic hardening $X_0 = 0$ and inelastic strain $\varepsilon_{pl0} = 0$, so the equation (5.10) can be simplified to the following form

$$X = \frac{2}{3} \cdot \frac{a}{c} \left(1 - \exp\left(-c\varepsilon_{pl}\right)\right). \tag{5.19}$$

At first the approximations have been done separately for each uniaxial test result, then the test's results have been cumulated for each strain rate and finally cumulated for each specimen's kind. At the end the mean value has been calculated. The results are presented in Tab. 5-4. This procedure is forced by high sensitivity of approximation to initial values, when four different parameters are estimated together. For the first approximation, the initial

parameters have been taken from the results of identification presented in [93]: $a = 4.7 \cdot 10^5$ MPa, $c = 5.4 \cdot 10^4$, $b = 7.4$, $R_1 = 213.3$ MPa. For all next estimations, the initial values have been replaced by those from previous calculations.

	a [MPa]	c [-]	b [-]	R_1 [MPa]
Along sheet's rolling	1019.9	7.5	129.9	18.1
Across sheet's rolling	3274.3	60.8	185.1	12.9
Mean values	**2147.1**	**34.2**	**157.5**	**15.5**

Tab. 5-4. Mean values of hardening material parameters

5.5. Verification of material parameters identification

The complete set of accepted constitutive law material parameters for aluminium alloy Al2017 is presented in Tab. 5-5. The verification of the obtained values is made by comparison of the numerical simulations of laboratory tests results with the uniaxial experiments results. The numerical calculations have been performed according to the description presented in Chapter 3. In the analysis the damage has not been taken into account, as the verification concerns the constitutive law material parameters only. The static scheme assumed in the uniaxial tension test simulations is the 1 mm thickness clamped bar, calculated in a two dimensional state of stress, presented in Fig. 5-10. The four node thick shell elements are used. To check and avoid the mesh density influence two different meshings are analyzed (coarse mesh – 180 elements and fine mesh – 720 elements). The loading is applied by the support right displacement. The numerical simulations have been performed for three different strain rates: 0.01, 0.001 and 0.0001 1/s.

E [MPa]	ν [-]	k [MPa]	a [MPa]	c [-]	b [-]	R_1 [MPa]	n [-]	K [MPa]
70.0	0.33	282.0	2150.0	34.0	157.5	15.5	10.0	5.0

Tab. 5-5. Final values of constitutive law material parameters

The numerical calculations for the first verification, the tensile test with 0.001 1/s strain rate, presented in Fig. 5-11 have been performed for two meshes: coarse and fine. It has been obtained almost full agreement between both results. Therefore, in all further uniaxial numerical calculations only the coarse mesh has been used. The comparison of numerical and

experimental results gives a very high correlation, the average correlation coefficient (the average value calculated for two experimental results: along and across sheet's rolling directions) reaches the value of 0.993.

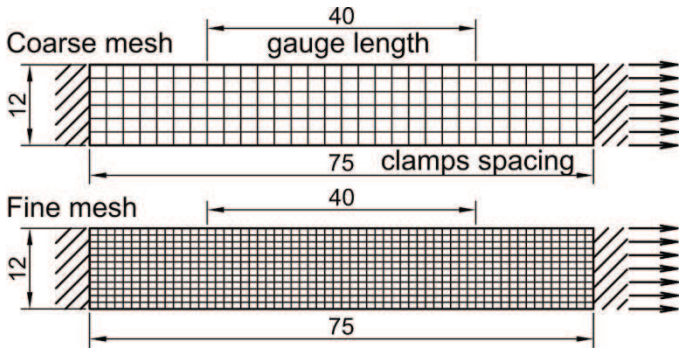

Fig. 5-10. Static scheme in uniaxial tension tests simulations

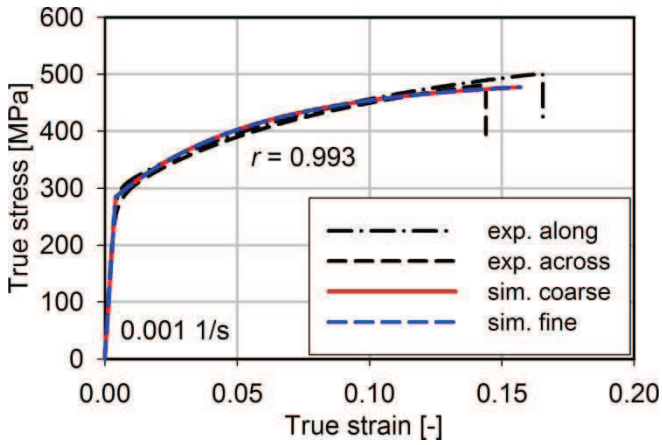

Fig. 5-11. Verification of numerical results, tension test 0.001 1/s

The next two verifications, the tension test with 0.01 and 0.0001 1/s strain rate, presented in Fig. 5-12 and Fig. 5-13, have confirmed high correlations between the numerical and experimental results. The obtained correlation coefficients *r* are 0.988 and 0.992.

The last question in this verification, which might be asked, is if the assumption of the material isotropy by taking the mean values of material parameters is not too strong. The parameters presented in Tab. 5-3 and Tab. 5-4, identified for two types of the specimens, are rather different. To answer that question the additional two simulations have been performed. In each, the material parameters identified separately (along and across sheet's rolling) have been used. The results of this analysis are presented in Fig. 5-14. The differences between the obtained plots and the previous one (simulation performed with the mean values of parameters) are rather small.

Therefore, after all verifications, it has been proofed that the material parameters have been identified correctly.

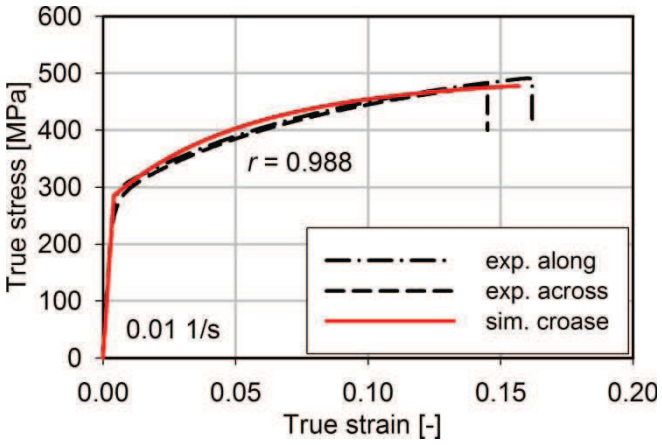

Fig. 5-12. Verification of numerical results, tension test 0.01 1/s

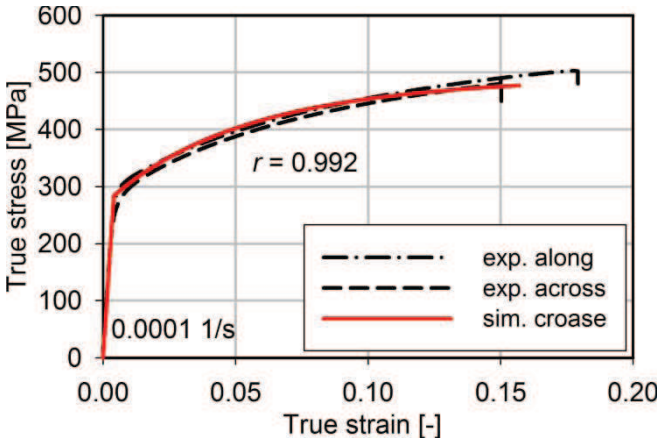

Fig. 5-13. Verification of numerical results, tension test 0.0001 1/s

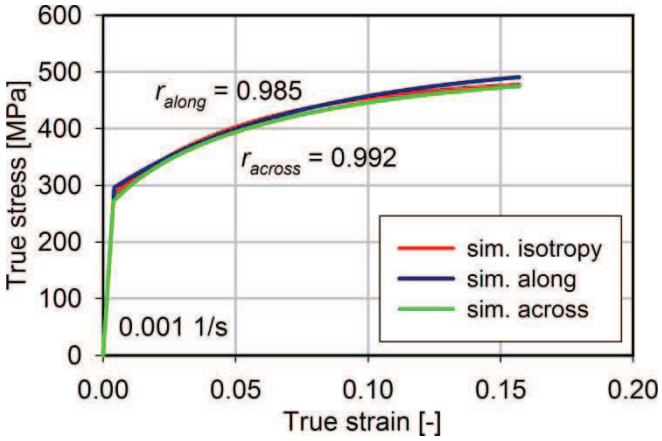

Fig. 5-14. Verification of material isotropy assumption, tension test 0.001 1/s

5.6. Identification of damage and its model material parameters

5.6.1. Damage measurement method

The damage measurement can be done using the direct or nondirect method [109]. The direct method is based on the damage definition (2.22), where the evaluation of damage consists in the evaluation of the total crack areas δS_D lying on a surface δS at mesoscale. This measurement can be done by observing micrograph pictures with a magnification of 1000. This method is destructive and difficult in practice. The nondirect methods give more possibilities. The measurement of the damage can be performed by using the variations of the elasticity modulus, microhardness, density, electrical resistance, cyclic plasticity response, tertiary creep response and acoustic emission etc.

The easiest in practice is the nondirect method based on the influence of damage on elastic properties of a material. The formula, which allows estimation of the damage, can be derived from the concept of effective stress (2.25) and the direct state coupling in uniaxial loading conditions

$$\varepsilon_{el} = \frac{\sigma}{E(1-D)} = \frac{\sigma}{\tilde{E}}, \tag{5.20}$$

where $\tilde{E}$ is considered as the effective elasticity modulus of the damaged material

$$\tilde{E} = E(1-D). \tag{5.21}$$

The values of the damage parameter may be evaluated from the following equation

$$D = 1 - \frac{\tilde{E}}{E}. \tag{5.22}$$

Performing this measurement requires the results of the uniaxial load-unload tension tests, presented in the previous chapter. The identification of elastic modulus for each load-unload cycle in this method is necessary. According to Celentano and Chaboche [39] the uniaxial modulus corresponding to an elastic path of a cycle *i* can be obtained with:

$$E_i = \frac{\frac{P_u - P_l}{A_l}}{\frac{L_u - L_l}{L_l}} \tag{5.23}$$

where P is the current axial load, A is the current transversal area of the sample, L is the current extensometer length and sub indexes u and l refer to the upper and lower points located in the elastic path of the stress-strain curve, respectively.

In the chosen method some precautions related to non-linearities have to be taken [109]. The most accurately damage measurement is obtained when the values of elastic modulus are estimated during unloadings. At the beginning and at the end of each unloading paths there are small non-linearities due to viscous or hardening effects and also caused by experimental devices. The best way is to ignore them and identify E_i in the range: $0.15P_{max}/A < P/A < 0.85P_{max}/A$.

In the present identification of the each cycle elastic modulus, the linear approximations are applied. In the assumed range, the function of uniaxial force vs. displacement has been approximated by a linear function $f(x) = a \cdot x + b$. The examples of this procedure are presented in Fig. 5-15 and Fig. 5-16. The values of axial load and extensometer length, necessary in equation (5.23), are taken as initial and final values of the linear functions after approximations. The current extensometer lengths in equation (5.23) are calculated as initial extensometer length (40 mm) plus obtained displacement.

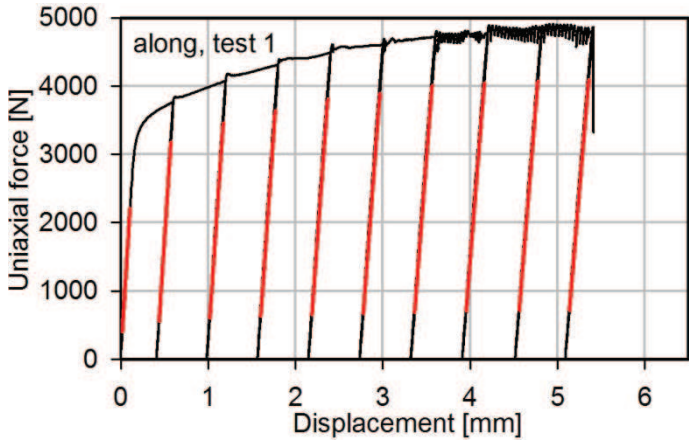

Fig. 5-15. Example of approximations used in elastic modulus identification (along, test 1)

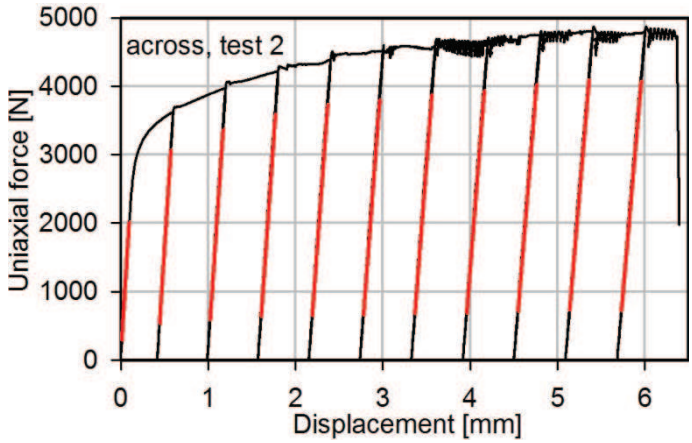

Fig. 5-16. Example of approximations used in elastic modulus identification (across, test 2)

Estimation of the elastic modulus according to equation (5.23) requires the values of the current transversal area of the specimen. This kind of measurement has not been realized during the laboratory tests. Two different approaches to overcome this problem are proposed.

5.6.2. Damage measurement, first approach

In the first variant, the constant transversal area during the test has been assumed. Its current value at the lower point of elastic path A_l is replaced by the initial value A_0. In this approach equation (5.23) is changed to the following formula

$$E_i = \frac{\frac{P_u - P_l}{A_0}}{\frac{L_u - L_l}{L_0}} \tag{5.24}$$

Cycle	P_u [N]	P_l [N]	A_0 [mm^2]	L_u [mm]	L_l [mm]	L_0 [mm]	E_i [MPa]
0	2213.5	398.5	11.7	40.107	40.019	40.0	70181
1	3177.0	555.0	11.7	40.575	40.441	40.0	68480
2	3460.3	601.3	11.7	41.175	41.022	40.0	67190
3	3637.6	630.4	11.7	41.770	41.604	40.0	67042
4	3807.7	644.7	11.7	42.370	42.190	40.0	66834
5	3888.9	669.2	11.7	42.967	42.778	40.0	66506
6	4010.0	685.2	11.7	43.566	43.366	40.0	66768
7	4045.7	701.0	11.7	44.164	43.956	40.0	66420
8	4071.9	712.4	11.7	44.777	44.564	40.0	66834
9	4095.9	712.6	11.7	45.359	45.138	40.0	66709

Tab. 5-6. Example of first approach elastic modulus identification (along, test 1)

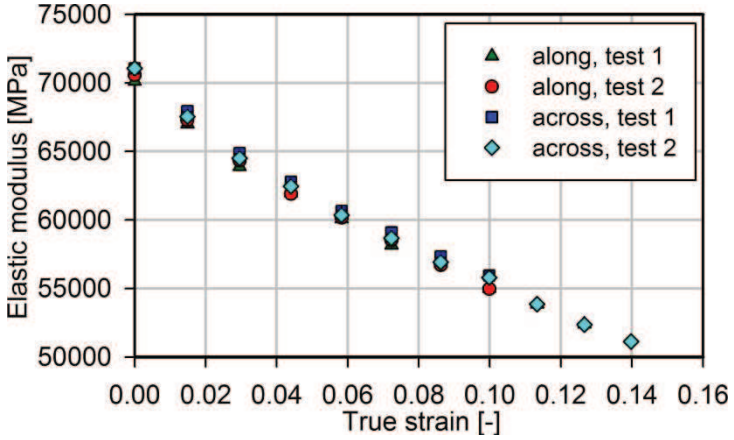

Fig. 5-17. Final results of first approach elastic modulus identification

Cycle	P_u [N]	P_l [N]	A_0 [mm^2]	L_u [mm]	L_l [mm]	L_0 [mm]	E_i [MPa]
0	2017.2	292.2	11.6	40.097	40.014	40.0	71066
1	3067.8	535.0	11.6	40.576	40.447	40.0	67545
2	3365.6	587.2	11.6	41.174	41.026	40.0	64516
3	3593.3	637.4	11.6	41.773	41.610	40.0	62455
4	3735.2	647.1	11.6	42.371	42.195	40.0	60366
5	3797.7	653.2	11.6	42.966	42.781	40.0	58674
6	3878.6	674.7	11.6	43.564	43.370	40.0	56920
7	3931.4	684.3	11.6	44.164	43.963	40.0	55789
8	4027.8	709.9	11.6	44.763	44.550	40.0	53865
9	4091.7	734.6	11.6	45.363	45.142	40.0	52357
10	4072.6	724.0	11.6	45.961	45.735	40.0	51116

Tab. 5-7. Example of first approach elastic modulus identification (across, test 2)

The detail results of first approach elastic modulus identification for two example tests are presented in Tab. 5-6 and Tab. 5-7. All results are shown in Fig. 5-17.

After estimation of the elastic modulus values in each cycle the damage may be evaluated directly from equation (5.22). The results are presented in Fig. 5-18.

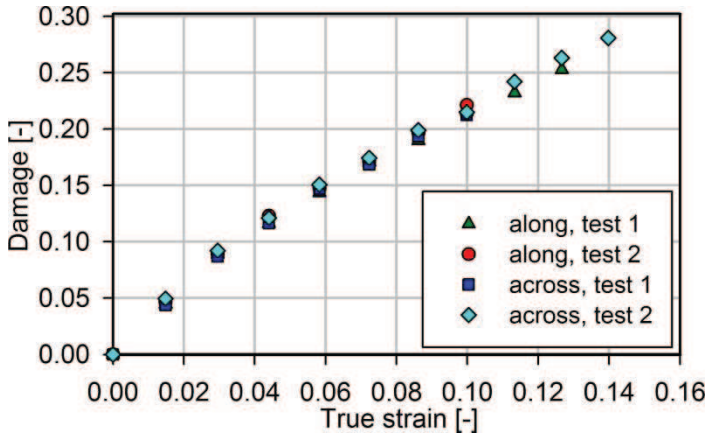

Fig. 5-18. Final results of first approach damage measurement

5.6.3. Identification of model material parameters for first damage approach

There are at least three different methods for the damage material parameters identification, which can be found in literature: Mashayekhi et al. in [120], Ambroziak in [6] and Daudonnet in [55]. Their description and verification are presented in [88]. This study shows that the best correlation between numerical and experimental results can be obtained by

the last mentioned method. After small modification this method is applied in the present work.

The base equations of these identifications are the damage function (2.40) and the damage strain energy function (2.33). Taking both in uniaxial loading conditions and substituting the second to the first one, the following formula is obtained

$$\dot{D} = \frac{dD(\varepsilon^I)}{dt} = \left(\frac{\sigma^2}{2E(1-D)^2 S} \right)^s (1-D)^{-\beta+1} \frac{d\varepsilon^I}{dt}. \tag{5.25}$$

Then by reducing *dt* this formula is simplified to following form

$$\frac{dD}{d\varepsilon^I} = \left(\frac{\sigma^2}{2E(1-D)^2 S} \right)^s (1-D)^{-\beta+1}. \tag{5.26}$$

The main difficulty in this identification is to obtain the function $dD\left(\varepsilon^I\right)$ from experimental results. This problem is solved by approximation of experimental values function $D\left(\varepsilon^I\right)$ by the formula, which assures very good fitting and can be easy differentiated analytically. The following function is proposed

$$D\left(\varepsilon^I\right) = a\left(1-\exp(-b\varepsilon^I)\right). \tag{5.27}$$

The derivative of this function with respect to the inelastic strain ε^I gives

$$\frac{dD}{d\varepsilon^I} = ab\exp(-b\varepsilon^I). \tag{5.28}$$

By comparison of the function (5.28) with equation (5.26) the final formula, from which the material parameters can be approximated, is obtained

$$\frac{dD}{d\varepsilon^I} = ab\exp(-b\varepsilon^I) = \left(\frac{\sigma^2}{2E(1-D)^2 S} \right)^s (1-D)^{-\beta+1}. \tag{5.29}$$

The detail presentation of preparation to final identification of the damage material parameters s, S and β is presented for two example tests. The necessary in this example identification experimental data are listed in Tab. 5-8 and Tab. 5-9. The approximations of $D\left(\varepsilon^I\right)$ functions are presented in Fig. 5-19. The final identified values of damage material parameters, obtained in approximation of formula (5.29) using all experimental data, are presented in Tab. 5-10.

cycle	0	1	2	3	4	5	6	7	8	9
D [-]	0.0	0.044	0.088	0.116	0.143	0.171	0.189	0.215	0.232	0.253
ε^I [-]	0.0	0.010	0.024	0.038	0.052	0.066	0.080	0.093	0.107	0.120
σ [MPa]	294	326	358	384	407	423	439	450	458	465

Tab. 5-8. Experimental data for damage material parameters identification (along, test 1)

cycle	0	1	2	3	4	5	6	7	8	9	10
D [-]	0.0	0.049	0.092	0.121	0.151	0.174	0.199	0.215	0.242	0.263	0.281
ε^I [-]	0.0	0.010	0.024	0.038	0.052	0.066	0.080	0.093	0.107	0.120	0.133
σ [MPa]	270	317	352	379	400	418	430	442	458	469	474

Tab. 5-9. Experimental data for damage material parameters identification (across, test 2)

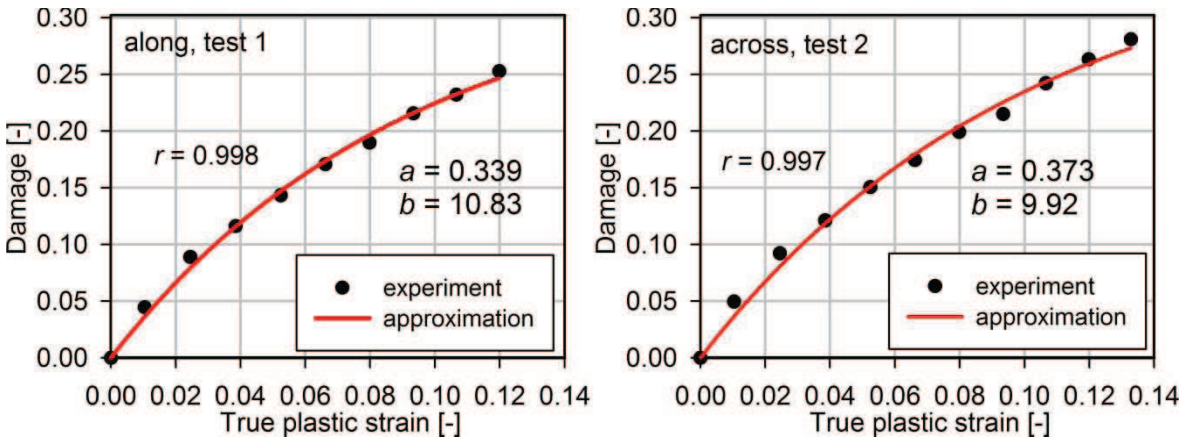

Fig. 5-19. Approximations of damage vs. plastic strain functions

S [GPa]	s [-]	β [-]
546.6	-0.099	-3.40

Tab. 5-10. Final values of first approach damage material parameters identification

5.6.4. Verification of first approach damage material parameters identification

The verification of the damage model material parameters identification has been performed using the same model as used in the verification of the constitutive law material parameters in Chapter 5.5. The only difference is that the damage model is included and the identified damage model material constants are applied. In the previous verification it has been found that the model behaves correctly for different strain rates. In the present verification the same conclusion are drawn. That is why here only one example, tension test

with 0.001 1/s strain rate, is presented in Fig. 5-20. The correlation between the numerical and experimental results is high. The correlation coefficient values are above 0.98.

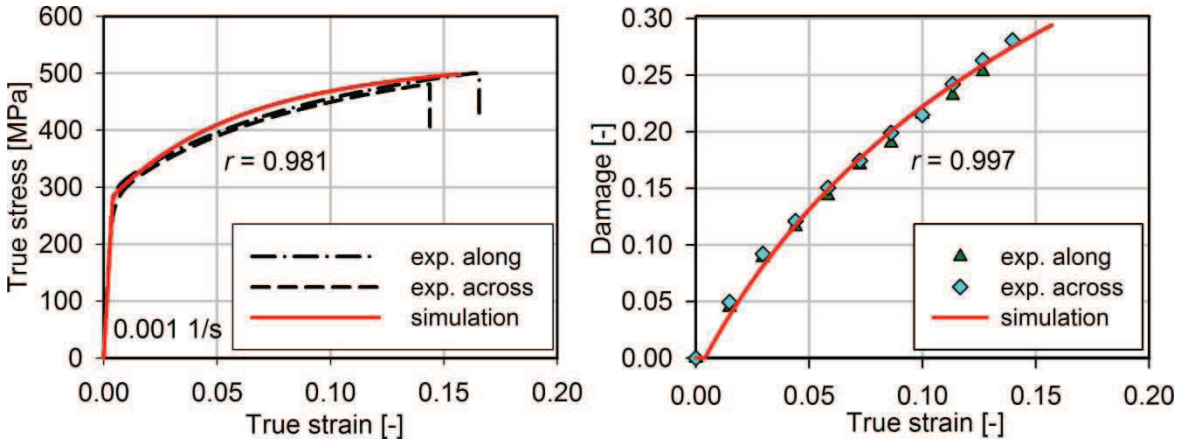

Fig. 5-20. Verification of numerical results, tension test 0.001 1/s

5.6.5. Damage measurement, second approach

The second approach to the damage measurement is more complicated. The values of current transversal area of the sample are calculated on the basis of the material incompressibility assumption given in [100]: $J = \det \mathbf{F} = 1$, where $\mathbf{F}$ is the deformation gradient. The current transversal area of the sample at the lower point of elastic path of the stress-strain curve A_l, which is necessary in equation (5.23), is calculated as

$$A_l = \frac{A_0}{1+\left(L_l - L_0\right)/L_0}. \tag{5.30}$$

The detail results of second approach elastic modulus identification for two example tests are presented in Tab. 5-11 and Tab. 5-12. All results are shown in Fig. 5-21.

The results obtained in the second approach give higher values of elastic modulus in the following cycles, the effect of elasticity weakening in material is smaller, even disappears (after four cycles the values of elastic modulus are similar). This identification is more precise than the first one, but consequently this new effect emerged. The observed effect is due to the triaxial stress state that occurs in the samples during tension tests, caused by necking, which decreases the load. This problem can be solved by application of the procedure proposed by Celentano and Chaboche [39] and obtaining the real values of elastic modulus through measurements of the corresponding uniaxial modulus using a correction factor f_E

$$E = f_E E_{1D}, \tag{5.31}$$

where E_{1D} is the elastic modulus obtained directly from experiment.

Cycle	P_u [N]	P_l [N]	A_l [mm^2]	L_u [mm]	L_l [mm]	E_i [MPa]
0	2213.5	398.5	11.70	40.107	40.019	70181
1	3177.0	555.0	11.57	40.575	40.441	68480
2	3460.3	601.3	11.41	41.175	41.022	67190
3	3637.6	630.4	11.25	41.770	41.604	67042
4	3807.7	644.7	11.09	42.370	42.190	66834
5	3888.9	669.2	10.94	42.967	42.778	66506
6	4010.0	685.2	10.79	43.566	43.366	66768
7	4045.7	701.0	10.65	44.164	43.956	66420
8	4071.9	712.4	10.50	44.777	44.564	66834
9	4095.9	712.6	10.37	45.359	45.138	66709

Tab. 5-11. Example of second approach elastic modulus identification (along, test 1)

Cycle	P_u [N]	P_l [N]	A_l [mm^2]	L_u [mm]	L_l [mm]	E_i [MPa]
0	2017.2	292.2	11.60	40.097	40.014	71114
1	3067.8	535.0	11,47	40.576	40.447	69064
2	3365.6	587.2	11,31	41.174	41.026	67867
3	3593.3	637.4	11,15	41.773	41.610	67583
4	3735.2	647.1	11,00	42.371	42.195	67172
5	3797.7	653.2	10,85	42.966	42.781	67117
6	3878.6	674.7	10,70	43.564	43.370	66916
7	3931.4	684.3	10,55	44.164	43.963	67392
8	4027.8	709.9	10,42	44.763	44.550	66817
9	4091.7	734.6	10,28	45.363	45.142	66683
10	4072.6	724.0	10,15	45.961	45.735	66823

Tab. 5-12. Example of second approach elastic modulus identification (across, test 2)

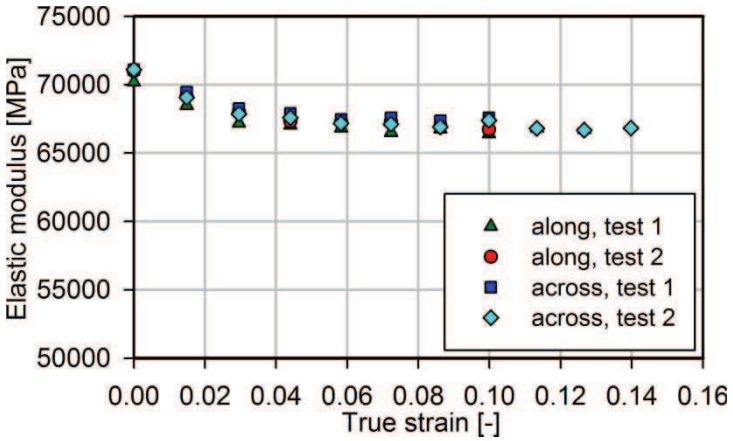

Fig. 5-21. Results of second approach elastic modulus identification

This procedure needs iterations and requires the following actions:

a) evaluation of E_{1D} via equation (5.23) (already done),

b) initialization of iteration (index $k = 0$) and defining the initial correction factor $f_E^{k=0} = E_0/E_{1D,\text{sim0}}$, where $E_{1D,\text{sim0}}$ is evaluated using numerical results obtained from a simulation without damage effects,

c) computation of $E_{exp} = f_E^k \cdot E_{1D}$ for every cycle i,

d) using E_{exp} computed in step (c), calculation of the parameter D according to equation (5.22),

e) application of identification of damage model material parameters using D calculated in step (d),

f) updating iterative index $k = k + 1$ and computation of a new correction factor $f_E^k = E_{\text{sim}}/E_{1D,\text{sim}}$, where E_{sim} and $E_{1D,\text{sim}}$ are both evaluated using numerical results obtained from a simulation with damage effects considering as damage material parameters those derived in step (e), E_{sim} is the average value of $E_0/(1-D)$ calculated in the necking zone of the sample,

g) checking convergence (ε_f – admissible tolerance, considered here as 10^{-3}):

- if $\left| f_E^{\,k} - f_E^{\,k-1} \right| \le \varepsilon_f$, f_E^k is the final correction factor that leads to the final damage parameters computed in step (e),
- if $\left| f_E^{\,k} - f_E^{\,k-1} \right| > \varepsilon_f$, go to step (c).

The first step of procedure – the results of evaluation of E_{1D} is presented in Fig. 5-21. The second step required the numerical simulations of uniaxial load-unload tension test without damage effects. The uniaxial model applied in verification of constitutive law material parameters identification presented in Chapter 5.5 has been used. The results of this simulation and calculation of the initial correction factor $f_E^{k=0}$ are presented in Tab. 5-13. The following step required computation of E_{exp} by multiplying the measured elastic modulus directly from experiments E_{1D} by the initial correction factor $f_E^{k=0}$. The result is presented in Fig. 5-22. Calculation of the damage using the new values of elastic modulus has given the result shown in Fig. 5-23. The last operation in initial iteration step is to apply identification of damage material parameters using the computed values of D. The identification procedure has been already described in the identification by the first approach in Chapter 5.6.3. The only difference is the formula, which approximates the function of the experimental values $D\left(\varepsilon^l\right)$. The formula in equation (5.27) is replaced by the function, which gives better fitting in this approach

$$D\left(\varepsilon^I\right)=a\left(1-\exp\left(-b\varepsilon^I\right)\right)+c\left(1-\exp\left(-d\varepsilon^I\right)\right). \tag{5.32}$$

The derivative of this function with inelastic strain is

$$\frac{dD}{d\varepsilon^I}=ab\exp\left(-b\varepsilon^I\right)+cd\exp\left(-d\varepsilon^I\right), \tag{5.33}$$

therefore, the final formula from which the material parameters can be approximated, has the following form

$$\frac{dD}{d\varepsilon^I}=ab\exp\left(-b\varepsilon^I\right)+cd\exp\left(-d\varepsilon^I\right)=\left(\frac{\sigma^2}{2E(1-D)^2S}\right)^s(1-D)^{-\beta+1}. \tag{5.34}$$

Two example approximations of the function $D\left(\varepsilon^I\right)$ are presented in Fig. 5-24. The values of damage material parameters obtained in initial iteration step are presented in Tab. 5-14.

Cycle	P_u [N]	P_l [N]	A_l [mm^2]	L_u [mm]	L_l [mm]	$E_{1D,\mathrm{sim}0}$ [MPa]	$f_E^{k=0}$ [-]
0	3053.2	0.0	12.00	40.146	40.000	70000	1,000
1	3868.5	137.4	11.87	40.623	40.442	70215	0,994
2	4320.7	58.6	11.70	41.238	41.026	70687	0,987
3	4640.3	168.3	11.53	41.856	41.629	71170	0,981
4	4867.3	194.3	11.36	42.479	42.237	71698	0,973
5	5028.5	163.2	11.20	43.110	42.852	72237	0,966
6	5142.1	186.8	11.04	43.749	43.481	72800	0,959
7	5220.8	179.7	10.88	44.401	44.122	73361	0,951
8	5273.4	240.9	10.72	45.070	44.786	73942	0,944
9	5306.2	194.3	10.56	45.766	45.470	74534	0,936
10	5323.6	223.0	10.39	46.504	46.203	75182	0,928

Tab. 5-13. Results of uniaxial numerical calculations and initial correction factor computing, $k = 0$

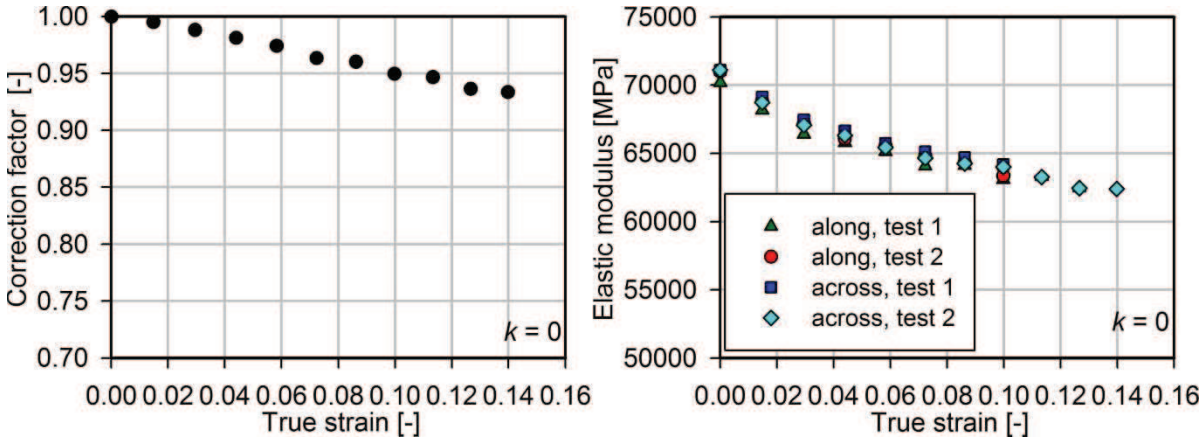

Fig. 5-22. Results of elastic modulus computing, $k = 0$

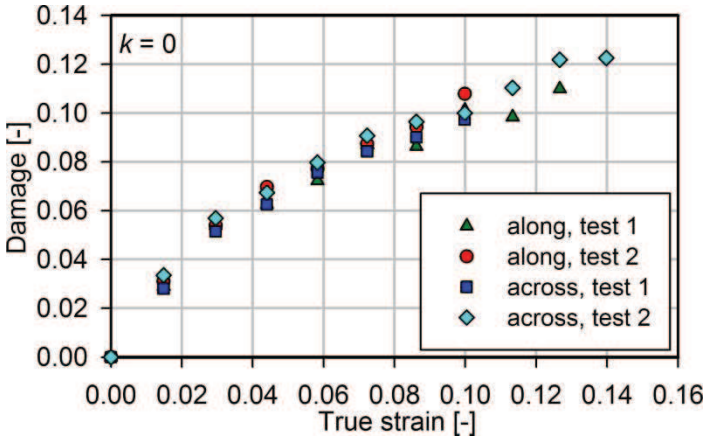

Fig. 5-23. Results of damage computing, $k = 0$

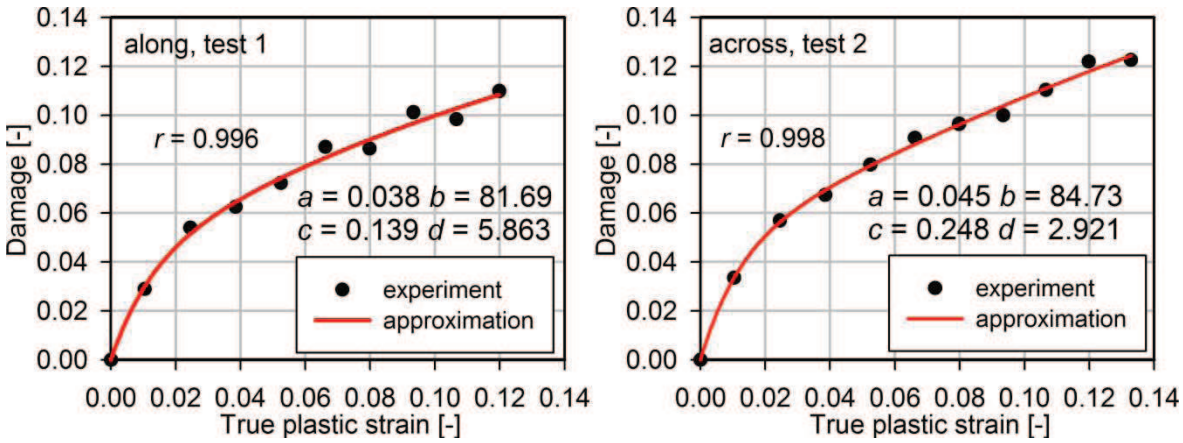

Fig. 5-24. Approximations of damage vs. plastic strain functions, $k = 0$

S [MPa]	s [-]	β [-]
2.25	-1.05	-10.6

Tab. 5-14. Values of damage material parameters identification, $k = 0$

The following steps of the procedure is to update the iterative index to $k = 1$, perform once again the numerical simulations (this time including damage effects), calculate the new correction factor $f_E^{k=1}$ and repeat all operations, which has been done in initial iteration step. Then if the difference between the actual and previous correction factors is still too large, repeat all in the next iteration step until the convergence is fulfilled. In the present procedure the convergence is fulfilled for $k = 2$. The final values of the correction factor, elastic modulus and damage are presented in Fig. 5-25 and Fig. 5-26. The final values of damage material parameters identified by second approach (obtained in the last iteration) are shown in Tab. 5-15.

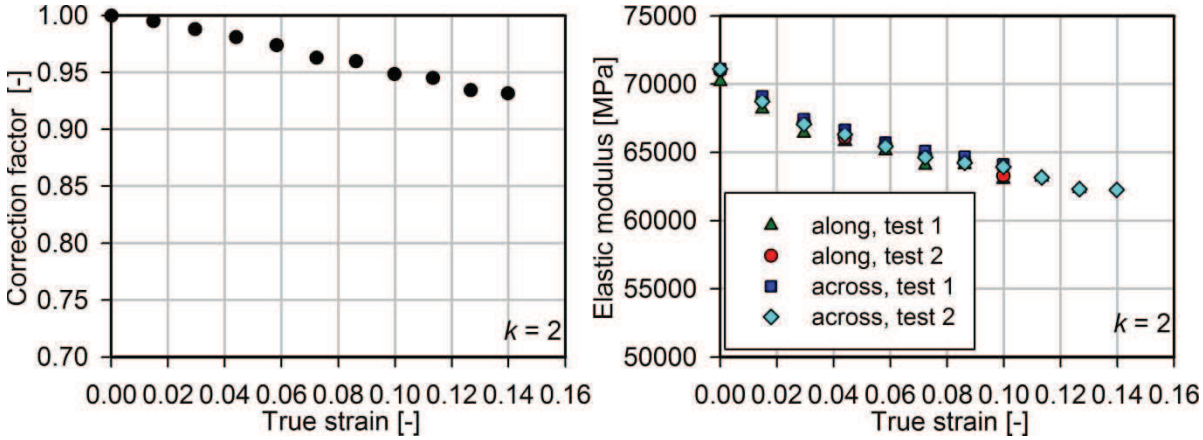

Fig. 5-25. Final results of elastic modulus computing, k = 2

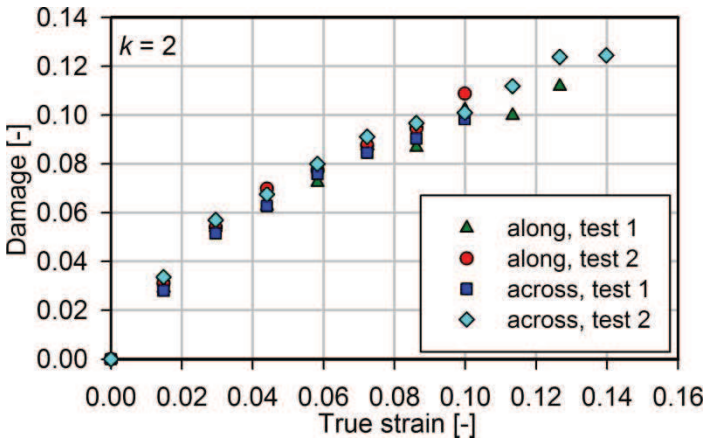

Fig. 5-26. Final results of damage computing, k = 2

S [MPa]	s [-]	β [-]
1.77	-1.23	-10.7

Tab. 5-15. Final values of second approach damage material parameters identification, k = 2

5.6.6. Verification of second approach damage material parameters identification

The verification of second approach damage model material parameters identification is performed using the same model, which have been used for the first approach presented in Chapter 5.6.4. The only difference is that the new damage material parameters are applied. The results are presented in Fig. 5-27. The correlation between the numerical and experimental results is high. The correlation coefficient values are above 0.99.

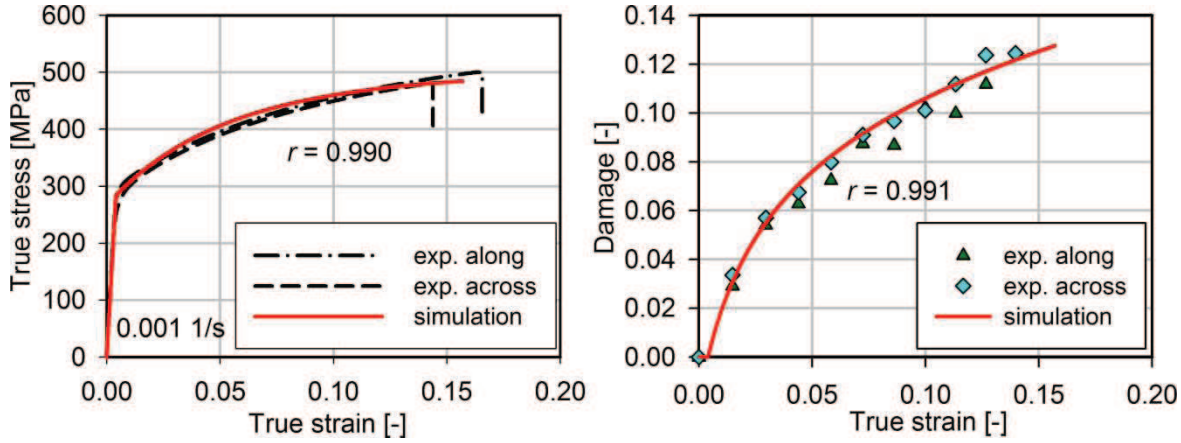

Fig. 5-27. Verification of numerical results, tension test 0.001 1/s

5.7. Summary

The identification of all assumed models material parameters necessary in numerical modelling has been done. The only problem has occurred during estimation of the damage. The lack of the specimens' current transversal area measurement in the laboratory tests has caused the necessity of finding alternative solutions to overcome this problem. Two different approaches have been proposed. All the uniaxial verifications have showed good correlations between the results obtained in numerical simulations and experiments.

6. Fracture criteria calibration

6.1. Abstract

The fracture criteria, which can be used in the current study, have been discussed in Chapter 2. From the presented possibilities, four different approaches have been chosen. Three of them represent the abrupt failure criteria, the fourth one represents the classic critical damage criterion in continuum damage mechanics. This chapter contains the description of calibration procedure, which has been performed to obtain the critical parameters.

6.2. Introduction

The calibration of fracture criteria parameters has been performed on the basis of the results obtained in the uniaxial experiments and their numerical simulations. In the numerical study presented in this chapter the tensile test model created for the verifications of material parameters identification, presented in Fig. 5-10, is used. The simulations are limited to the tensile tests with 0.001 1/s strain rate. In this numerical study, the fracture moment has been assumed to occur, when the total strain in the loading direction reaches the average value obtained in the experiments. The experimental values of the total true strain at fracture point ε_f for each test and the calculated averages ε_f^{av} are presented in Tab. 6-1.

Test	Specimens cut along sheet's rolling ε_f [-]	Specimens cut across sheet's rolling ε_f [-]
0.0001 1/s	0.179	0.150
0.0005 1/s, t1	0.170	0.148
0.0005 1/s, t2	0.158	0.150
0.001 1/s, t1	0.176	0.148
0.001 1/s, t2	0.166	0.144
0.005 1/s, t1	0.174	0.146
0.005 1/s, t2	0.163	0.146
0.01 1/s, t1	0.161	0.140
0.01 1/s, t2	0.162	0.145
average value ε_f^{av}	0.168	0.146
	0.157	

Tab. 6-1. Total true strain at fracture obtained in the experiments

6.3. Critical equivalent plastic strain criterion

Calibration of the equivalent plastic strain critical values requires numerical simulations of tension tests. During this analysis the searched variable is calculated according to equation (2.53). The numerical studies are computed until the total true strain, measured in the half high of the specimen, reaches the value of $\varepsilon_f^{av} = 0.157$. In the considered calibration three different analyses have been realised: the first one with no damage effects included, the second with damage effects taken from the first identification approach and the third also with damage effects but taken from the second identification approach. The growths of the equivalent plastic strain in each analysis are presented in Fig. 6-1.

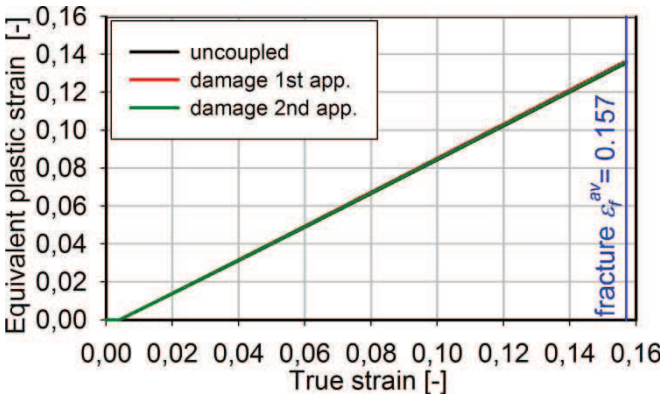

Fig. 6-1 Growth of the equivalent plastic true strain in the numerical study

The critical values of the equivalent plastic strain, which occur at assumed fracture moment, are presented in Tab. 6-2. The weakening of the material in the analyses with damage effects does not influence too much the result. The differences between the obtained values are minor.

	No damage effects (uncoupled)	Damage first approach	Damage second approach
Critical equivalent plastic true strain $\overline{\varepsilon}_f^I$ [-]	0.135	0.136	0.136

Tab. 6-2. Equivalent plastic true strain at fracture

6.4. Total strain energy density criterion

The criterion of total strain energy density is based on the assumption of its constancy. The critical values are evaluated in the analogical study as for the first criterion. In the

numerical analyses the strain energy is calculated according to the formula given in equation (2.58). The results of these computations are presented in Fig. 6-2. The obtained critical values at fracture are summarised in Tab. 6-3.

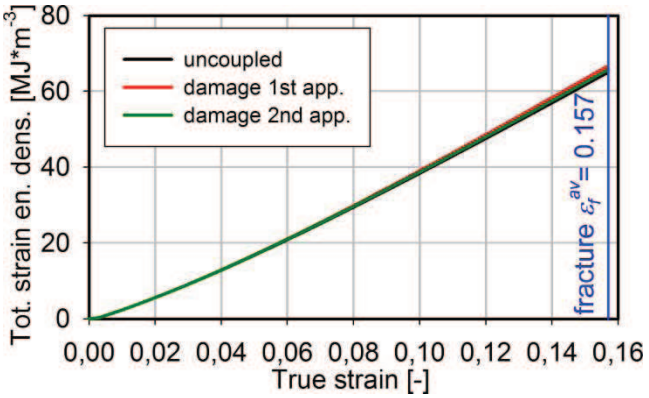

Fig. 6-2 Growth of the total strain energy density in the numerical study

	No damage effects (uncoupled)	Damage first approach	Damage second approach
Critical total strain energy density W_{cr} [MJ·m^{-3}]	64.98	66.38	65.75

Tab. 6-3. Total strain energy density at fracture in the numerical study

Test	Specimens cut along sheet's rolling W_{cr} [MJ·m^{-3}]	Specimens cut across sheet's rolling W_{cr} [MJ·m^{-3}]
0.0001 1/s	76.40	60.50
0.0005 1/s, t1	71.39	59.36
0.0005 1/s, t2	65.79	60.02
0.001 1/s, t1	74.37	59.32
0.001 1/s, t2	69.72	57.94
0.005 1/s, t1	73.90	58.02
0.005 1/s, t2	67.75	58.70
0.01 1/s, t1	66.89	55.45
0.01 1/s, t2	66.85	57.83
average value	70.34	58.57
	64.45	

Tab. 6-4. Total strain energy density at fracture in the experimental study

Additionally, the average value of the total strain energy density at fracture point during the experimental tests has been calculated. The critical values obtained in each test and the

evaluated averages are presented in Tab. 6-4. The maximum relative error between the numerical and experimental results does not exceed the value of 3%.

6.5. Stress triaxiality ratio based criterion

The stress triaxiality ratio during the uniaxial tensile tests considered in the calibrations is changing in a relatively narrow range and is always positive. This observation allows the introduction of the concept of average stress triaxiality during deformation

$$\left(\frac{\sigma_H}{\sigma_{eq}}\right)_{av} = \frac{1}{\bar{\varepsilon}_f^I}\int_0^{\bar{\varepsilon}_f^I} \frac{\sigma_H}{\sigma_{eq}} d\bar{\varepsilon}^I \tag{6.1}$$

and rewriting the fracture criterion given in (2.64) as

$$T_{cr} = \left(\frac{\sigma_H}{\sigma_{eq}}\right)_{av} \bar{\varepsilon}_f^I. \tag{6.2}$$

The results presenting the stress triaxiality ratio obtained in the numerical simulations for the three different analyzed damage effects are shown in Fig. 6-3. The average ratios evaluated in each case are almost the same and can be set to 0.333. By taking the equivalent

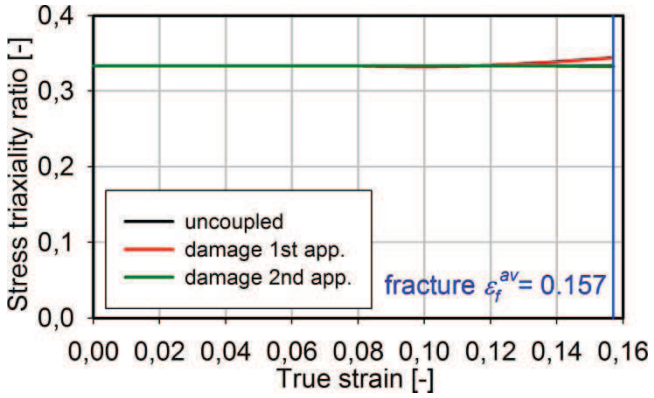

Fig. 6-3 Stress triaxiality ratio in the numerical study

	No damage effects (uncoupled)	Damage first approach	Damage second approach
$\bar{\varepsilon}_f^I$ [-]	0.135	0.136	0.136
$\left(\sigma_H/\sigma_{eq}\right)_{av}$ [-]	0.333	0.333	0.333
T_{cr} [-]	0.0450	0.0453	0.0453

Tab. 6-5. Critical parameters in the stress triaxiality ratio based criterion

plastic strain from the first fracture criterion and using equation (6.2) the critical values T_{cr} can be calculated. The final results are presented in Tab. 6-5.

6.6. Critical damage criterion

The calibration of three-dimensional critical damage criterion, given in the equation (2.44), requires evaluation of two parameters: the critical damage in uniaxial loading conditions and the ultimate stress. Theoretically both parameters can be measured directly using the results of load-unload cyclic experiments. Practically in these tests, which are the base of damage measurement, the fracture has occurred much faster than the average level obtained in the constant strain rate experiments. That is why in this calibration also the numerical simulations have been used. Of course, in this case the coupled analysis, where the damage effects are considered has been used. The results of the numerical study are presented in Fig. 6-4 and Fig. 6-5. The critical values of damage and ultimate stress obtained in this study are summarised in Tab. 6-6.

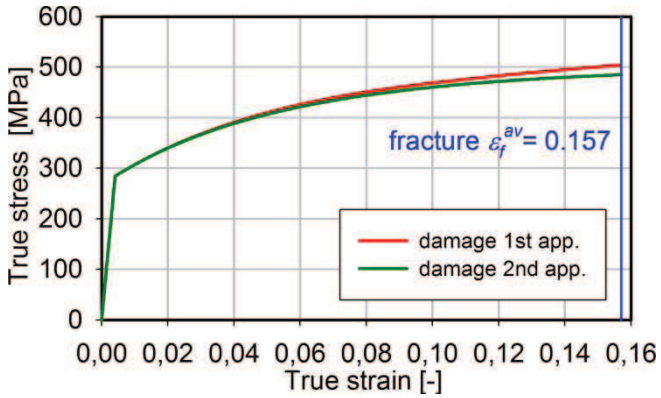

Fig. 6-4 Stress vs. strain plot in the numerical study

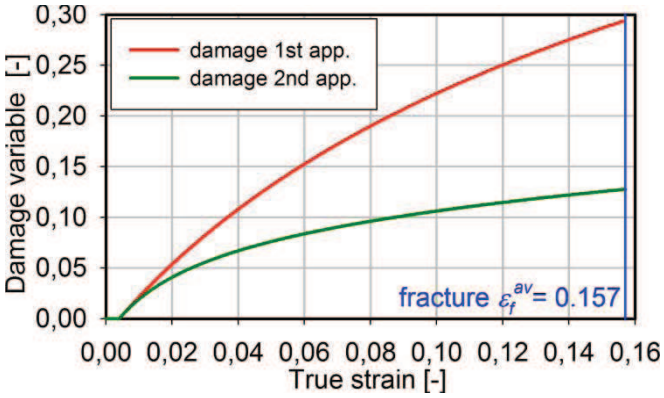

Fig. 6-5 Growth of the damage variable in the numerical study

Additionally, the average value of ultimate stress obtained in the experimental tests has been calculated, see Tab. 6-7. The first numerical result is higher, the second smaller than in the experiments, but the relative error between them is under the value of 3%.

	Damage first approach	Damage second approach
σ_u [MPa]	504	484.5
D_{1cr} [-]	0.293	0.127

Tab. 6-6. Critical parameters for the damage criterion

Test	Specimens cut along sheet's rolling σ_u [MPa]	Specimens cut across sheet's rolling σ_u [MPa]
0.0001 1/s	501.0	488.0
0.0005 1/s, t1	496.0	486.0
0.0005 1/s, t2	490.0	486.0
0.001 1/s, t1	499.0	487.0
0.001 1/s, t2	500.5	481.0
0.005 1/s, t1	504.0	480.0
0.005 1/s, t2	492.0	482.0
0.01 1/s, t1	494.0	475.0
0.01 1/s, t2	491.0	479.0
average value	496.4	482.7
	489.5	

Tab. 6-7. Ultimate stress in the experimental study

6.7. Summary

The critical fracture parameters have been calibrated for four different criteria. The obtained critical values and the material parameters identified in the previous chapter allow performing the numerical study, which is the last part of this work. These analyses are presented in next two chapters.

7. Numerical study – axisymmetrical model

7.1. Abstract

The first chapter in which the numerical study is presented focuses on the axisymmetrical model analysis. The main simulations are preceded by the determination of plate's fixing boundary conditions, which is described in detail. In the further part of this chapter, the results obtained in the numerical simulations are shown and discussed. The analyses have been performed using all approaches and fracture criteria, which have been described, chosen and prepared (identification of material parameters) in the previously presented part of this work.

7.2. Introduction

Performing the analyses, where the laboratory tests are simulated numerically, requires application of the model with suitable boundary conditions. The specimens (plates) have been fixed between two parts of the tube during the considered experiments. They have been tightened using four screws and the massive flanges. As it has been mentioned in the description of the dynamic tests in Chapter 4, this fixing has not assured the distinct support conditions. The plates during the tests have been slid and folded in the area where they should be clamped. That is why the main numerical simulations are preceded by the determination of suitable fixing conditions. A few different models are analyzed to find the most suitable boundary conditions. The verifications of these models are made using the results of static and dynamic experiments. In those verifications, a fitting between numerical simulations and experiments is indicated by the coefficient of correlation r.

7.3. Determination of plate's fixing boundary conditions

In the numerical analyses during the determination of fixing boundary conditions a relatively fine mesh in the axisymmetrical model is used, the applied element size is 1.2 mm. The damage effects in the first calculations are not taken into account.

The plates fixing conditions in the first analyzed approach is assumed as basic clamped or hinged supports presented in Fig. 7-1. The rounding of the additional plate fixed behind the specimen is modelled as the rigid contact body. The verification of these models is made by the numerical analysis of the plates' responses to quasi-static loading. The models are loaded by the increasing pressure used in this laboratory test. The calculated middle point deflections

are compared with the experimental values. The results are presented in Fig. 7-2. The maximum middle point deflections obtained in the simulations, for both kinds of boundary conditions, are almost 30 % lower than in experiments. In the next step, the plates' response to dynamic load is considered. The test performed with the initial pressure 0.25 bar is analyzed. The model is submitted to the pressure time history recorded during the real experiment. The results of numerical simulations compared with the experiment are presented in Fig. 7-3. The calculated middle point deflections are also over 35 % lower than the experimental one. The further verifications have been omitted due to poor correspondence of both variants of

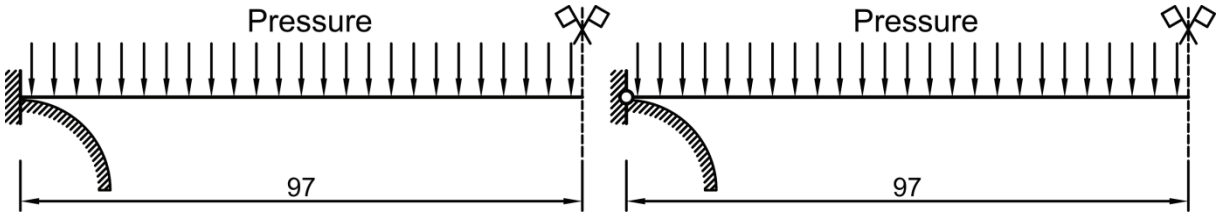

Fig. 7-1. Clamped and hinged models

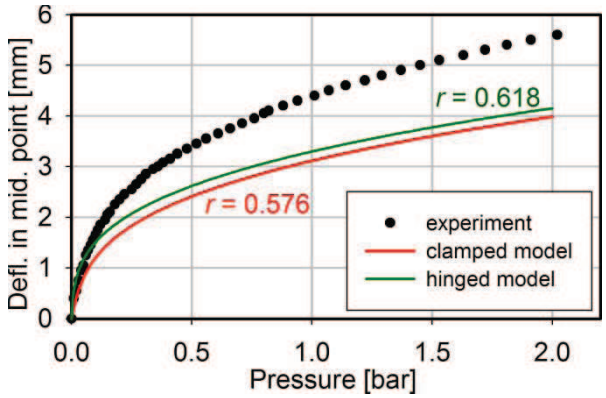

Fig. 7-2. Middle point deflections, quasi-static test, clamped and hinged models

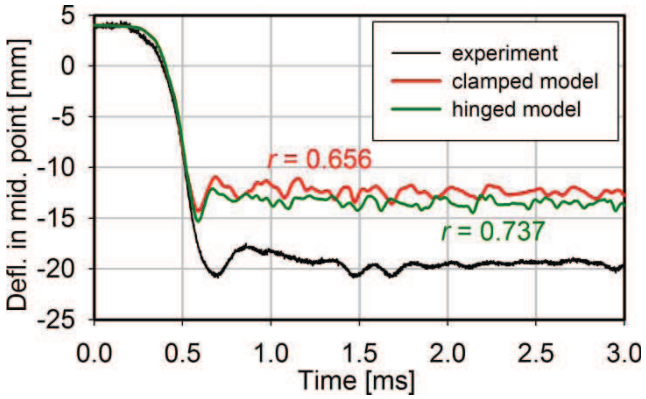

Fig. 7-3. Middle point deflections, test with initial pressure 0.25 bar, clamped and hinged models

boundary conditions. The presented results are sufficient to state that the basic models cannot give the right answers in the analyzed problem. The obtained deflections are considerably understated.

In the following approach, denoted as model No. 3, the fixed part of the plate is included. The 68 mm collar, which is the smallest segment size of the tube's flange, is introduced. The applied boundary conditions are presented in Fig. 7-4. The plate can slide horizontally in its fixing area. The results of quasi-static and dynamic (initial pressure 0.25 bar) simulations for this model are presented in Fig. 7-5 and Fig. 7-6. The solution obtained in the quasi-static analysis is much better than in the previous models. The calculated maximum deflection is only 5.5 % lower than the experimental one. Unfortunately, the results of dynamic analysis

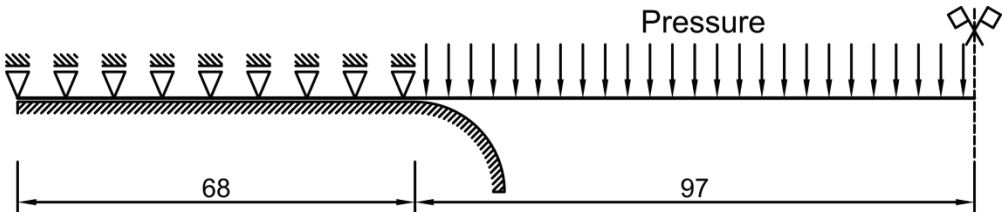

Fig. 7-4. Boundary conditions in model No. 3

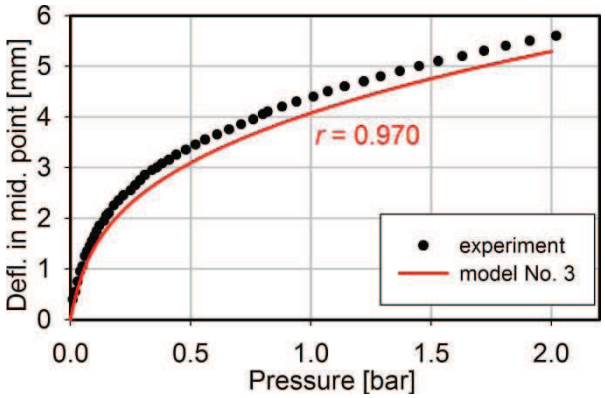

Fig. 7-5. Middle point deflections, quasi-static test, model No. 3

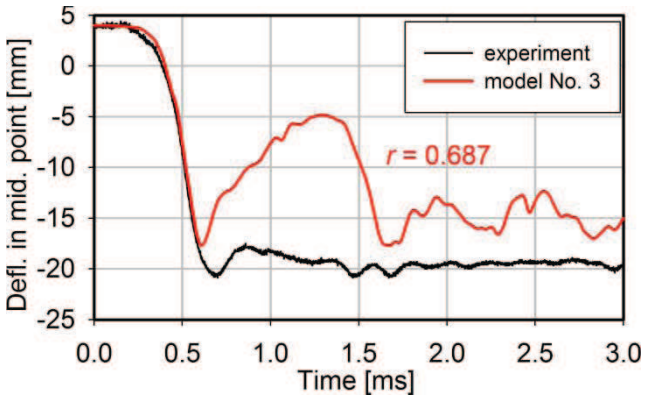

Fig. 7-6. Middle point deflections, test with initial pressure 0.25 bar, model No. 3

disqualify this model. The obtained deflections are still too small and the response of plate has quite different character.

The next idea is to introduce a gap in the fixing area. The maximum measured gap, which has occurred after fixing the plate, is 0.3 mm. This value is applied into the model No. 4. The chosen boundary conditions are presented in Fig. 7-7. The results of verifications are shown in Fig. 7-8 and Fig. 7-9. The quasi-static numerical analysis result is in very good agreement with the experiment, both displacement vs. pressure paths are almost overlapped. However, the dynamic study does not give a good solution. The character of response is again different. In the considered model the numerical problems have also occurred, in spite of using the

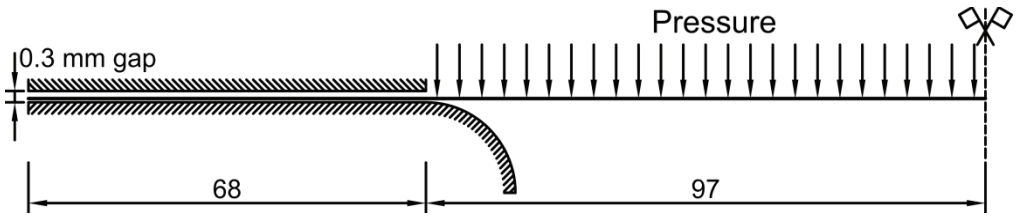

Fig. 7-7. Boundary conditions in model No. 4

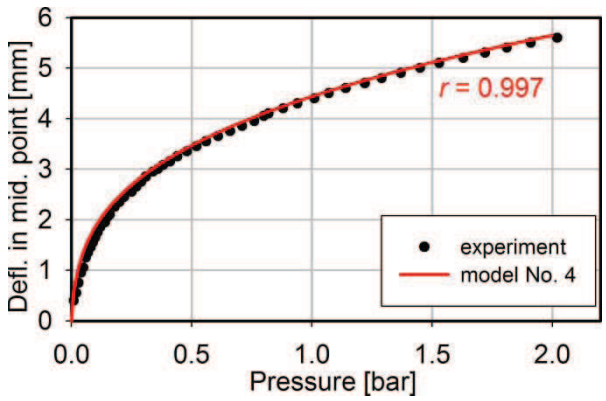

Fig. 7-8. Middle point deflections, quasi-static test, model No. 4

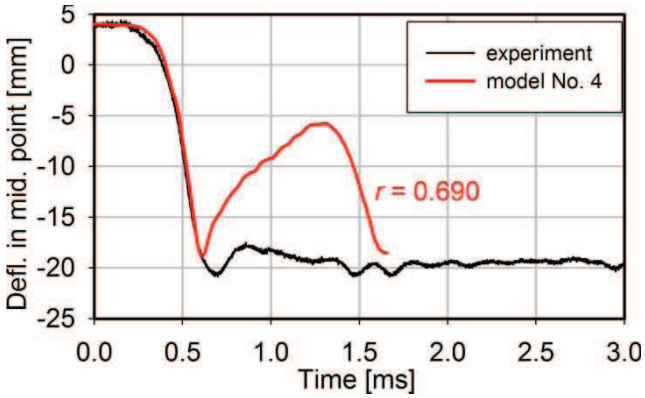

Fig. 7-9. Middle point deflections, test with initial pressure 0.25 bar, model No. 4

integration step three times shorter than in the previous calculations, reaching the convergence after about 1.6 ms has not been possible.

In the following models the gap idea is retreated. The research concentrates on reducing the plate's collar in the fixing area. Three different sizes of the collar are analyzed: 45, 30 and 15 mm. The free horizontal displacements of plate are maintained. The boundary conditions in the considered model, denoted as No. 5, are presented in Fig. 7-10. The results of verifications are shown in Fig. 7-11 and Fig. 7-12. In the quasi-static analysis, the best solution has been obtained using the model with 45 mm collar size. However, the dynamic study shows that in this model the rebound after reaching the first maximum deflection is too strong. Much better result has been obtained using the model with collar 15 mm. The

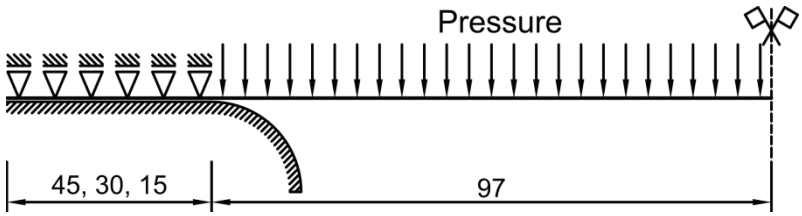

Fig. 7-10. Boundary conditions in model No. 5

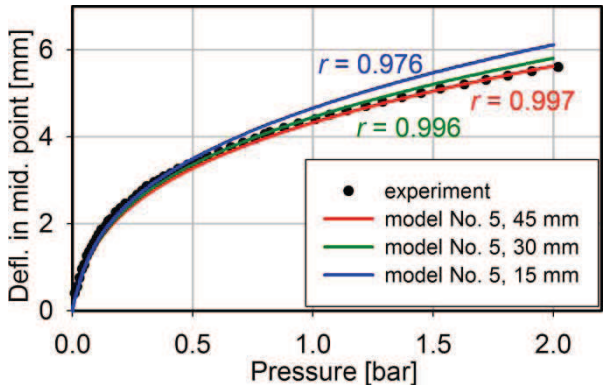

Fig. 7-11. Middle point deflections, quasi-static test, model No. 5

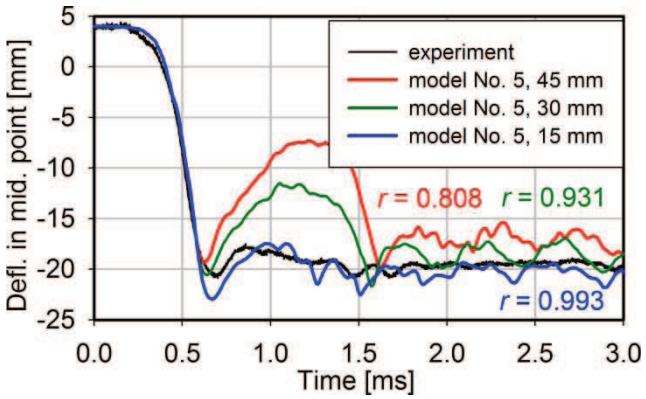

Fig. 7-12. Middle point deflections, test with initial pressure 0.25 bar, model No. 5

maximum deflection and the character of response (the coefficient of correlation above 0.99) are the closest to the experiment. This model has been chosen for the further analyses.

In the next step the dynamic experiment performed with the initial pressure 0.3 bar (test 03_2) is considered. The middle point deflection obtained in numerical study is compared with the permanent deflection measured for the tested plate in Fig. 7-13. The difference between the calculated and experimental values is higher than in the previous comparison for the lower initial pressure. The cross-sections presented in Fig. 7-14 show that the shapes of simulated and tested plates are also different. The explanation of these problems can be too high displacement (sliding) of the plate's model inside the fixing area. Some limitations for this movement are necessary.

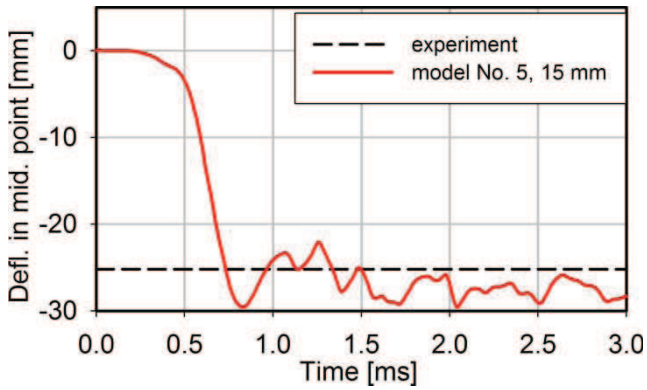

Fig. 7-13. Middle point deflections, test with initial pressure 0.3 bar, model No. 5

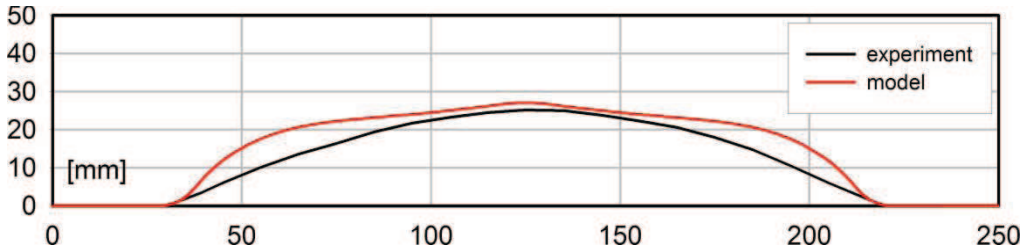

Fig. 7-14. Plate cross-sections, test with initial pressure 0.3 bar, model No. 5

The limitation of the displacement in the fixing area of the model has been applied using the spring element. The spring's stiffness is introduced as $k_{spr} = 0$ for the displacement from zero to the assumed limit and k_{spr} = 1e+10 (N/m)/m for the displacement higher than the limit (due to jamming of the plate). During the experiments, the observed values of the plates' movement in the fixing area oscillated between 1 to 3 mm. In the model, three values of allowed displacement are considered: 1, 2 and 3 mm. The introduced boundary conditions are presented in Fig. 7-15.

The verification omits the quasi-static analysis. The displacement in fixing area, which occurrs in these simulations, is lower than 1 mm. The applied limitations do not change the solution presented in Fig. 7-11. The results of dynamic simulations for the lowest initial pressure 0.25 bar are presented in Fig. 7-16. The comparison shows that model with the allowed displacement of 2 mm gives the closest solution to the experiment. The results for higher impulse 0.3 bar shown in Fig. 7-17 and Fig. 7-18 confirm this observation.

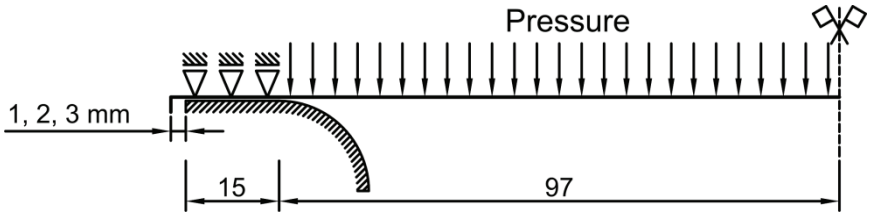

Fig. 7-15. Boundary conditions in model No. 5 with different displacement limits

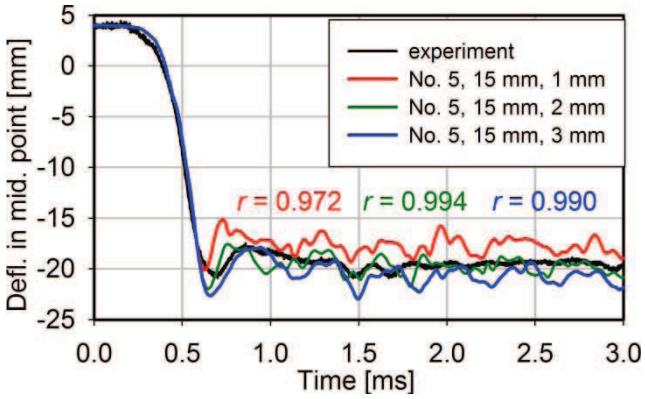

Fig. 7-16. Middle point deflections, test 0.25 bar, model No. 5 with displacement limit

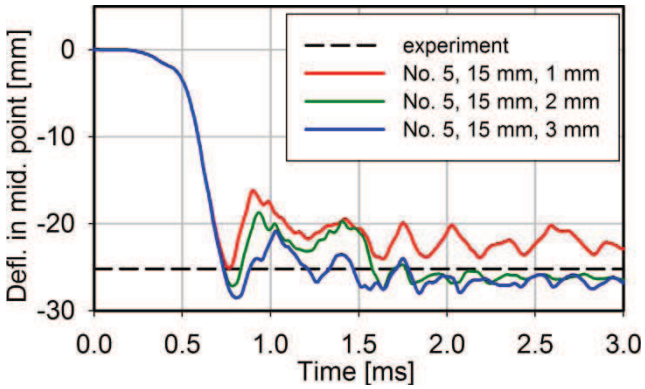

Fig. 7-17. Middle point deflections, test 0.3 bar, model no. 5 with displacement limit

For the final verification of plate's fixing boundary conditions the model with 15 mm collar and 2 mm displacement limit in the fixing area has been chosen. The verification contains the analysis of all applied initial pressures. This study gives the answer if the chosen model is universal and works well in all considered cases. Three different analyses have been

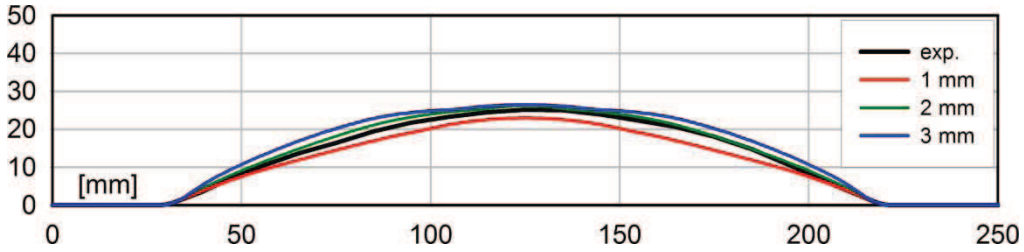

Fig. 7-18. Plate cross-sections, test 0.3 bar, model no. 5 with displacement limit

performed: study with no damage effects, with damage 1 effects (first approach in the damage identification – Chapter 5.6.2) and with damage 2 effects (second approach – Chapter 5.6.5). In this analysis, the fracture is not considered. The plate's cross-sections obtained in the simulations compared with the experimental result for one chosen example in each initial pressure level are presented in Fig. 7-19 – Fig. 7-23. The results for all performed tests are shown in Annex 7. The solutions obtained in this study show that the chosen model gives a very good response in almost all analyzed tests. Finally, the model that has been chosen as the most suitable for current problem is presented in Fig. 7-24.

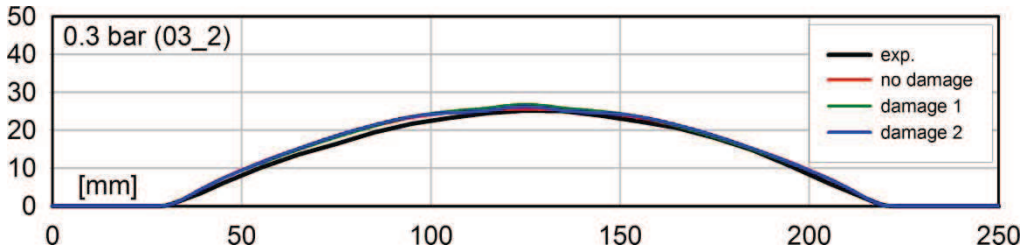

Fig. 7-19. Plate's cross-sections, test 0.3 bar, final verification

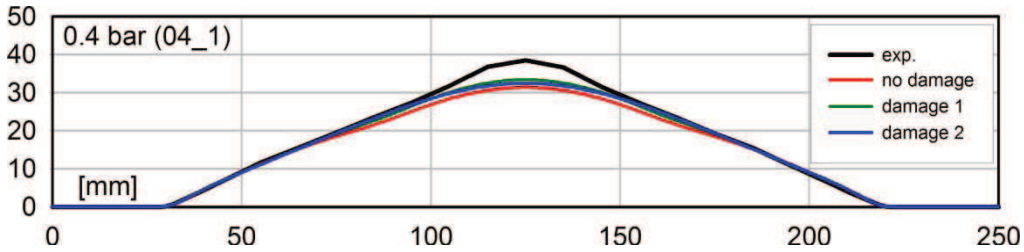

Fig. 7-20. Plate's cross-sections, test 0.4 bar, final verification

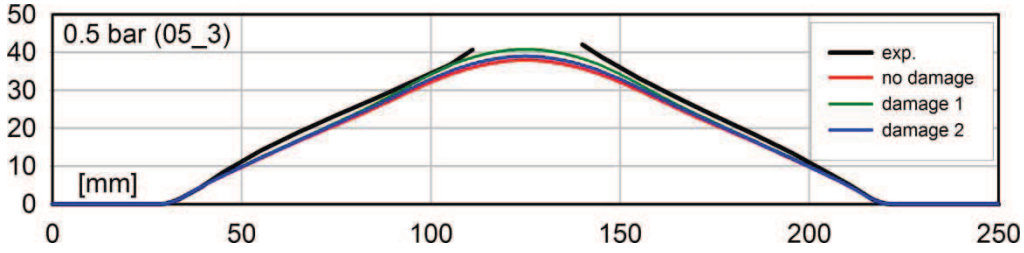

Fig. 7-21. Plate's cross-sections, test 0.5 bar, final verification

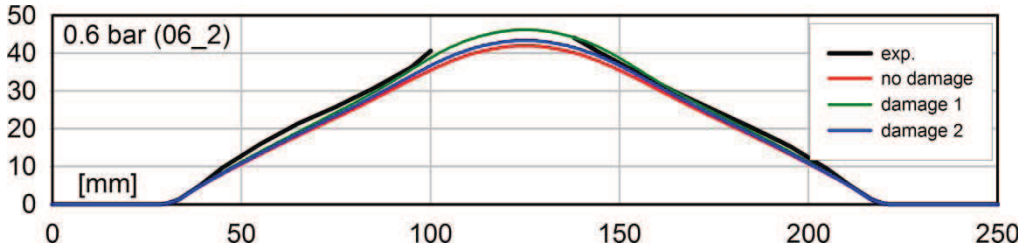

Fig. 7-22. Plate's cross-sections, test 0.6 bar, final verification

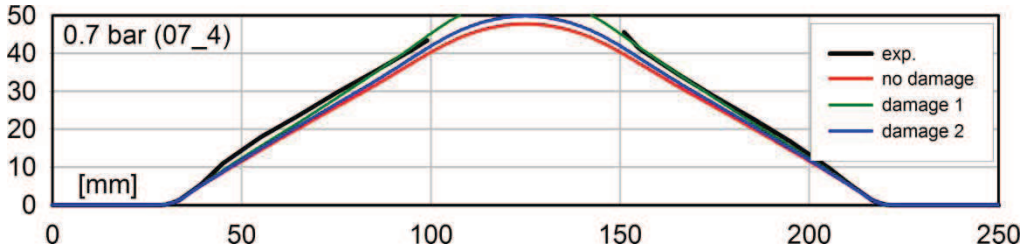

Fig. 7-23. Plate's cross-sections, test 0.7 bar, final verification

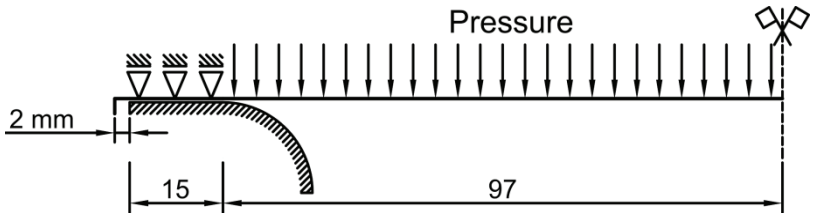

Fig. 7-24. Final model of boundary conditions

7.4. Investigation of mesh density influence – model with no fracture

The investigation of a mesh density influence is necessary in all finite element method applications. A result obtained in a numerical analysis can be assumed as reliable if performing the same calculation using usually a twice as dense mesh gives the same solution.

The considered axisymmetrical model is divided into 93 elements. This division gives the element size of 1.2 mm. For the density influence investigation, the model with the same boundary conditions but divided into 186 elements has been created. For this study, the pressure time history recorded during the test 06_1 has been used. Three analyses considered in this work have been performed: with no damage, damage first approach and damage second approach effects. The results are compared in two selected nodes presented in Fig. 7-25. The chosen nodes are: node 41 located at the centre of the plate and node 30 located at the area of possible crack initiation. In this mesh density investigation study, the fracture is not taken into account. The results presenting the equivalent total strain and the damage variable change in time are shown in Fig. 7-26 and Fig. 7-27. The obtained solutions for both axisymmetrical models are almost identical, therefore the results can be admitted as reliable.

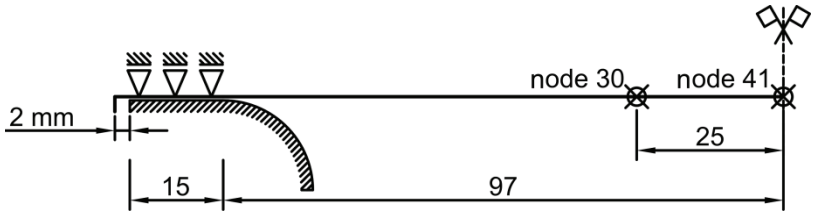

Fig. 7-25. Nodes selected for mesh density influence analysis

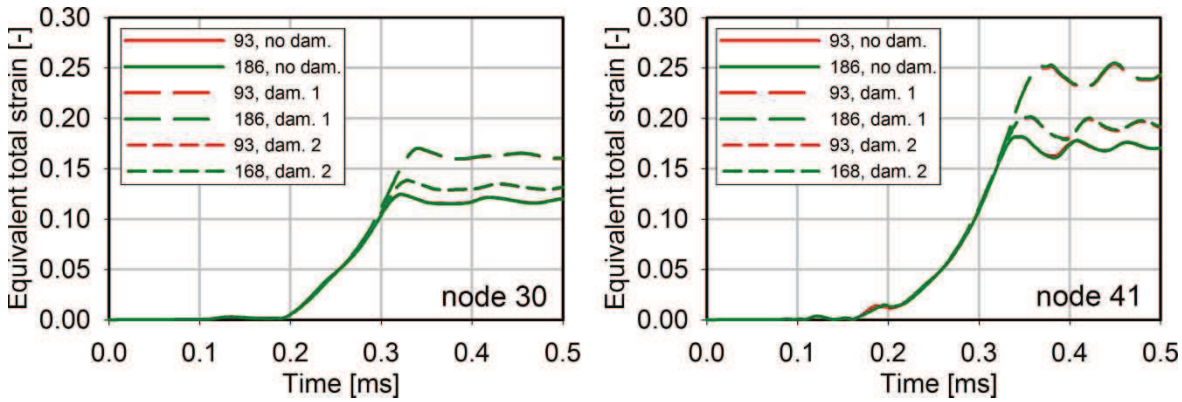

Fig. 7-26. Mesh density influence analysis – equivalent total strain

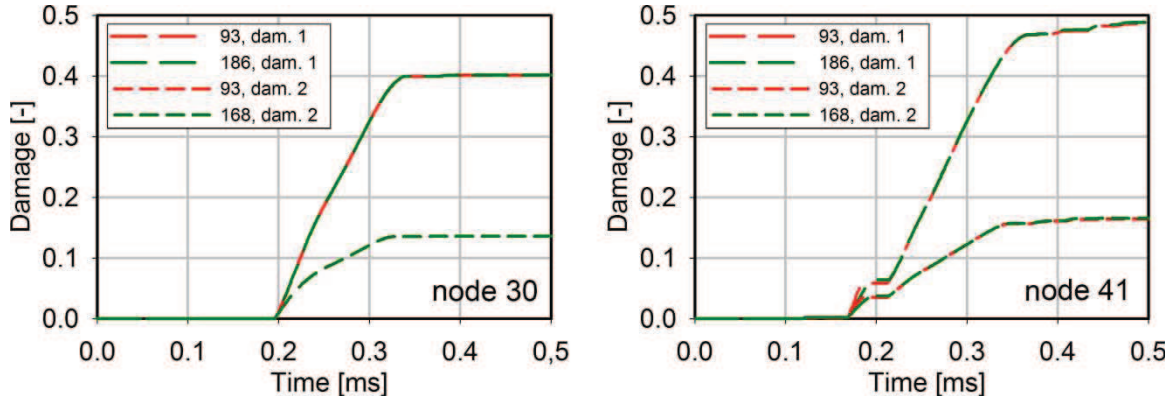

Fig. 7-27. Mesh density influence analysis – damage variable

7.5. Modelling of fracture prediction

The numerical simulations of the fracture prediction in the considered model have been realized using the axisymmetrical shell elements divided into five layers. The crack initiation is modelled by the deactivation of elements. In this approach, as it has been described in Chapter 3, three different approaches are analyzed. In the first an element is deleted when the assumed fracture criterion is fulfilled in each integration point of its any single layer (1/5 layer). In the second an element is removed when at least three layers (3/5 layers) are assumed to be fractured (criterion fulfilled in all integration points in three layers). In the third the deactivation of an element occurs when the criterion is fulfilled in its all integration points

(5/5 layers). The analyses are computed until a first element is deactivated. This moment is assumed as the occurrence of circumference fracture. The example presenting the initiation of crack during the analysis is shown in Fig. 7-28.

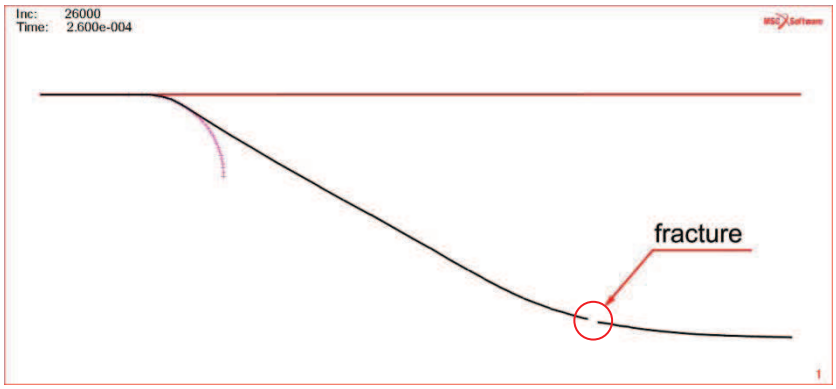

Fig. 7-28. Fracture occurrence in the numerical study

During the axisymmetrical model fracture prediction, in each analyzed approach, ten different numerical simulations have been performed. Each time the model is submitted to the pressure time histories registered during the succeeded, fracture effected experiments. The computed numerical solutions, which are the diameters of obtained holes, are compared individually with the experimental results. For each individual test, the relative error and for each method, their arithmetic mean values have been determined.

For each approach one chosen example (test 06_1) presenting the plates' cross-sections in the fracture moment is shown.

7.5.1. Uncoupled analysis – no damage effects

The uncoupled approach assumes that no coupling exists between a chosen variable, which is established as critical for fracture, and a constitutive law. It means that the material weakening is not considered. In this analysis, the three chosen abrupt failure criteria are investigated.

The first applied criterion is based on the critical value of plastic strain (Chapter 2.4.4). The value of this critical parameter has been determined during the calibration procedure presented in Chapter 6.3 and in the considered uncoupled approach is equal to $\bar{\varepsilon}_f^I = 0.135$. After performing all ten simulations, the reliable solutions have not been obtained in any case. In the analyses with the lowest applied fracturing initial pressure 0.5 bar, the critical value of plastic strain has not been reached at any point of the plate. During the simulations, in which the stronger impulses have been applied, the critical value occurs but the localisation of crack

is impossible. In all these cases, the element deactivation starts at the plate centre point. This fracture criterion is completely inefficient for the present study in the analyzed uncoupled approach model.

The second considered criterion is based on the constancy of the total strain energy density assumption (Chapter 2.4.4). The calibrated value of critical parameter in Chapter 6.4 is $W_{cr} = 64.98$ MJ·m^{-3}. The results of performed analyses are presented in Tab. 7-1. The empty cells, which occur in the table, mean that the crack localisation is impossible. Similarly to the previous study in these cases, the element deactivation starts at the plate centre point. In the considered criterion, the most efficient method is based on the assumption that the fracture occurs when the total strain energy density reaches its critical value in only one layer. However, in four cases the results still have not been obtained. In addition, the mean error – 27 % in this solution is relatively high. The methods "3/5 layers" and "5/5 layers" are inefficient, the crack indication is possible in only two tests with the strongest impulses. The plate's cross-sections for the chosen test are presented in Fig. 7-29.

Press. [bar]	Test	Exp.	1/5 layer		3/5 layers		5/5 layers		Average from 3 met.		
		d [mm]	*d* [mm]	error [%]	*d* [mm]	error [%]	*d* [mm]	error [%]	av. *d* [mm]	error [%]	stand. dev.
0.5	05_2	35.3	-		-		-				
	05_3	30.8	-		-		-				
	05_4	34.2	-		-		-				
0.6	06_0	41.9	27.4	34.6	-		-				
	06_1	45.2	36.6	19.0	-		-				
	06_2	34.5	28.6	17.1	-		-				
	06_3	38.7	-		-		-				
0.7	07_1	58.7	36.6	37.6	34.2	41.7	29.0	50.6	33.3	43.3	3.9
	07_2	39.3	26.0	33.8	-		-				
	07_3	56.5	19.6	19.6	47.2	16.5	37.0	34.5	50.6	10.4	15.6
Mean values				**27.0**		**29.1**		**42.6**		26.9	9.7

Tab. 7-1. Results of uncoupled fracture study, total strain energy density criterion

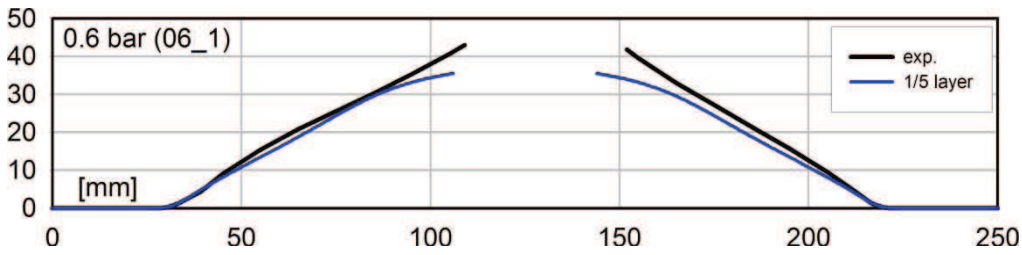

Fig. 7-29. Fracture in uncoupled model with the total strain energy density criterion, test 06_1

The last abrupt failure criterion, which has been chosen for the analyses (Chapter 2.4.4), is based on the direct dependency to the stress triaxiality. The calibrated critical parameter in Chapter 6.5 is Tcr = 0.045. The results are presented in Tab. 7-2. The meaning of the empty cells, which also occur in these results, is the same as in the previous table. The best solution, twith respect to the mean error – 13.3 %, has been obtained when the fracture condition is satisfied in at least three layers. However, in two individual cases the "1/5 layers" method gives the result, which is closer to experiment. The solution efficiency in the analyzed criterion is the best among the three considered in the uncoupled approach, but still not all solutions have been obtained. The analysis of average values calculated from the results succeeded in all three different methods gives relatively low error 7.1 %, the standard deviation, which is quite high – 16.7, shows that the simulations in the considered case are sensitive to the assumption concerning the number of layers, in which the criterion should be fulfilled to initiate a crack. The plate's cross-sections illustrating the fracture moment in the considered approach, for the chosen test 06_1, are presented in Fig. 7-30.

Press. [bar]	Test	Exp.	1/5 layer		3/5 layers		5/5 layers		Average from 3 met.		
		d [mm]	*d* [mm]	error [%]	*d* [mm]	error [%]	*d* [mm]	error [%]	av. *d* [mm]	error [%]	stand. dev.
0.5	05_2	35.3	27.6	21.8	-		-				
	05_3	30.8	33.6	9.1	-		-				
	05_4	34.2	-		-		-				
0.6	06_0	41.9	51.2	22.2	36.0	14.1	33.6	19.8	40.3	3.9	40.3
	06_1	45.2	69.0	52.7	43.8	3.1	31.0	31.4	47.9	6.0	47.9
	06_2	34.5	51.2	48.4	38.6	11.9	-				
	06_3	38.7	33.4	13.7	28.2	27.1	-				
0.7	07_1	58.7	64.0	9.0	51.4	12.4	33.6	42.8	49.7	15.4	49.7
	07_2	39.3	56.6	44.0	38.6	1.8	28.4	27.7	41.2	4.8	41.2
	07_3	56.5	78.2	38.4	69.4	22.8	30.8	45.5	59.5	5.3	59.5
Mean values				**28.8**		**13.3**		**33.4**		7.1	16.7

Tab. 7-2. Results of uncoupled fracture study, stress triaxiality dependency criterion

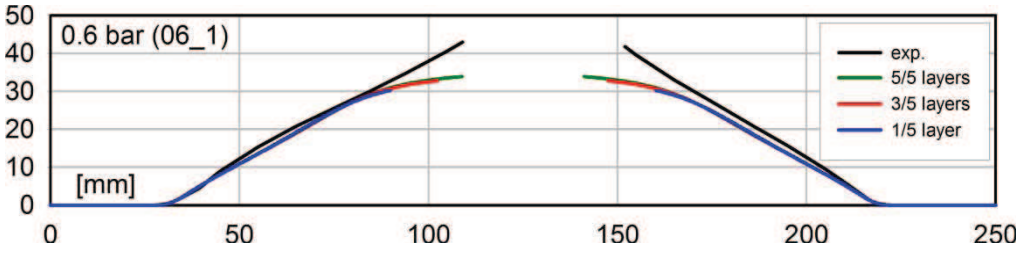

Fig. 7-30. Fracture in uncoupled model with the stress triaxiality dependency criterion, test 06_1

7.5.2. Coupled analysis – damage first approach effects

In the coupled approach, the continuum damage model is considered. It means that the material weakening, controlled by the damage variable and the effective stress concept, is taken into account. In the current case, the model based on the damage variable identified in the first approach, presented in Chapter 5.6.2, is used. The criterion in such analysis is based on the critical value of damage and the ultimate stress (Chapter 2.4.2). The calibrated parameters in Chapter 6.6 are D_{1cr} = 0.293 and σ_u = 504 MPa. The results of performed calculations are presented in Tab. 7-3. The solution efficiency is very good. In all considered cases, the crack localisation is possible. The mean error for the "1/5 layer" method is high – almost 45 %, but two others give much better solutions – mean error around 16 %. The average value obtained for all three methods is 18.8 %. The cross-sections for the example test are presented in Fig. 7-31.

Press. [bar]	Test	Exp.	1/5 layer		3/5 layers		5/5 layers		Average from 3 met.		
		d [mm]	*d* [mm]	error [%]	*d* [mm]	error [%]	*d* [mm]	error [%]	av. *d* [mm]	error [%]	stand. dev.
0.5	05_2	35.3	22.0	37.7	32.4	8.2	27.4	22.4	27.3	22.8	5.2
	05_3	30.8	40.0	29.9	35.0	13.6	32.6	5.8	35.9	16.5	3.8
	05_4	34.2	37.8	10.5	29.8	12.9	37.8	10.5	35.1	2.7	4.6
0.6	06_0	41.9	60.4	44.2	45.2	7.9	35.0	16.5	46.9	11.9	12.8
	06_1	45.2	75.8	67.7	53.2	17.7	40.2	11.1	56.4	24.8	18.0
	06_2	34.5	65.6	90.1	45.2	31.0	40.2	16.5	50.3	45.9	13.5
	06_3	38.7	42.6	10.1	40.2	3.9	37.6	2.8	40.1	3.7	2.5
0.7	07_1	58.7	68.0	15.8	65.8	12.1	35.0	40.4	56.3	4.1	18.5
	07_2	39.3	71.6	82.2	45.2	15.0	40.2	2.3	52.3	33.2	16.9
	07_3	56.5	86.8	53.6	79.8	41.2	40.6	28.1	69.1	22.2	24.9
Mean values				**44.2**		**16.4**		**15.6**		18.8	12.1

Tab. 7-3. Results of coupled, damage 1st approach fracture study, critical damage criterion

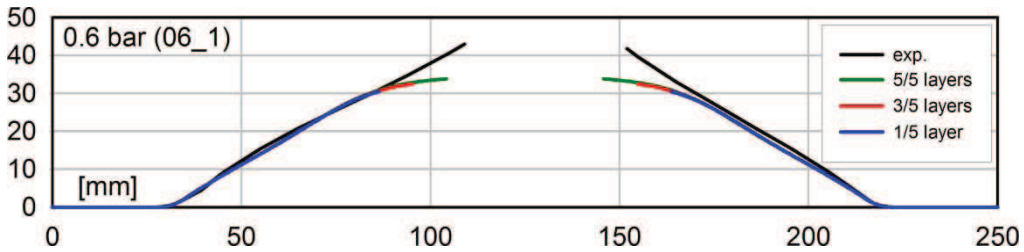

Fig. 7-31. Fracture in coupled, damage 1st approach model with the critical damage criterion, test 06_1

The critical damage criterion in the continuum damage analysis is the natural choice. However, it is also interesting how the abrupt fracture criteria, originally created for the uncoupled approach, would behave in the model in which the material weakening is considered. Such study, where the coupled model is used but the fracture is controlled by the abrupt criteria, has been also performed. The results are presented in Tab. 7-4 – Tab. 7-6. In all three criteria, the solution efficiency improved. However, it is still not as good as in the critical damage analyses. The results, obtained using the total strain energy density criterion, are much better than in the uncoupled approach. For example the mean error in the "3/5 layers" method is under 13 % and the maximum in the "3/5 layers" is still not too high – 22.3 % (the average error in all three methods – 12.6 %). Meanwhile the solutions obtained using the stress triaxiality dependency criterion deteriorated. Admittedly, the lowest mean error increased from 13.3 to 14.7 % (the best solution moves from "3/5 layers" method to "5/5 layers"), but the highest in the coupled approach is almost twice high, from 33.4 to 61.3 %. The cross-sections for the example test are presented in Fig. 7-32 – Fig. 7-34.

Press. [bar]	Test	Exp.	1/5 layer		3/5 layers		5/5 layers		Average from 3 met.		
		d [mm]	*d* [mm]	error [%]	*d* [mm]	error [%]	*d* [mm]	error [%]	av. *d* [mm]	error [%]	stand. dev.
0.5	05_2	35.3	-		-		-				
	05_3	30.8	-		-		-				
	05_4	34.2	-		-		-				
0.6	06_0	41.9	-		-		-				
	06_1	45.2	37.8	16.4	32.6	27.9	-				
	06_2	34.5	27.0	21.7	-		-				
	06_3	38.7	-		-		-				
0.7	07_1	58.7	32.4	44.8	32.6	44.5	-				
	07_2	39.3	-		-		-				
	07_3	56.5	56.4	0.2	46.2	18.2	41.0	27.4	47.9	15.3	7.8
Mean values				**18.5**		**30.2**		**27.4**		15.3	7.8

Tab. 7-4. Results of coupled, damage 1st approach fracture study, critical equivalent plastic strain criterion

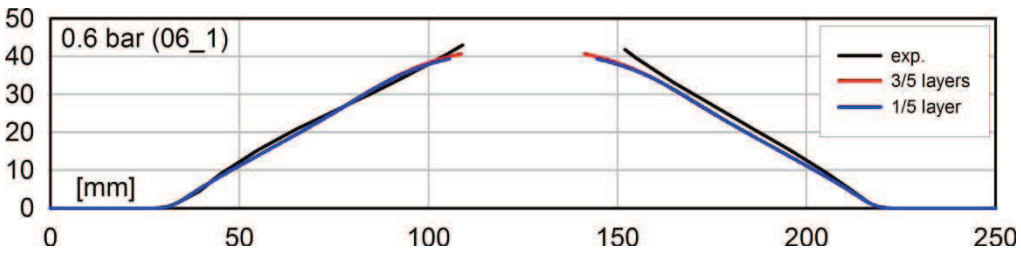

Fig. 7-32 Fracture in coupled, damage 1st approach model with the equivalent plastic strain criterion, test 06_1

Press. [bar]	Test	Exp.	1/5 layer		3/5 layers		5/5 layers		Average from 3 met.		
		d [mm]	*d* [mm]	error [%]	*d* [mm]	error [%]	*d* [mm]	error [%]	av. *d* [mm]	error [%]	stand. dev.
0.5	05_2	35.3	-		-		-				
	05_3	30.8	34.0	10.4	-		-				
	05_4	34.2	-		-		-				
0.6	06_0	41.9	36.6	12.6	36.8	12.2	35.6	15.0	36.3	13.3	0.6
	06_1	45.2	65.2	44.2	44.6	1.3	39.6	12.4	49.8	10.2	13.6
	06_2	34.5	44.4	28.7	39.4	14.2	38.2	10.7	40.7	17.9	3.3
	06_3	38.7	31.2	19.4	31.4	18.9	34.0	12.1	32.2	16.8	1.6
0.7	07_1	58.7	65.0	10.7	55.0	6.3	39.6	32.5	53.2	9.4	12.8
	07_2	39.3	43.2	9.9	42.0	6.9	39.6	0.8	41.6	5.9	1.8
	07_3	56.5	80.4	42.3	73.2	29.6	41.2	27.1	64.9	14.9	20.9
Mean values				**22.3**		**12.8**		**15.8**		12.6	7.8

Tab. 7-5. Results of coupled, damage 1st approach fracture study, total strain energy density criterion

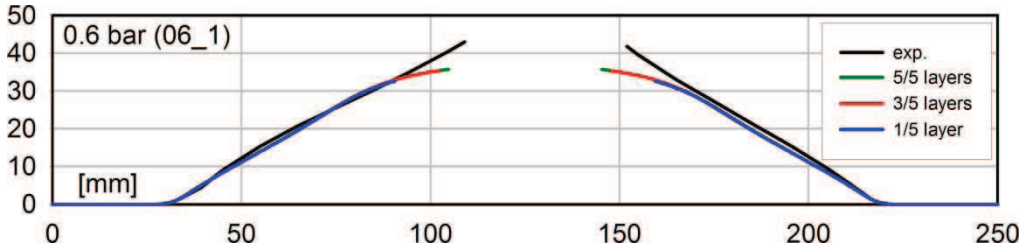

Fig. 7-33. Fracture in coupled, damage 1st approach model with the total strain energy density criterion, test 06_1

7.5.3. Coupled analysis – damage second approach effects

In the alternative coupled approach, the model is based on the damage variable taken from the results of second identification (Chapter 5.6.5). The values of damage obtained in this case are smaller than in the first approach, it means that the material weakening effect is also less intensive. As in the previous study, initially the analyses based on the critical damage criterion have been performed. The calibrated parameters in Chapter 6.6 are D_{1cr} = 0.127 and σ_u = 484.5 MPa. The results of performed calculations are presented in Tab. 7-3. The best solution with respect to the mean error – 15 %, has been obtained when the fracture condition is satisfied in a first layer of shell element – 1/5 layer. In this case, the obtained mean error is 15 % (in five simulations is under 8 %). The average error calculated for all three methods is18.4 %. The relatively low mean standard deviation shows that these calculations are not very sensitive to the chosen number of layers assumed in the crack initiation method. The plate's

cross-sections illustrating the fracture moment in the considered approach, for the chosen test 06_1, are presented in Fig. 7-35.

Press. [bar]	Test	Exp.	1/5 layer		3/5 layers		5/5 layers		Average from 3 met.		
		d [mm]	*d* [mm]	error [%]	*d* [mm]	error [%]	*d* [mm]	error [%]	av. *d* [mm]	error [%]	stand. dev.
0.5	05_2	35.3	-		-		-				
	05_3	30.8	43.6	41.6	38.6	25.3	-				
	05_4	34.2	-		-		-				
0.6	06_0	41.9	64.0	52.7	56.6	35.1	35.0	16.5	51.9	23.8	15.1
	06_1	45.2	76.8	69.9	69.4	53.5	41.2	8.8	62.5	38.2	18.8
	06_2	34.5	71.6	107.5	46.4	34.5	38.8	12.5	52.3	51.5	17.2
	06_3	38.7	61.4	58.7	41.2	6.5	38.8	0.3	47.1	21.8	12.4
0.7	07_1	58.7	69.0	17.5	69.4	18.2	31.0	47.2	56.5	3.8	22.1
	07_2	39.3	69.0	75.6	64.4	63.9	41.4	5.3	58.3	48.3	14.8
	07_3	56.5	94.2	66.7	84.6	49.7	41.2	27.1	73.3	29.8	28.2
Mean values				**61.3**		**35.8**		**14.7**		31.0	18.4

Tab. 7-6. Results of coupled, damage 1st approach fracture study, stress triaxiality dependency criterion

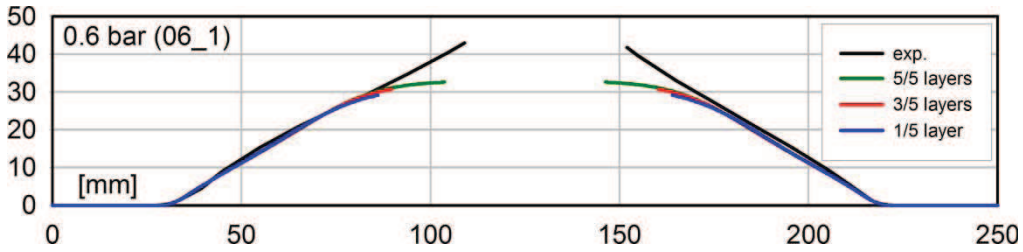

Fig. 7-34. Fracture in coupled, damage 1st approach model with the stress triaxiality dependency criterion, test 06_1

Analogically to the first presented coupled approach, the application of abrupt fracture criteria is also considered in this study. This time, due to lower values of the damage variable, the material weakening effect is not as strong as it has been observed in the previous approach. In such conditions, the first criterion based on the critical value of equivalent plastic strain is again (as it has been observed in the uncoupled approach) completely ineffective. No results or wrong results have been obtained.

The solutions computed in the analyses with two other criteria are presented in Tab. 7-8 and Tab. 7-9. The crack localisation efficiency in these cases is worse than in the previous approach, but still better than in the uncoupled one. The best results have been obtained in the calculations with the stress triaxiality dependency criterion, where the mean error in the "3/5 layers" method is 11.3 % and the average calculated for three different 16.8 %. Similarly as in

the other approaches, this criterion is sensitive due to the number of layers taken to the crack initiation. The mean standard deviation calculated for the individual mean errors is 16.1.

Press. [bar]	Test	Exp.	1/5 layer		3/5 layers		5/5 layers		Average from 3 met.		
		d [mm]	*d* [mm]	error [%]	*d* [mm]	error [%]	*d* [mm]	error [%]	av. *d* [mm]	error [%]	stand. dev.
0.5	05_2	35.3	27.2	22.9	19.4	45.0	11.2	68.3	19.3	45.4	8.0
	05_3	30.8	28.6	7.1	35.8	16.2	33.2	7.8	32.5	5.6	3.6
	05_4	34.2	32.8	4.1	33.2	2.9	27.8	18.7	31.3	8.6	3.0
0.6	06_0	41.9	32.6	22.2	31.6	24.6	30.2	27.9	31.5	24.9	1.2
	06_1	45.2	41.8	7.5	36.8	18.6	33.0	27.0	37.2	17.7	4.4
	06_2	34.5	35.2	2.0	26.2	24.1	30.2	12.5	30.5	11.5	4.5
	06_3	38.7	27.3	29.5	30.0	22.5	27.6	28.7	28.3	26.9	1.5
0.7	07_1	58.7	61.0	3.9	43.2	26.4	33.0	43.8	45.7	22.1	14.2
	07_2	39.3	31.4	20.1	32.8	16.5	32.8	16.5	32.3	17.7	0.8
	07_3	56.5	74.0	31.0	62.8	11.2	38.2	32.4	58.3	3.2	18.3
Mean values				**15.0**		**20.8**		**28.4**		18.4	6.0

Tab. 7-7. Results of coupled, damage 2nd approach fracture study, critical damage criterion

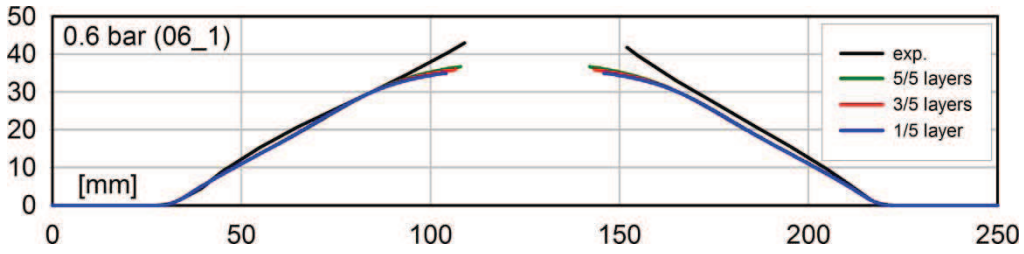

Fig. 7-35. Fracture in coupled, damage 2st approach model with the critical damage criterion, test 06_1

Press. [bar]	Test	Exp.	1/5 layer		3/5 layers		5/5 layers		Average from 3 met.		
		d [mm]	*d* [mm]	error [%]	*d* [mm]	error [%]	*d* [mm]	error [%]	av. *d* [mm]	error [%]	stand. dev.
0.5	05_2	35.3	-		-		-				
	05_3	30.8	23.4	24.0	-		-				
	05_4	34.2	-		-		-				
0.6	06_0	41.9	31.2	25.5	31.2	25.5	28.8	31.3	30.4	27.4	1.4
	06_1	45.2	41.8	7.5	36.8	18.6	27.8	38.5	39.3	13.1	7.1
	06_2	34.5	36.6	6.1	-		-				
	06_3	38.7	26.0	32.8	-		-				
0.7	07_1	58.7	52.0	11.4	39.4	32.9	34.2	41.7	41.9	28.7	9.2
	07_2	39.3	31.2	20.6	-		-				
	07_3	56.5	72.8	28.8	57.8	2.3	39.6	29.9	56.7	0.4	16.6
Mean values				**19.6**		**19.8**		**35.4**		19.5	8.6

Tab. 7-8. Results of the coupled, damage 2st approach fracture study, total strain energy density criterion

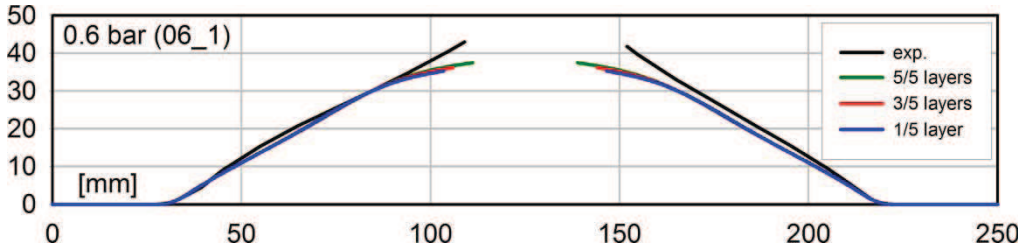

Fig. 7-36. Fracture in coupled, damage 2st app. model with the total strain energy density crit., test 06_1

Press. [bar]	Test	Exp.	1/5 layer		3/5 layers		5/5 layers		Average from 3 met.		
		d [mm]	*d* [mm]	error [%]	*d* [mm]	error [%]	*d* [mm]	error [%]	av. *d* [mm]	error [%]	stand. dev.
0.5	05_2	35.3	-		-		-				
	05_3	30.8	38.6	25.3	28.2	8.4	-				
	05_4	34.2	-		-		-				
0.6	06_0	41.9	59.0	40.8	41.2	1.7	33.6	19.8	44.6	6.4	13.0
	06_1	45.2	71.6	58.4	46.4	2.7	38.8	14.2	52.3	15.6	17.2
	06_2	34.5	64.0	85.5	43.8	27.0	28.4	17.7	45.4	31.6	17.9
	06_3	38.7	43.6	12.7	36.2	6.5	-				
0.7	07_1	58.7	66.6	13.5	61.8	5.3	33.6	42.8	54.0	8.0	17.8
	07_2	39.3	64.0	62.8	43.8	11.5	36.2	7.9	48.0	22.1	14.4
	07_3	56.5	84.0	48.7	74.4	31.7	-				
Mean values				**43.5**		**11.3**		**20.5**		16.8	16.1

Tab. 7-9. Results of coupled, damage 2st approach fracture study, stress triaxiality dependency criterion

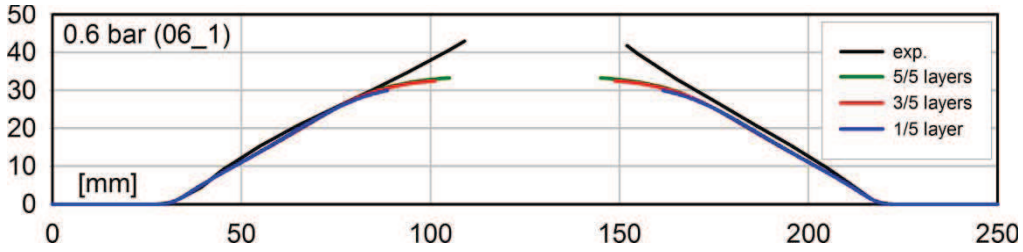

Fig. 7-37. Fracture in coupled, damage 1st approach model with the stress triaxiality dependency criterion, test 06_1

7.6. Investigation of mesh density influence – model with fracture

The already presented investigation the mesh density influence analysis has shown that the chosen model gives the results, which can be admitted as reliable, if the failure is not considered (elements have not been deactivated). However, it is also interesting, whether the results are still mesh density independent, when the fracture prediction is analyzed. To check the reliability of the presented above results, the additional study has been performed. For the chosen test 06_1, the same crack initiation analyses have been computed, but this time the fine mesh model (the same as in Chapter 7.4 – 186 elements model) has been used. The

results are presented in Tab. 7-10. For each solution the percentage difference between the results obtained in both models have been calculated. The differences are low, the maximum value is 4.9 %, and therefore the results again can be admitted as reliable.

Criterion		1/5 layer			3/5 layers			5/5 layers		
		93 *d* [mm]	186 *d* [mm]	diff. [%]	93 *d* [mm]	186 *d* [mm]	diff. [%]	93 *d* [mm]	186 *d* [mm]	diff. [%]
Uncoupl. analysis	tot. strain en. density	36.6	35.4	**3.3**	-	-		-	-	
	stress triax. dependency	69.0	69.0	**0.0**	43.8	42.6	**2.8**	31.0	32.4	**4.4**
Coupled analysis, damage 1st app.	critical damage	75.8	76.2	**0.5**	53.2	55.8	**4.8**	40.2	40.6	**1.0**
	crit. equiv. pl. strain	37.8	38.6	**2.1**	32.6	34.0	**4.2**	-	-	
	tot. strain en. density	65.2	68.2	**4.5**	44.6	45.2	**1.3**	39.6	39.4	**0.5**
	stress triax. dependency	76.8	78.0	**1.6**	69.4	68.8	**0.9**	41.2	40.4	**2.0**
Coupled analysis, damage 2nd app.	critical damage	41.8	41.8	**0.0**	36.8	38.0	**3.2**	33.0	33.6	**1.8**
	crit. equiv. pl. strain	23.8	25.0	**4.9**	-	-		-	-	
	tot. strain en. density	41.8	41.8	**0.0**	36.8	35.6	**3.3**	27.8	26.9	**3.3**
	stress triax. dependency	71.6	73.0	**1.9**	46.4	46.8	**0.9**	38.8	37.4	**3.7**

Tab. 7-10. Results obtained in the investigation of mesh density influence

7.7. Summary

The complex study in the fracture prediction in the axisymmetrical model has been made. The analysis has been preceded by the determination of the fixing boundary conditions, which have been applied to the model. This stage of the presented work is a key for the further analysis. The proper answer of the model is necessary in the later fracture prediction modelling. The various verifications have confirmed that the assumed conditions are sufficient in the considered problem. The simulations of fracture prediction have been performed for all considered approaches and criteria. As it has been shown some of the criteria are completely inefficient. The critical equivalent plastic strain criterion in the

considered problem is useless. The two criteria are chosen as the most reliable. The first is the stress triaxiality stress dependency criterion, where the lowest mean errors have been obtained (the uncoupled approach, 3/5 layers – 13.3 %, the coupled 2nd damage approach – 11.3 %). The second is the critical damage criterion, where the relatively low mean error has been obtained for the "1/5 layer" method – 15 %. Additionally in this second criterion the 100 % efficiency of the obtained solutions has been observed and the low mean standard deviation has shown that these calculations are not very sensitive to the number of layers assumed in the crack initiation condition.

8. Numerical study – plate's quarter model

8.1. Abstract

In the following stage of the numerical study the 2-D shell analyses have been performed. The present chapter begins with the description of assumed boundary conditions and meshing of the model. At first four different meshes proposed for this study are presented. After the first analyses, the selection of two has been made. Then, for selected types of mesh, the verification of solution symmetry and mesh density influence is investigated. The main analyses contain the numerical simulations only for the criteria, which have been found as the most reliable in the previous chapter. The obtained results are compared with the results of experiments and axisymmetrical analyses.

8.2. Introduction

The specimens used in the experiments were prepared as square sheet metal plates. The measurements presented in Chapter 4.3.3 have shown that this shape do not interfere the axisymmetrical deformation of plates during the tests. Therefore, also in the 2-D shell analysis the assumption of model's axisymmetry is maintained. It allows application of the same fixing boundary conditions to the model as used in the previous study. Due to the willingness of decreasing task's size (the analysis is highly time-consuming), the model is limited to the quarter of plate. On the symmetry edges, the appropriate boundary conditions have been applied.

8.3. Finite elements mesh geometry

At the beginning of analysis four different meshes have been created, see Fig. 8-1 and Fig. 8-2 (the dashed lines show the fixing area). The first presented – mesh A, built mainly using the three node shell elements, has been generated by the MSC.Marc automesh feature. The three next (four node shell element meshes) have been formed using the AutoCad software tools. To solve the problem of laying for mesh B and C the regular square region of the four node elements at the plate's centre has been created. For mesh D the centre row elements has been reduced to triangles.

During first performed analyses, damage second approach effects (Chapter 5.6.5) are considered and the fracture is not taken into account. The investigation concentrates on

models' answer to the dynamic impact. For this study, the pressure time history recorded during the test 06_1 has been used. The results of these simulations (four selected time steps for each analysis) are presented in Fig. 8-3 and Fig. 8-4. In each case, the maps of damage variable in the elements' bottom layers are presented. The worst results have been obtained using mesh A. There is no axisymmetry of the solution, especially in the fixing region. The irregularities in damage distribution, which appeared in this area, may lead to undesirable deactivation of elements in the fracture prediction analysis. The similar, though smaller, effect is also observed for mesh B. It is caused by the elements geometry in the fixing area, which is not perfectly axisymmetrical. This problem has not occurred for mesh C, where the axisymmetry of elements' geometry is kept for three rows of elements near inner and outer side of the fixing edge. Therefore, for the main study, two geometries – mesh C and D are chosen.

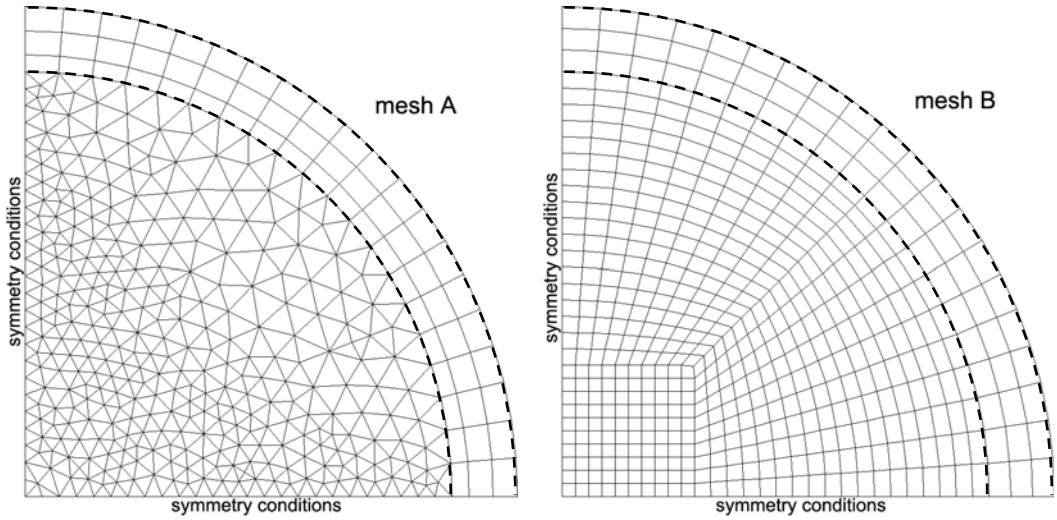

Fig. 8-1. Finite element mesh A and mesh B

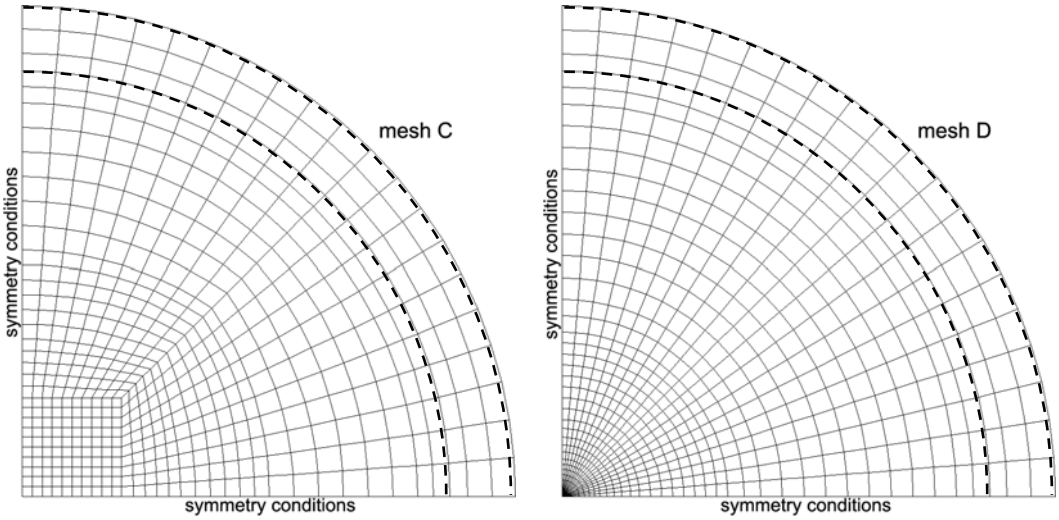

Fig. 8-2. Finite elements mesh C and mesh D

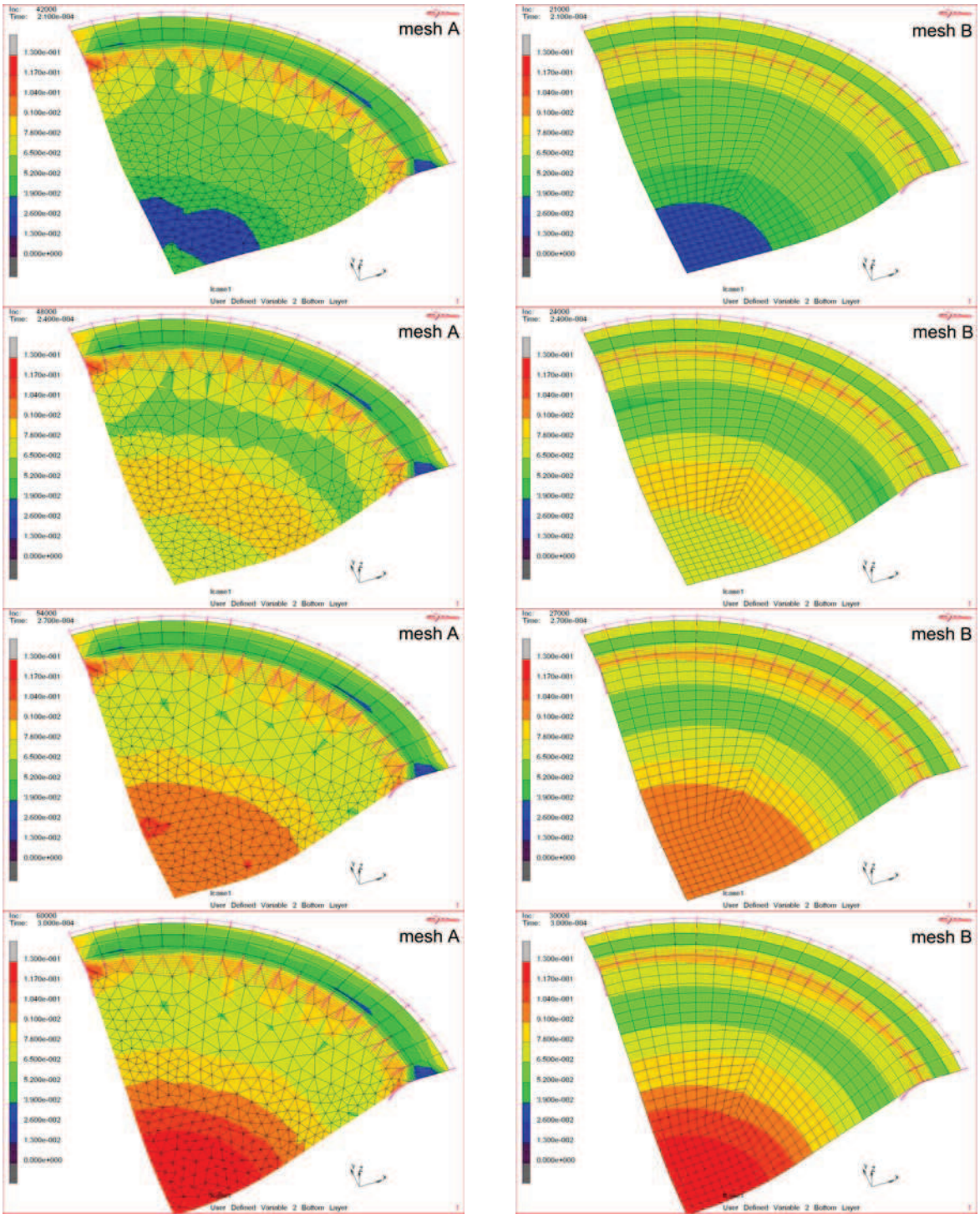

Fig. 8-3. Dynamic analysis – test 06_1, time steps: t_1 = 0.21 ms, t_2 = 0.24 ms, t_3 = 0.27 ms, t_4 = 0.3 ms, mesh A and mesh B

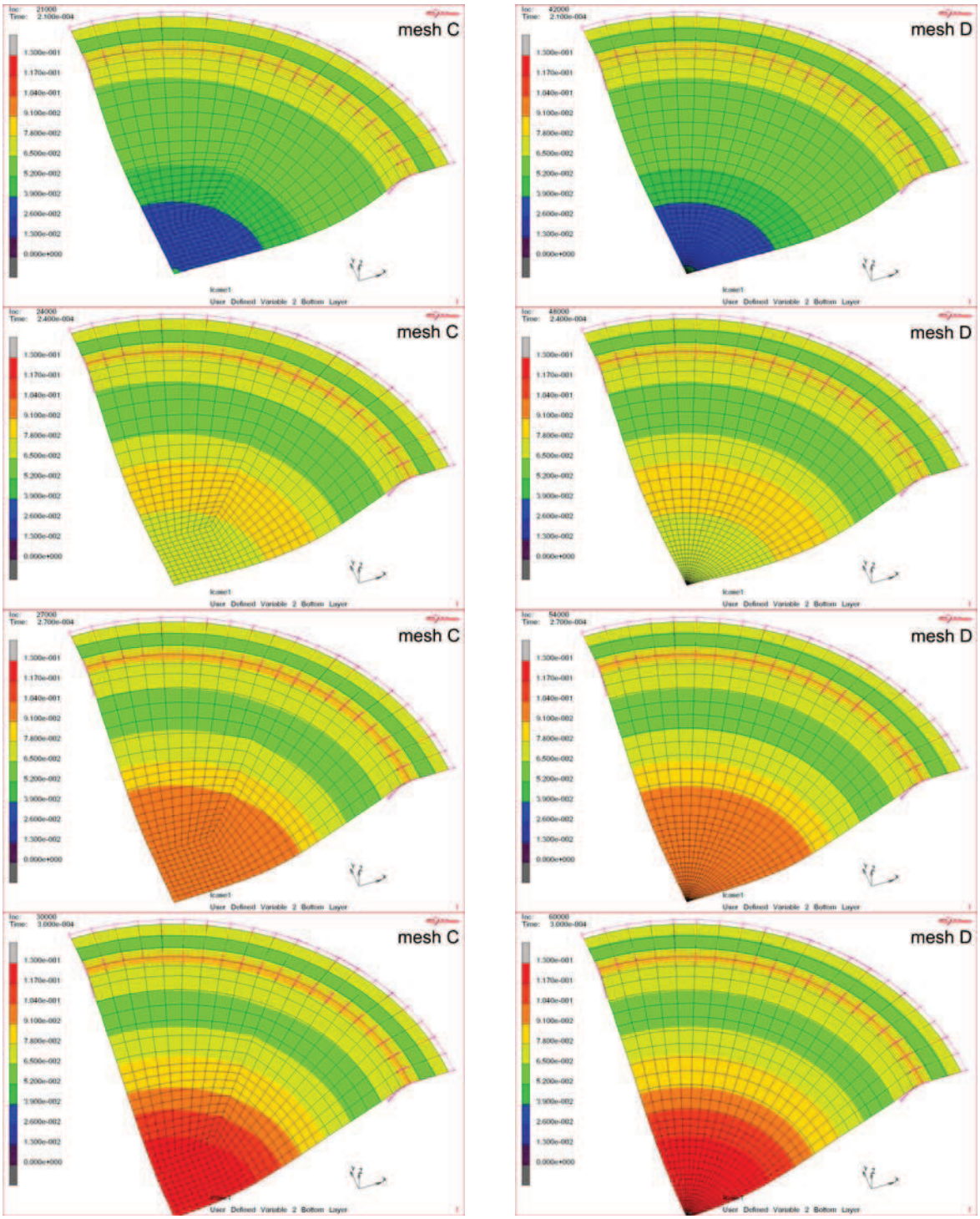

Fig. 8-4. Dynamic analysis – test 06_1, time steps: t_1 = 0.21 ms, t_2 = 0.24 ms, t_3 = 0.27 ms, t_4 = 0.3 ms, mesh C and mesh D

8.4. Finite elements mesh quality

After choosing the meshing types for the further analyses, their quality investigation should be performed. At first, the verification of symmetry has been carried out to exclude errors during meshing. For each mesh two pairs of nodes, lying on the opposite sides of the

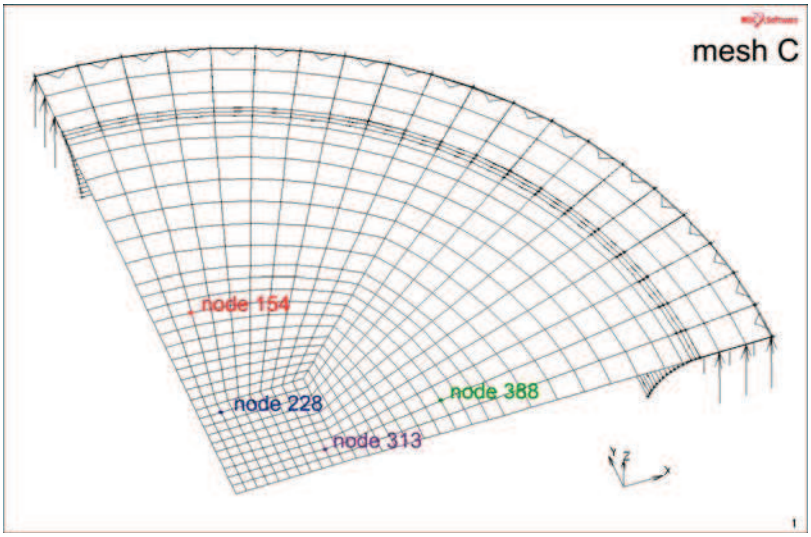

Fig. 8-5. Nodes chosen for the verification of symmetry in mesh C

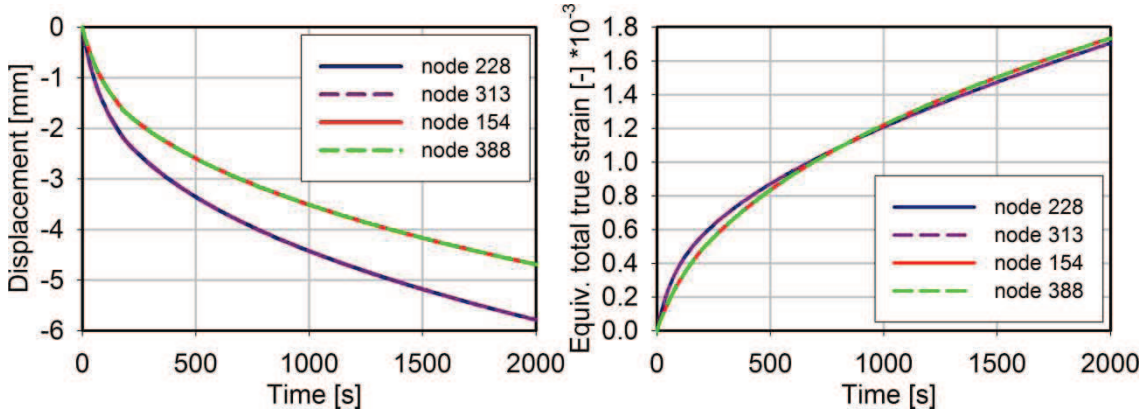

Fig. 8-6. Verification of symmetry in mesh C – quasi-static test

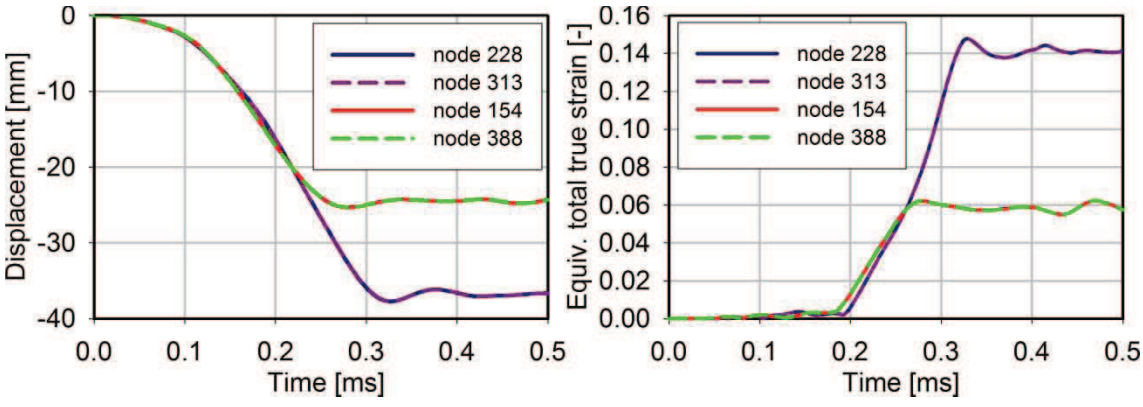

Fig. 8-7. Verification of symmetry in mesh C – dynamic test 06_1

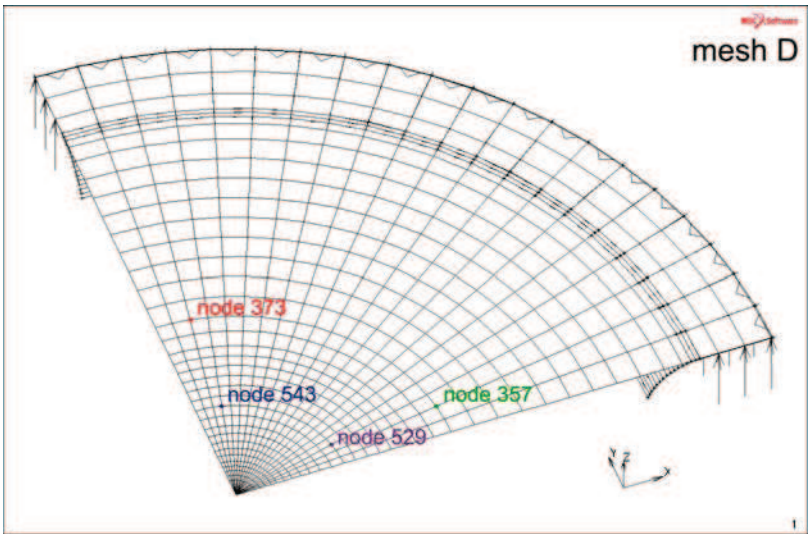

Fig. 8-8. Nodes chosen for the verification of symmetry in mesh D

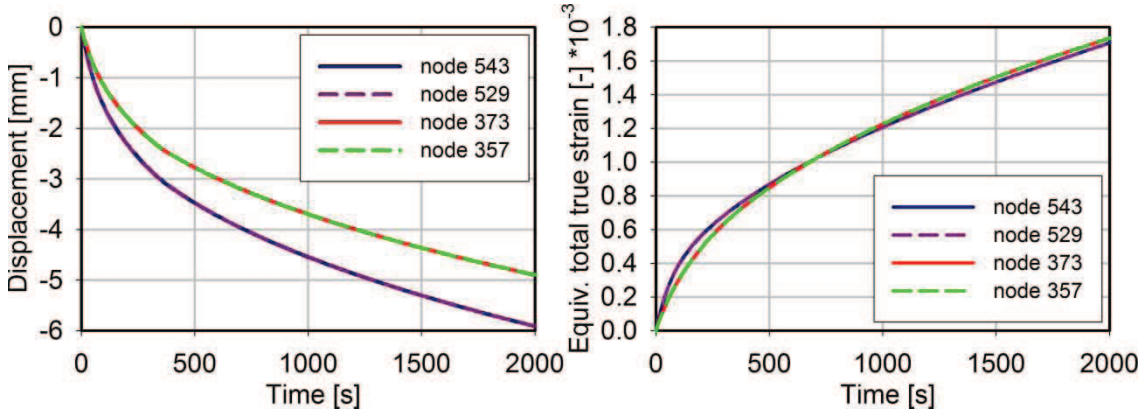

Fig. 8-9. Verification of symmetry in mesh D – quasi-static test

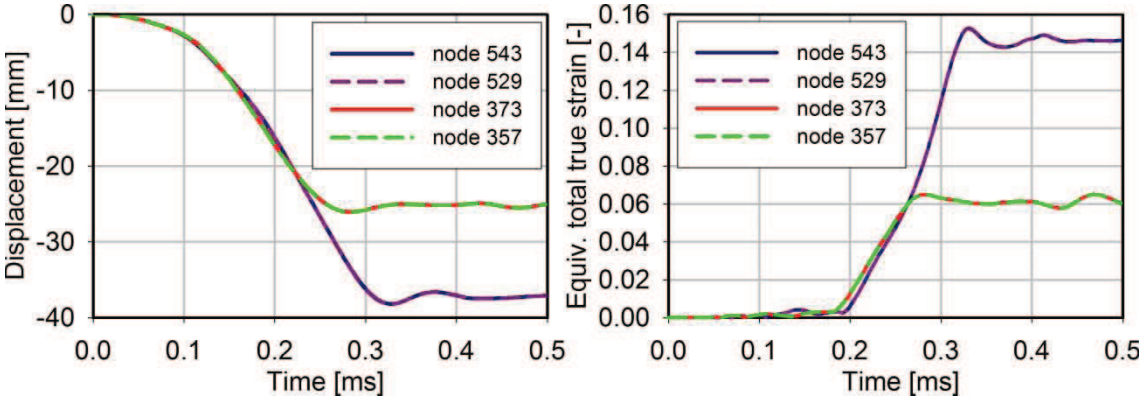

Fig. 8-10. Verification of symmetry in mesh D – dynamic test 06_1

plate's quarter symmetry line, have been chosen – Fig. 8-5 and Fig. 8-8. For both meshes two different analyses have been performed: the quasi-static test and the dynamic test 06_1. In the dynamic test only the damage second approach effects (Chapter 5.6.5) with no fracture has been considered. The results of simulations, vertical displacements and the equivalent total

true strain in bottom layer for mesh C are presented in Fig. 8-6, Fig. 8-7 and for mesh D in Fig. 8-9, Fig. 8-10. For each mesh, the results obtained for selected pairs of nodes are identical. These results confirm good quality of selected types of meshing.

The second investigation concerns the mesh density influence. The considered models are divided into 540 elements – mesh C and 680 elements – mesh D. For this study, the number of elements in each mesh is four times higher than for the standard mesh. Also in this analysis the pressure time history recorded during test 06_1 and the damage second approach

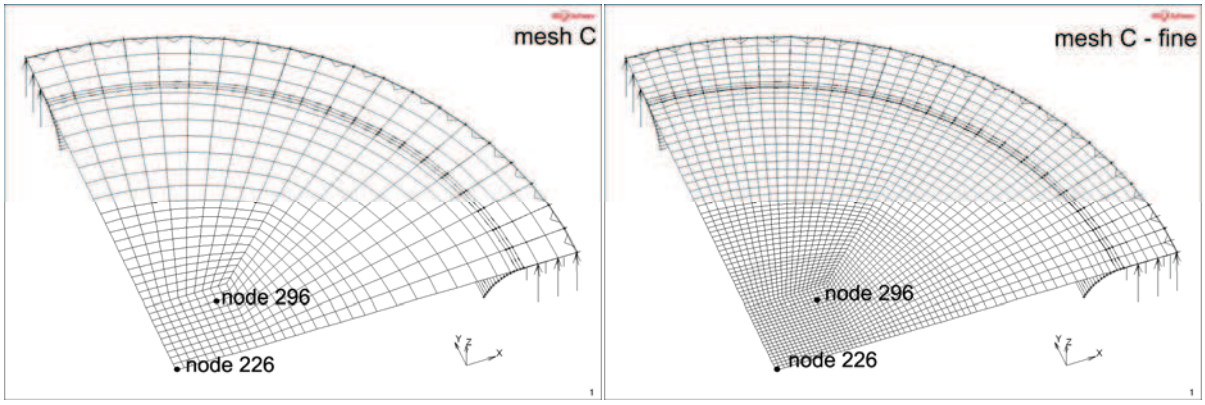

Fig. 8-11. Nodes chosen for mesh C dense influence analysis

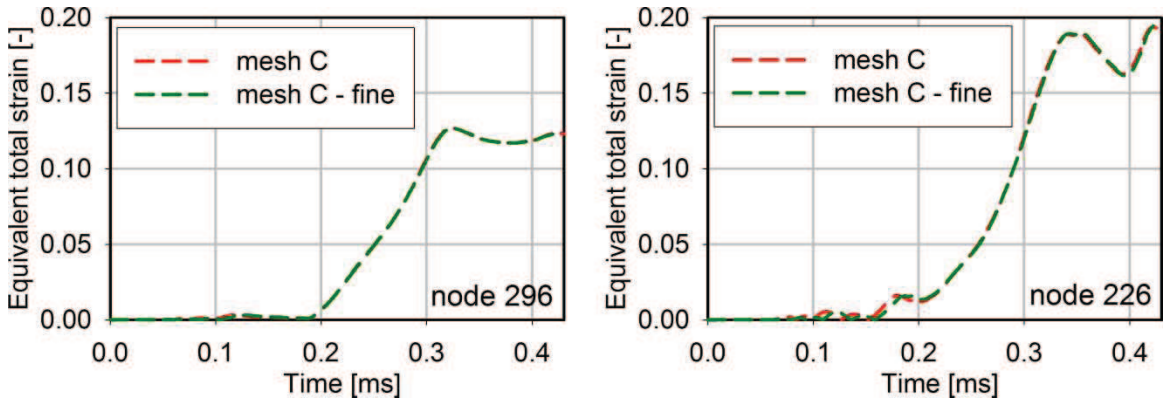

Fig. 8-12. Mesh C dense influence analysis – equivalent total strain

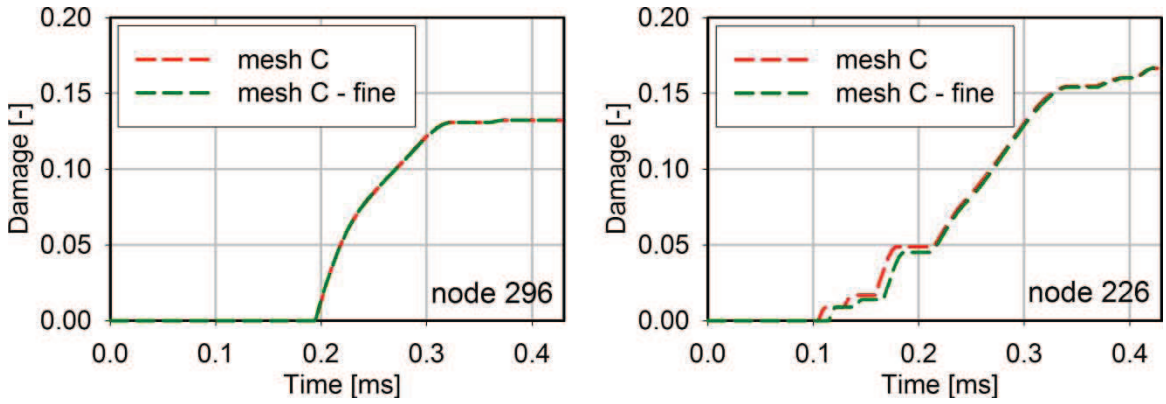

Fig. 8-13. Mesh C dense influence analysis – damage variable

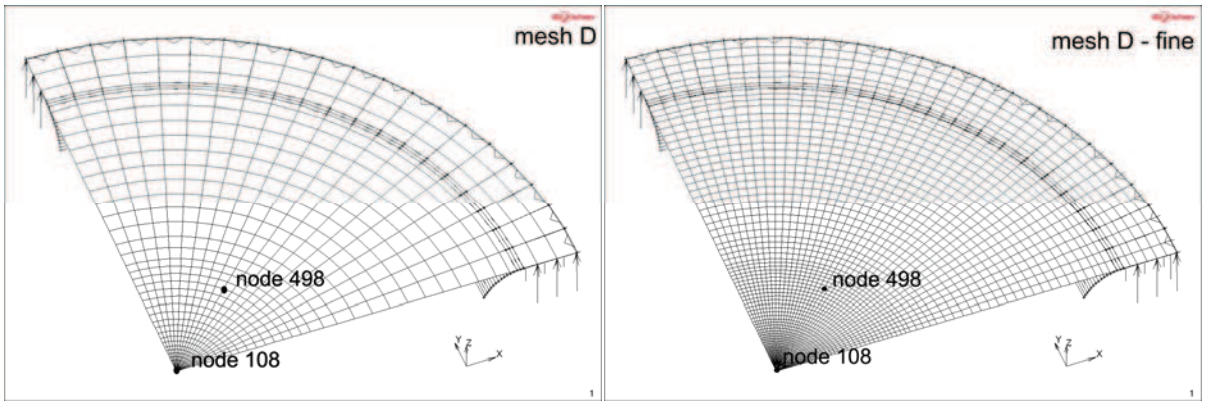

Fig. 8-14. Nodes chosen for mesh D dense influence analysis

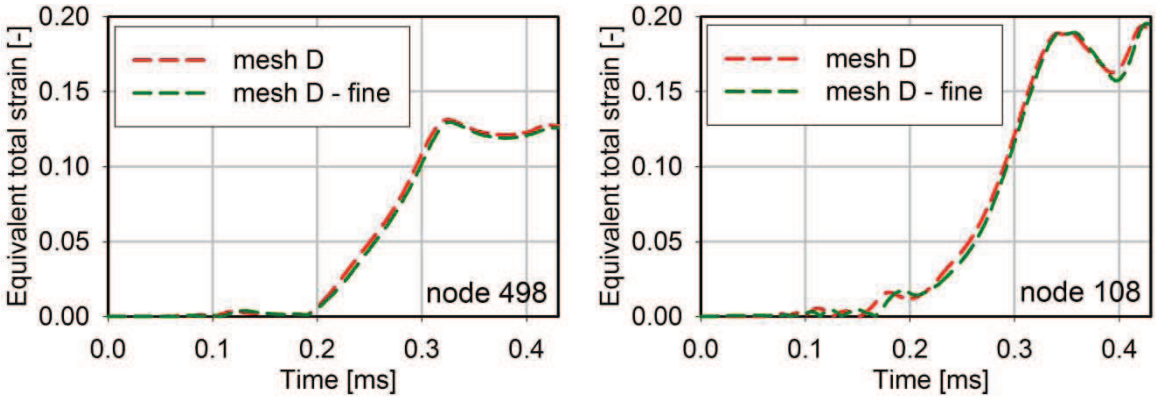

Fig. 8-15. Mesh D dense influence analysis – equivalent total strain

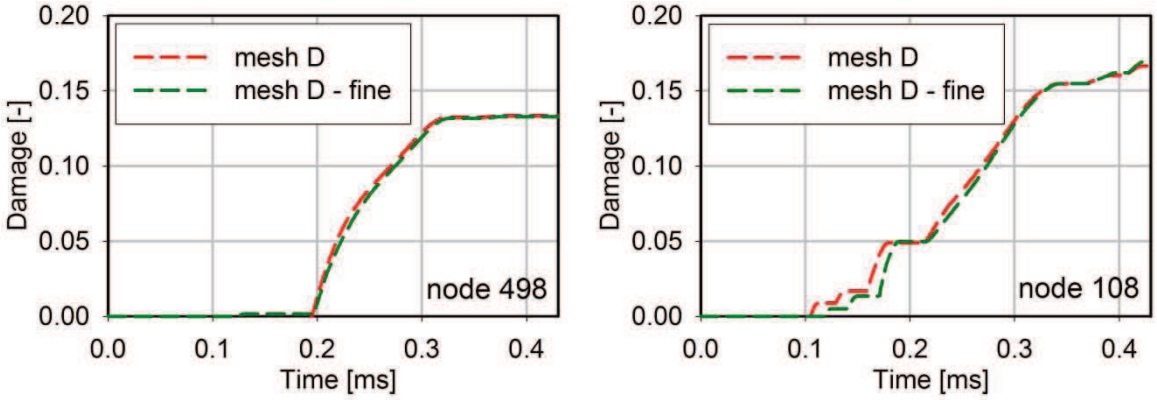

Fig. 8-16. Mesh D dense influence analysis – damage variable

effects with no fracture has been applied. The results are compared for two selected nodes for each mesh, see Fig. 8-11 and Fig. 8-14. The results, which are the equivalent total true strain and the damage variable in the bottom layer, are shown for mesh C in Fig. 8-12, Fig. 8-13 and for mesh D in Fig. 8-15, Fig. 8-16. At the nodes located in the plate's centre there are small differences between the obtained results at the beginning of the analyses, but later the paths of the equivalent total true strain and the damage variable are close to each other. At the nodes located beyond the plate's centre, the solutions are almost overlapped during all analysis time.

According to obtained results, the standard density of meshing can be considered as dense enough.

8.5. Modelling of fracture prediction

The modelling of fracture prediction in 2D shell studies is limited to the fracture criteria, which have been chosen as the most reliable in Chapter 7. That is why only the following three analyses are considered: uncoupled (no damage effects) with the stress triaxiality dependency criterion and coupled – damage second approach effects with two different criteria based on the critical damage and the stress triaxiality dependency. For each case three example tests are investigated: 05_3 (equivalent hole diameter d = 30.8 mm), 06_1 (d = 45.2 mm) and 07_1 (d = 58.7 mm). The results are compared with the experiments and the axisymmetrical analysis.

As in the previous study, the shell elements are divided into five layers and the crack is modelled by deactivation of elements with three different approaches: "1/5 layer", "3/5 layers", "5/5 layers". The analyses have been continued until a clear crack appeared. In the area of its possible initiation the adaptive mesh feature (described in Chapter 3.8) has been applied. During adaptive procedure, an element is divided into four elements after satisfying the criterion of equivalent total strain equal to 0.001.

8.5.1. Uncoupled analysis – no damage effects

The first considered approach is the uncoupled study with the stress triaxiality dependency criterion. For each selected test, two analyses using mesh C and mesh D have been made.

The results obtained in the test 05_3 simulations, where the "1/5 layer" approach is used, are shown in Fig. 8-17. The hole diameter could be identified only from the analysis with the D type of meshing. Additionally, the plate's deflections in six selected time steps and the criterion parameter for the fracture moment (the values in top and bottom layers), both set up together with the axisymmetrical solutions, are plotted in Fig. 8-18 and Fig. 8-19. The arrows show the fracture localization. Obtained diameters of damage circle d compared with the experiment and the previous study is presented in Tab. 7-1. The next two simulations: "3/5 layers" and "5/5 layers" did not give any clear solutions.

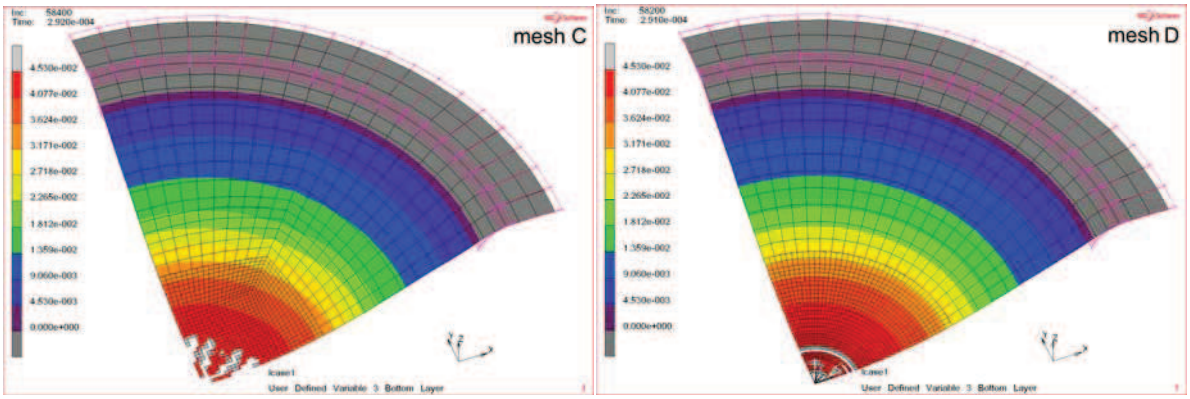

Fig. 8-17. Fracture in uncoupled model with the stress triaxiality dependency criterion, test 05_3

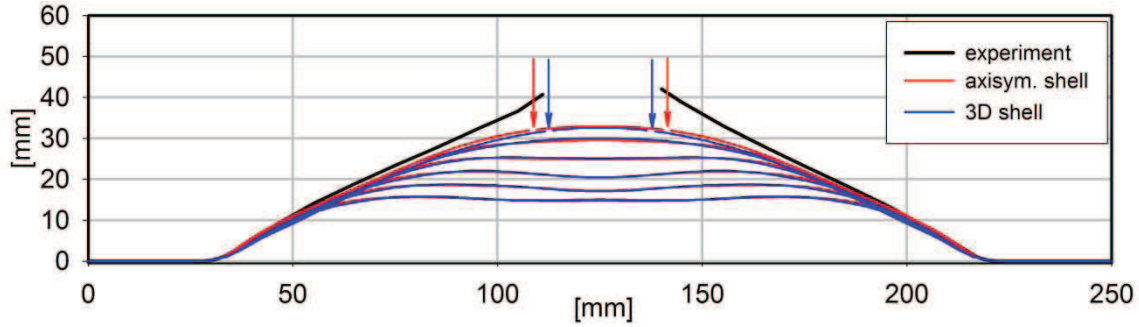

Fig. 8-18. Dynamic analysis – test 05_3, time steps: t_1 = 0.2 ms, t_2 = 0.22 ms, t_3 = 0.24 ms, t_4 = 0.26 ms, t_5 = 0.28 ms, t_6 = 0.29 ms

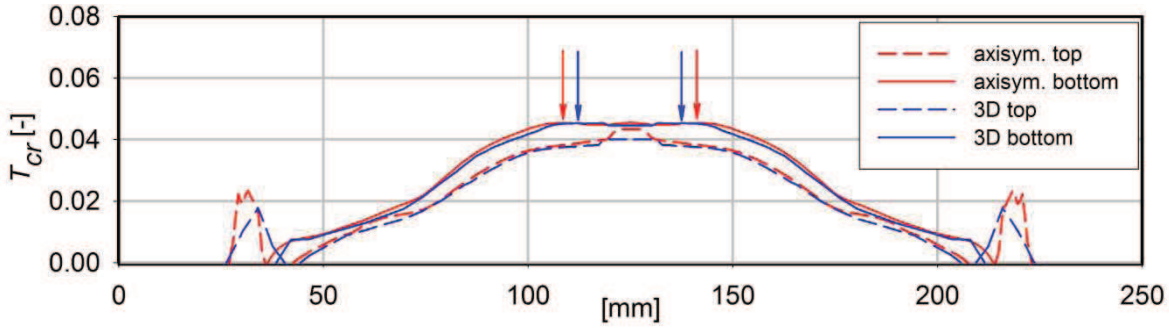

Fig. 8-19. Stress triaxiality dependency criterion parameter in the plate's cross-section in the fracture moment, t = 0.29 ms, uncoupled study, test 05_3

Model	Test	Exp.	1/5 layer		3/5 layers		5/5 layers	
		d [mm]	*d* [mm]	error [%]	*d* [mm]	error [%]	*d* [mm]	error [%]
2-D shell	05_3	30.8	24.8	19.5	-		-	
axisym. shell			33.6	9.1	-		-	
Difference	[%]		30.1		-		-	

Tab. 8-1. Results of uncoupled fracture study, stress triaxiality dependency criterion, test 05_3

The numerical simulation results of tests 06_1 and 07_1 with "1/5 layer" approach are presented in Fig. 8-20 and Fig. 8-23. In both cases the cracks obtained in the analyses using mesh C characterize strong influence of the mesh geometry, but generally the solutions are comparable with mesh D. The six selected time steps deflections and the criterion parameter in the fracture moment for the mesh D analyses are presented in Fig. 8-21, Fig. 8-22 (test 06_1) and Fig. 8-24, Fig. 8-25 (test 07_1). All results including "3/5 layers" and "5/5 layers" approaches are presented in Tab. 8-2 and Tab. 8-3.

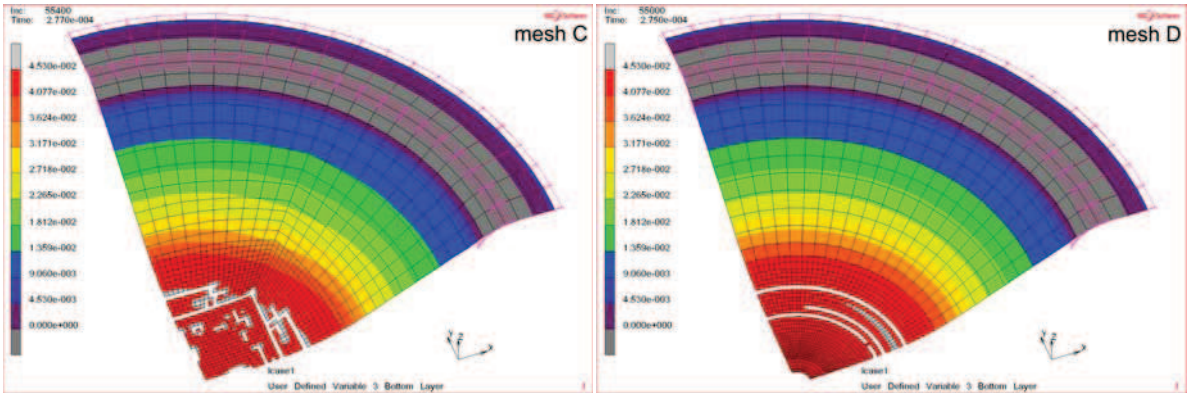

Fig. 8-20. Fracture in uncoupled model with the stress triaxiality dependency criterion, test 06_1

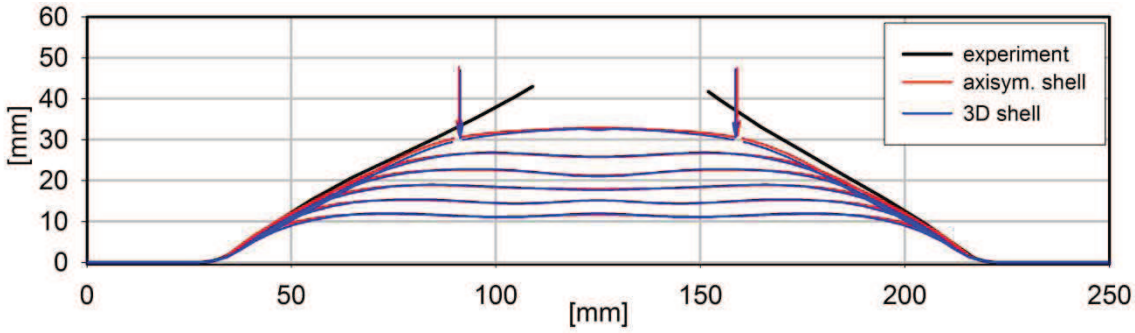

Fig. 8-21. Dynamic analysis – test 06_1, time steps: t_1 = 0.17 ms, t_2 = 0.19 ms, t_3 = 0.21 ms, t_4 = 0.23 ms, t_5 = 0.25 ms, t_6 = 0.27 ms

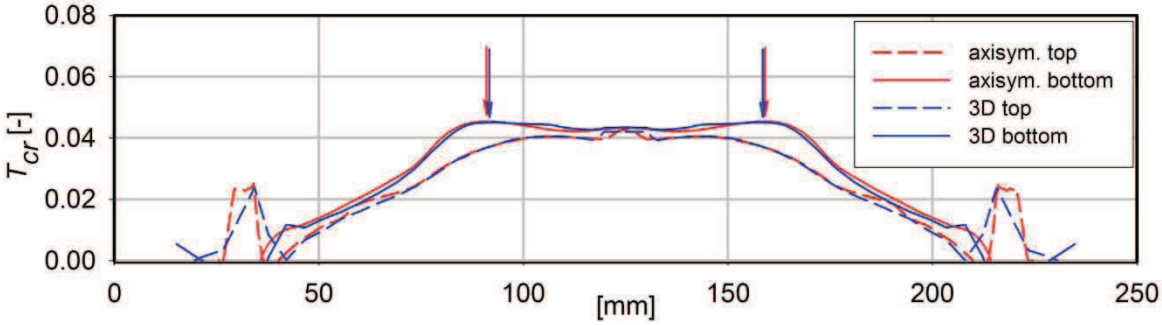

Fig. 8-22. Stress triaxiality dependency criterion parameter in the plate's cross-section in the fracture moment, t = 0.27 ms, uncoupled study, test 06_1

Model	Test	Exp.	1/5 layer		3/5 layers		5/5 layers	
		d [mm]	*d* [mm]	error [%]	*d* [mm]	error [%]	*d* [mm]	error [%]
2-D shell	06_1	45.2	68.8	52.2	40.7	10.0	35.2	33.0
axisym. shell			69.0	52.7	43.8	3.1	31.0	31.4
Difference	[%]		0.3		7.3		12.7	

Tab. 8-2. Results of uncoupled fracture study, stress triaxiality dependency criterion, test 06_1

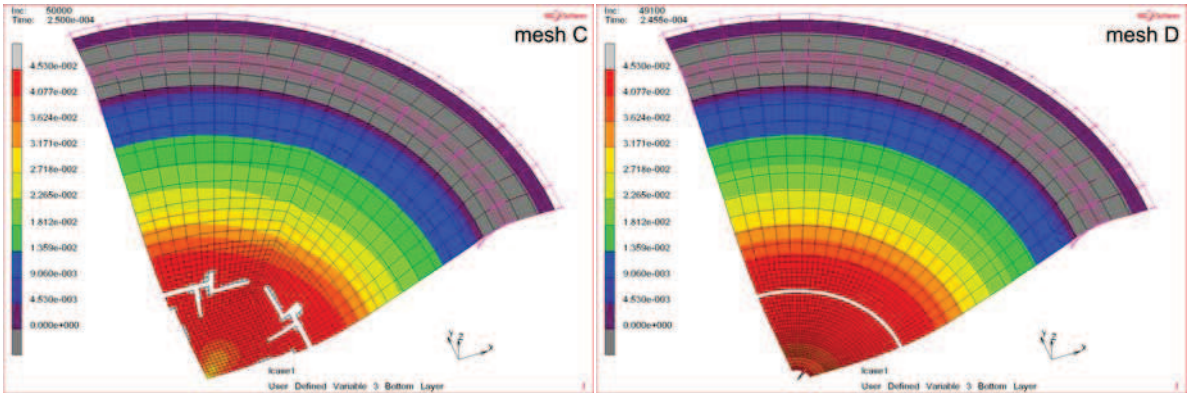

Fig. 8-23. Fracture in uncoupled model with the stress triaxiality dependency criterion, test 07_1

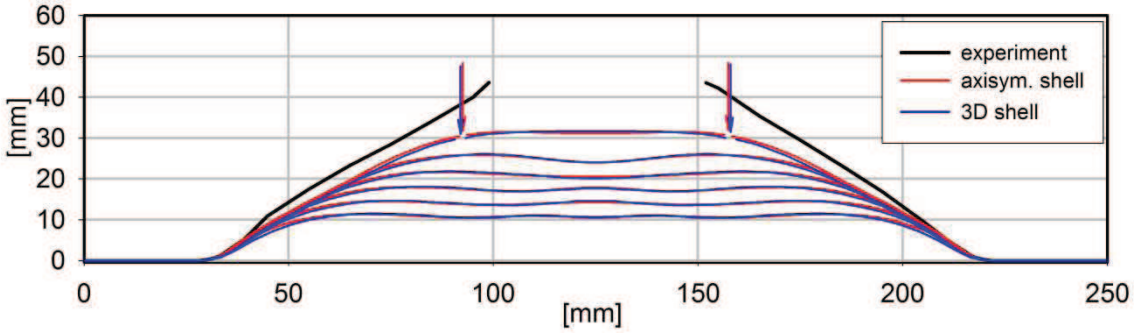

Fig. 8-24. Dynamic analysis – test 07_1, time steps: t_1 = 0.14 ms, t_2 = 0.16 ms, t_3 = 0.18 ms, t_4 = 0.2 ms, t_5 = 0.22 ms, t_6 = 0.24 ms

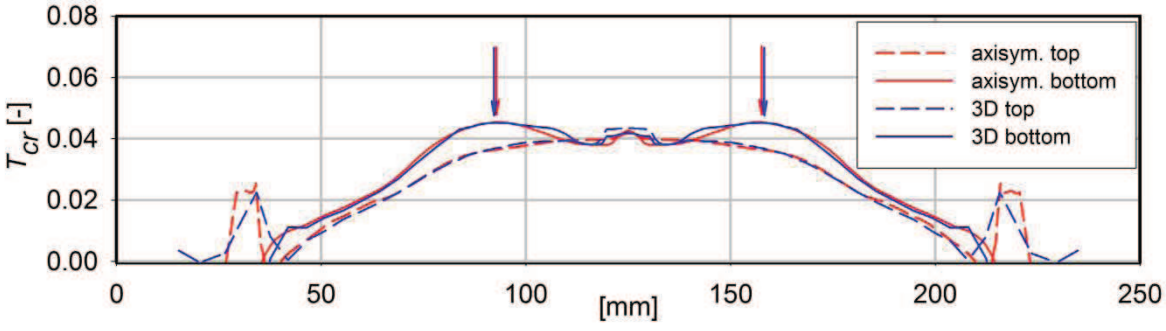

Fig. 8-25. Stress triaxiality dependency criterion parameter in the plate's cross-section in the fracture moment, t = 0.24 ms, uncoupled study, test 07_1

Model	Test	Exp.	1/5 layer		3/5 layers		5/5 layers	
		d [mm]	*d* [mm]	error [%]	*d* [mm]	error [%]	*d* [mm]	error [%]
2-D shell	07_1	58.7	66.0	12.4	49.6	15.5	42.6	27.4
axisym. shell			64.0	9.0	51.4	12.4	33.6	42.8
Difference	[%]		3.1		3.6		23.6	

Tab. 8-3. Results of uncoupled fracture study, stress triaxiality dependency criterion, test 07_1

Generally, in the considered uncouple approach with the stress triaxiality dependency criterion, the results (hole diameters *d*) obtained in the 2-D and axisymmetrical shell studies are similar. The presented dynamic analyses showing the following stages of plate's deflections and the plots of criterion parameter in the fracture moment exhibit small differences between these two solutions, but they almost did not influence on the final results – the localization of a crack.

8.5.2. Coupled analyses – damage second approach effects

The next considered analysis is the coupled study, where the damage second approach effects are taken into account. Also here, the calculations have been performed using both type of meshing – C and D. At first, the critical damage condition, as the fracture criterion, is used. The results of numerical simulations for all analyzed tests, where the deactivation is applied according to "1/5 layer" approach, are presented in Fig. 8-26, Fig. 8-29 and Fig. 8-32. The solutions obtained for both meshes are comparable, although for the higher impacts the crack shape is quite fuzzy. In contrary to the previous uncoupled analysis the results differ much more in comparison to axisymmetrical study. The difference is higher when the stronger impact is considered. The detailed results for each test are given in Tab. 8-4, Tab. 8-5 and Tab. 8-6. The obtained hole diameters seem to be independent from the loading conditions, for each analysis the result is close to $d = 30$ mm. Comparing the analyses presented in Fig. 8-27, Fig. 8-30 and Fig. 8-33 with the analogical one in uncoupled study it can be noticed that the fracture in the present solutions occurs later. For example in test 07_1 in the previous approach the crack occurred at time $t = 0.24$ ms while in the present study at time $t = 0.26$ ms. During deformation process the plate's geometry turns into the dome-like shape. This causes that the little differences obtained in axisymmetrical and 2-D shell analyses (the plate modelled by 2-D shell elements is a bit stiffer) have higher influence on the final solutions. For each test, the damage variable at the fracture moments is presented in Fig. 8-28, Fig. 8-31 and Fig. 8-34.

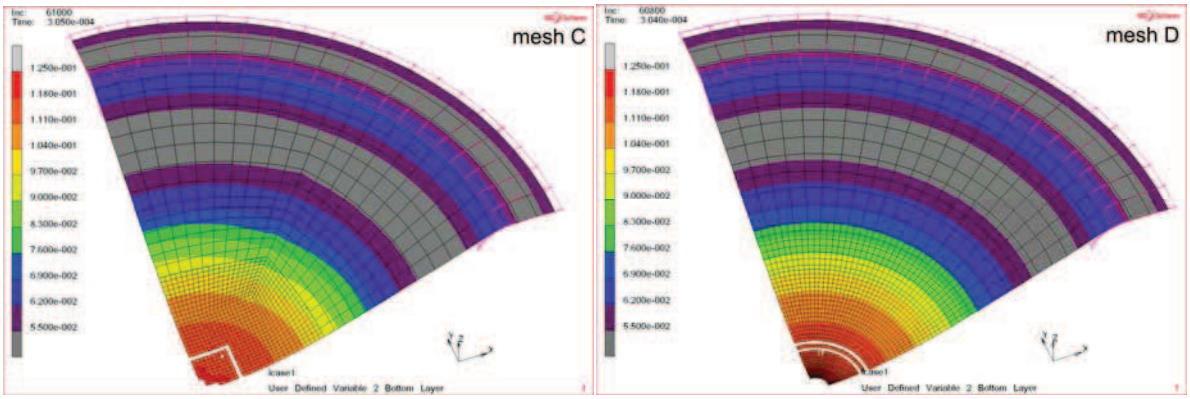

Fig. 8-26. Fracture in coupled model with the critical damage criterion, test 05_3

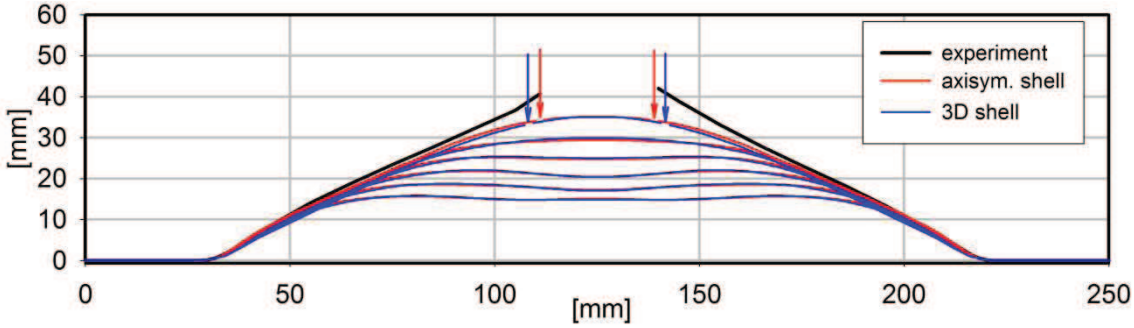

Fig. 8-27. Dynamic analysis – test 05_3, time steps: $t_1 = 0.2$ ms, $t_2 = 0.22$ ms, $t_3 = 0.24$ ms, $t_4 = 0.26$ ms, $t_5 = 0.28$ ms, $t_6 = 0.3$ ms

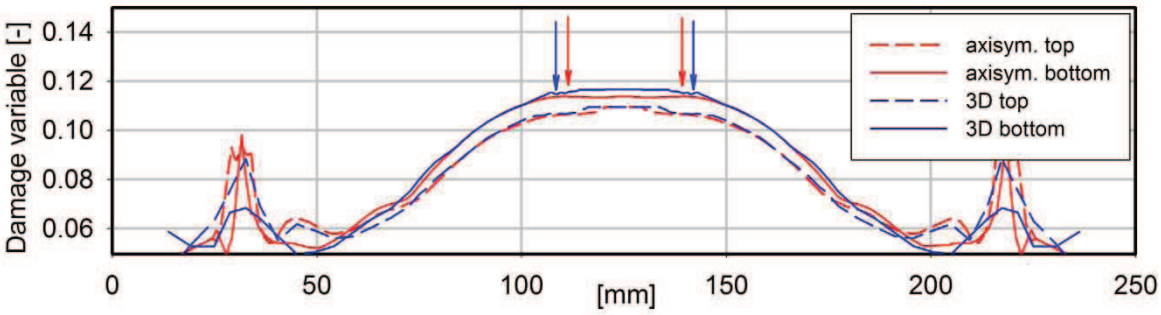

Fig. 8-28. Damage variable in the plate's cross-section in the fracture moment, t = 0.3 ms, coupled study, test 05_3

Model	Test	Exp.	1/5 layer		3/5 layers		5/5 layers	
		d [mm]	*d* [mm]	error [%]	*d* [mm]	error [%]	*d* [mm]	error [%]
2-D shell	05_3	30.8	33.4	8.4	25.4	17.5	-	
axisym. shell			28.6	7.1	35.8	16.2	33.2	7.8
Difference	[%]		15.5		34.0		-	

Tab. 8-4. Results of coupled fracture study, critical damage criterion, test 05_3

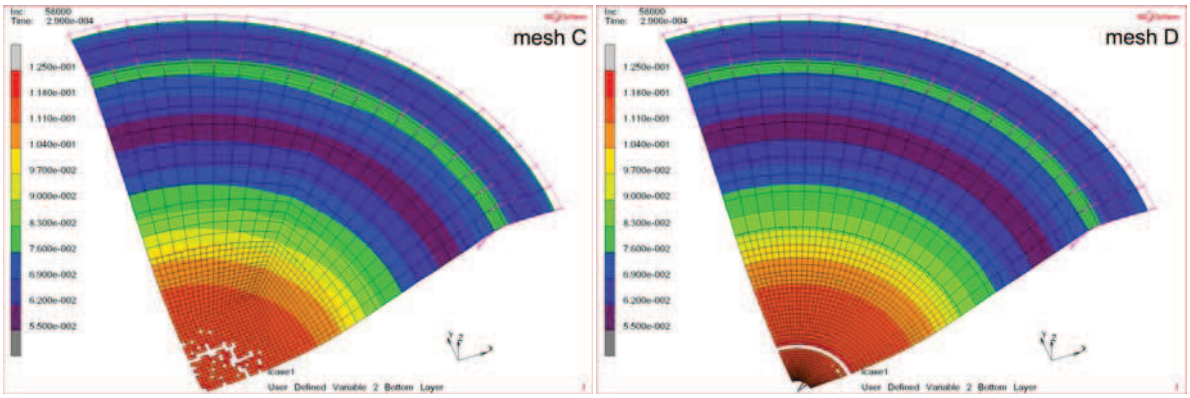

Fig. 8-29. Fracture in coupled model with the critical damage criterion, test 06_1

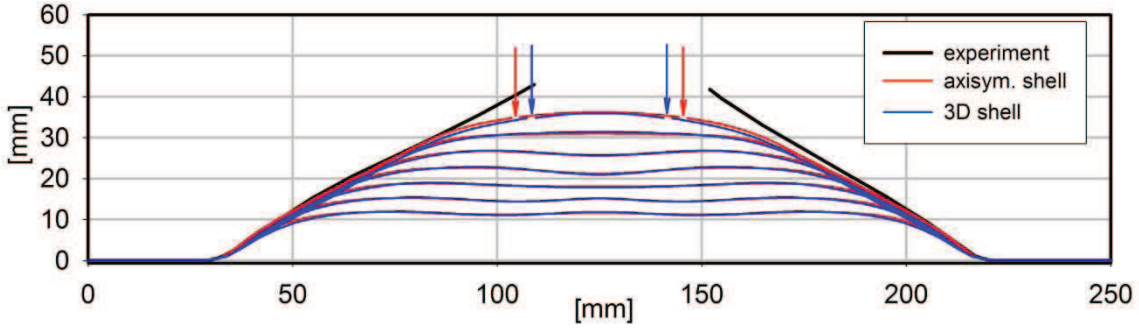

Fig. 8-30. Dynamic analysis – test 06_1, time steps: t_1 = 0.17 ms, t_2 = 0.19 ms, t_3 = 0.21 ms, t_4 = 0.23 ms, t_5 = 0.25 ms, t_6 = 0.27 ms, t_6 = 0.29 ms

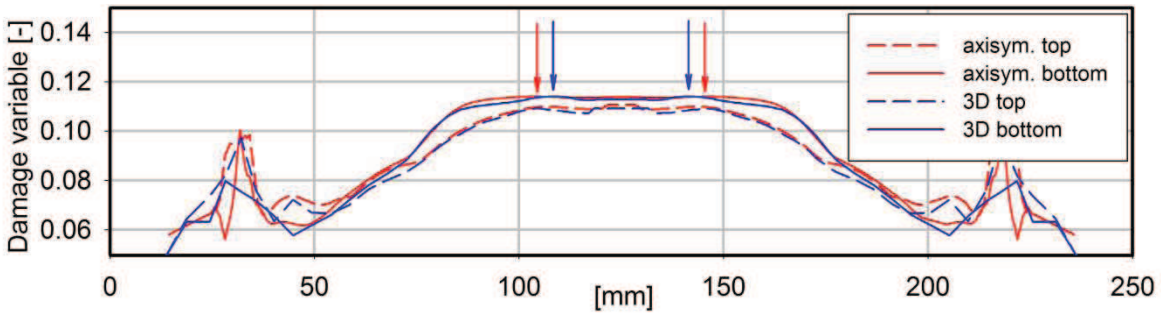

Fig. 8-31. Damage variable in the plate's cross-section in the fracture moment, t = 0.29 ms, coupled study, test 06_1

Model	Test	Exp.	1/5 layer		3/5 layers		5/5 layers	
		d [mm]	*d* [mm]	error [%]	*d* [mm]	error [%]	*d* [mm]	error [%]
2-D shell	06_1	45.2	33.4	26.1	32.4	28.3	36.8	18.6
axisym. shell			41.8	7.5	36.8	18.6	33.0	27.0
Difference	[%]		22.3		12.7		10.9	

Tab. 8-5. Results of coupled fracture study, critical damage criterion, test 06_1

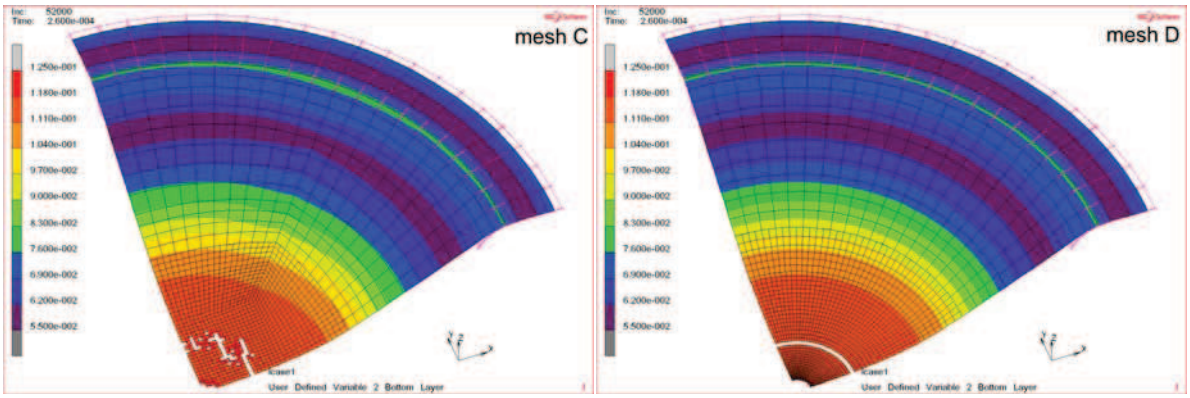

Fig. 8-32. Fracture in coupled model with the critical damage criterion, test 07_1

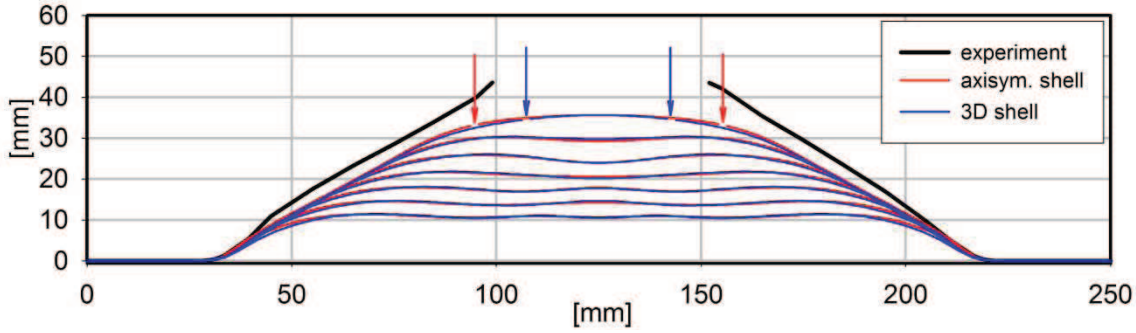

Fig. 8-33. Dynamic analysis – test 07_1, time steps: t_1 = 0.14 ms, t_2 = 0.16 ms, t_3 = 0.18 ms, t_4 = 0.2 ms, t_5 = 0.22 ms, t_6 = 0.24 ms, t_7 = 0.26 ms

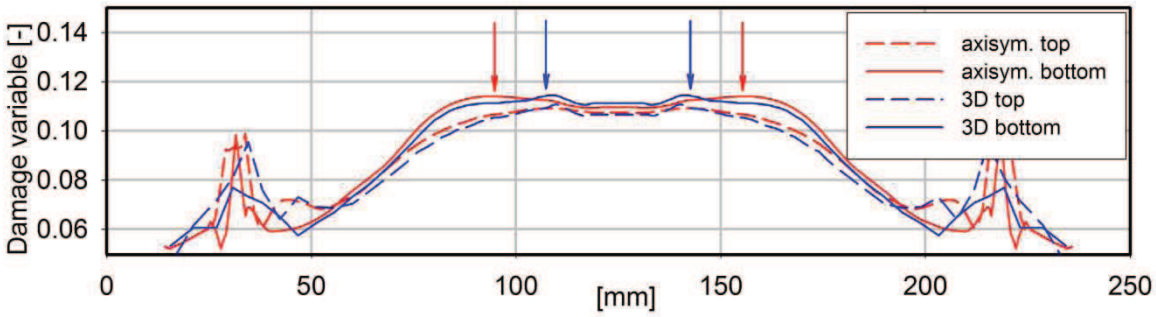

Fig. 8-34. Damage variable in the plate's cross-section in the fracture moment, t = 0.26 ms, uncoupled study, test 07_1

Model	Test	Exp.	1/5 layer		3/5 layers		5/5 layers	
		d [mm]	*d* [mm]	error [%]	*d* [mm]	error [%]	*d* [mm]	error [%]
2-D shell	07_1	58.7	35.4	39.7	30.2	48.6	32.4	44.8
axisym. shell			61.0	3.9	43.2	26.4	33.0	43.8
Difference	[%]		53.1		35.4		1.8	

Tab. 8-6. Results of coupled fracture study, critical damage criterion, test 07_1

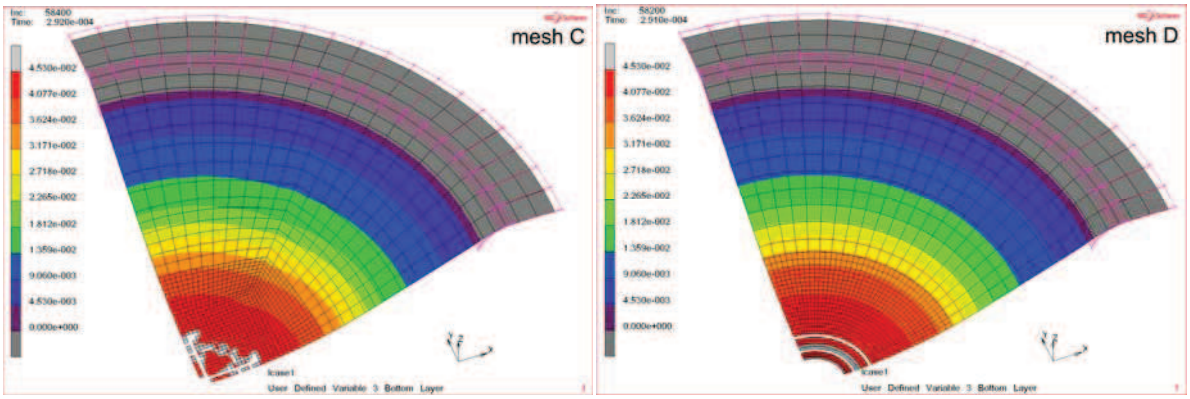

Fig. 8-35. Fracture in coupled model with the stress triaxiality dependency criterion, test 05_3

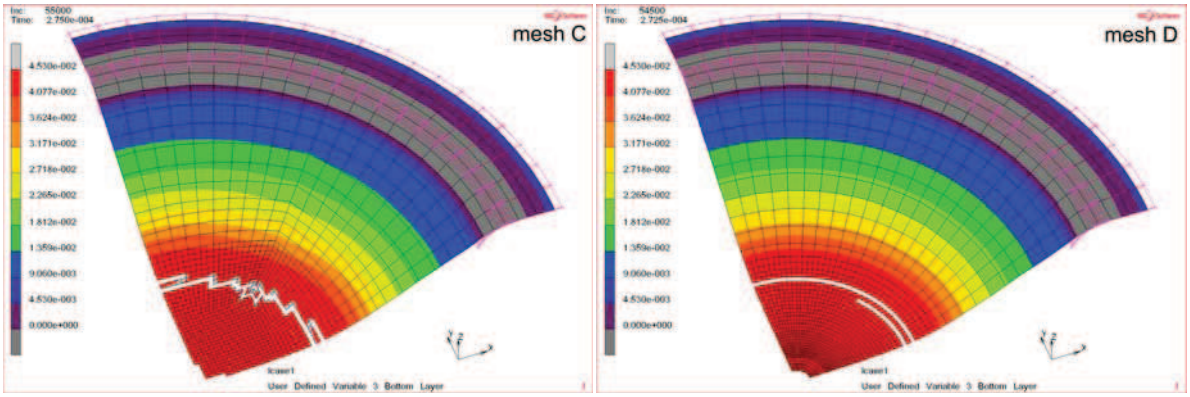

Fig. 8-36. Fracture in coupled model with the stress triaxiality dependency criterion, test 06_1

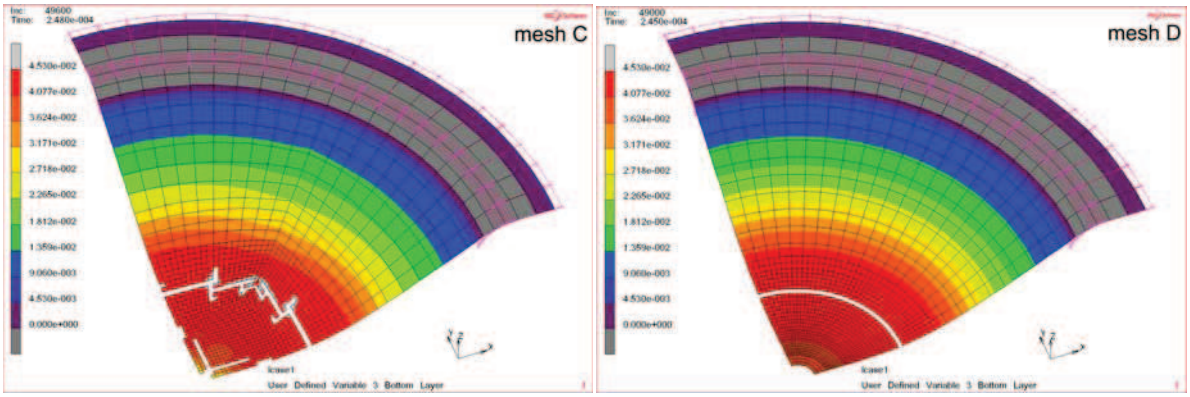

Fig. 8-37. Fracture in coupled model with the stress triaxiality dependency criterion, test 07_1

For the third type of analysis the coupled approach is used with the stress triaxiality dependency criterion (originally from the uncoupled study). In such case, the differences between axisymmetrical and 2-D shell studies significantly decreased. The value of this criterion parameter increases faster, thereby the crack occurs earlier, just as it has been observed in the uncoupled analysis. The results presenting the fracture obtained in calculations with mesh C and D, where the deactivation is applied according to "1/5 layer"

approach, are shown in Fig. 8-35, Fig. 8-36 and Fig. 8-37. The hole diameters d taken from all simulations are given in Tab. 8-7.

Model	Test	Exp.	1/5 layer		3/5 layers		5/5 layers	
		d [mm]	d [mm]	error [%]	d [mm]	error [%]	d [mm]	error [%]
2-D shell	05_3	30.8	34.8	13.0	23.2	24.7	-	
axisym. shell			38.6	25.3	28.2	8.4	-	
Difference	[%]		10.4		16.9		-	
2-D shell	06_1	45.2	74.0	63.7	45.1	0.2	37.4	17.3
axisym. shell			71.6	58.4	46.4	2.7	38.8	14.2
Difference	[%]		3.3		2.8		3.7	
2-D shell	07_1	58.7	65.9	12.3	47.8	18.6	28.8	50.9
axisym. shell			66.6	13.5	61.8	5.3	33.6	42.8
Difference	[%]		1.1		25.5		15.4	

Tab. 8-7. Results of coupled fracture study, stress triaxiality dependency criterion, tests 05_3, 06_1, 07_1

8.6. Investigation of mesh density influence – model with fracture

The last analysis considered the influence of mesh density on the localization of crack occurrence. The investigation has been performed for D-type of meshing. The old and new finite element division is presented in Fig. 8-38. The number of elements has increased from 680 to 840. The densification is mainly applied close the area of possible crack initiation.

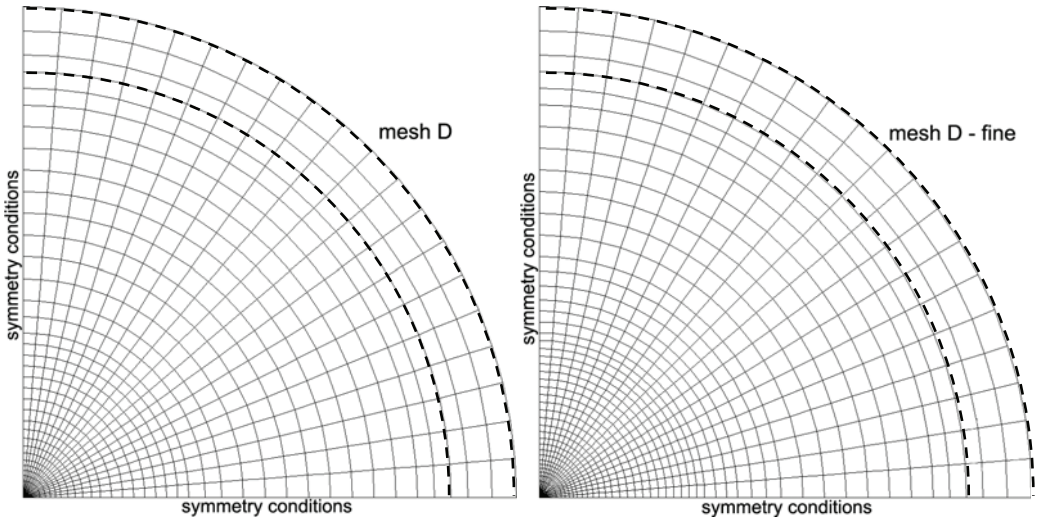

Fig. 8-38. Mesh D before and after the densification of elements

The investigation is limited to two tests 05_3 and 06_1. For each, three different analyses are performed: uncoupled with the stress triaxiality dependency criterion, coupled with the critical damage and the stress triaxiality dependency criteria. In all cases, the elements have been deactivated according to "1/5 layer" approach. The results are presented in Fig. 8-39 and Fig. 8-40 (particular solutions are shown in the analyses order given above). The obtained hole diameters are given and compared in Tab. 8-8.

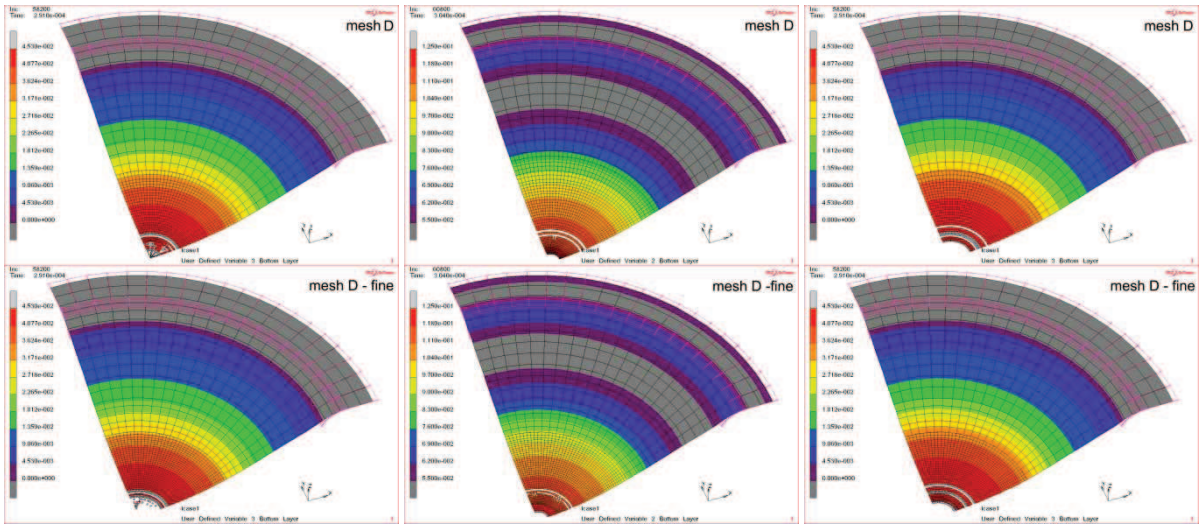

Fig. 8-39. Investigation of mesh dense influence, test 05_3

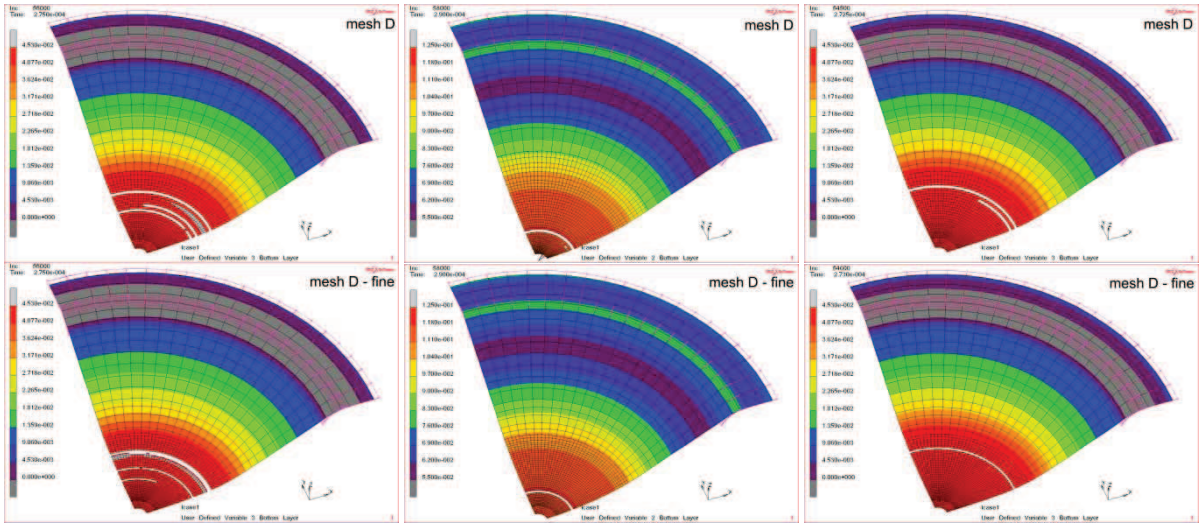

Fig. 8-40. Investigation of mesh dense influence, test 06_1

The results obtained in the analyses with both meshes (mesh D and mesh D – fine) are almost identical. The maximum differences do not exceed 5%. It shows that the sensitiveness of solutions due to the density of mesh is very low.

Model	Test	first analysis 1/5 layer	second analysis 1/5 layer	third analysis 1/5 layer
		d [mm]	*d* [mm]	*d* [mm]
mesh D	05_3	24.8	33.4	34.8
mesh D - fine		25.9	32.4	33.2
Difference	[%]	**4.2**	**3.1**	**4.8**
mesh D	06_1	68.8	32.4	74.0
mesh D - fine		68	32.6	71.8
Difference	[%]	**1.2**	**1.5**	**3.1**

Tab. 8-8. Hole diameters in the investigation of mesh dense influence, tests 05_3 and 06_1

8.7. Summary

The presented chapter contains the study in the fracture prediction in the 2-D shell model. In the analyses, the plate's quarter model has been investigated. The boundary conditions have been applied according to those which have been determined in Chapter 7. In the numerical simulations two different meshes have been used. The study is limited to the approaches, which gave the most reliable solutions for the previous axisymmetrical analyses and to three example tests 05_3, 06_1 and 07_1. The results have shown that the expansion of model to two dimensional case not always leads to the same results. The coupled approach with its original critical damage criterion, in the considered simulations, gives the solutions, which differs from the previous analysis ones. The obtained hole diameters do not depend on the loading conditions (the impulse strength). The second applied stress triaxiality dependency criterion in both analyses (uncoupled and coupled) gives much better results. The solutions are very close to those, which have been presented in Chapter 7. The investigation of shell density influence shows that this study is not very sensitive for this kind of problem.

9. Final summary and conclusions

The presented work considers the investigation of plate-shell structures response due to impact loadings caused by gas mixture explosions. The investigation has been stated in the first chapter, where the main field of interest (aim and range) has been established and the area of potential applications has been specified. This chapter also contains the literature review concerning the area of different approaches to failure designing. As it has been shown, the problem has been investigated since early 1920s and up to now is still in the high interest of many researchers. The overview includes different theories, different approaches to numerical modelling and the historical survey of the scientists' activities in the research concerning the plates' response to dynamic loadings.

The more precise description of theoretical foundations in the considered problem has been presented in Chapter 2. At first, the appropriate constitutive law has been specified. The investigated plates have been submitted to large plastic deformations and fracture. From the two natural classes of large deformation problems, here the large displacement – small strain analysis has been chosen. Additionally, the assumption of material's isotropy has been introduced. This approach has been often used in the shock wave-loaded plates' numerical simulations performed by many authors. It allows applying the viscoplastic model proposed by Chaboche, based on the strain rate additive decomposition. This constitutive law has been chosen by the author, suggested by the earlier experiences and successful implementations by Kłosowski, Woznica and Stoffel ([96], [195], [196], [162], [163]). Such law selection has been also determined by the good recognition in the material parameters identification. It is the first step in the model development. In the future, extension to the class of large strain and material's anisotropy problems is planned. It will be linked with section and implementation of new constitutive laws and the new identification rocedures of the material parameters.

The latter part of the second chapter contains the description of damage and fracture models. The theories, which are nowadays the most popular, have been described. Also the models and fracture criteria for the further analyses have been selected. The chosen approaches give the possibility of modelling crack initiation and propagation. The models in which the evolution of a pre-existing crack is only considered have been rejected. In the work, the problem of crack localisation is investigated and initialisation of the crack must be found by algorithm itself.

In Chapter 3 the numerical tools, used in all realized finite element method simulations, have been presented. For the dynamic, geometrically and materially non-linear analyses three different element types have been selected. The updated Lagrangian approach, used in MSC.Marc software in the large displacement analyses, has been described. In detail, the user-defined subroutines, used in the performed simulations, have been presented. The descriptions of the chosen integration method for the motion equation and the features such as the contact phenomena and the adaptive mesh have also been attached.

The fourth chapter contains the description of all experimental tests carried out during the realization of this work. Two types of laboratory tests have been executed. The first are the experiments on plates. Their results have been used as the testing material in the model's fixing boundary conditions calibration and for the verification of results obtained in the main fracture prediction numerical simulations. The second are the uniaxial experiments. Their results have been used for the identification of model's material parameters.

The material parameters identification is the main subject of the next chapter. At first, the estimations of elastic modulus and yield stress have been presented. In each case the values have been identified using the results of experiments performed for the specimens cut along and across sheet's rolling. The difference between the obtained parameters for two orthogonal directions is 2 % for the elastic modulus and 8 % for the yield stress. Therefore, the assumption of material's isotropy is justified and the final parameters have been taken as the mean values. The results of hardening parameters identification performed later shows much higher differences. However, calculating of the mean values in this case has also been possible, due to the fact of low sensitivity in the model's answer to changes of these parameters observed in the verification process. The considered material has shown very weak viscous properties. It has caused problems in the identification of parameters controlling viscosity in the model. Despite of this difficulty, the author has decided to keep the chosen constitutive law. It gives higher universality of the model in possible analyses with different materials or for higher temperatures. The necessary values of viscosity parameters have been finally taken from the literature as the first approximation. As it has been presented in the final verification, all these treatments leads to the correct values, reaching very high correlation in the comparison analyses (numerical model vs. experiment). In the second part of this chapter the identification of the damage and its model parameters have been presented. The main difficulty, which has been encountered in this analysis, is the lack of current transversal area measurement in the specimen during the laboratory tests. Two different approaches have been proposed to overcome this problem. Therefore, two separate identifications have been

presented. After each, the appropriate verifications have confirmed correctness of the estimations.

The next chapter contains the description of fracture criteria calibration. In each chosen for the further analyses condition, the critical parameter has been identified. This procedure has been based on the results of experiments and numerical simulations.

Two following chapters present the numerical study of the considered problem. At first, the determination of plate's fixing boundary conditions has turned out to be necessary. The basic hinged or clamped supports have underrated the values of maximum middle point deflections in all analyzed simulations. After the extensive study, the conditions, which have assured the best correlation between the results of numerical analyses and experiments in all applied impact strength levels, have been accepted. The problem of fixing conditions in the considered experiments will be continued in the author's further scientific research. One of the new ideas is to develop the existing plate's mounting in the experimental tube by adding additional elements and thereby reaching clearer fixing of the plate specimens.

The numerical study has been performed for two types of analyses: the axisymmetrical shell and the 2-D shell models. At first, for both the investigation of mesh density influence in the study without fracture have been applied. Additionally in the 2-D case, for the chosen types of meshing, the symmetry of the solution has been successfully checked. The full study containing all chosen models and fracture criteria has been performed using the axisymmetrical model (1-D model). Additionally, the deactivation of elements with three different conditions: "1/5 layer", "3/5 layers" and "5/5 layers" has been investigated. After the summary of all obtained results, the most reliable approaches have been selected. It is the uncoupled analysis (no damage effects) with the stress triaxiality dependency criterion, and the coupled (damage second approach effects) analysis with two different criteria based on the critical damage and the stress triaxiality dependency. The 2-D shell study has been limited to the analysis with the selected above approaches. For each, three example tests have been investigated: 05_3, 06_1 and 07_1. The obtained solutions have shown that the expansion of model to two dimensional case does not always lead to the same results.

After both: axisymmetrical and 2D shell studies, the investigation of mesh density influence for the study, where the fracture is considered, has been carried out. The local approach, which is applied in presented simulations, often causes problems in the finite element method. It leads to the pathological localization and the mesh dependence associated with materials softening. In the considered analyses such effect has not occurred. All performed investigations have shown the weak dependence of mesh size in the transient

response. The analogical conclusions have been drawn by Børovik et al. [33] or Lee and Wierzbicki [107]. This positive effect might be caused by using in all this analyses shell elements, which are always divided into the specified number of layers and thereby integrated over the thickness. However, the non-local models and the regularization techniques are in the author's high interest and will be investigated in the further research.

The main conclusions, which have been finally drawn, are:

- The presented study belongs to the large displacement – small strain class of large deformation problems. It allows implementation of the constitutive laws based on the strain rate additive decomposition. The presented investigation (encouraged by successful verifications) has shown that such approach is also possible in the damage analyses, but of course the extension to large strain models is planned.
- The assumption of material's isotropy (constitutive and damage models) in the considered study have not caused obtaining the adverse solutions. The investigated aluminium has shown, during the material parameters identification procedure, small orthotropic properties. The implementation of anisotropy to the model is considered as the further development.
- In the considered model, the viscoplastic constitutive law is applied in spite of the investigated material's weak viscous properties. It gives higher universality of the model in the possible further analyses.
- After the elaboration of experimental results, the axisymmetry of model has been assumed. It has been observed that the initial shape of the specimens (they have been prepared as a square plates) has not influenced on the plates' deflections during the experiments.
- The boundary conditions have played a key role in the investigated analysis. The special process of its determination has been applied. The simple supports (hinged or clamped) have not assured the adequate plate's answer in the analyses. The development of fixing conditions in the research stand is planned for the future.
- The numerical simulations have been performed using the axisymmetrical and the 2D shell elements. Such analyses as considered should be performed with a high accuracy. As it has been turned out the results are not always identical. The axisymmetrical elements have proved better usability in the analyzed calculations. They are much less time consuming and thanks to them, much denser discretization of the model can be applied.

- The study includes four different criteria in three approaches and three conditions of elements' deactivation. The best solutions have been pointed (uncoupled analysis with the stress triaxiality dependency criterion and the coupled analysis with the critical damage and the stress triaxiality dependency criteria).
- After each analysis, the mesh density influence has been investigated. Very weak influence has been stated in the applied simulations. The development of model to non-local approach is considered in the further studies.

This work has shown that the numerical investigation of plate-shell structures response due to impact loadings may lead to the results, which are in the high correlation with the experiments. Maybe it does not give the evident answer which considered approach is the only correct one, but gives the field to discussion and the direction to the further analysis in the ductile fracture prediction.

References

[1] Abdelaziz Y., Hamouine A.: A survey of the extended finite element. *Computers and Structures*, 86 (2008), 1141-1151.

[2] Addessi D., Marfia S., Sacco E.: A plastic nonlocal damage model. *Computer Methods in Applied Mechanics and Engineering*, 191 (2002), 1291-1310.

[3] Allen D.H.: Homogenization principles and their application to continuum damage mechanics. *Compost Science and Technology*, 61 (2001), 2223-2230.

[4] Alves M., Yu J., Jones N.: On the elastic modulus degradation in continuum damage mechanics. *Computers and Structures*, 76 (2000), 703-712.

[5] Amar G., Dufailly J.: Identification and validation of viscoplastic and damage constitutive equations. *European Journal of Mechanics A/Solids*, 12 (1993), 197–218.

[6] Ambroziak A.: Identification and validation of damage parameters for elasto-viscoplastic Chaboche model. *Engineering Transactions*, 55 (2007), 3-28.

[7] Anderson T.,L.: *Fracture mechanics. Fundamentals and applications.* CRC Press Taylor & Francis Group, USA 2005.

[8] Andersson H., Persson C., Hansson T.: Crack growth in IN718 at high temperature. *International Journal of Fracture*, 23 (2001), 817–827.

[9] Armero F., Oller S.: A general framework for continuum damage models. I. Infinitesimal plastic damage models in stress space. *International Journal of Solids and Structures*, 37 (2000), 7409-7436.

[10] Atkins A.G.: Possible explanation for unexpected departures in hydrostatic tension-fracture strain relations. *Metal Science*, 15 (1981), 81-83.

[11] Babuška I., Melenk J.M.: The partition of unity method. *International Journal of Numerical Methods in Engineering*, 40 (1997), 727-758.

[12] Bai Y., Wierzbicki T.: Application of extended Mohr–Coulomb criterion to ductile fracture. *International Journal of Fracture*, 161 (2010), 1–20.

[13] Bao Y.: *Prediction of ductile crack formation in uncracked bodies.* PhD Thesis, Massachusetts Institute of Technology, Cambridge, 2003.

[14] Bao Y., Wierzbicki T.: A comparative study on various ductile crack formation criteria. *Journal of Engineering Materials and Technology*, 126 (2004), 314-324.

[15] Bao Y., Wierzbicki T.: On fracture locus in the equivalent strain and stress triaxiality space. *International Journal of Mechanical Sciences*, 46 (2004), 81-98.

[16] Barenblatt G.I.: On the equilibrium cracks, formed in brittle fracture. *Journal of Applied Mathematics and Mechanics*, 23 (1959), 434-444.

[17] Barenblatt G.I.: The mathematical theory of equilibrium of cracks in brittle fracture. *Advances in Applied Mechanics*, 7 (1962), 55-129.

[18] Bathe K-J., Ramm E., Wilson E.: Finite element formulation for large deformation dynamic analysis. *International Journal of Numerical Methods in Engineering*, 9 (1975), 353-386.

[19] Belytschko T., Black T.: Elastic crack growth in finite elements with minimal remeshing. *International Journal for Numerical Methods in Engineering*, 45 (1999), 601-620.

[20] Belytschko T., Gracie R.: On XFEM applications to dislocations and interface. *International Journal of Plasticity*, 23 (2007), 1721-1738.

[21] Belytschko T., Lu Y.Y.: Element-free Galerkin methods for static and dynamic fracture. *International Journal of Solids and Structures*, 32 (1995), 2547-2570.

[22] Benvenuti E.: A regularized XFEM framework for embedded cohesive interfaces. *Computer Methods in Applied Mechanics and Engineering*, 197 (2008), 4367-4378.

[23] Benzerga A.A., Besson J., Pineau A.: Coalescence-controlled anisotropic ductile fracture. *Journal of Engineering Materials and Technology*, 121 (1999), 221-229.

[24] Besson J., Abouaf M.: Rheology of porous alumina and simulation of hot isotropic pressing. *Journal of the American Ceramic Society*, 75 (1992), 2165-2172.

[25] Besson J., Steglich D., Brocks W.: Modeling of crack growth in round bars and plane strain specimens. *International Journal of Solids and Structures*, 38 (2001), 8259-8284.

[26] Bodner S.R., Symonds P.S.: Experiments on viscoplastic response of circular plates to impulsive loading. *Journal of the Mechanics and Physics of Solids*, 27 (1979), 91–113.

[27] Bonfoh N., Lipinski P., Carmasol A., Tiem S.: Micromechanical modeling of ductile damage of polycrystalline materials with heterogeneous particles. *International Journal of Plasticity*, 20 (2004), 85–106.

[28] Bonora N.: A nonlinear CDM model for ductile failure. *Engineering Fracture Mechanics*, 58 (1997), 11-28.

[29] Bonora N., Gentile D., Pirondi A., Newaz G.: Ductile damage evolution under triaxial state of stress: theory and experiments. *International Journal of Plasticity*, 21 (2005), 981-1007.

[30] Bordas S., Rabczuk T., Zi G.: Three-dimensional crack initiation, propagation, branching and junction in non-linear materials by an extended meshfree method without asymptotic enrichment. *Engineering Fracture Mechanics*, 75 (2008), 943-960.

[31] Borouchaki H., Cherouay A., Laug P., Saanouni K.: Adaptive remeshing for ductile fracture prediction in metal forming. *Comptes Rendus Mecanique*, 330 (2002), 709-716.

[32] Børovik T., Hopperstad O.S., Berstad T.: On the influence of stress triaxiality and strain rate on the behaviour of a structural steel. Part II. Numerical study. *European Journal of Mechanics A/Solids*, 22 (2003), 15-32.

[33] Børovik T., Hopperstad O.S., Berstad T., Langseth M.: Perforation of 12 mm thick steel plates by 20 mm diameter projectiles with flat, hemispherical and conical noses. Part II: numerical simulations. *International Journal of Impact Engineering*, 27 (2002), 37-64.

[34] Bouchard P.O., Bay F., Chastel Y.: Numerical modelling of crack propagation: automatic remeshing and comparison of different criteria. *Computer Methods in Applied Mechanics and Engineering*, 192 (2003), 3887-3908.

[35] Bouchard P.O., Bay F., Chastel Y., Tovena I.: Crack propagation modelling using an advanced remeshing technique. *Computer Methods in Applied Mechanics and Engineering*, 189 (2000), 723-742.

[36] Brozzo P., Deluca B., Rendina R.: A new method for the prediction of the formability limits of metals sheets. *Proc.7th Biennial Conf. Int. Deep Drawing Research Group.*

[37] Brünig M.: A framework for large strain elastic-plastic damage mechanics based on metric transformations. *International Journal of Engineering Science*, 39 (2001), 1033-1056.

[38] Carpinteri A., Francesco C., Pugno N.: Boundary element method for the strain-softening response of quasi-brittle materials in compression. *Computers and Structures*, 79 (2001), 389-401.

[39] Celentano D.J., Chaboche J.L.: Experimental and numerical characterization of damage evolution in steels. *International Journal of Plasticity*, 23 (2007), 1739-1762.

[40] Chaboche J.L.: Anisotropic creep damage in the framework of continuum damage mechanics. *Nuclear Engineering and Design*, 79 (1984), 309-319.

[41] Chaboche J.L.: Continuous damage mechanics – A tool to describe phenomena before crack initiation. *Nuclear Engineering and Design*, 64 (1981), 233-247.

[42] Chaboche J.L., Boudifa M., Saanouni K.: A CDM approach of ductile damage with plastic compressibility. *International Journal of Fracture*, 137 (2006), 51–75.

[43] Chaboche J.L., Feyel F., Monerie Y.: Interface debonding models: a viscous regularization with a limited rate dependency. *International Journal of Solids and Structures*, 38 (2001), 3127-3160.

[44] Chandrakanth S., Pandey P.C.: A new ductile damage evolution model. *International Journal of Fracture*, 60 (1993), 73-76.

[45] Chapra S.C., Canale R.P.: *Numerical methods for engineers.* McGraw-Hill Inc., New York 1988.

[46] Chow C.L., Wang J.: An anisotropic theory of continuum damage mechanics for ductile fracture. *Engineering Fracture Mechanics*, 27 (1987), 547–563.

[47] Chróścielewski J., Makowski J., Pietraszkiewicz W.: *Statyka i dynamika powłok wielopłatowych; Nieliniowa teoria i metoda elementów skończonych*. Wydawnictwo Instytutu Podstawowych Problemów Techniki, PAN, Warszawa 2004 (in Polish).

[48] Chung J., Hulbert G.M.: A family of single-step Houbolt time integration algorithms for structural dynamics. *Computer Methods in Applied Mechanics and Engineering*, 118 (1994), 1-11.

[49] Clift S.E., Hartley P., Sturgess C.E., Rowe G.W.: Fracture prediction in plastic deformation processes. *International Journal of Mechanical Sciences*, 32 (1990), 1-17.

[50] Cirak F., Ortiz M., Pandolfi A.: A cohesive approach to thin-shell fracture and fragmentation. *Computer Methods in Applied Mechanics and Engineering*, 194 (2005), 2604-2618.

[51] Cockcroft M.G., Latham D.J.: Ductility and the workability of metals. *Journal Institute of Metals*, 96 (1968), 33-39.

[52] Combescure A., Yin J.: Finite element method for large displacement and large strain elasto-plastic analysis of shell structures and some application of damage mechanics. *Engineering Fracture Mechanics*, 36 (1990), 219-231.

[53] Coulomb C.: Essai sur une application des regles des maximis et minimis a quelues problemes de statique relatifs a l´c6architecture. *Mem Acad Roy des Sci*, 1776 (in French)

[54] Datsko, J.: *Material properties and manufacturing process.* John Wiley & Sons, New York 1966.

[55] Daudonnet B.: *Etude numeriqe de la rapture d'elements de structures constituant des reservoirs sous chargement dynamique.* PhD Thesis, University of Orleans, Bourges, 2006 (in French).

[56] Dey S., Børovik T., Hopperstad O.S., Langseth M.: On the influence of fracture criterion in projectile impact of steel plates. *Computational Materials Science*, 38 (2006), 176-191.

[57] Dhar S., Dixit P.M., Serhuraman R.: A continuum damage mechanics model for ductile fracture. *International Journal of Pressure Vessels and Piping*, 77 (2000), 335-344.

[58] Duffey T.A.: The large deflection dynamic response of clamped circular plates subject to explosive loadings. *Sandia Laboratories Research Report SC-RR-67-532*, (1967).

[59] Duflot M., Nguyen-Dang H.: A meshless method with enriched weight functions for fatigue crack growth. *International Journal for Numerical Methods in Engineering*, 59 (2004), 1945-1961.

[60] Dugdale D.S.: Yielding of steel sheets containing slits. *Journal of the Mechanics and Physics of Solids*, 8 (1960), 100-104.

[61] Edlund U., Volgers P.: A composite ply failure model based on continuum damage mechanics. *Composite Structures*, 65 (2004), 347-355.

[62] Faleskog J., Gao X., Shih C.: Cell model for nonlinear fracture analysis – I. Micromechanics calibration. *International Journal of Fracture*, 89 (1998), 355–373.

[63] Faming L., Zongjin L.: Continuum damage mechanics based modelling of fiber reinforced concrete in tension, *International Journal of Solids and Structures*, 38 (2001), 777-793.

[64] Florence A.L.: Circular plate under a uniformly distributed impulse. *International Journal of Solids and Structures*, 2 (1966), 37–47.

[65] Flórez-López J.: Frame analysis and continuum damage mechanics. *European Journal of Mechanics A/Solids*, 17 (1998), 269-283.

[66] Frangi A.: Fracture propagation in 3D by the symmetric Galerkin boundary element method. *International Journal of Fracture*, 116 (2002), 313–330.

[67] Freudenthal A.M.: *The inelastic behaviour of engineering materials and structures.* John Wiley & Sons, New York 1950.

[68] Gao X., Faleskog J., Shih C.: Cell model for nonlinear fracture analysis – II. Fracture-process calibration and verification. *International Journal of Fracture*, 89 (1998), 375–398.

[69] German J.: *Podstawy mechaniki pękania*. Wydawnictwo Politechniki Krakowskiej, Kraków 2005 (in Polish).

[70] Gologanu M., Leblond J., Devaux J.: Approximate models for ductile metals containing non-spherical voids-Case of axisymmetric prolate ellipsoidal cavities. *Journal of Mechanics and Physics of Solids*, 41 (1993), 1723-1754.

[71] Griffith A.A: The phenomena of rupture and flow in solid. *Philosophical Transactions of the Royal Society*, A221 (1920), 163-197.

[72] Griffith A.A: The theory of rupture. *Proceedings of the First Pan American Congress of Applied Mechanics*, (1924), 55-63.

[73] Guinea G.V., Planan J., Elices M.: K_I evaluation by the displacement extrapolation technique. *Engineering Fracture Mechanics*, 66 (2000), 243-255.

[74] Gurson A.L.: Continuum theory of ductile rupture by void nucleation and growth: Part I – Yield criteria and flow rules for porous ductile media. *Journal of Engineering Materials and Technology*, 99 (1977), 2-15.

[75] Gurson A.L.: *Plastic flow and fracture behavior of ductile materials incorporating void nucleation, growth and interaction*. Brown University, Ph.D. Thesis.

[76] Hambli R.: Finite element model fracture prediction during sheet-metal blanking processes. *Engineering Fracture Mechanics*, 68 (2001), 365-378.

[77] Hambli R., Badie-Levet D.: Damage and fracture simulation during the extrusion processes. *Computer Methods in Applied Mechanics and Engineering*, 186 (2000), 109-120.

[78] Hancock J.W., Mackenzie A.C.: On the mechanism of ductile fracture in high-strength steels subjected to multiaxial stress states. *Journal of the Mechanics and Physics of Solids*, 24 (1976), 147-169.

[79] Hao S., Liu W.K., Klein P.A., Roaskis A.J.: Modeling and simulation of intersonic crack growth. *International Journal of Solids and Structures*, 41 (2004), 1773-1799.

[80] Hillerborg A., Modeer M., Petersson P.E.: Analysis of Crack Formation and Crack Growth in Concrete by Means of Fracture Mechanics and Finite Elements. *Cement and Concrete Research*, 6 (1976), 773-782.

[81] Huber M. T.: Przyczynek do podstaw teoryi wytrzymałości. *Czasopismo Techniczne. Lwów*, 22 (1904), 81 (in Polish).

[82] Inglis C.E.: Stresses in a plane due to the presence of cracks and sharp corners. *Proc. Institution of Naval Architects*, 60 (1913), 219-241.

[83] Irwin G.R: Analysis of stresses and strain near the end of a crack traversing a plate. *Journal of Applied Mechanics*, 79 (1957) 361-364.

[84] Jacinto A.C., Ambrosini R.D., Danesi R.F.: Experimental and computational analysis of plates under air blast loading. *International Journal of Impact Engineering*, 25 (2001), 927-947.

[85] Johnson G.R., Cook W.H.: Fracture characteristics of three metals subjected to various strains, strain rates, temperatures and pressures. *Engineering Fracture Mechanics*, 21 (1985), 31-48.

[86] Johnson G.R., Holmquist T.J.: *Test data and computational strength and fracture model constants for 23 materials subjected to large strain, high strain rates and high temperature*. Technical Report LA-11463-MS, Los Alamos National Laboratory, 1989.

[87] Jones N.: Impulsive loading of a simply supported rigid-plastic circular plate. *Journal of Applied Mechanics*, 35 (1968), 59-68.

[88] Kachanov L.M.: Time of the rupture process under creep conditions. *IZV Akad. Nauk. S.S.R., Otd. Tekhn. Nauk.*, 8 (1958), 26-31 (in Russian).

[89] Kaji Y., Gu W., Ishihara M., Arai T., Nakamura H.: Development of structural analysis program for non-linear elasticity by continuum damage mechanics. *Nuclear Engineering and Design*, 206 (2001), 1-12.

[90] Kaliske M., Nasdala L., Rothert H.: On damage modelling for elastic and viscoelastic materials at large strain. *Computers and Structures*, 79 (2001), 2133-2141.

[91] Kaplan M.F.: Crack propagation and the fracture of concrete. *Journal of American Concrete Institute*, 58 (1961), 591–610.

[92] Kelly J.M., Wilshaw T.R.: A theoretical and experimental study of projectile impact on clamped circular plates. *Proceedings of the Royal Society*, A306 (1968), 435-447.

[93] Kłosowski P.: *Nieliniowa analiza numeryczna i badania doświadczalne drgań sprężysto-lepkoplastycznych płyt i powłok*. Wydawnictwo Politechniki Gdańskiej, Gdańsk 1999.

[94] Kłosowski P., Pyrzowski Ł., Woznica K.: Methods of material parameters identification for isotropic damage in viscoplastic flow conditions. *Machines Dynamics Problems*, 32(3) (2008), 44-50.

[95] Kłosowski P., Woznica K.: *Nieliniowe lepkoplastyczne prawa konstytutywne w wybranych zastosowaniach analizy konstrukcji*. Wydawnictwo Politechniki Gdańskiej, Gdańsk 2007.

[96] Kłosowski P., Woznica K., Weichert D.: Comparison of numerical modelling and experiments for the dynamic response of circular elasto-viscoplastic. *European Journal of Mechanics A/Solids*, 19 (2000), 343-359.

[97] Kracinovic D.: Continuous damage mechanics revisited: basic concepts and definitions. *Journal of Applied Mechanics*, 52 (1985), 829–834.

[98] Krajcinovic D., Fonseka G.U.: The continuous damage theory of brittle materials. Part 1: General theory. *Journal of Applied Mechanics*, 48 (1981), 809-815.

[99] Krajcinovic D., Fonseka G.U.: The continuous damage theory of brittle materials. Part 2: Uniaxial and plane response modes. *Journal of Applied Mechanics*, 48 (1981), 816-824.

[100] Kreja I.: *Mechanika ośrodków ciągłych*. Centre for Urban Construction and Rehabilitation CURE, Gdańsk 2003.

[101] Kreja I., Schmidt R.: *Plastic ductile damage evolution and collapse of plates and shells*. Damage and Fracture Mechanics VIII/ Computer Aided Assessment and Control, Boston 2004.

[102] Kreja I., Schmidt R., Weichert D.: Modelling and FE-simulation of plastic ductile damage evolution in plates and shells. *Archive of Applied Mechanics*, 71 (2001), 146-163.

[103] Kuna-Ciskał H., Skrzypek J.: CDM based modelling of damage and fracture mechanisms in concrete under tension and compression. *Engineering Fracture Mechanics*, 71 (2004), 681-698.

[104] Labergere C., Rassineux A., Saanouni K.: Improving numerical simulation of metal forming processes using adaptive remeshing technique. *International Journal of Material Forming*, 1 (2008), 539-542.

[105] Leckie F.A., Onat E.T.: *Tensorial nature of damage measuring internal variables*. Physical non-linearities in structures, Springer, Berlin 1981.

[106] Lee E.H., Shaffer B.W.: The theory of plasticity applied to a problem of machining. *Journal of Applied Mechanics, Trans. ASME*, 18 (1951), 405-413.

[107] Lee Y.-W., Wierzbicki T.: Fracture prediction of thin plates under localized impulsive loading. Part II: discing and petalling. *International Journal of Impact Engineering*, 31 (2005), 1277-1308.

[108] Lee Y.-W., Woertz J.C., Wierzbicki T.: Fracture prediction of thin plates under hemi-spherical punch with calibration and experimental verification. *International Journal of Mechanical Sciences*, 46 (2004), 751-781.

[109] Lemaitre J.: *A course on damage mechanics*. Springer, Berlin, 1996.

[110] Lemaitre J.: Anisotropic damage law of evolution. *European Journal of Mechanics A/Solids*, 19 (2000), 187-208.

[111] Lemaitre J.: How to use damage mechanics. *Nuclear Engineering and Design*, 80 (1984), 233-245.

[112] Lemaitre J., Chaboche J.L.: *Mechanics of solid materials*. Cambridge University Press, Cambridge 1990.

[113] Lemaitre J., Dufailly J.: Damage measurement. *Engineering Fracture Mechanics*, 28 (1987), 643-661.

[114] Lin Y., Lingcang C., Yinglei L., Jianxiang P., Fuqian J., Dongquan C.: Simplified model for prediction of dynamic damage and fracture of ductile materials. *International Journal of Solids and Structures*, 41 (2004), 7063-7074.

[115] Liu X.L., Lemos J.V.: Procedure of contact detection in discrete element analysis. *Advances in Engineering Software*, 32 (2001), 409-415.

[116] Lu T.J., Chow C.L.: On constitutive equations of inelastic solids with anisotropic damage. *Theoretical and Applied Fracture Mechanics*, 14 (1990), 187-218.

[117] Łodygowski T., Perzyna P.: Localized fracture in inelastic polycrystalline solids under dynamic loading process. *International Journal of Damage Mechanics*, 6 (1997), 364-407.

[118] Łodygowski T., Perzyna P.: Numerical modelling of localized fracture of inelastic solids in dynamic loading process. *International Journal for Numerical Methods in Engineering*, 40 (1997), 4137-4158.

[119] Maire J.F., Chaboche J.L.: A new formulation of continuum damage mechanics for composite materials. *Aerospace Science and Technology*, 1 (1997), 247-257.

[120] Mashayekhi M., Ziaei-Rad S., Parvizian J., Niklewicz J., Hadavinia H.: Ductile crack growth based on damage criterion: Experimental and numerical studies. *Mechanics of Materials*, 39 (2007), 623-636.

[121] McClintock F.A.: A criterion for ductile fracture by the growth of holes. *Journal of Applied Mechanics*, 35 (1968), 363-371.

[122] McClintock F.A., Walsh J.B.: Friction of Griffith cracks in rock under pressure. *Proceedings of the Fourth U.S. Congress of Applied Mechanics*, (1962), 1015-21.

[123] Mediavilla J., Peerlings R.H.J., Geers M.G.D.: Discrete crack modelling of ductile fracture driven by non-local softening plasticity. *International Journal for Numerical Methods in Engineering*, 66 (2006), 661-688.

[124] Menzel A., Steinmann P.: A theoretical and computational framework for anisotropic continuum damage mechanics at large strains. *International Journal of Solids and Structures*, 38 (2001), 9505-9523.

[125] Meschke G., Dumstorff P.: Energy-based modeling of cohesive and cohesionless cracks via X-FEM. *Computer Methods in Applied Mechanics and Engineering*, 196 (2007), 2338-2357.

[126] Miller O., Freund L.B., Needleman A.: Modeling and simulation of dynamic fragmentation in brittle materials. *International Journal of Fracture*, 96 (1999), 101–125.

[127] Moës N., Dolbow J., Belytschko T.: A finite element method for crack growth without remeshing. *International Journal for Numerical Methods in Engineering*, 46 (1999), 131-150.

[128] Mohr O.: *Abhandlungen aus dem Gebiete der Technischen Mechanik* (2nd ed). Ernst, Berlin 1914 (in German).

[129] Murakami S.: Notion of continuum damage mechanics and its application to anisotropic creep damage theory. *Journal of Engineering Materials and Technology*, 105 (1983), 99-105.

[130] Murakami S., Ohno N.: A continuum theory of creep and creep damage. *Creep in Structures, IUTAM*, (1981), 422- 444.

[131] Norris D.M., Reaugh J.E., Moran B., Quiñones D.F.: A plastic-strain, mean-stress criterion for ductile fracture. *Journal of Engineering Materials and Technology*, 100 (1978), 279-286.

[132] Nurick G.N.: A new technique to measure the deflection-time history of a structure subjected to high strain rates. *International Journal of Impact Engineering*, 3 (1985), 17-26.

[133] Nurick G.N., Martin J.B.: Deformation of thin plates subjected to impulsive loading—A review: Part II: Experimental studies. *International Journal of Impact Engineering*, 8 (1989), 171-186.

[134] Oden J.T., Pires E.B.: Nonlocal and nonlinear friction laws and variational principles for contact problems in elasticity. *Journal of Applied Mechanics*, 50 (1983), 67-77.

[135] Odqvist F.K.G., Hult J.: Some aspects of creep rupture. *Arkiv for Fysik*, 26 (1961), 379.

[136] Oh S., Chen C.C., Kobayashi S.: Ductile failure in axisymmetric extrusion and drawing. Part 2: Workability in extrusion and drawing. *Journal of Engineering for Industry-Transactions*, 101 (1979), 36-44.

[137] Olson M.D., Nurick G.N., Fagnan J.R.: Deformation and rupture of blast loaded square plates – prediction and experiments. *International Journal of Impact Engineering*, 13 (1993), 279-291.

[138] Onyane M., Shima S., Tabata T.: Considerations of basic equations and their application in the forming of metal powders and porous metals. *Journal of Mechanical Working Technology*, 1 (1979), 325-341.

[139] Peng X., Meyer C.: A continuum damage mechanics model for concrete reinforced with randomly distributed short fibers. *Computers and Structures*, 78 (2000), 505-515.

[140] Pennetier O., Renard J.: Structures minces face à une explosion, application à la gestion de risques industriels. *Mécanique Industrielle et Matériaux*, 51 (1998), 67-69 (in French).

[141] Perrone N.: Impulsively loaded strain-rate sensitive plates. *Journal of Applied Mechanics*, 34 (1967), 489-492.

[142] Perzyna P.: The constitutive equations for rate sensitive plastic materials. *Quarterly of Applied Mathematics*, 20 (1963), 321-332.

[143] Pęcherski R.B., Nowacki W.K., Nowak Z., Perzyna P.: Effect of strain rate on ductile fracture. A new methodology. *Proc. Workshop in Memory of prof. J.R. Klepaczko, Dynamic Behavior of Materials*, LPMM, Metz, (2009), 65-73.

[144] Prahl U., Bourgeois S., Pandorf T., Aboutayeb M., Debordes O., Weichert D.: Damage parameter identification by a periodic homogenization approach. *Computational Materials Science*, 25 (2002), 159-165.

[145] Rabczuk T., Belytschko T.: Cracking particles: a simplified meshfree method for arbitrary evolving cracks. *International Journal for Numerical Methods in Engineering*, 61 (2004), 2316-2343.

[146] Rabotnov Y.N.: On a mechanism of delayed fracture. *Vopr. Prochn. Mat. Konstr.*, 5 (1959) (in Russian).

[147] Rice J. R.: A path independent integral and the approximate analysis of strain concentration by notches and cracks. *Journal of Applied Mechanics*, 35 (1968), 379–386.

[148] Rice J.R., Tracy D.M.: On ductile enlargement of voids in triaxial stress fields. *Journal of Mechanics and Physics of Solids*, 17 (1969), 210-217.

[149] Rivalin F., Besson J., Pineau A., Di Fant M.: Ductile tearing of pipeline-steel wide plates: II. Modeling of in-plane crack propagation. *Engineering Fracture Mechanics*, 68 (2001), 347-364.

[150] Rodriguez-Ferran A., Morata I., Huerta A.: A new damage model based on non-local displacements. *International Journal for Numerical and Analytical Methods in Geomechanics*, 29 (2005), 473-493.

[151] Rousselier G.: Ductile fracture models and their potential In local approach of fracture. *Nuclear Engineering and Design*, 105 (1987), 97-111.

[152] Saanouni K.: On the numerical prediction of the ductile fracture in metal forming. *Engineering Fracture Mechanics*, 75 (2008), 3545-3559.

[153] Schacht T., Untermann N., Steck E.: The influence of crystallographic orientation on the deformation behaviour of single crystals containing microvoids. *International Journal of Plasticity*, 19 (2003), 1605–1626.

[154] Shao J.F., Khazraei R.: A continuum damage mechanics approach for time independent and dependent behaviour of brittle rock. *Mechanics Research Communications*, 3 (1996), 257-265.

[155] Shen W.: A study on the failure of circular plates struck by masses. Part 2: theoretical analysis for the onset of failure. *International Journal of Impact Engineering*, 27 (2002), 413-432.

[156] Shockey D.A., Seaman L., Curran D.R.: The microstatistical fracture mechanics approach to dynamic fracture problems. *International Journal of Fracture*, 27 (1985), 145-157.

[157] SigmaPlot 10 User's manual.

[158] Siruguet K., Leblond J.B.: Effect of void locking by inclusions upon the plastic behavior of porous ductile solids – parts I and II. *International Journal of Plasticity*, 20 (2004), 225-268.

[159] Souiyah M., Alshoaibi A., Muchtar A., Ariffin A.K.: Finite element model for linear-elastic mixed mode loading using adaptive mesh strategy. *Journal of Zhejiang University - Science A*, 9 (2008), 32-37.

[160] Springmann M., Kuna M.: Identification of material parameters of the Rousselier model by non-linear optimization. *Computational Materials Science*, 26 (2003), 202-209.

[161] Springmann M., Kuna M.: Identification of material parameters of the Gurson–Tvergaard–Needleman model by combined experimental and numerical techniques. *Computational Materials Science*, 32 (2005), 544-552.

[162] Stoffel M.: Experimental validation of anisotropic ductile damage and failure of shock wave-loaded plates. *European Journal of Mechanics A/Solids*, 26 (2007), 592-610.

[163] Stoffel M., Schmidt R., Weichert D.: Shock wave-loaded plates. *International Journal of Solids and Structures*, 38 (2001), 7659-7680.

[164] Symonds P.S., Chon C.T.: Finite viscoplastic deflections of an impulsively loaded plate by the mode approximation technique. *Journal of the Mechanics and Physics of Solids*, 27 (1979), 114–125.

[165] Tai W.H., Yang B.X.: A new microvoid-damage model for ductile fracture. *Engineering Fracture Mechanics*, 25 (1986), 377-384.

[166] Taupin E., Breitling J., Wu W.-T., Altan T.: Material fracture and burr formation in blanking, results of FEM simulation and comparison with experiments. *Journal of Materials Processing Technology*, 59 (1996), 68-78.

[167] Taylor M., Verdonschot N., Huiskes R.: A combined finite element method and continuum damage mechanics approach to simulate the in vitro fatigue behaviour of human cortical bone. *Journal of Materials Science: Materials in Medicine*, 10 (1999), 841-846.

[168] Teeling-Smith R.G., Nurick G.N.: The deformation and tearing of thin circular plates subjected to impulsive loads. *International Journal of Impact Engineering*, 11 (1991), 77-91.

[169] Teng X.: Numericap prediction of slant fracture with continuum damage mechanics. *Engineering Fracture Mechanics*, 75 (2008), 2020-2041.

[170] Thomason P.F.: A three-dimensional model for ductile fracture by the growth and coalescence of micro-voids. *Acta Metallurgica*, 33 (1985), 1087-1095.

[171] Trädegård A., Nilsson F., Östlund S.: FEM-remeshing technique applied to crack growth problems. *Computer Methods in Applied Mechanics and Engineering*, 160 (1998), 115-131.

[172] Tvergaard V.: Influence of voids on shear band instabilities under plane strain conditions. *International Journal of Fracture*, 17 (1981), 389-407.

[173] Tvergaard V.: On localization in ductile materials containing spherical voids.. *International Journal of Fracture*, 18 (1982), 237-252.

[174] Tvergaard V., Needleman A.: Analysis of the cup-cone fracture in a round tensile bar. *Acta Metallurgica*, 32 (1984), 157-169.

[175] Tvergaard V., Niordson C.: Nonlocal plasticity effects on interaction of different size voids. *International Journal of Plasticity*, 20 (2004), 107–120.

[176] User manual: *MSC.MARC Volume A: Theory and user information, Version 2008r1.* MSC.Software Corporation, USA 2008.

[177] User manual: *MSC.MARC Volume B: Element library, Version 2008r1.* MSC.Software Corporation, USA 2008.

[178] User manual: *MSC.MARC Volume D: User subroutines and special routines, Version 2008r1.* MSC.Software Corporation, USA 2008.

[179] Veldman R.L., Ari-Gur J., Clum C.: Response of pre-pressurizated reinforced plates under blast loading. *International Journal of Impact Engineering*, 35 (2008), 240–250.

[180] Veldman R.L., Ari-Gur J., Clum C., De Young A., Folkert J.: Effects of pre-pressurization on blast response of clamped aluminium plates. *International Journal of Impact Engineering*, 32 (2006), 1678–1695.

[181] Von Kármán T.: Festigkeitsversuche unter allseitigem Druck. *Zeitschrift des Vereins Deutscher Ingenieure*, 55 (1911), 1749-1757 (in German).

[182] Voyiadjis G.Z., Kattan P.I.: *Advances In damage mechanics: metals and metal matrix composites.* Elsevier, Amsterdam 1999.

[183] Voyiadjis G.Z., Park T.: Anisotropic damage effect tensors for the symmetrization of the effective stress tensor. *Journal of Applied Mechanics*, 64 (1997), 106-110.

[184] Wang T.J.: Unified CDM model and local criterion for ductile fracture – I Unified CDM model for ductile fracture. *Engineering Fracture Mechanics*, 42 (1992), 177-183.

[185] Wells A.A.: Unstable crack propagation in metals: cleavage and fast fracture. *Proceedings of the Crack Propagation Symposium*, 1 (1961).

[186] Wen J., Huang Y., Hwang K.C., Liu C., Li M.: The modified Gurson model accounting for the void size effect. *International Journal of Plasticity*, 21 (2005), 381–395.

[187] Westergaard H.M.: Bearing pressures and cracks. *Journal of Applied Mechanics, Trans ASME*, 6 (1937), A.49-A.53.

[188] Wieghardt K.: Uber das Spalten und Zerreissen elastischer Korper. *Z. Mathematik und Physik*, 55 (1907), 60-103.

[189] Wierzbicki T.: Petalling of plates under explosive and impact loading. *International Journal of Impact Engineering*, 22 (1999), 935-954.

[190] Wierzbicki T.: Viscoplastic flow of rationally symmetric shells with particular application to dynamic loading. *Journal of the Mechanics and Physics of Solids*, 3 (1954), 22-37.

[191] Wierzbicki T., Bao Y., Lee Y.-W., Bai Y.: Calibration and evaluation of seven fracture models. *International Journal of Mechanical Sciences*, 47 (2005), 719-743.

[192] Wierzbicki T., Florence A.L.: A theoretical and experimental investigation of impulsively loaded clamped circular viscoplastic plates. *International Journal of Solids and Structures*, 6 (1970), 555-568.

[193] Wilkins M.L, Streit R.D., Reaugh J.E.: *Cumulative-strain-damage model of ductile fracture: simulation and prediction of engineering fracture tests*. Technical Report UCRL-53058, Lawrence Livermore National Laboratory, 1980.

[194] Wiśniewski K., Kowalczyk P., Turska E.: Analytical DSA for explicit dynamics of elastic-plastic shells. *Computational Mechanics*, 39 (2007), 761-785.

[195] Woznica K., Kłosowski P.: Evaluation of viscoplastic parameters and its application for dynamic behaviour of plates. *Archive of Applied Mechanics*, 70 (2000), 561-570.

[196] Woznica K., Pennetier O., Renard J.: Experiments and numerical simulations on thin metallic plates subjected to an explosion. *Journal of Engineering Materials and Technology*, 123 (2001), 203-209.

[197] Xu X.-P., Needleman A.: Numerical simulation of fast crack growth in brittle solids. *Journal of the Mechanics and Physics of Solids*, 42 (1994), 1397-1434.

[198] Xu Y., Yuan H.: On damage accumulations in the cyclic cohesive zone model for XFEM analysis of mixed-mode fatigue crack growth. *Computational Materials Science*, 46 (2009), 579-585.

[199] Xue L.: Damage accumulation and fracture initiation in uncracked ductile solids subject to triaxial loading, *International Journal of Solids and Structures*, 44 (2007), 5163-5181.

[200] Zhang Z.L.: *A complete Gurson Model*. In: Nonlinear Fracture and Damage Mechanics, WIT Press Southampton, UK 2001 223-248.

[201] Zohu F., Molinari J.-F., Shioya T.: A rate-dependent cohesive model for simulating dynamic crack propagation in brittle materials. *Engineering Fracture Mechanics*, 72 (2005), 1383-1410.

Annex 1

This annex contains the setting-up of all pressure time histories, which have been registered during the experiments. For each test the direct results from both sensors and the recalculated real active pressure (the difference between pressure recorded before and behind the specimen) are presented.

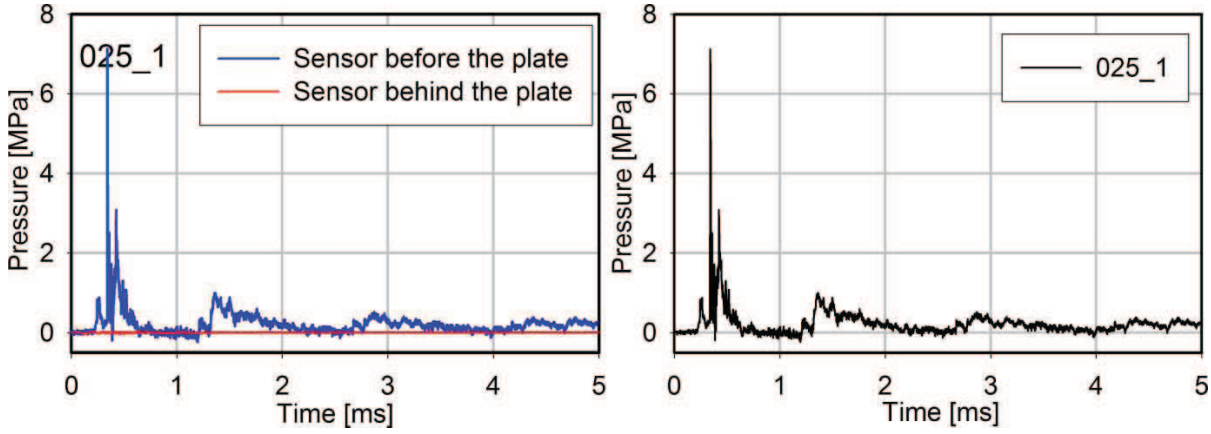

Fig. A1-1. Registered and active pressure time histories, test 025_2 (0.25 bar)

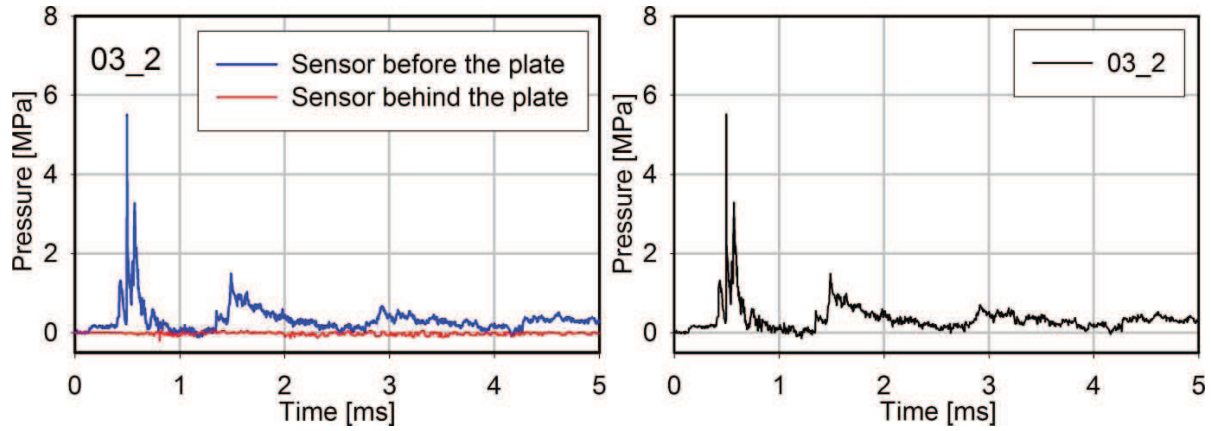

Fig. A1-2. Registered and active pressure time histories, test 03_2 (0.3 bar)

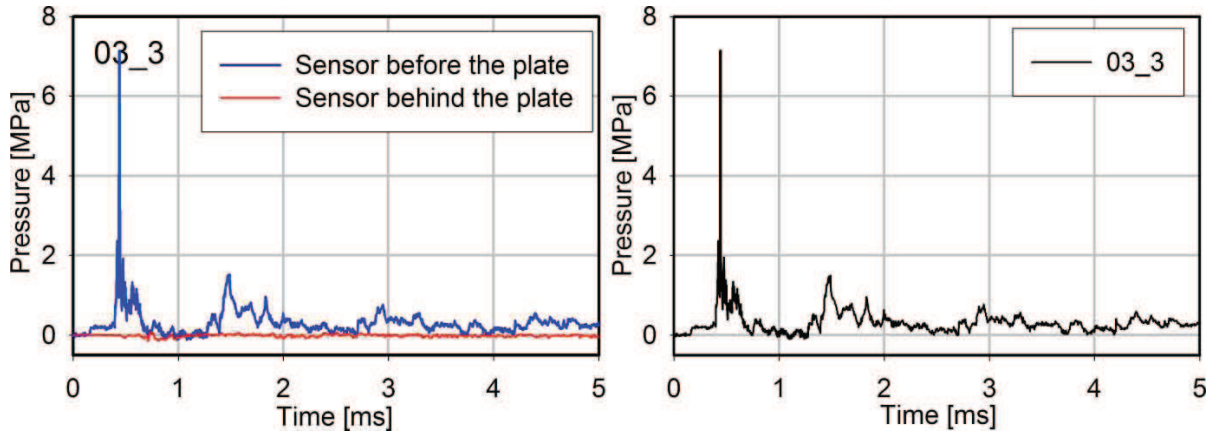

Fig. A1-3. Registered and active pressure time histories, test 03_3 (0.3 bar)

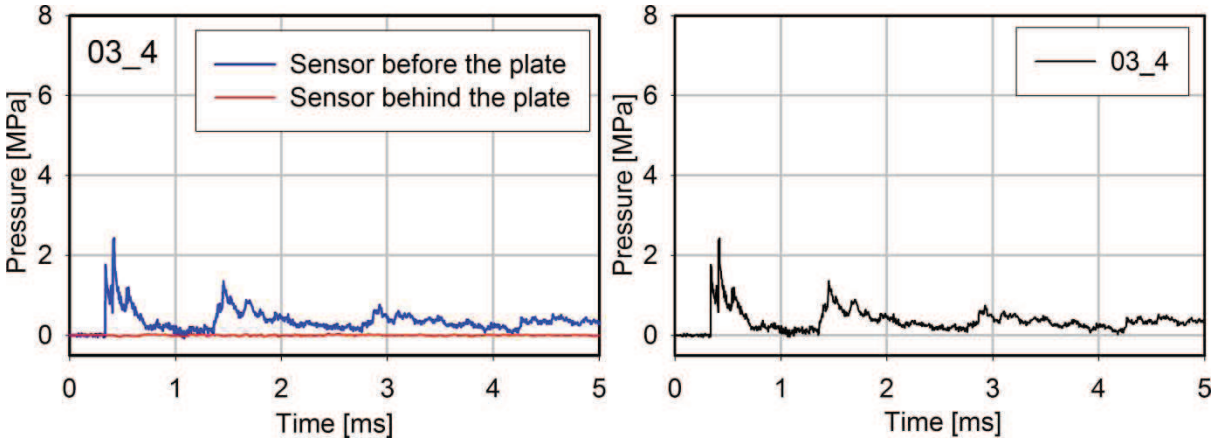

Fig. A1-4. Registered and active pressure time histories, test 03_4 (0.3 bar)

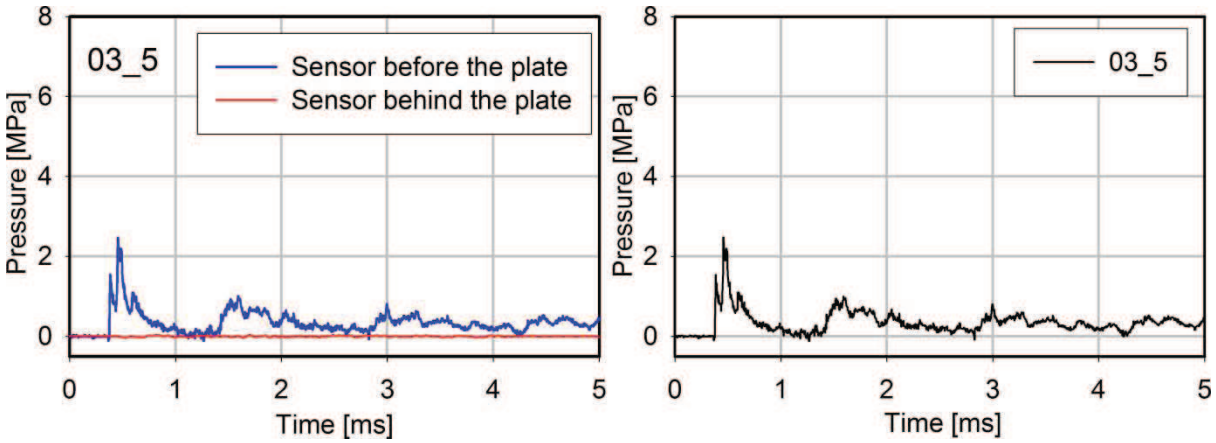

Fig. A1-5. Registered and active pressure time histories, test 03_5 (0.3 bar)

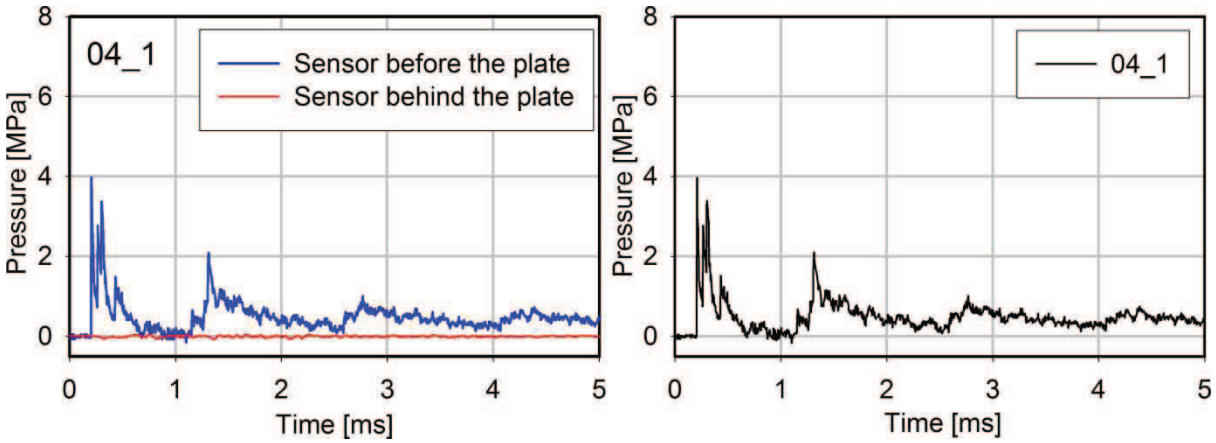

Fig. A1-6. Registered and active pressure time histories, test 04_1 (0.4 bar)

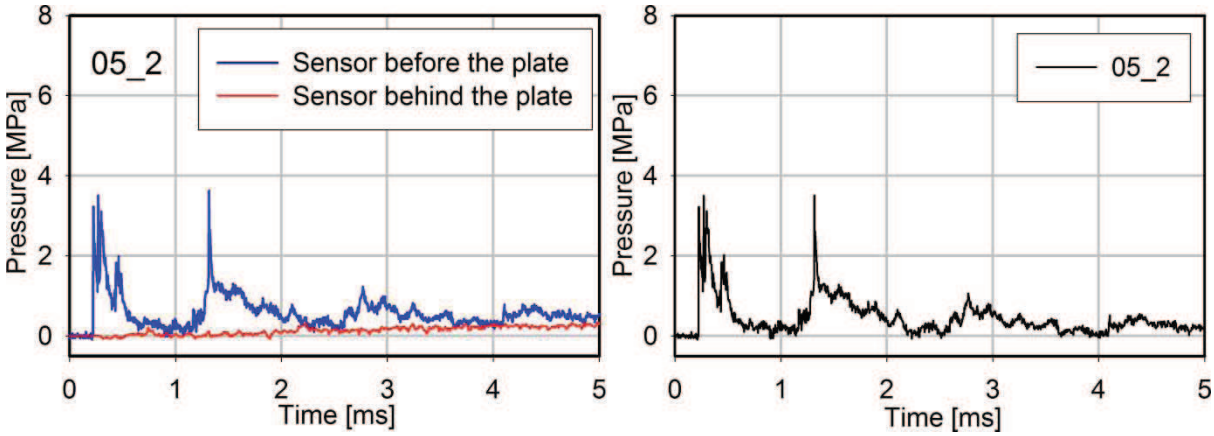

Fig. A1-7. Registered and active pressure time histories, test 05_2 (0.5 bar)

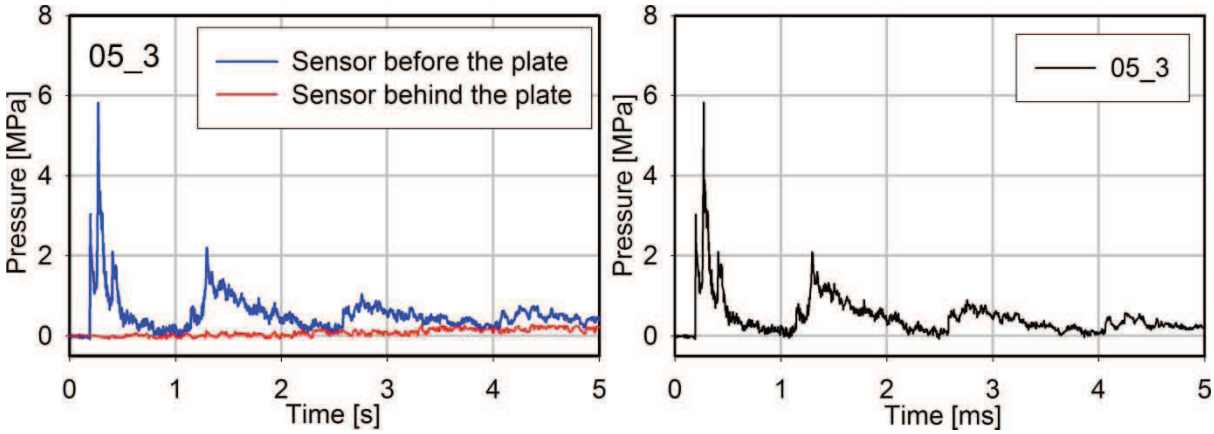

Fig. A1-8. Registered and active pressure time histories, test 05_3 (0.5 bar)

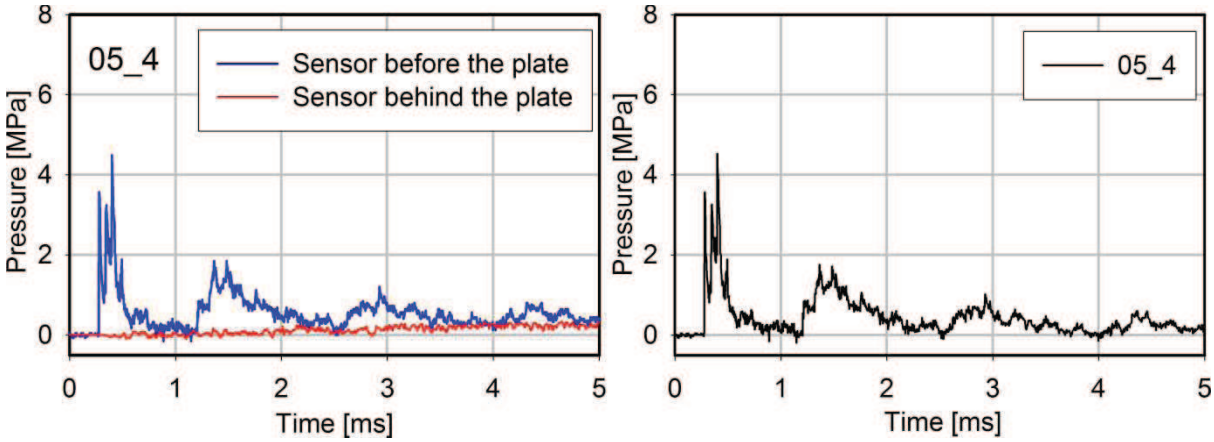

Fig. A1-9. Registered and active pressure time histories, test 05_4 (0.5 bar)

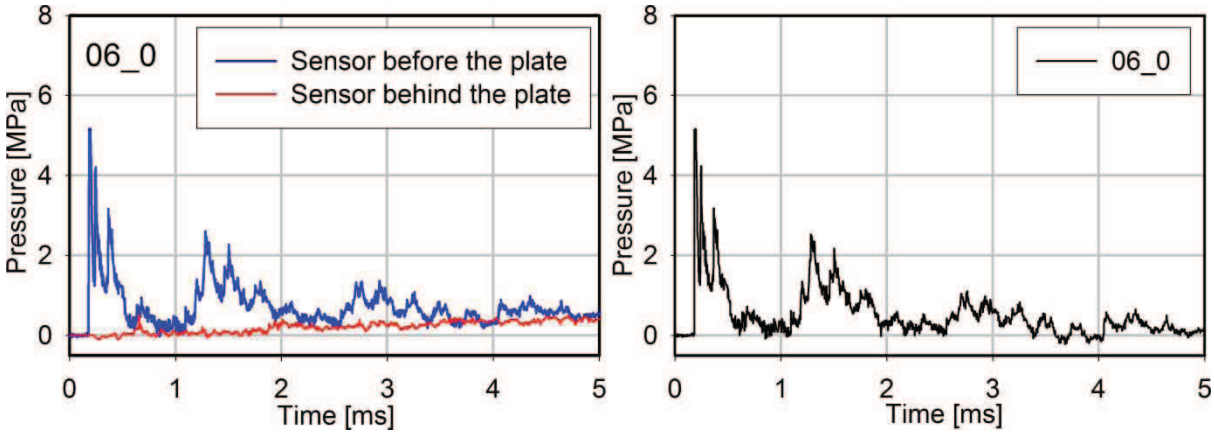

Fig. A1-10. Registered and active pressure time histories, test 06_0 (0.6 bar)

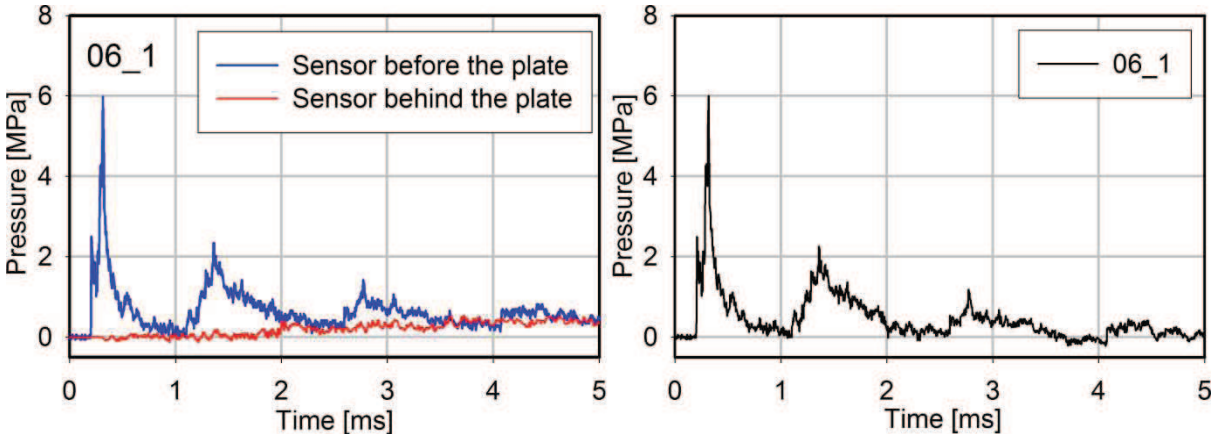

Fig. A1-11. Registered and active pressure time histories, test 06_1 (0.6 bar)

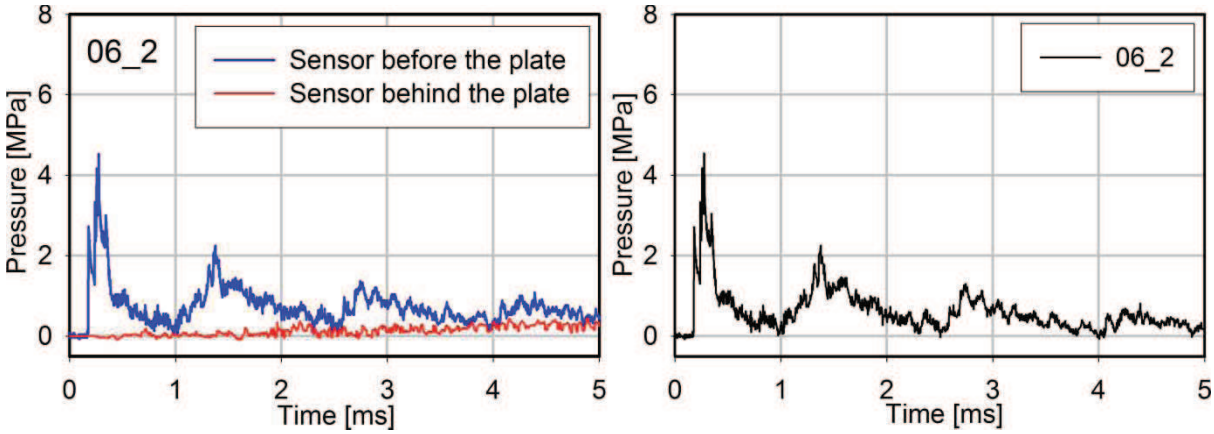

Fig. A1-12. Registered and active pressure time histories, test 06_2 (0.6 bar)

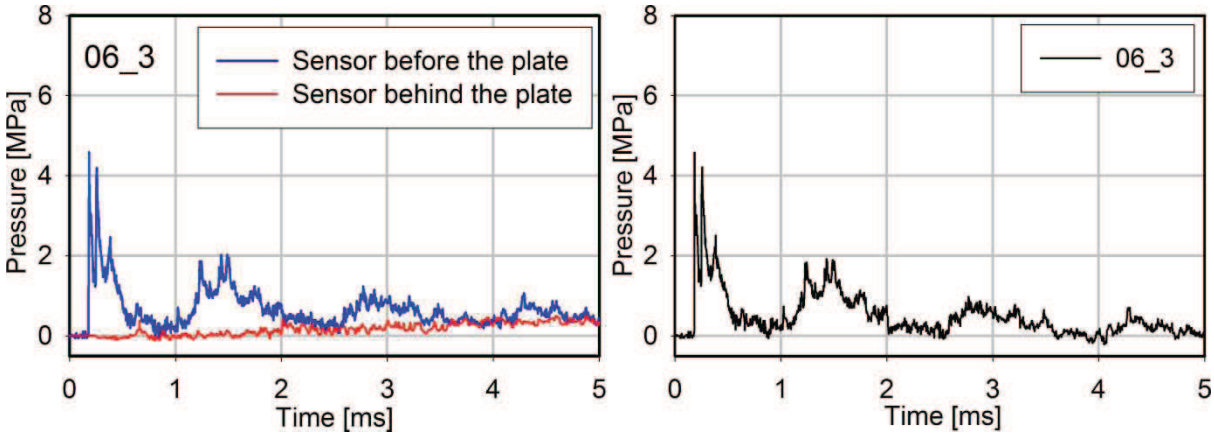

Fig. A1-13. Registered and active pressure time histories, test 06_3 (0.6 bar)

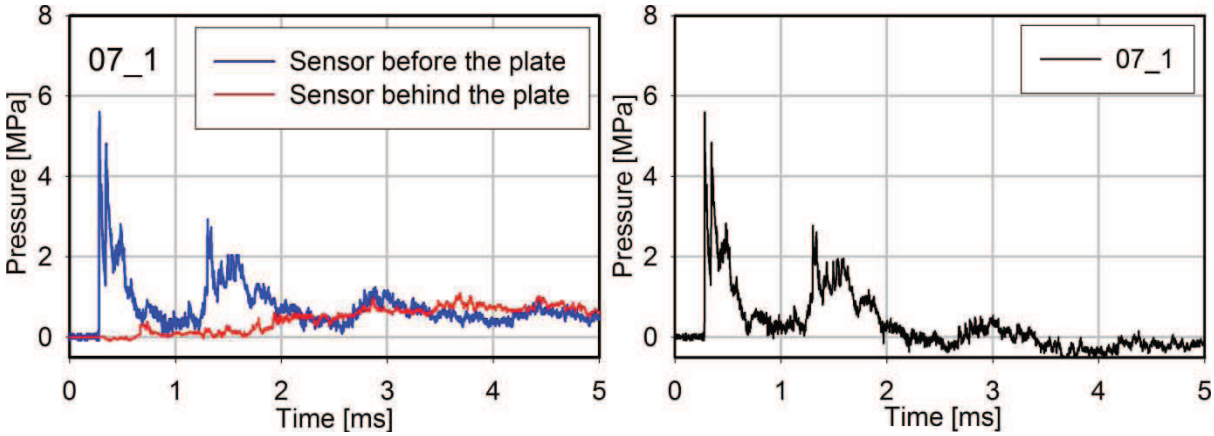

Fig. A1-14. Registered and active pressure time histories, test 07_1 (0.7 bar)

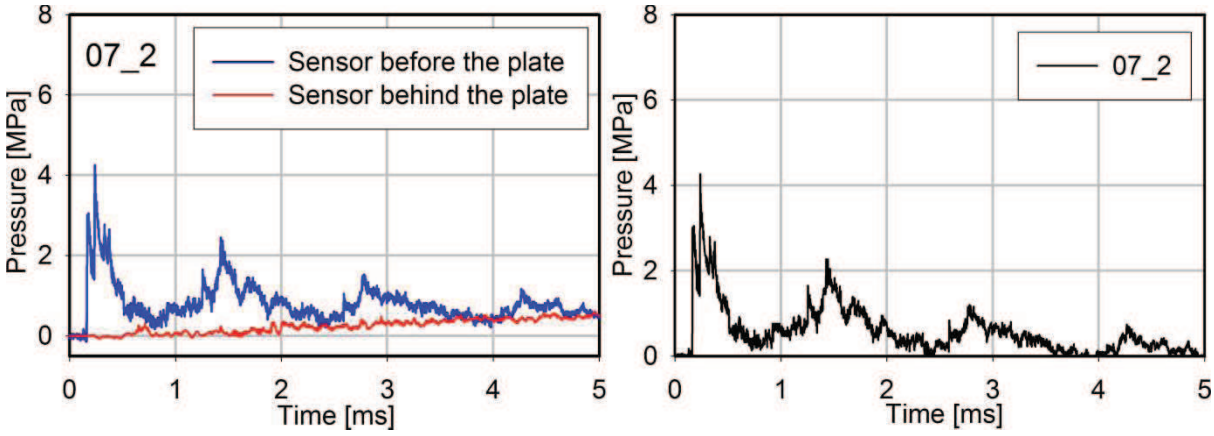

Fig. A1-15. Registered and active pressure time histories, test 07_2 (0.7 bar)

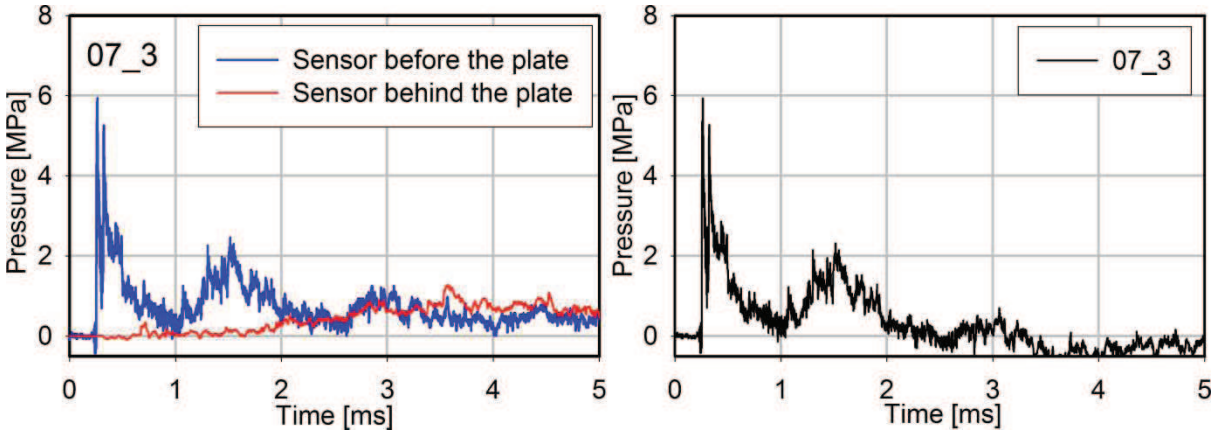

Fig. A1-16. Registered and active pressure time histories, test 07_3 (0.7 bar)

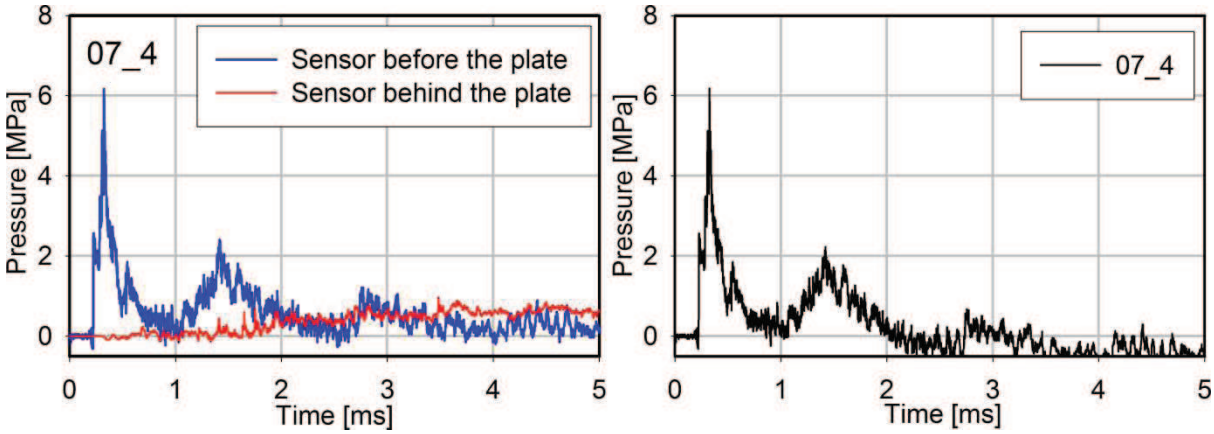

Fig. A1-17. Registered and active pressure time histories, test 07_4 (0.7 bar)

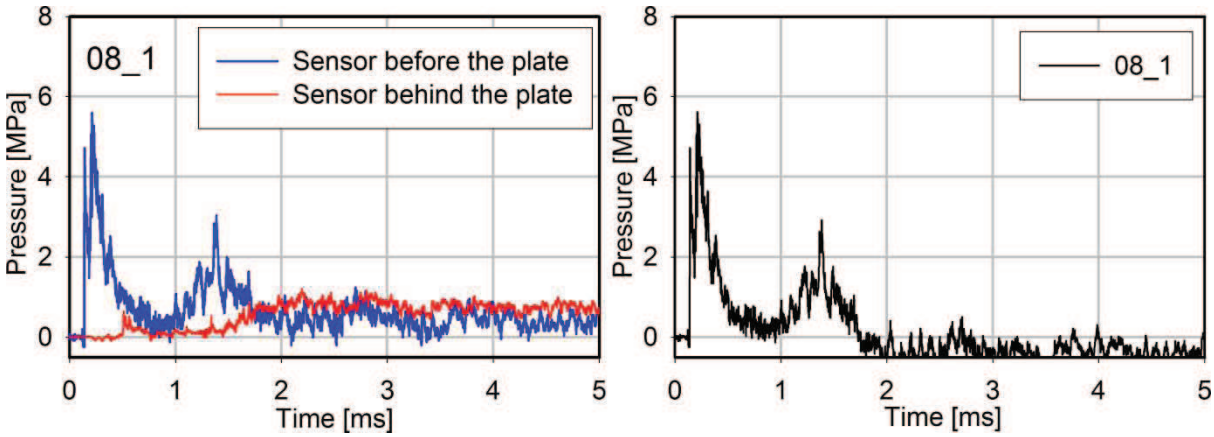

Fig. A1-18. Registered and active pressure time histories, test 08_1 (0.8 bar)

Annex 2

This annex contains the pictures of tested plates. The plates are shown in the order of the gas mixture initial pressure level used in the experiments, from the lowest to the highest.

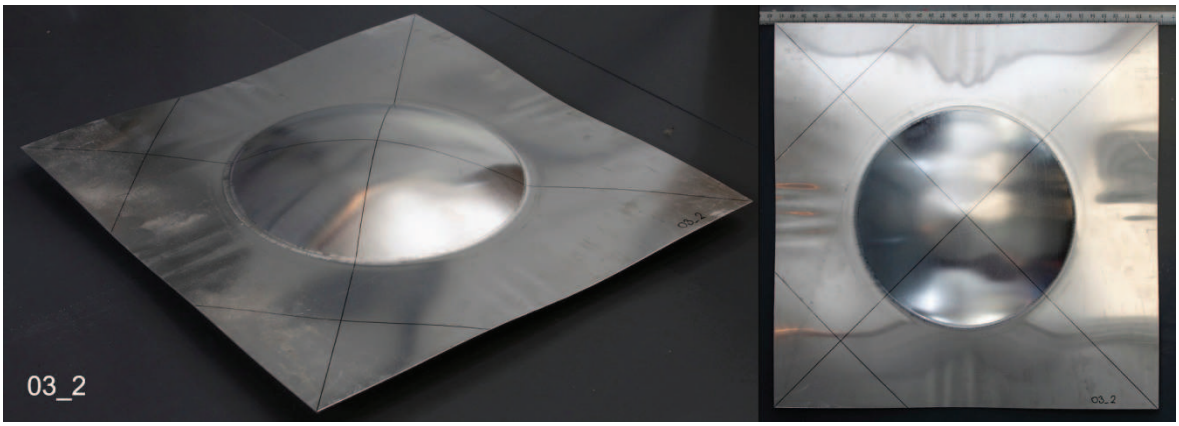

Fig. A2-1. Tested plate 03_2 (0.3 bar)

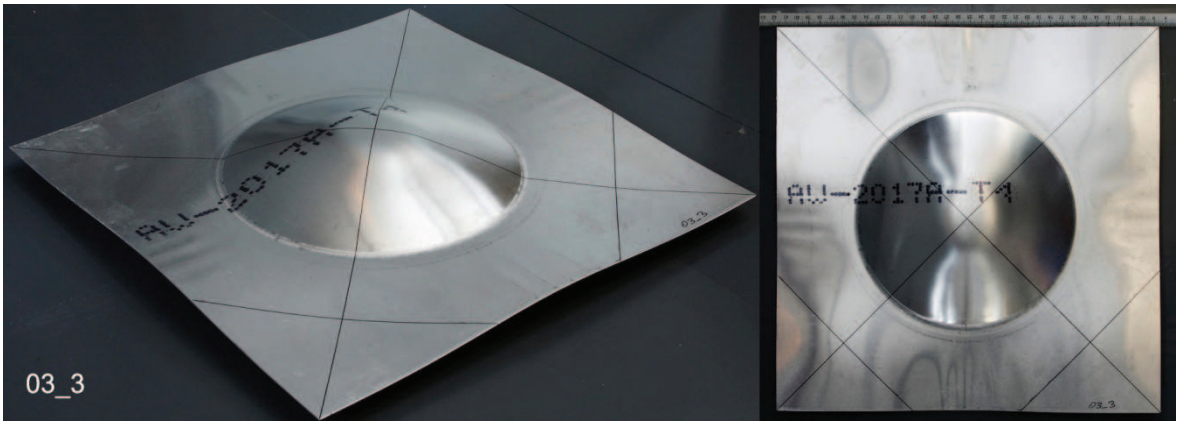

Fig. A2-2. Tested plate 03_3 (0.3 bar)

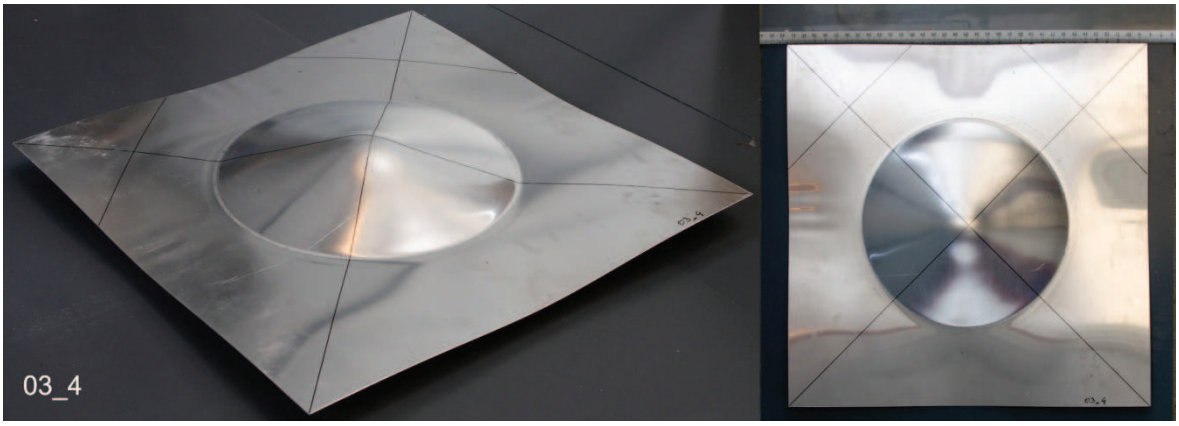

Fig. A2-3. Tested plate 03_4 (0.3 bar)

Fig. A2-4. Tested plate 03_5 (0.3 bar)

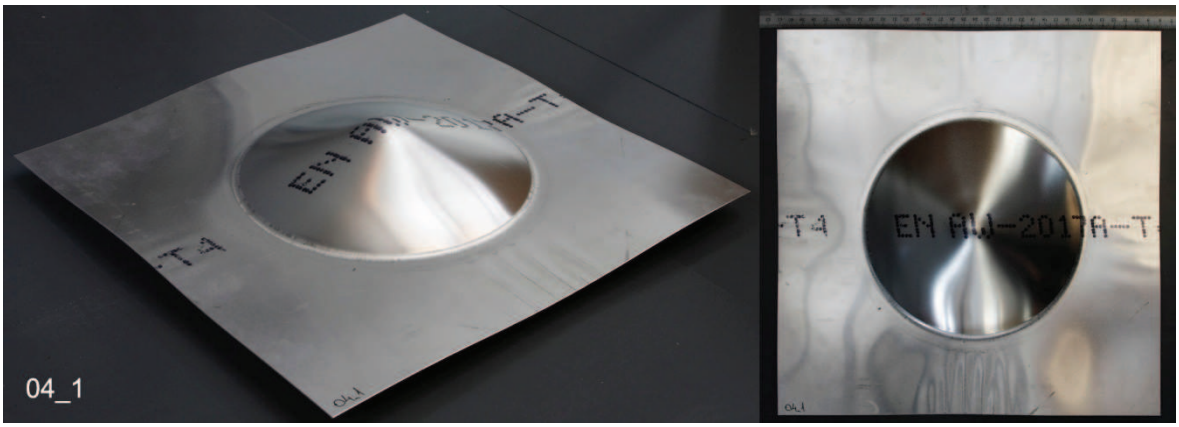

Fig. A2-5. Tested plate 04_1 (0.4 bar)

Fig. A2-6. Tested plate 05_2 (0.5 bar)

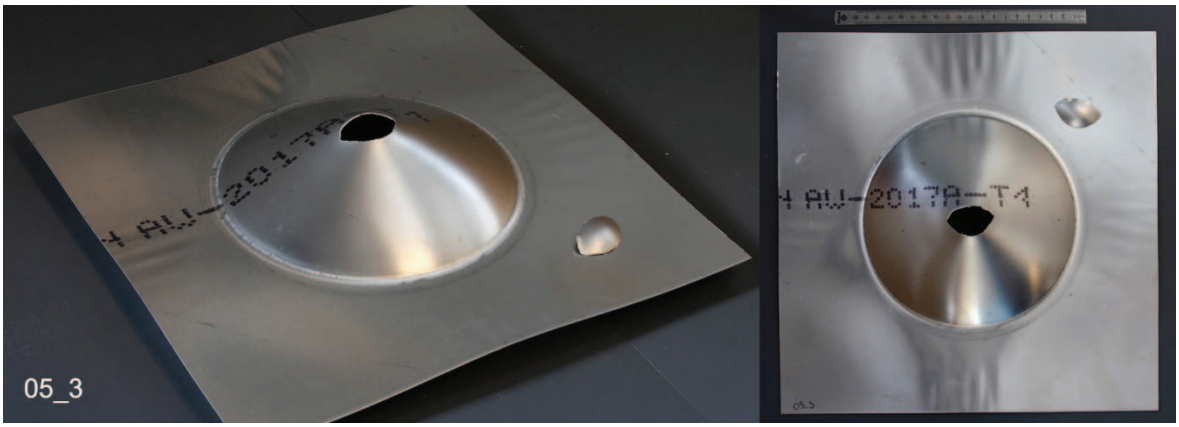

Fig. A2-7. Tested plate 05_3 (0.5 bar)

Fig. A2-8. Tested plate 05_4 (0.5 bar)

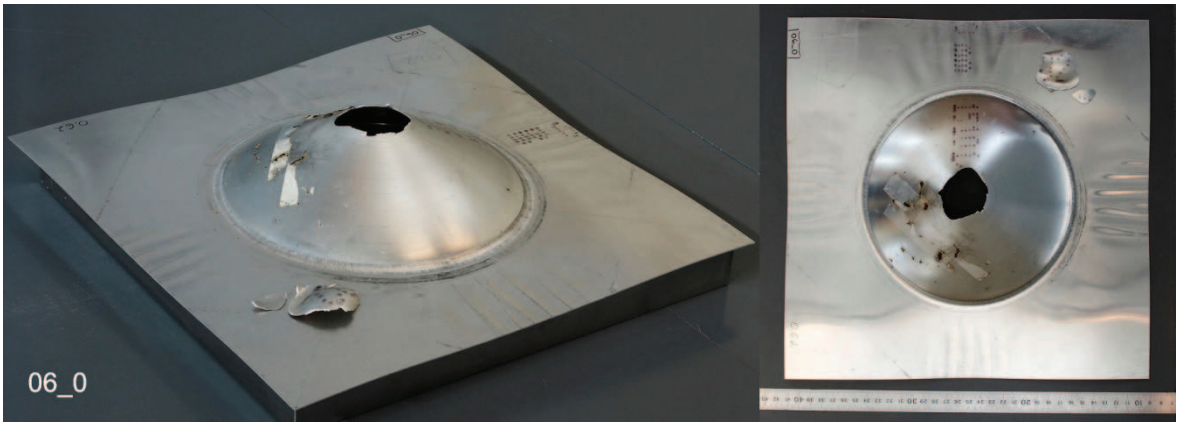

Fig. A2-9. Tested plate 06_0 (0.6 bar)

Fig. A2-10. Tested plate 06_1 (0.6 bar)

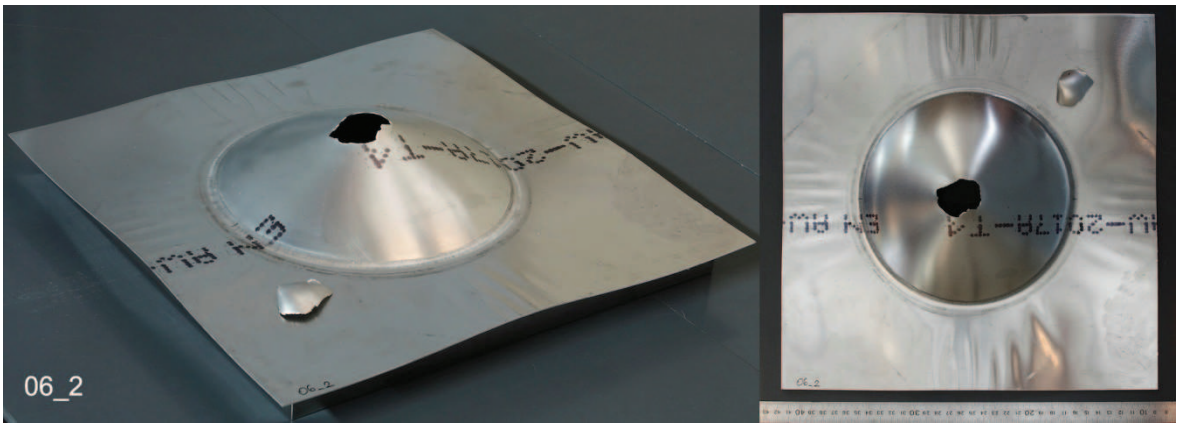

Fig. A2-11. Tested plate 06_2 (0.6 bar)

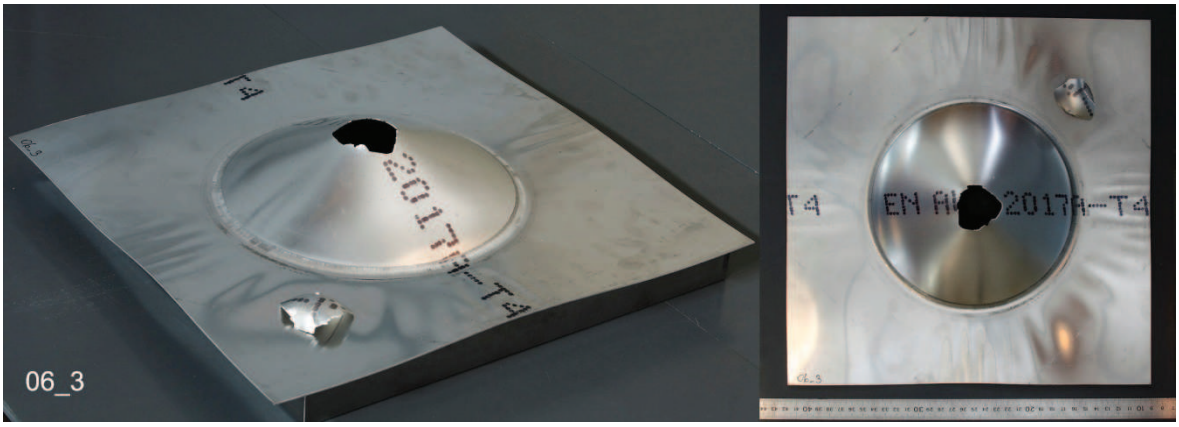

Fig. A2-12. Tested plate 06_3 (0.6 bar)

Fig. A2-13. Tested plate 07_1 (0.7 bar)

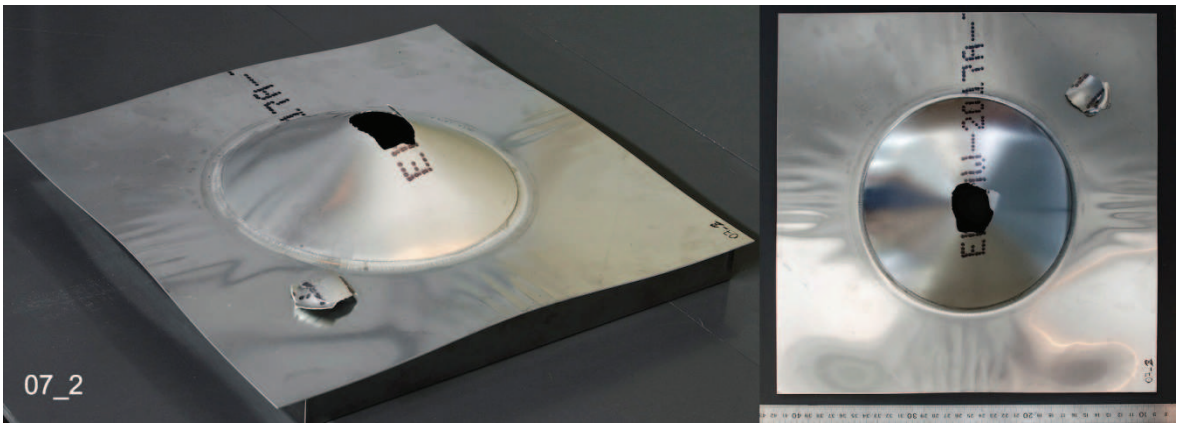

Fig. A2-14. Tested plate 07_2 (0.7 bar)

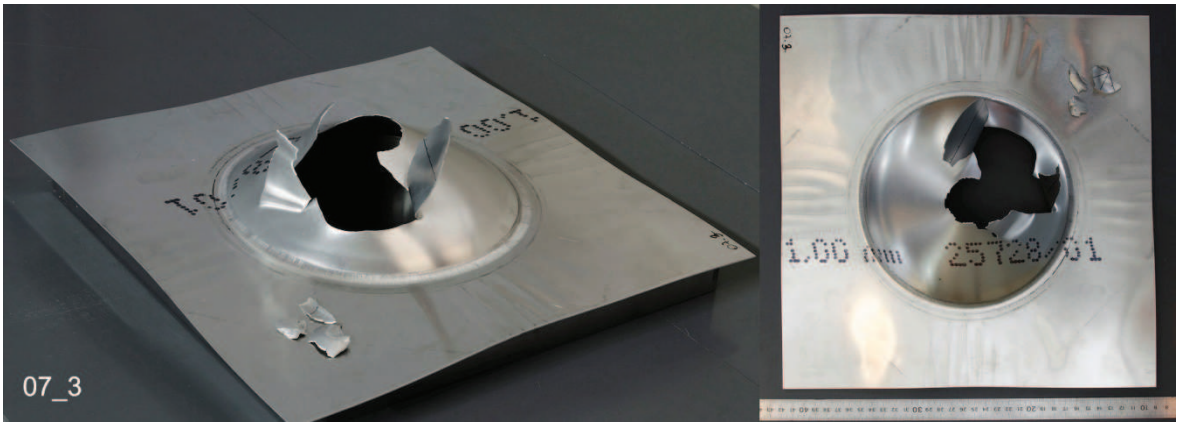

Fig. A2-15. Tested plate 07_3 (0.7 bar)

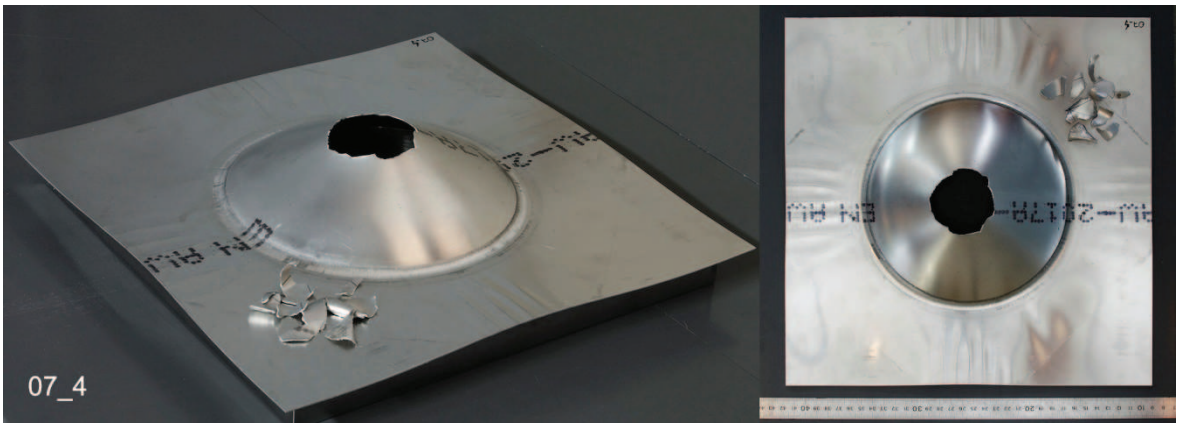

Fig. A2-16. Tested plate 07_4 (0.7 bar)

Fig. A2-17. Tested plate 08_1 (0.8 bar)

Annex 3

This annex contains the setting-up of results obtained in the cross-section measurements. The figures present the average geometries calculated from two measurements which have been performed for each plate.

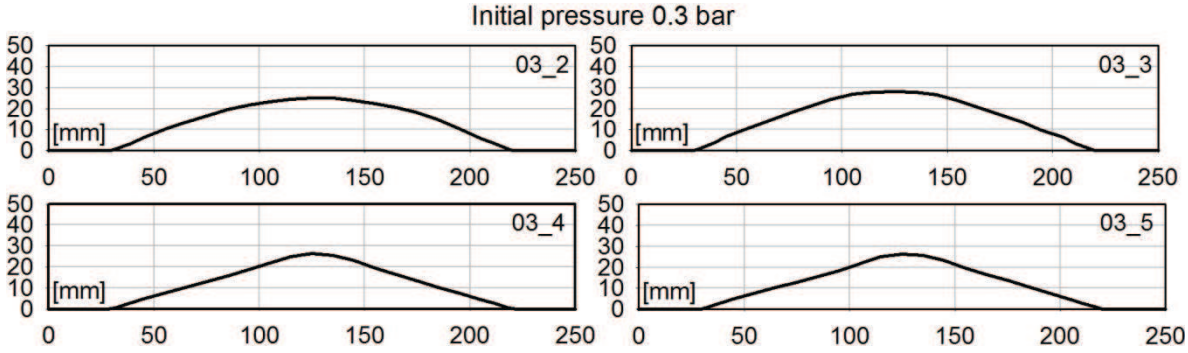

Fig. A3-1. Cross-sections of the tested plates, initial pressure 0.3 bar

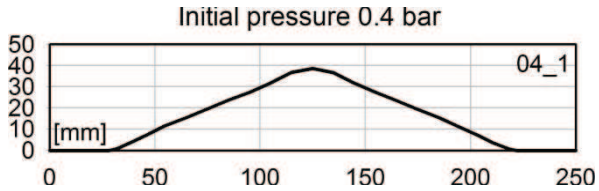

Fig. A3-2. Cross-section of the tested plate, initial pressure 0.4 bar

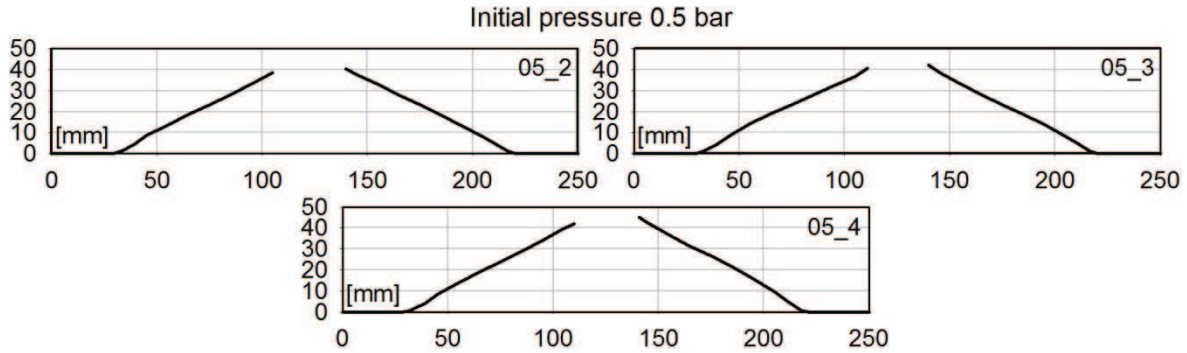

Fig. A3-3. Cross-sections of the tested plates, initial pressure 0.5 bar

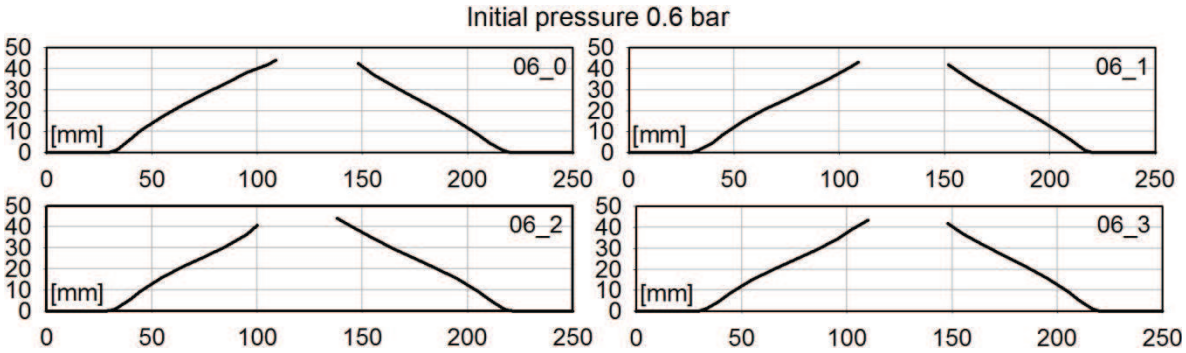

Fig. A3-4. Cross-sections of the tested plates, initial pressure 0.6 bar

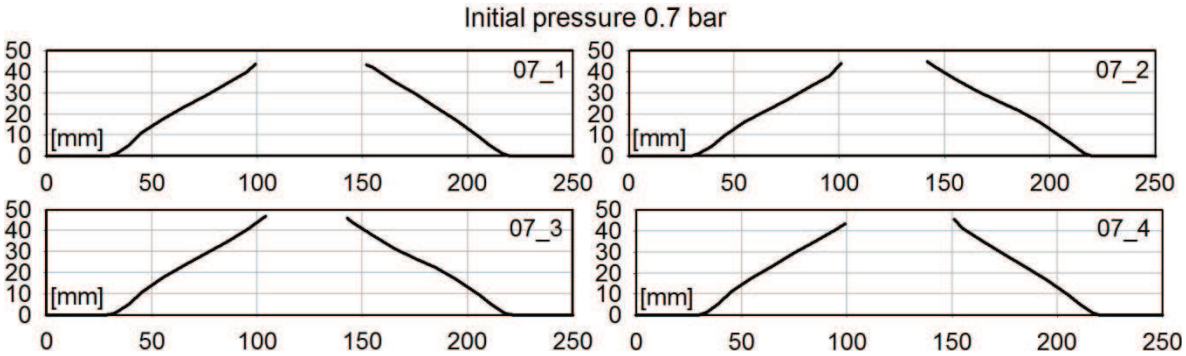

Fig. A3-5. Cross-sections of the tested plates, initial pressure 0.7 bar

Annex 4

This annex contains the setting-up of results obtained in the equivalent hole diameters measurements.

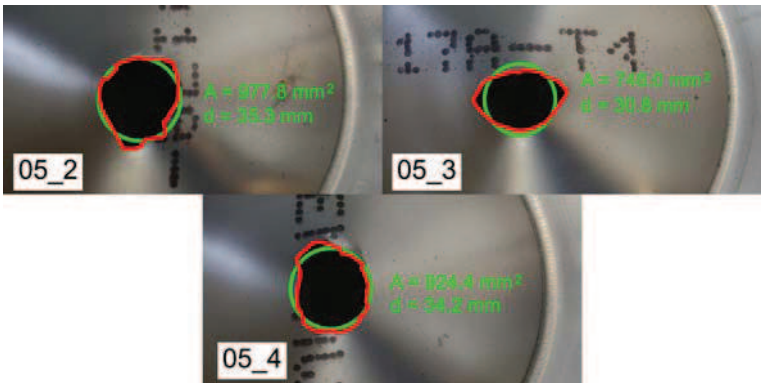

Fig. A4-1. Measurement of equivalent hole diameters, experiments with initial pressure 0.5 bar

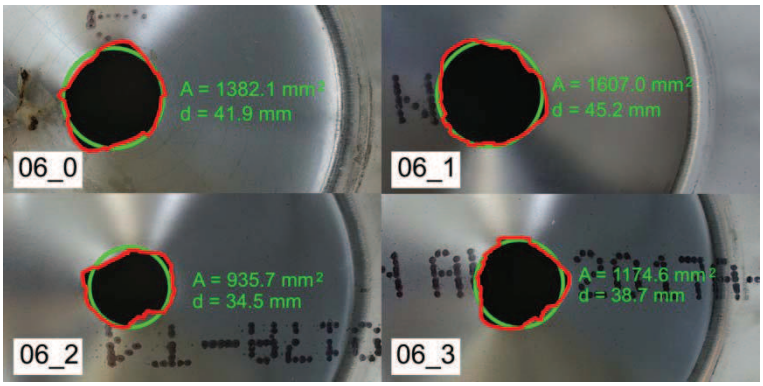

Fig. A4-2. Measurement of equivalent hole diameters, experiments with initial pressure 0.6 bar

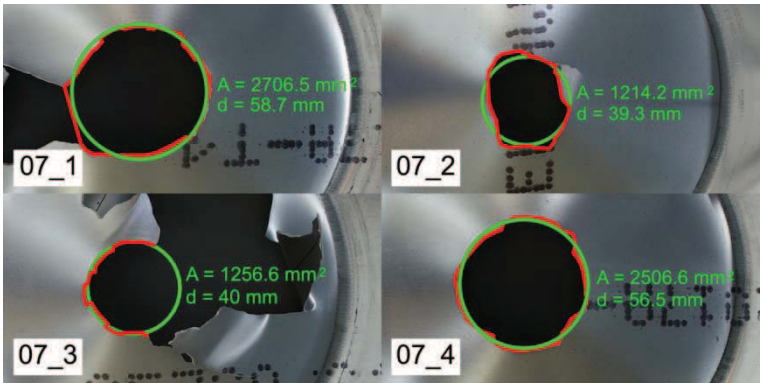

Fig. A4-3. Measurement of equivalent hole diameters, experiments with initial pressure 0.7 bar

Annex 5

This annex contains the setting-up of results obtained in the uniaxial tension tests (tension tests with constant strain rate, load-unload tension cyclic tests). The experiments have been performed on the specimens cut along and across sheet's rolling.

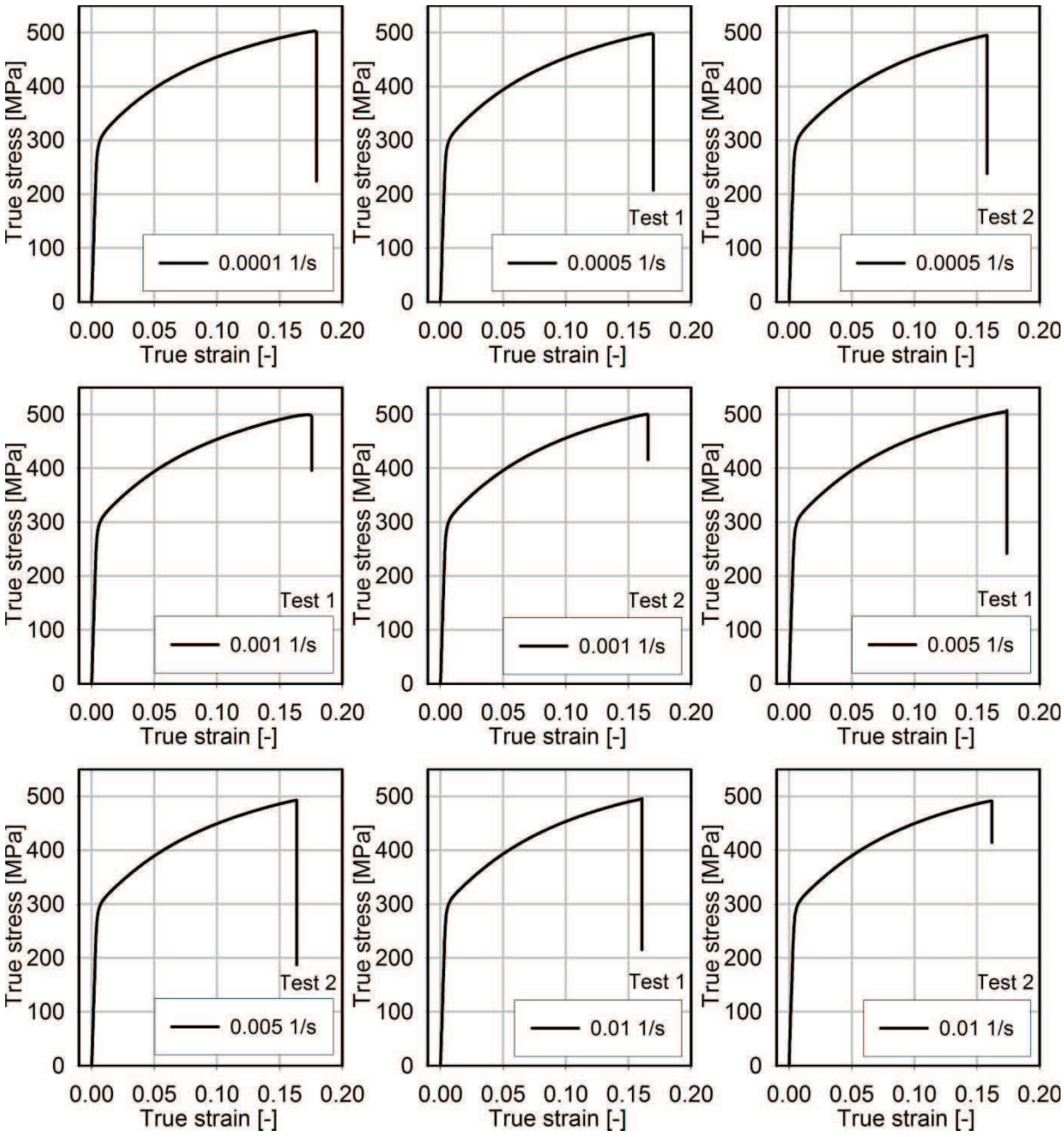

Fig. A5-1. Constant strain rate tension tests on the specimens cut along sheet's rolling

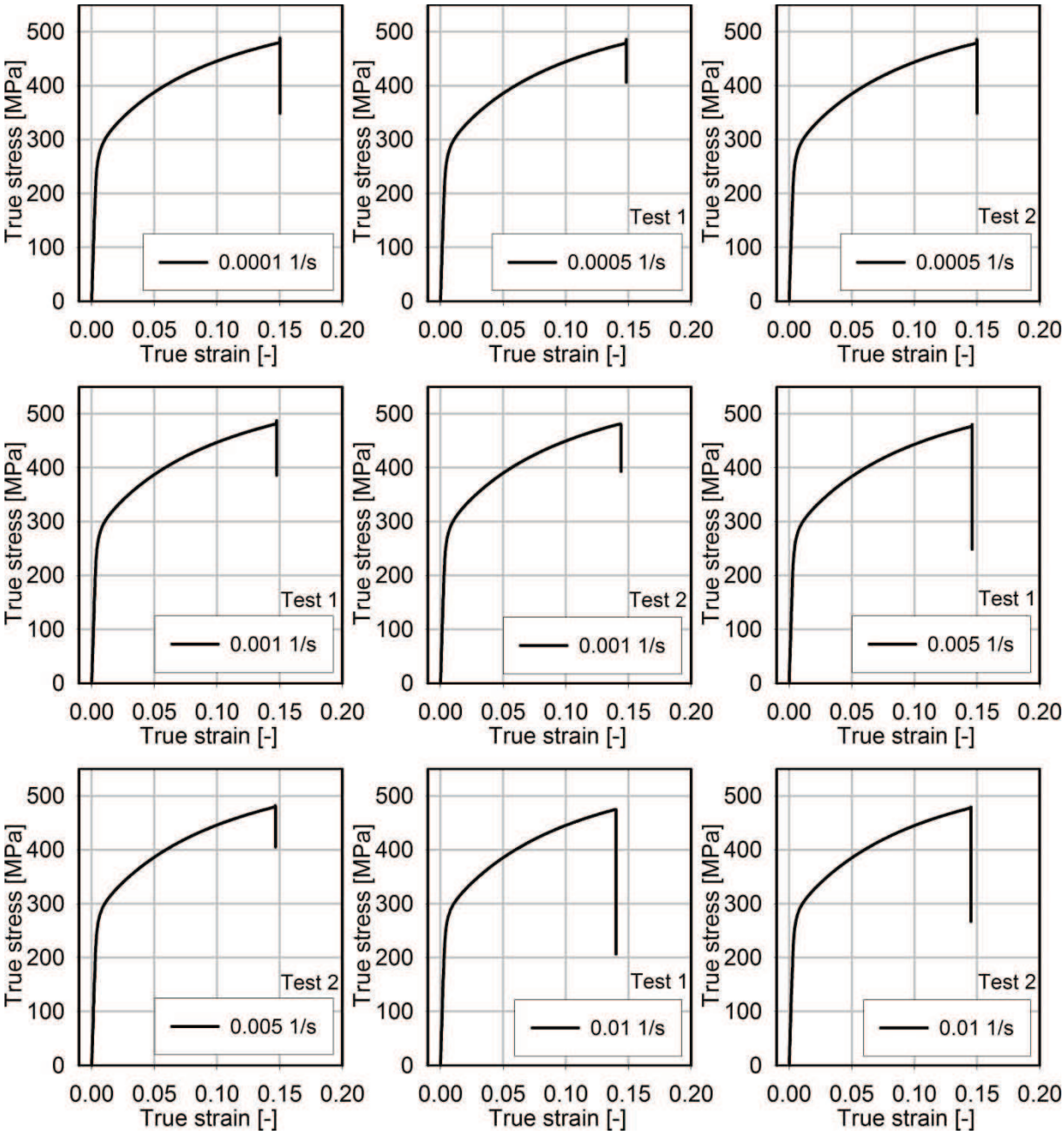

Fig. A5-2. Constant strain rate tension tests on the specimens cut across sheet's rolling

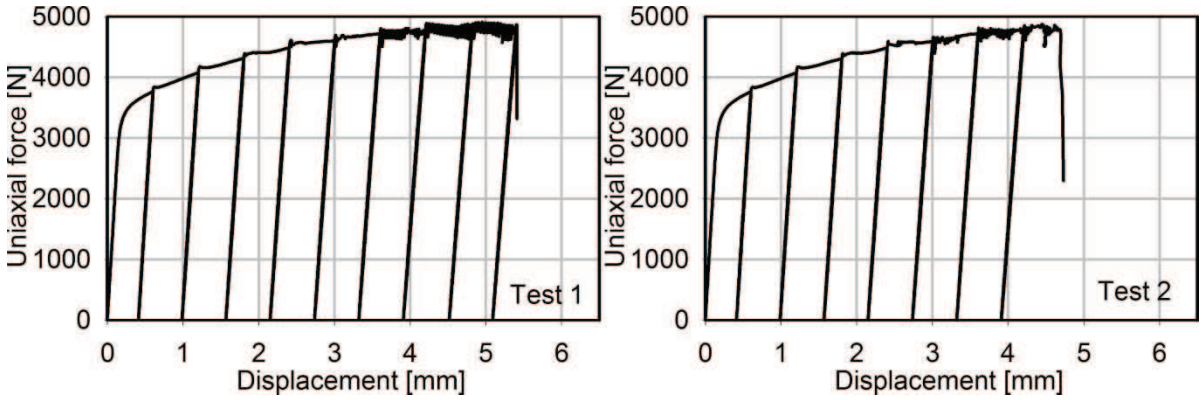

Fig. A5-3. Load-unload tension cyclic tests on the specimens cut along sheet's rolling

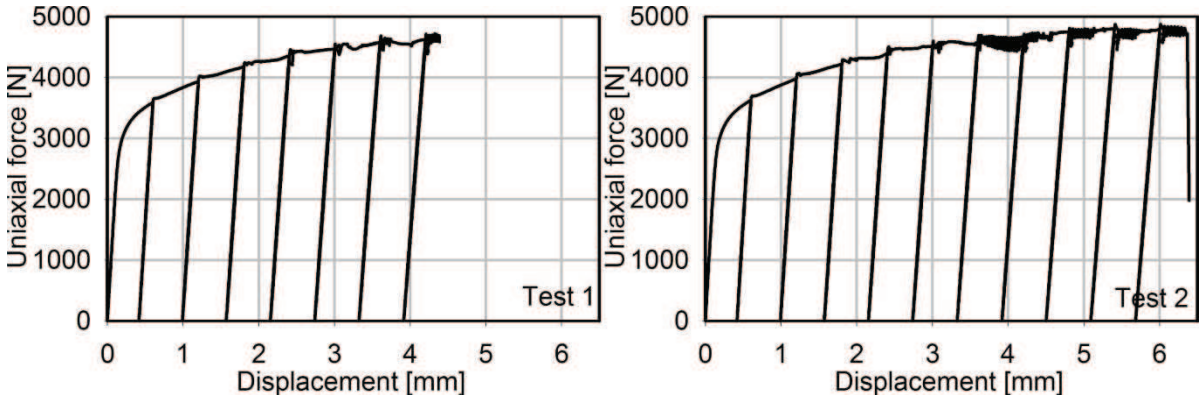

Fig. A5-4. Load-unload tension cyclic tests on the specimens cut across sheet's rolling

Annex 6

This annex contains the setting-up of all results obtained in the elastic modulus and offset yield stress identifications.

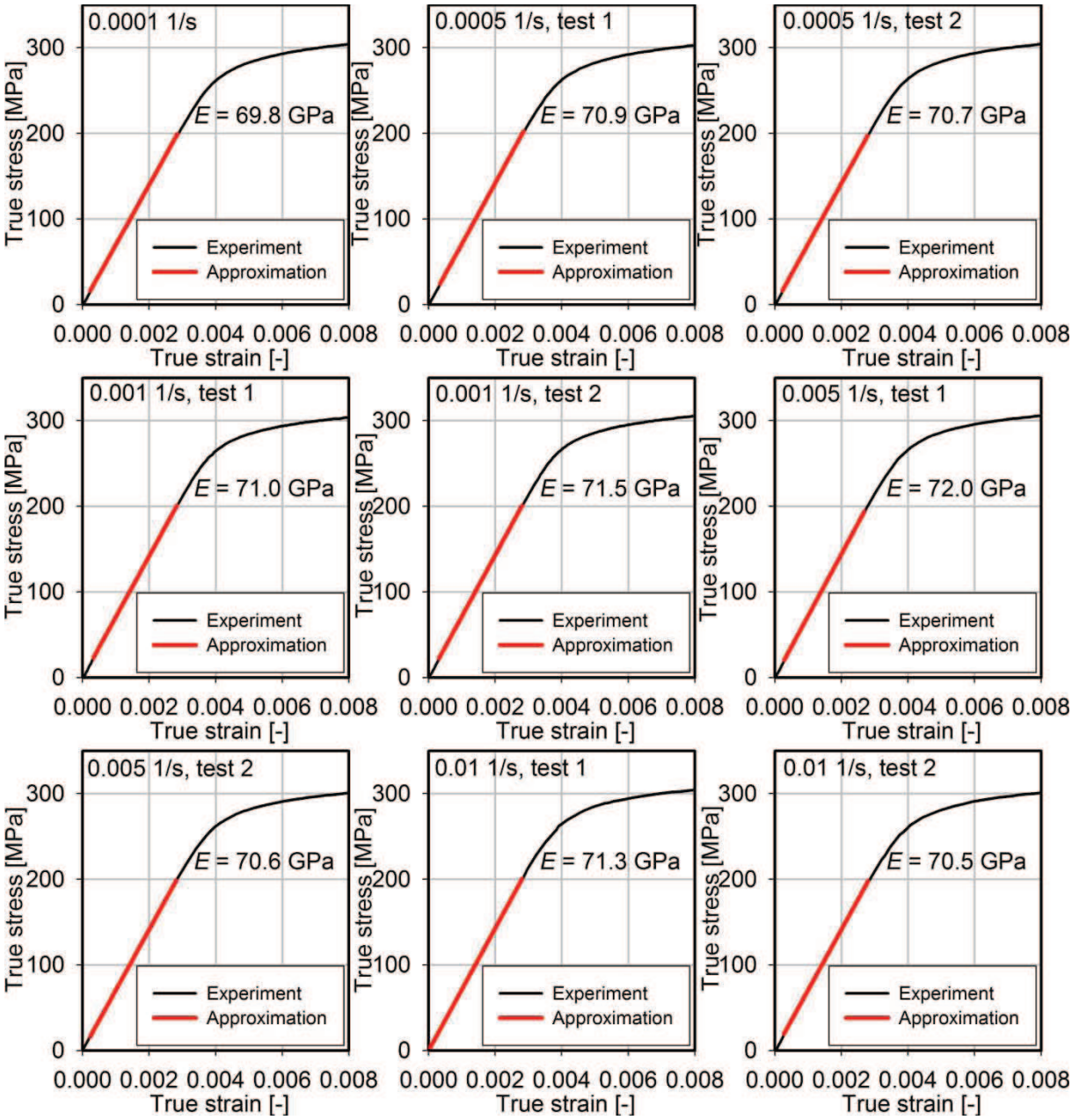

Fig. A6-1. Elastic modulus identifications, the specimens cut along sheet's rolling

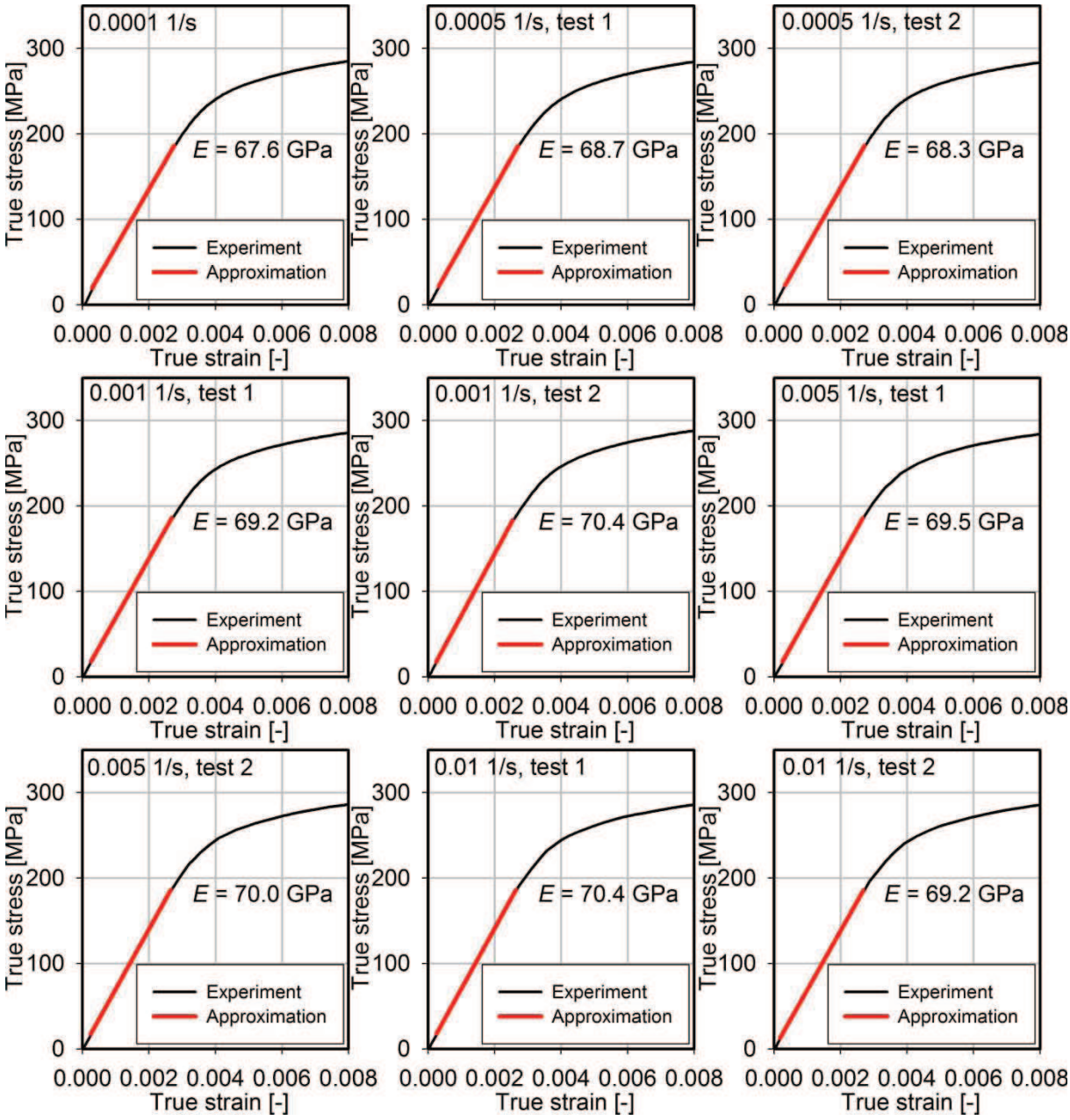

Fig. A6-2. Elastic modulus identifications, the specimens cut across sheet's rolling

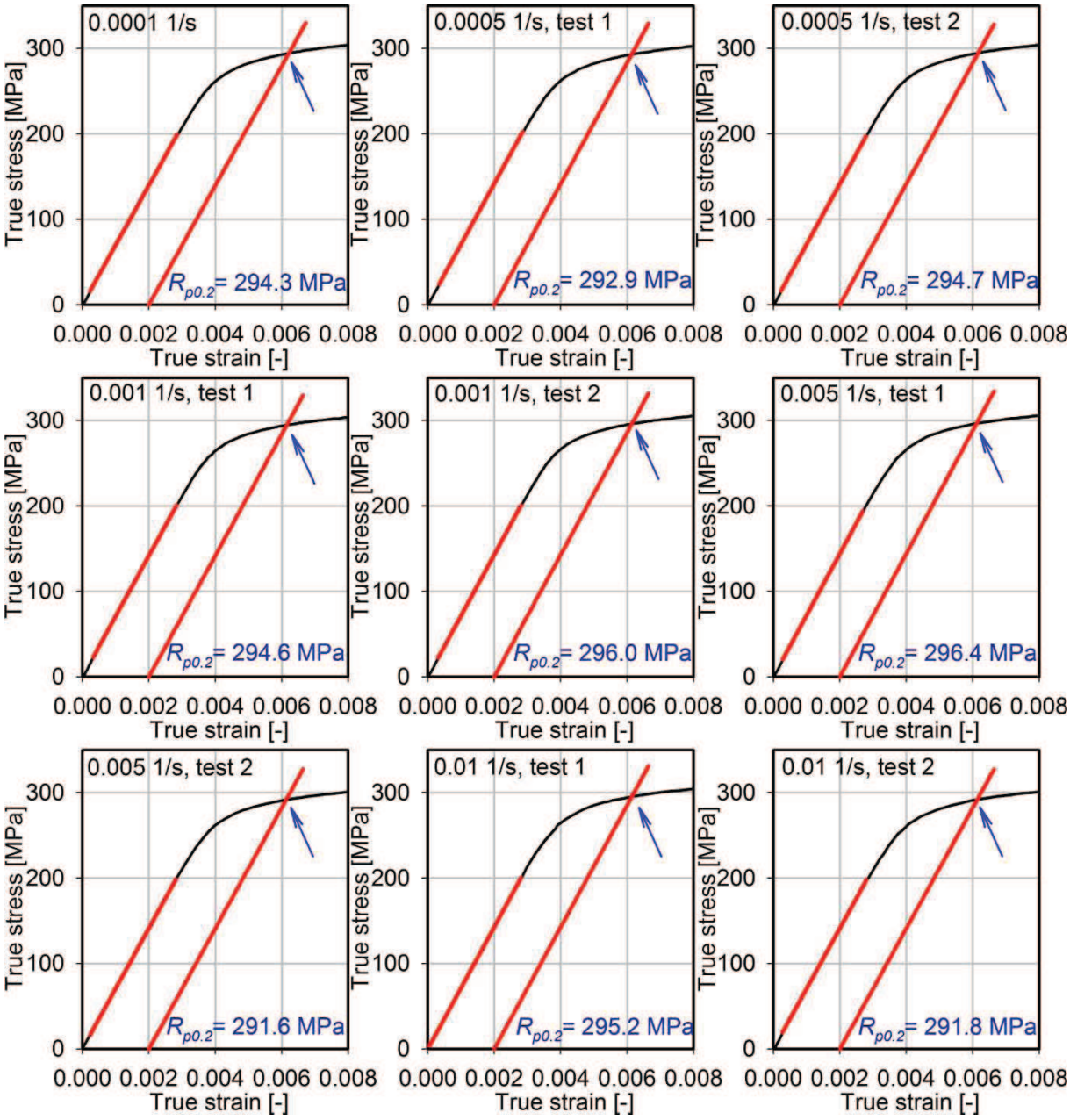

Fig. A6-3. Offset yield strength identifications, the specimens cut along sheet's rolling

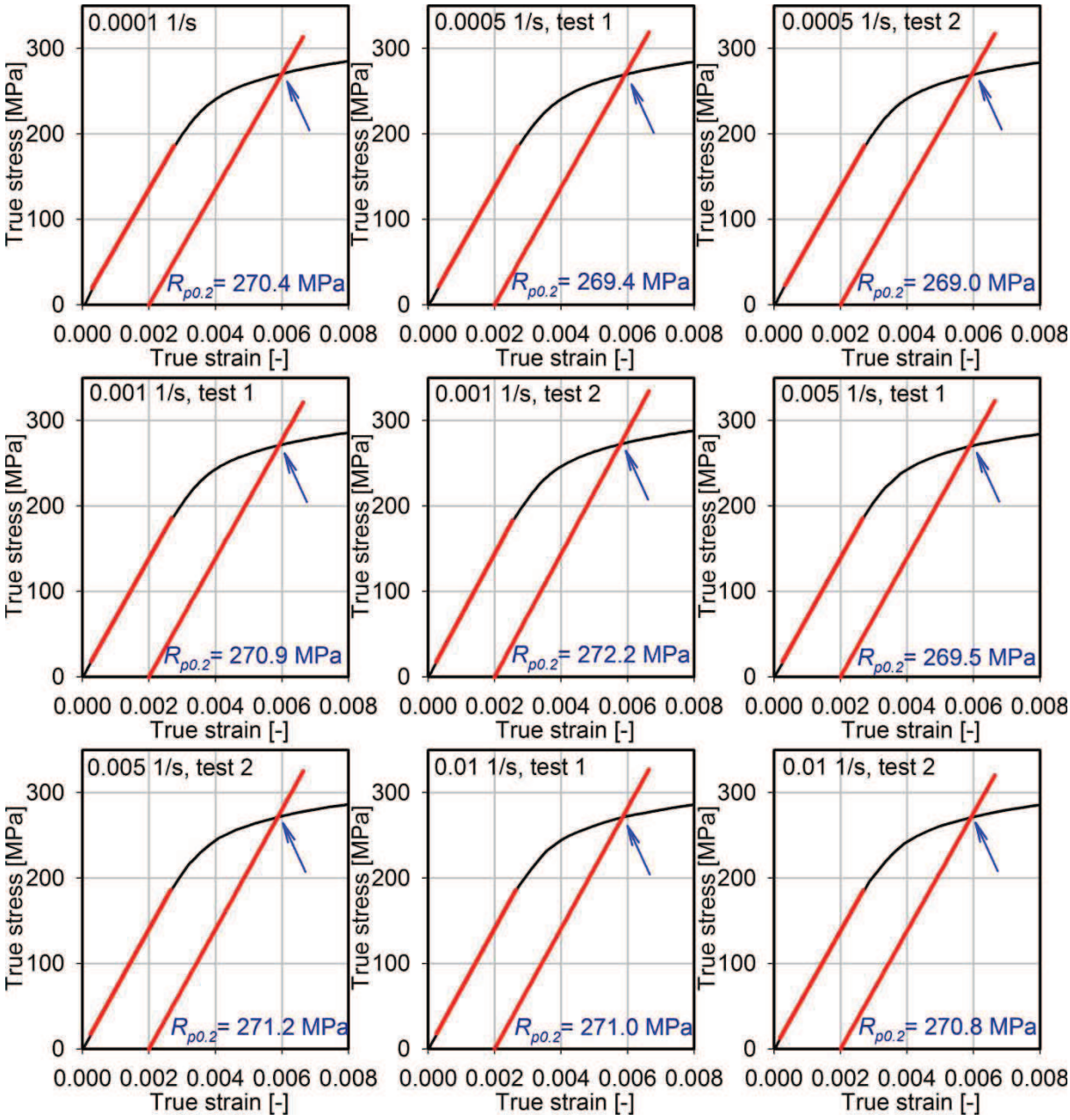

Fig. A6-4. Offset yield strength identifications, the specimens cut across sheet's rolling

Annex 7

Annex contains the results of final verification in the determination of plate's fixing boundary conditions. The plate's cross-sections obtained in the simulations compared with the experimental result for each test are presented.

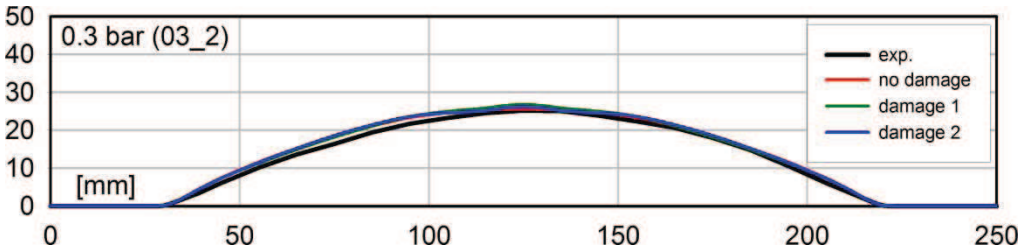

Fig. A8-1. Plate's cross-sections, test 03_2 (0.3 bar)

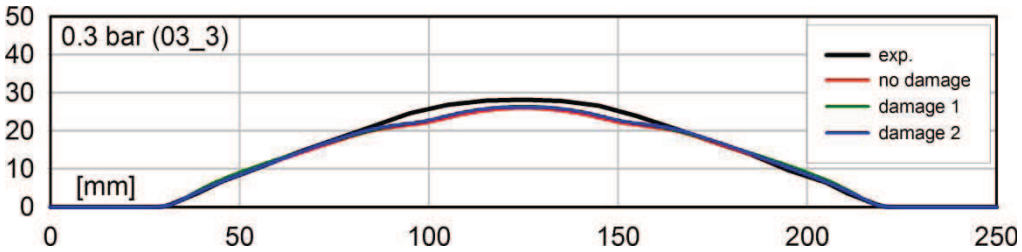

Fig. A8-2. Plate's cross-sections, test 03_3 (0.3 bar)

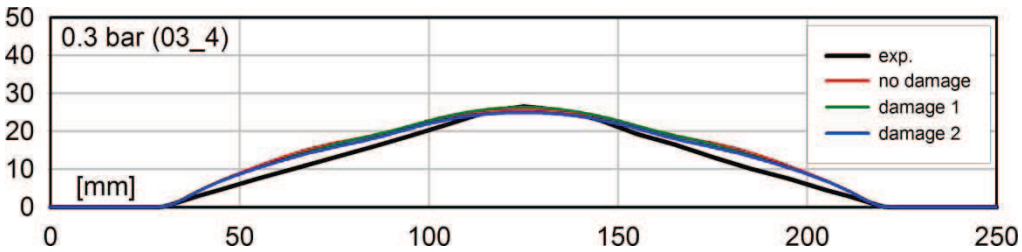

Fig. A8-3. Plate's cross-sections, test 03_4 (0.3 bar)

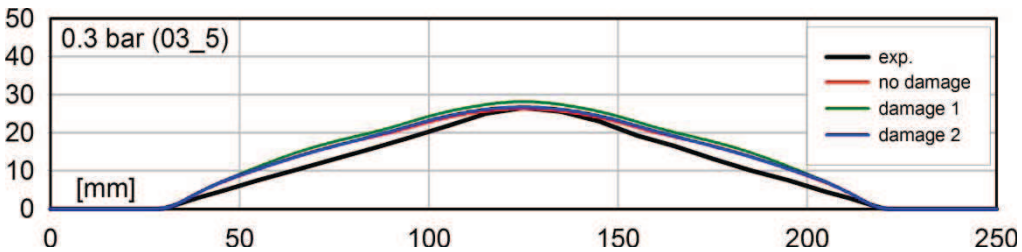

Fig. A8-4. Plate's cross-sections, test 03_4 (0.3 bar)

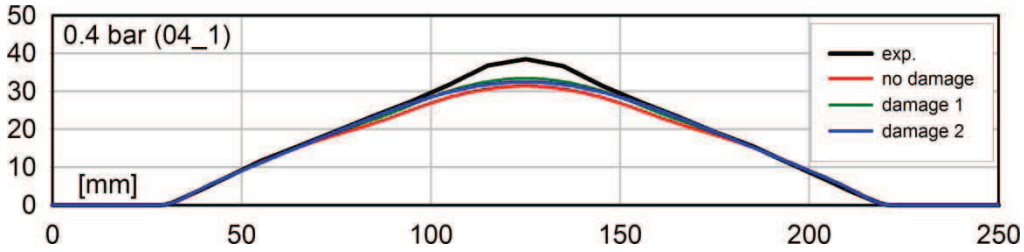

Fig. A8-5. Plate's cross-sections, test 04_1 (0.4 bar)

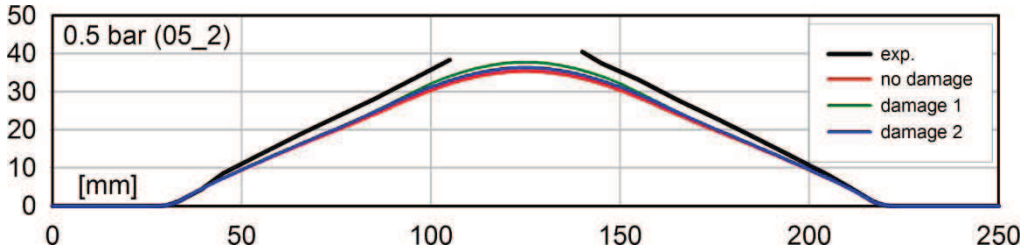

Fig. A8-6. Plate's cross-sections, test 05_2 (0.5 bar)

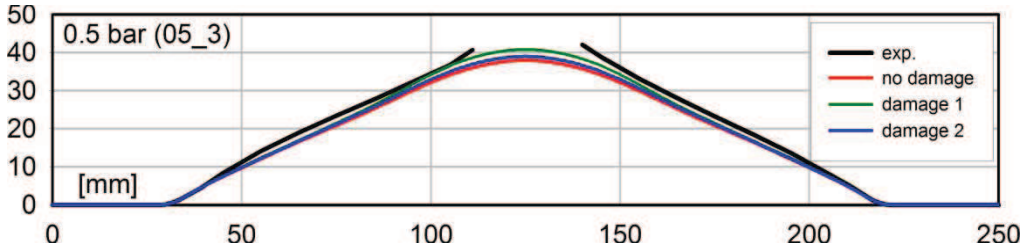

Fig. A8-7. Plate's cross-sections, test 05_3 (0.5 bar)

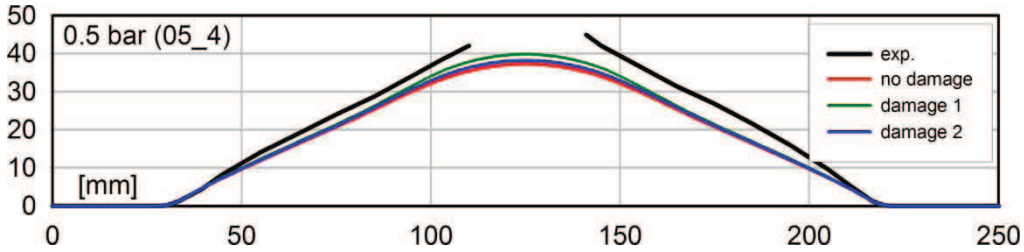

Fig. A8-8. Plate's cross-sections, test 05_3 (0.5 bar)

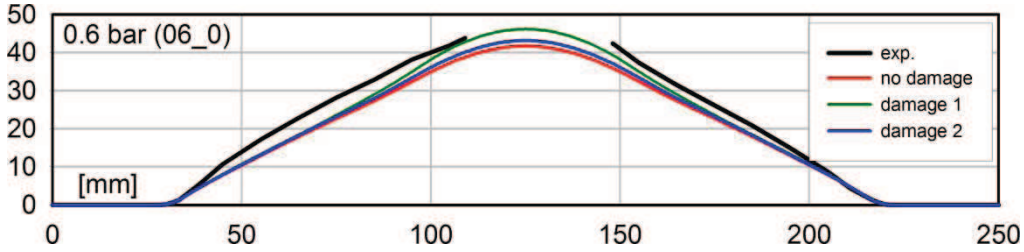

Fig. A8-9. Plate's cross-sections, test 06_0 (0.6 bar)

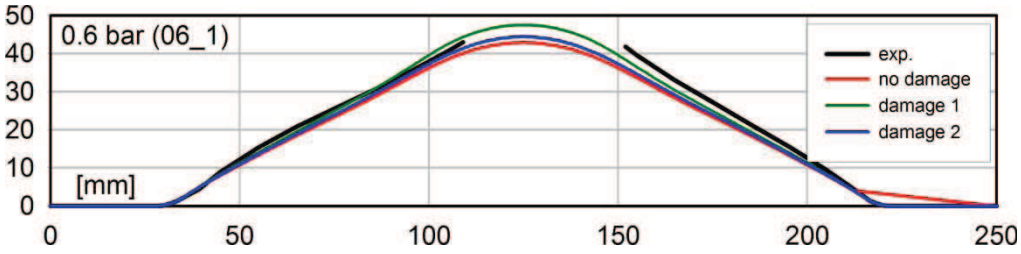

Fig. A8-10. Plate's cross-sections, test 06_1 (0.6 bar)

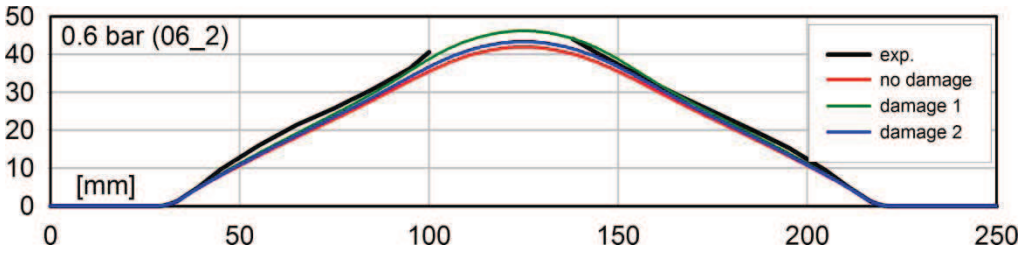

Fig. A8-11. Plate's cross-sections, test 06_2 (0.6 bar)

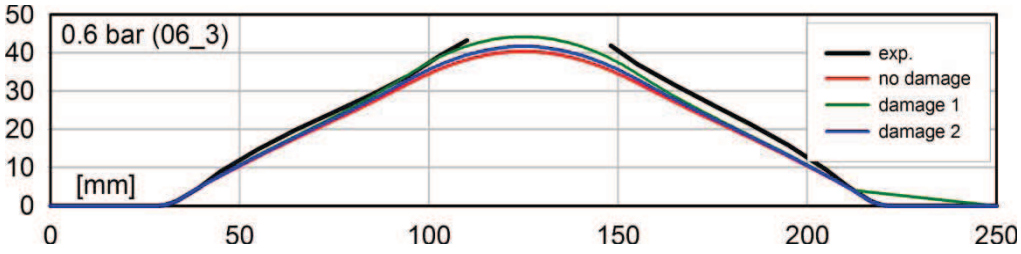

Fig. A8-12. Plate's cross-sections, test 06_3 (0.6 bar)

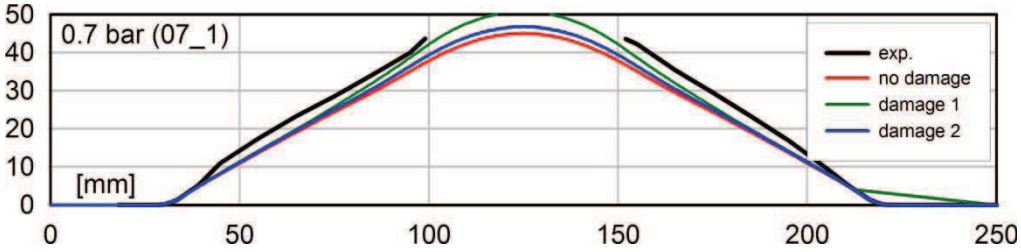

Fig. A8-13. Plate's cross-sections, test 07_1 (0.7 bar)

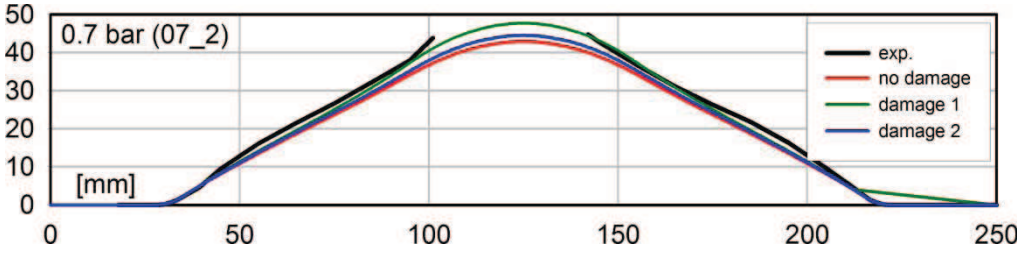

Fig. A8-14. Plate's cross-sections, test 07_2 (0.7 bar)

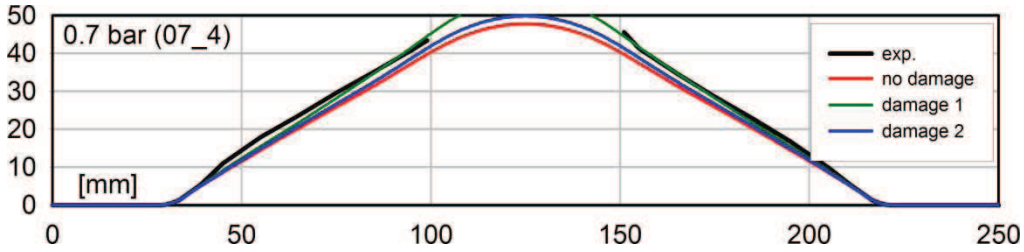

Fig. A8-15. Plate's cross-sections, test 07_4 (0.7 bar)

Łukasz PYRZOWSKI

Analyse visco-plastique de l'endommagement des plaques et coques soumises aux impacts

Le travail concerne le comportement des plaques et coques soumises à des charges dynamiques dues à des explosions des mélanges gazeux. Des problèmes mécaniques d'apparition des fissures et d'endommagement ductile sont analysés. En introduction, la revue de la littérature a été présentée ainsi que les théories actuellement les plus souvent utilisées dans ce domaine. Une brève description des outils numériques qui ont servi dans l'étude a été également donnée. Les essais expérimentaux et les résultats des mesures ont été discutés dans la deuxième partie du mémoire. Ils ont permis d'identifier les paramètres matériels du modèle constitutif viscoplastique et d'endommagement nécessaires pour mener une analyse numérique du comportement des plaques, de faire la vérification des nombreuses simulations discutées à la fin du travail. Dans les conclusions, est présenté le bilan des modélisations en exposant surtout celles qui ont conduit à de meilleurs résultats. L'auteur discute les hypothèses utilisées, les limitations du modèle et esquisse des perspectives et l'évolution possible à l'avenir.

mots-clés : dynamique des plaques, endommagement, fissuration, lois de comportement

Viscoplastic damage analysis of plate-shell structures subjected to impact loading

The work presents the investigation in the response of plate-shell structures subjected to impact loadings (gas mixture explosions). This phenomenon is studied in the context of its mechanical aspects, mainly the ductile fracture prediction. The work starts with the literature review and the description of theories, which are nowadays the most popular in the damage and fracture modelling. After selecting the theoretical models and the numerical tools for the further analysis, the detailed report of all realized experimental tests and their results is presented. Then, for the assumed constitutive and damage laws, the identification of material and fracture criteria parameters is realized. Finally, the numerical simulations are performed and their results, verified by the experiments, are summarized and commented. The work finishes with the conclusions, where the best approaches (from those, which have been tested) are pointed, all assumptions or limitations used in the study are discussed and the objectives for the further research are indicated.

Plates under impact loadings, fracture criteria, fracture modelling, damage

Institut PRISME, Université d'Orléans,
8 rue Léonard de Vinci
45072 Orléans Cedex, France